Politecnico di Milano
School of Industrial and Information Engineering
Department of Physics

Master Degree in Engineering Physics

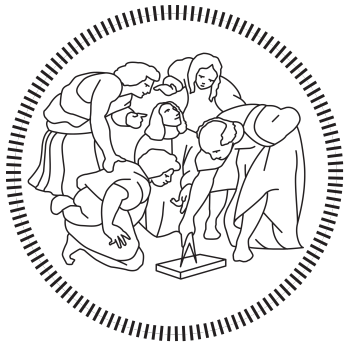

Ultrashort-pulse laser system for stand-off detection of bacterial spores by coherent anti-Stokes Raman spectroscopy

Supervisor: Prof. Nicola COLUCCELLI

Candidate: Valter VITALI, Matr. 913157

Academic Year 2020/2021

Abstract

This thesis focuses on the realisation of an ultra-short pulse source for coherent anti-Stokes Raman spectroscopy and its use in molecular detection of chemical and biological weapons, which requires stand-off configurations capable of preventing operator contamination, speed in measurement and ability to scan large samples.

Raman spectroscopy is widely used in medical and biological field due to its high specificity and speed of analysis compared to classical microbiological or chemical testing techniques. This particular phenomenon of light-matter interaction allows very fast identification of the substances in a sample by recognising spectral patterns that make up the Raman fingerprint of each molecule. The progress of machine learning algorithms has contributed to develop molecular recognition automatism and imaging systems.

However, low Raman cross section has so far relegated the Raman spectroscopy to microscopy setups. The future development, in which fits this thesis work, is to exploit the technique for distant and scattering samples also: this would allow the analysis of objects, surfaces or items which might be contaminated, such as in airports or post offices. Although, the requirement of remote detection drastically reduces the amount of signal that can be collected. In order to ensure a sufficiently strong Raman scattering signal, a high-energy ultrashort pulsed laser source must be employed, together with high sensitivity detectors.

The broadband CARS source was designed with known well principles of non-linear optics, including SHG and OPA. Pulse spectral shaping was exploited to handle time-resolved hybrid-CARS technique. After source set up, it was used for measurement on samples simulating spores of anthrax bacterium, which is one of the most dangerous threats of the last century and has recently claimed victims in the United States. Lastly, a scanning system for stand-off imaging purposes was built and successfully tested on simulants generating higher Raman signal.

A side project involved the construction of a system to amplify and spectral widen a laser comb for metrology purposes. The experiment, carried out by an external team of researchers and based on Doppler broadening thermometry, should lead to a more resolute definition of the Boltzmann constant in the International System.

Contents

List of Figures

Introduction

Over the last hundred years, advances in biology and medicine have meant that life expectancy has more than doubled. The availability of antibiotics, drugs and vaccines has dramatically lowered the lethality rate, allowing serious and fatal diseases to be cured. However, infections from external agents that may lead to death must be identified early enough to be treated. Speed of diagnosis and proximity to hospital facilities are essential to ensure the necessary treatments: two things that are by no means taken for granted, especially in poorer countries. Because of this, until the middle of the last century biological agents were often used as weapons during wars, when health care organization and institutions were already flooded or collapsed. Bacteria, viruses, fungi, algae or toxins produced by them were used to contaminate territories and humans or to make food and water supplies worthless in a quiet and invisible way.

In particular, among bacteria the one causing anthrax, *Bacillus anthracis*, is one of the most fearsome since it affects both animals and humans, causing them serious symptoms which can lead to death in a very high percentage of cases. Pneumonia anthrax infection is fatal in 50–80 % of cases, even with treatments. Its endospores resist heat, drying, and many disinfectants, so that it can persist in the environment for several years. Moreover, the principal spread method for humans is via spores, either by contact or inhalation.

As biological weapon, *B. Anthracis* spores can be disseminated both by releasing them into air or contaminating specific targets. Even though the practice, along with others biological weapons, has been curbed from 1975 by the Biological Weapons Convention, both the possible use by terrorist groups and the high spore resistance in natural environment make it a current issue. Cases of anthrax poisoning are well known, such as the 2001 cases in the USA where five people died and seventeen others were injured, after opening letters addressed to them containing anthrax spores.

The search for the presence of anthrax bacteria and spores can be done by means of cultures, microbiological analyses and genetic sequencing or mass spectrometry, which require incubation time of many hours, equipped laboratories and, most importantly, direct contact with the contaminant. Moreover, the contaminants research in large open areas is almost impossible. By way of example, the little Scottish island of Gruinard, contaminated as a result of British Army experiments, was entirely reclaimed and sheep were used to test the effectiveness of remediation.

Therefore, in recent decades it has arisen the need to design biological hazards detection systems that give an immediate response without direct contact with pathogens (so called *stand-off* detection). Existing laser-based configurations allow to rapidly scan large areas for remote sensing purposes. This is the frame in which this project is inserted:

design a non-invasive, efficient, rapid and wide-ranging technique to detect the presence of spores and other biological contaminants in targeted environments (e.g. airports or postal offices).

Raman scattering is a well known effect which has been used so long as a technique for chemical identification in complex environments, as it results from interaction with molecular vibration and thus with atomic bonds, which are unique from molecule to molecule: a certain pattern of resonance peaks can precisely identify a specific substance, as a fingerprint [1]. Therefore, by suitably illuminating a sample, it is theoretically possible to acquire Raman radiation and extract data from it that can make viable the identification of biological substances (e.g. bacterial spores) from a stand-off configuration and without damaging the surface under investigation [2]. However, its application is limited by very low Raman scattering cross section, which allows the technique to be used only in microscopy configuration, with long acquisitions that are not compatible with scan of wide areas [3].

Over the decades, spontaneous Raman scattering has been at the heart of numerous techniques which exploit coherence to enhance Raman signal, such Stimulated Raman Scattering (SRS) or Coherent Anti-Stokes Raman Spectroscopy (CARS) that have been used in different biomedical applications as cancer detection. Broadband CARS has allowed the simultaneous analysis of vast bands of Raman vibration spectrum, with shorter measurement times. More sophisticated techniques such as time-resolved CARS or hybrid CARS have enabled a further improvement on the amount of information that can be obtained from Raman resonances, enabling the possibility of resolve in time molecular events of few femtoseconds. Now, the availability of high energy ultra-short broadband pulse lasers has paved the way for the use of Raman spectroscopy in stand-off configuration also [4].

This thesis work is aimed to present the design process of a CARS source for Raman spectroscopy on bacterial spores, combined with a scanning setup for imaging purpose as well as an acquisition layout for scattered radiation and its analysis. All activities have been carried out in the laboratory of Optics, in the Department of Physics in Politecnico di Milano. The laboratory job was divided into three parts: in the first period, the laser source was built, optimised and characterised; then, it was used on several samples, measuring CARS signals and working on both the illumination-detection setup and the source for further optimisation. In the third period, another project in the field of metrology, detached at all from the main one, was carried out.

The thesis is therefore structured on the same partitioning: after the introduction and theoretical presentation, it is composed of three chapters.

In **Chapter 1: Theoretical principles** some subject which can be useful to fully understand the subsequent topics is discussed, starting from the basis of ultrashort pulses propagation inside materials. Mathematical description of linear and non-linear optics is presented. In particular second order effects as Second Harmonic Generation (SHG) and Optical Parametric Amplification (OPA) are described in detail, including technical indications on phase-matching and non-linear crystals that were essential to realise the laser source. The discussion then turns to third order optics and self-effects, also exploited for seed generation in the source design. Finally, Raman scattering is comprehensively

presented, starting from the physical phenomena governing it, moving on coherence techniques, focusing particularly on CARS and all modern setups that include the one on which this work is based.

The source for CARS is showed in **Chapter 2: Hybrid-CARS source design**. After a short presentation of the laboratory equipment, the overall setup is introduced, which is composed on three lines corresponding to the three pulses needed (called probe, pump and Stokes). Always bearing in mind the diagram on page 66 (Fig. 2.6), each line is explained, devoting special section to the most important stages and techniques (SHG, WLC, OPA, spectral shaping, prisms compressor, etc.). A brief parenthesis to analyse the phenomenon of spontaneous fluorescence in non-linear crystals is discussed at page 78. Lastly, the source output used for measures is characterized.

The **Chapter 3: CARS detection** introduces the measure process and data. Firstly, illumination and detection setup is presented, describing also its calibration. Then, some TR-CARS maps are presented and analysed, with a focus on Raman fingerprint for different substances, both liquid and solid. The signal intensity tunability and scalability is discussed. Finally, measures on a dipicolinic acid salt (NaDPA), which is present at high concentrations as calcium dipicolinate in bacterial spores, are conducted, as well as on spores of *B. subtilis* that simulate the *anthracis*, which could not be used in the laboratory for safety reasons [5]. The chapter ends with a brief discussion on the imaging setup used to scan a wide sample area and the subsequent creation of hyperspectral images for molecular identification. Machine learning algorithms are used to recognize spectral patterns and identify whereas the molecule is present or not in each scanned point, returning the image of molecular concentration in the sample.

As mentioned before, during the laboratory activities a separate project was carried out: it involved the design of an amplification system for a frequency comb laser that will be used by a research group for metrology purposes. In particular, the comb should stabilize a laser for a Doppler Broadening Thermometry (DBT) experiment aimed to measure the Boltzmann constant with a higher resolution than is currently defined by the International System. Optical beat notes are exploited for stabilization. **Chapter 4: Absolute referencing of a 1015 nm laser for Boltzmann constant metrology** introduces, without presumption of completeness, the framework within the DBT experiment is inserted. Some theoretical hints are discussed, before the presentation of the designed setup for a laser comb spectrum widener and the obtained results.

Chapter 1

Theoretical principles

In this chapter the basis of physical principles developed during the thesis are presented [6][7]. In Section 1.1, the master wave equation for pulse propagation is introduced, deriving time and spectral evolution of a Gaussian pulse as it passes through a material, both in a linear and non-linear regime. In the next Section 1.2 the focus is put on second order optics: mathematical description precedes the discussion on specific phenomena as Second Harmonic Generation and Optical Parametric Amplification, which are used in the experimental setup to amplify pulses and handle their time and spectral characteristics. Furthermore, Section 1.3 presents third order optics in a general way, together with degenerate phenomena (self-effects) which provide the seed signal for source. Finally, in the last Section 1.4, Raman scattering and its physical description are introduced, followed by different spectroscopic techniques for coherence enhancing and background removal.

1.1 Ultrashort pulse propagation

1.1.1 Introduction to wave equations

Any electromagnetic travelling in a medium can be described from the classical wave equation, derived from Maxwell's equations. Under the hypothesis of source-free material (i.e. $\rho = 0$ and $\vec{j} = 0$), isotropic (i.e. ε and μ tensors simplify in scalar quantities) and non-ferromagnetic medium (i.e. $\mu = \mu_0$), the master wave equation can be written in the form of

$$\nabla^2 \vec{E} - \frac{1}{c}\frac{\partial^2 \vec{E}}{\partial t^2} = \mu_0 \frac{\partial^2 \vec{P}}{\partial t^2} \tag{1.1}$$

where c is the speed of light in vacuum, $\vec{E}$ is the electric field vector and $\vec{P}$ is the polarization density vector (henceforth referred as polarization). Considering now a linearly polarized electric field along x axis ($\vec{E} = E\,\hat{u}_x$) travelling along z direction ($\vec{k}_0 = k_0\,\hat{u}_z$), which simplifies the vectorial equation into a scalar one, and the *plane wave approximation* thus $E(x, y, z, t) = E(z, t)$ (i.e. assuming to be sufficiently far from the source to consider spherical phase fronts flat and the field is constant along (x, y)-plane), and applying the

same reasoning to vector $\vec{P}$, the master equation simplifies in

$$\frac{\partial^2 E}{\partial z^2} - \frac{1}{c}\frac{\partial^2 E}{\partial t^2} = \mu_0 \frac{\partial^2 P}{\partial t^2} \tag{1.2}$$

which can be shifted in frequency domain using the properties of Fourier transform in order to get rid of temporal derivates, i.e. $\mathscr{F}\left\{\frac{d^n E(t)}{dt^n}\right\} = (i\omega)^n \tilde{E}(\omega)$ (where $\mathscr{F}\{E(t)\} = \tilde{E}(\omega)$), thus obtaining

$$\frac{\partial^2 \tilde{E}}{\partial z^2} + \frac{\omega^2}{c^2}\tilde{E} = -\mu_0 \omega^2 \tilde{P} \tag{1.3}$$

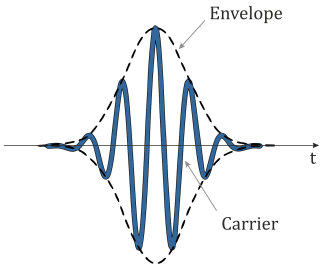

Figure 1.1: Ultrashort pulse carrier-envelope model.

Generally speaking, a short pulses can be modelled as an oscillating carrier wave modulated by an envelope function, as pictured in Figure 1.1. In the above frame, the electric field can be written as

$$E(z,t) = A(z,t)\cos(\omega_0 t - k_0 z + \phi(z,t)) = \frac{1}{2}[A(z,t)e^{i(\omega_0 t - k_0 z + \phi(z,t))} + c.c.] \tag{1.4}$$

where ω_0 is the carrier angular central frequency, ϕ its phase and k_0 is the carrier wavevector which is bound to angular frequency, i.e. $k_0 = \frac{\omega_0}{c} n(\omega_0)$, with n representing the refractive index. The expression *c.c.* substitutes its complex conjugate.

The same reasoning can applied to the polarization, which will result in

$$P(z,t) = p(z,t)\cos(\omega_P t - k_P z + \phi_P(z,t)) = \frac{1}{2}[p(z,t)e^{i(\omega_P t - k_P z + \phi_P(z,t))} + c.c.] \tag{1.5}$$

In a linear regime, whose description is a few line below, the polarization angular frequency and wavevector are the same of the electric field one, i.e. $\omega_0 = \omega_P$ and $\vec{k}_0 = \vec{k}_P$.

Without going into too much mathematical formalism details, the two Ansatz can be easily Fourier transformed as

$$\tilde{E}(z,\omega) = e^{-ik_0 z}\tilde{A}(z,\omega-\omega_0) \qquad \tilde{P}(z,\omega) = e^{-ik_P z}\tilde{p}(z,\omega-\omega_0) \tag{1.6}$$

and inserting it in (1.3) the obtained equation is

$$2ik_0\frac{\partial \tilde{A}}{\partial z} + (k_0 - \frac{\omega^2}{c^2})\tilde{A} = \mu_0\,\omega^2\tilde{P} \tag{1.7}$$

where the term $\frac{\partial^2 \tilde{A}}{\partial z^2}$ has been neglected for the *Slowly Envelope Function Approximation* (SVEA), which consider the second derivative lower in magnitude than the first derivative, which is a valid approximation for a free propagating pulse, being

$$\left|\frac{\partial^2 \tilde{A}}{\partial z^2}\right| \ll 2k_0 \left|\frac{\partial \tilde{A}}{\partial z}\right| \tag{1.8}$$

The equation (1.7) describes how the pulse changes when travels a medium which is not vacuum. In fact, when the electric field travels through materials it induces atoms or molecules, which are characterized by a permanent or induced dipole moment, to oscillates at the same frequency thus producing the polarization field. Oscillating charges drive an electromagnetic field emission as they are source points of new electric fields, which will further excite other particles, resulting in the transmission of light in such material. Emitted light will have of course new properties compared with the incoming light, such as different wave vector, velocities, pulse shape, spectrum, etc. All these information can be found in a quantity, called *electric susceptibility* whose symbol is χ, which relates the electric with the polarization fields, being

$$\vec{P} = \varepsilon_0 \chi \vec{E} \tag{1.9}$$

In general, χ is a tensor, relating each component of polarization in a different way, since medium properties can vary from axis to axis

$$\begin{bmatrix} P_x \\ P_y \\ P_z \end{bmatrix} = \varepsilon_0 \begin{bmatrix} \chi_{xx} & \chi_{xy} & \chi_{xz} \\ \chi_{yx} & \chi_{yy} & \chi_{yz} \\ \chi_{zx} & \chi_{zy} & \chi_{zz} \end{bmatrix} \cdot \begin{bmatrix} E_x \\ E_y \\ E_z \end{bmatrix} \tag{1.10}$$

As mentioned before, in an a isotropic material symmetry properties guarantee same interaction in any direction, so the tensor simplify in a scalar quantity.

In case the incoming electrical field has low intensity, we can assume the resulting polarization to be linearly dependant

$$\vec{P}_L = \varepsilon_0 \chi^{(1)} \vec{E} \tag{1.11}$$

where $\chi^{(1)}$ means the linear component of χ. This is the hypothesis that underlies the field of *linear optics*, which will be briefly analysed in the Section 1.1.2.

Generally speaking, the interaction could be not linear and it can be developed in series as sum of contributes

$$\vec{P} = \vec{P}_L + \vec{P}_{NL} = \varepsilon_0 \left[\chi^{(1)} \vec{E} + \chi^{(2)} \vec{E}^2 + \chi^{(3)} \vec{E}^3 + \cdots + \chi^{(n)+\cdots} \vec{E}^n \right] \tag{1.12}$$

such that the polarization vector is a sum of several contributes. The first is the linear one, while all the others give rise to *non-linear optics* effects, some of which will be analysed in the Section 1.1.3: the second term provides second order effects, the third one third order effects and so on. This kind of phenomena rise when the electric field has high magnitude. Note that while $\chi^{(1)}$ is dimensionless, the other n^{th}-terms are measured in $\mathrm{m}^{n-1}/\mathrm{V}^{n-1}$.

1.1.2 Linear optics

Operating in linear regime under the hypothesis of linearly polarized plane wave in a isotropic source-free non-ferromagnetic material, the polarization density can be related to the electric field with the identity

$$P = P_L = \varepsilon_0 \chi^{(1)} E = \varepsilon_0 [n^2(\omega) - 1] E \tag{1.13}$$

since $\chi^{(1)} = \varepsilon_r - 1$ and $n^2 = \varepsilon_r$. In addition, in linear regime the propagating direction of polarization and electric field vector does not change in the material, so $\vec{k}_0 = \vec{k}_P$.

Under these assumptions, the equation (1.7) can represent the pulse evolution referring only at electric field envelope spectrum as defined in eq. (1.6), which is represented by the envelope Fourier transform $\tilde{A}(\omega)$

$$2ik_0 \frac{\partial \tilde{A}}{\partial z} = \left[k^2(\omega) - k_0^2\right] \tilde{A} \tag{1.14}$$

where k is defined as $k^2(\omega) = n^2(\omega)\dfrac{\omega^2}{c^2}$.

Considering that all k-vector values (pulse k-sepctrum) are close to the central value k_0, $k(\omega)$ will be a value pretty similar (i.e. $k(\omega) \approx k_0$) and the term into square brackets can be decomposed as

$$k^2(\omega) - k_0^2 = [k(\omega) + k_0][k(\omega) - k_0] \approx 2k_0[k(\omega) - k_0] \tag{1.15}$$

Finally, the wave vector $k(\omega)$ can be expanded in series, resulting in

$$k(\omega) = k_0 + \frac{1}{v_g}(\omega - \omega_0) + \frac{1}{2} GVD(\omega - \omega_0)^2 + \dots \tag{1.16}$$

where it has been used the definition of *Group Velocity* and *Group Velocity Dispersion*, respectively

$$\frac{1}{v_g} = \left.\frac{dk}{d\omega}\right|_{\omega_0} \qquad\qquad GVD = \left.\frac{d^2k}{d\omega^2}\right|_{\omega_0} \tag{1.17}$$

At the end, truncating $k(\omega)$ at the second order term, the equation (1.14) is returned into time domain anti-Fourier transforming, or $\mathscr{F}^{-1}\{\omega^n \tilde{A}(w)\} = (-1)^n \dfrac{d^n A(t)}{dt^n}$, obtaining

$$\frac{\partial A(z,t)}{\partial z} + \frac{1}{v_g}\frac{\partial A(z,t)}{\partial t} - \frac{i}{2} GVD \frac{\partial^2 A(z,t)}{\partial t^2} = 0 \tag{1.18}$$

By transferring the description just completed into a reference system travelling at the same velocity as the impulse, i.e. by implementing the Lorentzian transformation $z \longrightarrow z'$ and $t \longrightarrow t' + \frac{z}{v_g}$, the final *parabolic equation* is stated

$$\frac{\partial A(z,t)}{\partial z} - \frac{i}{2} GVD \frac{\partial^2 A(z,t)}{\partial t^2} = 0 \tag{1.19}$$

Now, considering a pulse travelling in a non-dispersive material ($k(\omega) = \frac{\omega}{c} n_0$) or in vacuum ($n_0 = 1$), the group velocity is equal to the phase velocity while the GVD must be zero

$$v_g = \left[\frac{d}{d\omega}(k(\omega))\right]^{-1} = \frac{c}{n_0} = v_p \qquad GVD = 0 \tag{1.20}$$

So the parabolic equation (1.19) results in $\dfrac{\partial A}{\partial z} = 0$, suggesting that no change in the pulse envelope shape occurs during propagation. In fact, being group and phase velocity equal, each frequency of the pulse spectrum travels at the same speed so the pulse does not get time deformation, as represented in Figure 1.2.a.

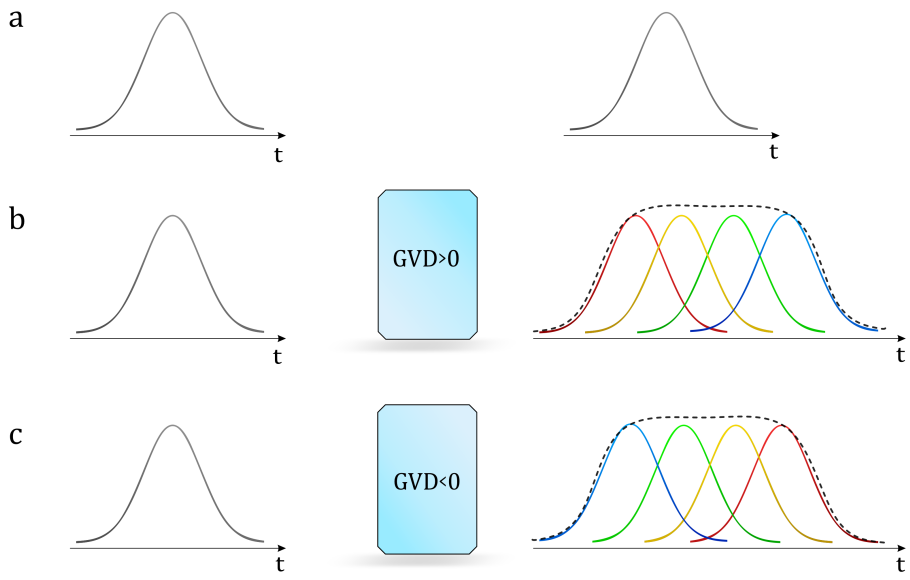

Figure 1.2: Representation of an ultrashort pulse travelling in *a)* vacuum. *b)* positive dispersed material. *c)* negative dispersed material.

Conversely, in a dispersive medium, the pulse envelop gets time-expanded: each frequency travels at different velocity which depends on the refractive index first derivative

$$v_g = \left[\frac{d}{d\omega}(k(\omega))\right]^{-1} = \left[\frac{\omega}{c}\frac{d\,n(\omega)}{d\omega} + \frac{n(\omega)}{c}\right]^{-1} \tag{1.21}$$

A Gaussian pulse is considered a good model for ultrashort pulses, whose time evolution is represented by the expression

$$A(t) = A_0 e^{-\frac{t^2}{2\tau_p^2}} \tag{1.22}$$

where τ_p is the pulse duration, intended as the full pulse width at $1/e$ amplitude point.

Substituting eq. (1.22) in the parabolic (1.19), the final expression for an ultrashort Gaussian pulse travelling in a medium for a distance L is

$$A(L,t) = \frac{A_0\tau_p}{\sqrt{\tau_p^2 + iD_2}}\, e^{-\frac{t^2}{2\tau_p^2}} \qquad \text{with} \qquad D_2 = GDD = GVD \cdot L \tag{1.23}$$

where it has been introduced the quantity *Group Delay Dispersion* (GDD) or *second order dispersion* (D_2) which represents the second derivative of the pulse phase, i.e. $GDD = \left.\frac{d^2\phi}{d\omega^2}\right|_{\omega_0}$. For extension, Third Order Dispersion (TOD) is defined as $TOD = \left.\frac{d^3\phi}{d\omega^3}\right|_{\omega_0}$.

Travelling in a dispersive material, the pulse envelope has changed its temporal duration τ and phase. In fact, with some mathematical trick it can be rewritten as

$$\begin{aligned} A(z,t) = \frac{A_0\tau_p}{\sqrt{\tau_p^2 + iD_2}}\, e^{-\frac{t^2}{2\tau_{out}^2}}\, e^{i\varphi_{out}(t)} \qquad & \text{with} \qquad \tau_{out} = \tau_p\sqrt{1 + \left(\frac{D_2}{\tau_p^2}\right)^2} \\ & \text{and} \qquad \varphi_{out}(t) = \frac{D_2}{2(D_2^2 + \tau_p^4)}t^2 \end{aligned} \tag{1.24}$$

So, as the pulse propagates in the medium, it gets more and more time-broadened since τ_{out} increases, because D_2, which is proportional to the travelled distance L, increases.

It is worth noting that the pulse spectrum does not change its magnitude during propagation, since $\left|\tilde{A}(0,\omega)\right| = \left|\tilde{A}(z,\omega)\right|$: no change in frequency or new frequencies generation is attributable to linear optics.

Another noticeable effect is the so called *frequency chirp*: since each frequency in the pulse spectrum travels at a different velocity due to dispersion, some frequencies arrives before or after the others, as it is represented in Figure 1.2. The time pulse evolution in a fixed position $z = \bar{z}$ can be analysed looking at the output pulse in equation (1.24), recalling the envelope-carrier description. The pulse envelope is given by the amplitude term $\frac{A_0\tau_p}{\sqrt{\tau_p^2+iD_2}}\, e^{-\frac{t^2}{2\tau_{out}^2}}$, while the carrier information is contained in the phase term, i.e. $e^{i(\omega_0 t - kz + \varphi_{out})}$. Computing the instantaneous frequency in $z = \bar{z}$, the result is

$$\omega(t) = \left.\frac{d\phi}{dt}\right|_{z=\bar{z}} = \frac{d}{dt}(\omega_0 t - k\bar{z} + \varphi_{out}) = \omega_0 + \frac{D_2}{2(D_2^2 + \tau_p^4)}t \tag{1.25}$$

where it is evident that the frequency changes over time, which is a phenomenon bearing a resemblance to bird's *chirp*.

1.1.3 Non-linear optics

If the incoming electric field has an intensity which does not allow the use of the linear approximation, also higher order effects on polarization must be taken into account

$$P = \varepsilon_0 \left[\underbrace{\chi^{(1)}E}_{P_L} + \underbrace{\chi^{(2)}E^2 + \chi^{(3)}E^3 + \dots}_{P_{NL}} \right] \tag{1.26}$$

For the sake of clarity, this kind of description is valid in a isotropic material. If this hypothesis was to fail, the tensor character of optical susceptibility would have to be taken into account, i.e. each polarization direction would be a sum of different combinations, such as $P_i = \varepsilon_0 \sum_j \chi^{(1)}_{ij} E_j + \varepsilon_0 \sum_{j,k} \chi^{(2)}_{ijk} E_j E_k + \varepsilon_0 \sum_{j,k,l} \chi^{(3)}_{ijkl} E_j E_k E_l + \dots$. It is worth nothing that in case of centre-symmetric materials, i.e. invariant to inversion symmetry (point reflection), second order susceptibility $\chi^{(2)}$ is null.

As the polarization has now two contributes, the linear and non-linear ones, the equation (1.2) must be modified as

$$\frac{\partial^2 E}{\partial z^2} - \frac{1}{c}\frac{\partial^2 E}{\partial t^2} = \mu_0 \frac{\partial^2 P_L}{\partial t^2} + \mu_0 \frac{\partial^2 P_{NL}}{\partial t^2} \tag{1.27}$$

Using the same process as seen in Section 1.1.2, with the SVEA assumption and the properties of Fourier transform, the resulting equation is

$$\frac{\partial A}{\partial z} + \frac{1}{v_g}\frac{\partial A}{\partial t} - \frac{i}{2} GVD \frac{\partial^2 A}{\partial t^2} = -i \frac{\mu_0 \omega_0 c}{2 n_0} p_{NL} e^{i\Delta k z} \tag{1.28}$$

where n_0 is the refractive index at central carrier frequency $n(\omega_0)$, p_{NL} is the non-linear polarization envelope and Δk the *wave-vector mismatch*, representing the quantity $\Delta k = k_P - k_0$. The envelope (A or p_{NL}) dependence on space and time has been not expressed for notation simplicity. Note that it is a scalar quantity because propagation on z-axis only is considered. With respect to the previous equation (1.18), there is the new non-linear term that acts as a further source of radiation. It directly involves the medium properties contained in χ_{NL}.

In the next section, pulse propagation with second order effects ($\chi^{(2)}$) are analysed, while in Section 1.3 third order ones will be briefly reviewed.

1.2 Second order optics

In the this part, second order optics is taken into account, going into two of the non-linear effects exploited in laboratory: Second Harmonic Generation (SHG, Sect. 1.2.2) and Difference Frequency Generation (DFG), which are observed in non-linear crystals at particular conditions (Sect. 1.2.3). DFG is the optical phenomenon at the basis of Optical Parametric Amplifier (OPA), which will be comprehensively described in Sections 1.2.4–1.2.7.

1.2.1 Master equation

Second order polarization must consider the interaction of two pulses, oscillating at two carrier frequency ω_1 and ω_2 being

$$P^{(2)}_{NL}(t) = \varepsilon_0 \chi^{(2)} \left[\frac{1}{2} \left(A_1(t) e^{i\omega_1 t} + c.c. + A_2(t) e^{i\omega_2 t} + c.c. \right) \right]^2 \tag{1.29}$$

where the spatial terms ($e^{-ik_1 z}$ and $e^{-ik_2 z}$) are neglected for the moment. Doing the quadrinomial square, the calculus results in

$$P_{NL}^{(2)}(t) = \frac{\varepsilon_0 \chi^{(2)}}{4} \Big[A_1^2 e^{i2\omega_1 t} + c.c. + A_2^2 e^{i2\omega_2 t} + c.c. + 2A_1^* A_2 + 2A_1 A_2^* + \\ + 2A_1 A_2 e^{i(\omega_1+\omega_2)t} + c.c. + 2A_1^* A_2 e^{i(\omega_1-\omega_2)t} + c.c. \Big] \quad (1.30)$$

There are two terms oscillating at $2\omega_1$, two at $2\omega_2$ (the squares), two constant terms, two oscillating at $\omega_1 + \omega_2$ and two at $\omega_1 - \omega_2$ (the cross products). So a second order interaction gives rise to new frequencies: it has created new fields which has doubled the initial frequency (Second Harmonic Generation, SHG), summed the two frequencies (Sum Frequency Generation, SFG) and subtracted them (Difference Frequency Generation, DFG). Therefore, three waves has to be considered, each one will have its own propagation equation. The overall pulse will contain three contributions, i.e.

$$E(z,t) = \frac{1}{2} \Big[A_1(z,t) e^{i(\omega_1 t - k_1 z)} + A_2(z,t) e^{i(\omega_2 t - k_2 z)} + A_3(z,t) e^{i(\omega_3 t - k_3 z)} + c.c. \Big] \quad (1.31)$$

whose envelope amplitude will vary in time according to the equation (1.28). All the processes described above can be modelled assuming the relation $\omega_3 = \omega_1 + \omega_2$ between the waves. This kind of processes in fact are often called *three-wave mixing*. In case of SFG, for example, the third wave will be the frequency sum between the other two, namely $\omega_3 = \omega_{SFG} = \omega_1 + \omega_2$: it is logical to presume that envelope A_3 has zero amplitude at the starting point, where no material interaction has occurred, and will gain intensity during propagation while A_1 and A_2 will lose it, in favour of the third. While in case of DFG ω_{DFG} is defined as $\omega_1 = \omega_3 - \omega_2$. In this case the envelope amplitude A_1 will increase while A_2 and A_3 will decrease.

Assuming $\omega_3 = \omega_1 + \omega_2$, from expression (1.31) it is possible to get the polarization general formula $P_{NL}(z,t) = \varepsilon_0 \chi^{(2)} E^2(z,t)$ which contains 21 terms. Since the frequencies which appear in the the expression are ω_1, ω_2 and ω_3, all the other terms can be neglected, hence obtaining the second order polarization contributions, which oscillates at ω_1, ω_2 and ω_3 respectively

$$\begin{cases} P_{NL}^{\omega_1}(z,t) = \dfrac{\varepsilon_0 \chi^{(2)}}{4} 2A_2^* A_3 \, e^{i[(\overbrace{\omega_3 - \omega_2}^{\omega_1})t - (k_3 - k_2)z]} + c.c. \\ P_{NL}^{\omega_2}(z,t) = \dfrac{\varepsilon_0 \chi^{(2)}}{4} 2A_1^* A_3 \, e^{i[(\overbrace{\omega_3 - \omega_1}^{\omega_2})t - (k_3 - k_1)z]} + c.c. \\ P_{NL}^{\omega_3}(z,t) = \dfrac{\varepsilon_0 \chi^{(2)}}{4} 2A_1 A_2 \, e^{i[(\overbrace{\omega_1 + \omega_2}^{\omega_3})t - (k_1 + k_2)z]} + c.c. \end{cases} \quad (1.32)$$

Inserting such there source expressions in the equation (1.28), the three master equations

for pulse envelope propagation are obtained

$$\begin{cases} \dfrac{\partial A_1}{\partial z} + \dfrac{1}{v_{g_1}}\dfrac{\partial A_1}{\partial t} - \dfrac{i}{2}GVD_1\dfrac{\partial^2 A_1}{\partial t^2} = -i\dfrac{\mu_0\omega_1 c}{2n_1}\dfrac{\varepsilon_0\chi^{(2)}}{2}A_2^* A_3 e^{-i\Delta kz} \\ \dfrac{\partial A_2}{\partial z} + \dfrac{1}{v_{g_2}}\dfrac{\partial A_2}{\partial t} - \dfrac{i}{2}GVD_2\dfrac{\partial^2 A_2}{\partial t^2} = -i\dfrac{\mu_0\omega_2 c}{2n_2}\dfrac{\varepsilon_0\chi^{(2)}}{2}A_1^* A_3 e^{-i\Delta kz} \\ \dfrac{\partial A_3}{\partial z} + \dfrac{1}{v_{g_3}}\dfrac{\partial A_3}{\partial t} - \dfrac{i}{2}GVD_3\dfrac{\partial^2 A_3}{\partial t^2} = -i\dfrac{\mu_0\omega_3 c}{2n_3}\dfrac{\varepsilon_0\chi^{(2)}}{2}A_1 A_2 e^{i\Delta kz} \end{cases} \tag{1.33}$$

recalling the wave-vector mismatch as $\Delta k = k_3 - k_1 - k_2$. The equations can be simplified introducing the quantity $\gamma_i = \dfrac{\omega_i\,\chi^{(2)}}{4\,c\,n_i}$ and neglecting the GVD. In addition, it is convenient to refer all equations to the same reference system, travelling on the ω_3, i.e. Lorentzian transforming $t \longrightarrow t' + \frac{z}{v_{g_3}}$. They are subtracted two by two and the quantity of *Group Velocity Mismatch* defined as $\delta_{ij} = \dfrac{1}{v_i} - \dfrac{1}{v_j}$ is introduced, getting

$$\begin{cases} \dfrac{\partial A_1}{\partial z} + \delta_{13}\dfrac{\partial A_1}{\partial t} = -i\gamma_1 A_2^* A_3 e^{-i\Delta kz} \\ \dfrac{\partial A_2}{\partial z} + \delta_{23}\dfrac{\partial A_2}{\partial t} = -i\gamma_2 A_1^* A_3 e^{-i\Delta kz} \\ \dfrac{\partial A_3}{\partial z} = -i\gamma_3 A_1 A_2 e^{i\Delta kz} \end{cases} \tag{1.34}$$

These are the three master equations that rule on the propagation behaviour of pulse envelopes with a carrier frequency respectively at ω_1, ω_2 and ω_3. Each pulse envelope A_i changes shape over propagation (which motion is described from the left-hand side expression) due to the presence of other two pulse envelopes (right-hand side of the equation). This is the simple non-linear effect, since it involves the interaction of two electric field. Third non-linearities should involve similar equations, with the only difference being that the source term (i.e. the right-hand side expression) will contain three interacting fields instead of two. It is essential to note the presence of the exponential term $e^{-i\Delta kz}$: if Δk has a large value, i.e. the wave-vectors are strongly mismatched, the NL term will be infinitesimal so the process efficiency will be very low. In order for non-linear processes to be observed, it is necessary to approach the so-called *phase-matching* condition, namely $\Delta k = 0$. In this way the highest efficiency of the source terms is achieved. Recalling the definition of wave-vector and wave-vector mismatch (cfr. 1.1.1), the phase-matching condition is reached only if

$$\Delta k = k_3 - k_2 - k_1 = 0 \qquad \Longrightarrow \qquad \frac{\omega_3}{c}n(\omega_3) = \frac{\omega_2}{c}n(\omega_2) + \frac{\omega_1}{c}n(\omega_1) \tag{1.35}$$

This kind of condition is not normally satisfied in a normal medium, which is why non-linear optics phenomena need specific conditions and materials to be seen. The topic will be discussed in more detail in the Section 1.2.3.

1.2.2 Second Harmonic Generation

The SHG phenomenon is one of the second order effects described in Section 1.2.1. In particular, this is the case of a degenerate three-wave mixing where $\omega_1 = \omega_2 = \omega_{FF}$, thus only a field interacts with itself, called *Fundamental Field*. The new frequency generated is its second harmonic, namely $\omega_{SH} = \omega_3 = \omega_1 + \omega_2 = 2\omega_{FF}$. For understanding how the SHG works, the general second order master equation (1.34) is now applied to this specific case, where $A_1 = A_2 = \frac{A_{FF}}{\sqrt{2}}$ and $A_3 = A_{SH}$

$$\begin{cases} \dfrac{1}{\sqrt{2}}\dfrac{\partial A_{FF}}{\partial z} + \delta_{FF,\,SH}\dfrac{1}{\sqrt{2}}\dfrac{\partial A_{FF}}{\partial t} = -i\gamma_{FF}\dfrac{A_{FF}^*}{\sqrt{2}}A_{SH}e^{-i\Delta kz} \\ \dfrac{\partial A_{SH}}{\partial z} = -i\gamma_{SH}\left(\dfrac{A_{FF}}{\sqrt{2}}\right)^2 e^{i\Delta kz} \end{cases} \tag{1.36}$$

In the equations only pulse envelope appears explicitly, whose propagation description is the goal of this section. However, quantities as γ, δ or Δk directly depend on the frequency ω. An ultrashort pulse, as seen in Section 1.1.1, has a spectrum of several frequencies centred in ω_0. Hence, the equations can be solved for each frequency of the spectrum, starting from ω_0. Even if it may seem un-logical from a physical point of view, it is now assumed the pulse to be monochromatic: this allows to conclude the procedure and only at the end to remove the assumption, looking for the pulse behaviour when frequencies deviates from ω_0 by a certain bandwidth $\Delta\omega$. Therefore, considering a monochromatic wave (i.e. a plane wave) then $\dfrac{\partial A_i}{\partial t} = 0$. Removing the temporal derivative the equation is simplified in

$$\begin{cases} \dfrac{dA_{FF}(z)}{dz} = -i\gamma_{FF}A_{FF}^*(z)A_{SH}(z)e^{-i\Delta kz} \\ \dfrac{dA_{SH}(z)}{dz} = -i\gamma_{SH}\dfrac{A_{FF}^2(z)}{2}e^{-i\Delta kz} \end{cases} \tag{1.37}$$

which are two coupled differential equation. Setting the initial conditions as

$$\begin{cases} A_{FF}(z=0) = A_{FF,\,0} \\ A_{SH}(z=0) = 0 \end{cases} \tag{1.38}$$

and by using the *no depletion approximation*, i.e. the incident field remains constant through the material ($A_{FF}(z) \simeq A_{FF,\,0}$), which is a reasonable assumption as the second harmonic field is weaker than the fundamental one, it is possible to solve the second equation which is no more coupled

$$\begin{cases} \dfrac{dA_{FF}(z)}{dz} = 0 \\ \dfrac{dA_{SH}(z)}{dz} = -i\gamma_{SH}\dfrac{A_{FF,\,0}^2}{2}e^{-i\Delta kz} \end{cases} \tag{1.39}$$

Leaving out calculation steps, the solution describing the pulse second harmonic evolution travelling across a non-linear medium is

$$A_{SH}(z) = -i\,\gamma_{SH}\,e^{i\frac{\Delta kz}{2}}\,A_{FF,\,0}^2\,\frac{z}{2}\,\mathrm{sinc}\left(\frac{\Delta kz}{2}\right) \tag{1.40}$$

while its intensity is

$$I_{SH}(z) = \frac{1}{2}\varepsilon_0 cn\left|A_{SH}(z)\right|^2 \propto \gamma_{SH}^2 I_{FF,0}^2 \frac{z^2}{4} \operatorname{sinc}^2\left(\frac{\Delta k z}{2}\right) \tag{1.41}$$

or equivalently, making explicit all the constants and introducing the *effective nonlinear optical coefficient* $d_{eff} = \frac{\chi^{(2)}}{2}$

$$I_{SH}(z) = \frac{\pi^2 d_{eff}^2}{\varepsilon_0 c \lambda_{SH}^2 n_{SH}^2 n_{FF}} \frac{z^2}{2} I_{FF,0}^2 \operatorname{sinc}^2\left(\frac{\Delta k z}{2}\right) \tag{1.42}$$

From the expression (1.41) some SHG property can be derived. Its intensity depends on the square of the fundamental field intensity, so when the input field increases the second harmonic increases quadratically. Note that this happens only under no-depletion approximation, so until $I_{SH} \ll I_{FF}$: after, the conversion efficiency is reduced. Then, the phase-matching condition is essential: when it is reached, namely when $\Delta k = 0$, then $\operatorname{sinc}^2\left(\frac{\Delta k\, z}{2}\right) \xrightarrow[\Delta k \to 0]{} 1$ and the intensity grows quadratically with distance travelled z: thicker medium will result in higher second harmonics. Instead, if $\Delta k \neq 0$ the intensity has an oscillating behaviour with a spatial period which is commonly defined as *coherence length*

$$l_c = \frac{2\pi}{\Delta k/2} = \frac{\pi}{\Delta k} \tag{1.43}$$

The two behaviours are illustrated in Figure 1.3.a. Phase-matching condition, recalled equation (1.35), is retrieved when $k(\omega_{SH}) - 2k(\omega_{FF}) = 0$. This kind of situation can be achieved in particular materials which will be better described in Section 1.2.3.

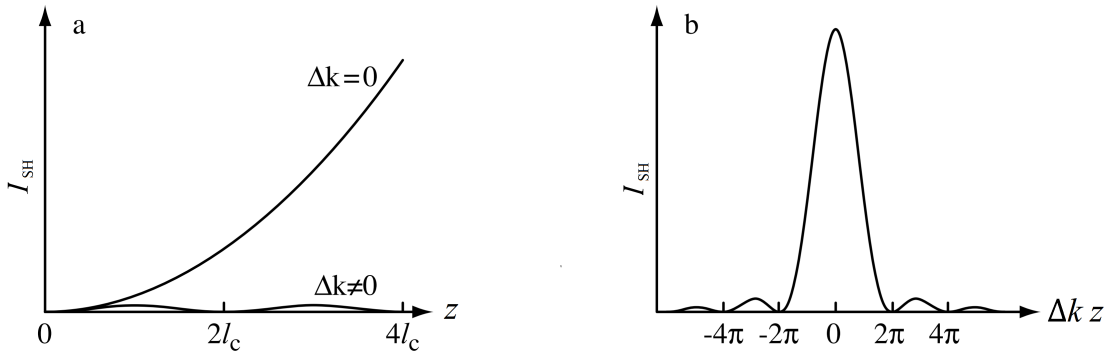

Figure 1.3: Effect of phase-matching on monochromatic SHG: a. SH intensity in the non-depletion approximation, as a function of distance into the non-linear material, both with and without phase-matching; *b.* SH intensity as a function of phase mismatch. Adapted from [6].

The behaviour of SHG in a non-linear material from a monochromatic plane wave has been retrieved in eq (1.41). Considering a proper ultrashort pulses having a spectrum with a certain bandwidth centred in ω_0, even if the phase-matching condition for the central frequencies has been reached all the other frequencies within the band will be phase-mismatched. In Figure 1.3.b it is shown the trend of phase mismatch, whose shape

is a sinc. It can be assumed that all frequencies whose phase mismatch falls within the first sinc node can achieve the SHG process, while those on the outside can not. The phase-matched band is defined from the central frequency: $\omega_0 \pm \Delta\omega$. In the particular case of SHG, considering the spectrum centred in ω_{FF} as represented in Fig. 1.4, its relative phase mismatch can be estimated expanding in series from central frequency

$$\begin{aligned}\Delta k &= k(\omega_{SH} + 2\Delta\omega) - k(\omega_{FF} + \Delta\omega) = \\ &= \cancel{k(\omega_{SH})} + \left.\frac{\partial k}{\partial \omega}\right|_{\omega_{SH}} 2\Delta\omega - \cancel{2k(\omega_{FF})} - 2\left.\frac{\partial k}{\partial \omega}\right|_{\omega_{FF}} = \\ &= 2\Delta\omega\left(\frac{1}{v_{g_{SH}}} - \frac{1}{v_{g_{FF}}}\right) = 2\delta_{SH,\,FF}\Delta\omega\end{aligned} \tag{1.44}$$

where the definition of group velocity and group velocity mismatch has been used and the phase-matching condition is considered fulfilled for central frequencies, i.e. $k(\omega_{SH}) = k(2\,\omega_{FF}) = 2k(\omega_{FF})$. Being the FWHM of $\mathrm{sinc}(x)$ function equal to $0{,}88\,\pi$, the phase-matching bandwidth can be estimated as

$$2\,\frac{\Delta k_{FWHM}\,z}{2} = 0{,}88\,\pi \tag{1.45}$$

and inserting the relationship obtained in (1.44), i.e. $\Delta k_{FWHM} = 2\delta_{SH,\,FF}\Delta\omega$, the band within which SHG is possible, at least within half of the intensity (FWHM), is

$$\Delta\omega_{FWHM} = \frac{0{,}88\,\pi}{\delta_{SH,\,FF}\,z} \tag{1.46}$$

This result underlines that travelling along the NL material (i.e. increasing z) tighten the SHG band: this effect must be carefully taken into account when managing ultrashort pulses, since they have large bandwidth.

1.2.3 Non-linear crystals and SHG phase-matching

In this section, a brief overview of the principal methods to achieve phase-matching is discussed. The phase-matching condition is essential, as seen in equation (1.7), to obtain non-linear optical phenomena. The latter only occur if all the three wave carrier wave frequency ω_1, ω_2 and ω_3 are in phase, constructively interfere while travelling. This happens if and only if the phase velocities are equal. Using the previously described phenomenon of SHG as an example, the fundamental field and its second harmonic must oscillate together in the non-linear material, namely

$$v_{p_{SH}} = v_{p_{FF}} \quad \Longrightarrow \quad \frac{c}{n(\omega_{SH})} = \frac{c}{n(\omega_{FF})} \quad \Longrightarrow \quad n(\omega_{SH}) = n(\omega_{FF}) \tag{1.47}$$

which can never be verified in a common material, since the refractive index is mostly a monotonic function in optical spectral ranges. This condition is the same retrievable from the phase-matching condition, being

$$\begin{aligned}\Delta k &= k_{SH} - k_{FF} - k_{FF} = \frac{1}{c}\left[\omega_{SH}\,n(\omega_{SH}) - 2\omega_{FF}\,n(\omega_{FF})\right] \\ &= \frac{2\,\omega_{FF}}{c}\left[n(2\omega_{FF}) - n(\omega_{FF})\right] = 0\end{aligned} \tag{1.48}$$

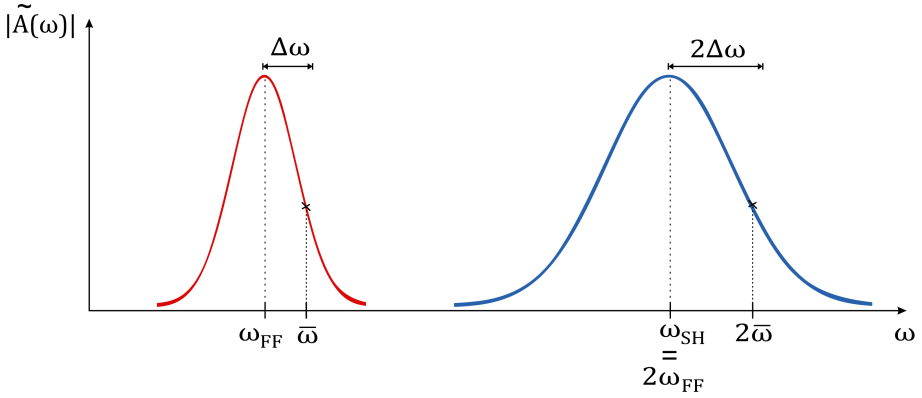

Figure 1.4: Spectrum shape of FF pulse and relative second harmonic. A generic frequency $\bar{\omega}$ is shifted by $\Delta\omega$ from ω_{FF} and its second harmonic by $2\Delta\omega$ from ω_{SH}.

The most widespread method for phase-matching makes use of *birefringent media*, which are anisotropic crystals, not-centrosymmetric, having $\chi^{(2)} \neq 0$. In this kind of materials the refractive index is not unique but depends on polarization of the incoming field. The additional degree of freedom is exploited for compensating the refractive index variation with frequency. Fortunately, lot of the media with high $\chi^{(2)}$ are also linear birefringent crystals and can be used for phase-matching.

Without entering into much details, birefringence occurs when the electric field $\vec{E}$ is not parallel to electric displacement field $\vec{D} = \varepsilon_0\vec{E} + \vec{P}$, therefore the direction of energy flow, i.e. the Poynting vector $\vec{S} = \vec{E} \times \vec{H}$, is not parallel to $\vec{k}$. This happens because of the tensor behaviour of $\chi^{(2)}$ modifies in a different way the propagation of fields with different polarization orientations (cfr. 1.1.3). In particular, this is the case of *uniaxial crystals*, namely materials where there is a single direction, called *optical axis*, governing the optical anisotropy. The dielectric tensor ε which makes explicit the relation between $\vec{D}$ and $\vec{E}$, namely $\vec{D} = \varepsilon\vec{E} = \varepsilon_0\varepsilon_r\vec{E}$, is written as

$$\varepsilon = \varepsilon_0 \begin{bmatrix} n_o^2 & 0 & 0 \\ 0 & n_o^2 & 0 \\ 0 & 0 & n_e^2 \end{bmatrix} \tag{1.49}$$

where it is highlighted the presence of two axis, called *ordinary* (labelled with "o") and *extraordinary* (labelled with "e") acting on fields different polarization orientations. So, the refractive index seen by a beam propagating in the crystal depends on its propagation direction and its polarization, which can be either ordinary or extraordinary, as shown in the Figure 1.5.a. The ordinary one is independent from the incidence angle, i.e. the angle θ between propagation direction $\vec{k}$ and the optical axis, while the extraordinary polarization varies from n_o to n_e as a function of θ (Fig. 1.5.b). In summary, there are two kind of propagation: an ordinary one, with $k_o = \dfrac{\omega\, n_o}{c}$ and an extraordinary one

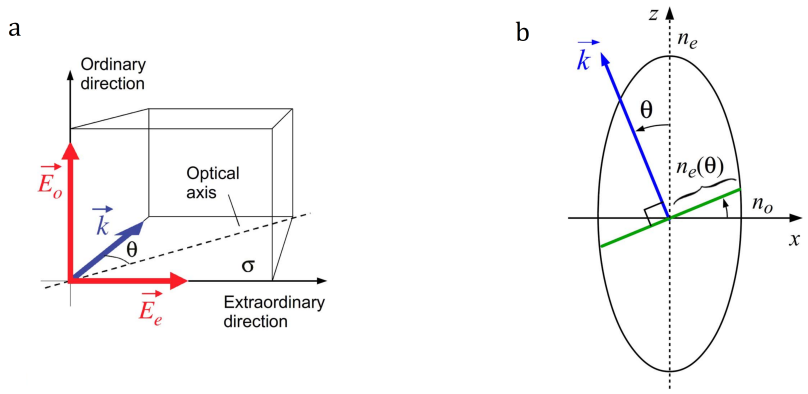

Figure 1.5: *a.* Uniaxial birefringent crystals, with ordinary and extraordinary directions; *b.* Section of the index ellipsoid for a positive uniaxial crystal, assuming the the optical axis is in the z-direction [8].

$k_e = \dfrac{\omega\, n_e(\theta)}{c}$, whose refractive index value is $n_e \leq n_e(\theta) \leq n_o$ and it can be extracted from the index ellipsoid, namely

$$\frac{1}{n_e^2(\theta)} = \frac{\cos^2(\theta)}{n_o^2} + \frac{\sin^2(\theta)}{n_e^2} \tag{1.50}$$

Uniaxial birefringent crystals are classified in two groups: if $n_e > n_o$ they are called *positive* uniaxial crystal, and conversely $n_e < n_o$ *negative* uniaxial crystals.

The crystal used in laboratory are usually cut at the θ angle (for a certain defined ω, usually suitable for common laser sources) with respect to the optical axis, in such a way that a light beam can propagate perpendicularly to the crystal surface. Referring for convenience at the Figure 1.5.a, if the ordinary index is required, the beam must vertically linearly polarized, while if the extraordinary one is required, the light polarization is set horizontally; in addition, rotating the crystal it is possible to tune the required n_e, as it depends on θ.

Returning to the topic of phase-matching condition, birefringent crystals are used to phase-match waves with different frequencies, since they feel different refractive index which may validate the condition (1.48). In fact, the correct value of $n(\omega_{SH})$ can be finely tuned by selecting the right angle θ which gives the correct index value for extraordinary polarization. Since in the optical region the refractive index have a has an increasing trend with frequency, as shown in Figure 1.6, in the case of positive crystal ($n_o < n_e$) the fundamental field must be coupled with the lowest refractive index, thus the extraordinary one, and the second harmonic will be paired with the ordinary axis; conversely, in a negative crystal ($n_o > n_e$) the fundamental will be associated with the highest refractive index while SHG will gain amplitude with polarization aligned to extraordinary axis. Therefore, for SHG the phase-matching condition is reached when

$$\begin{cases} n_e(\omega_{FF}, \theta) = n_o(2\omega_{FF}) & \text{if } n_e > n_o \\ n_o(\omega_{FF}) = n_e(2\omega_{FF}, \theta) & \text{if } n_e < n_o \end{cases} \tag{1.51}$$

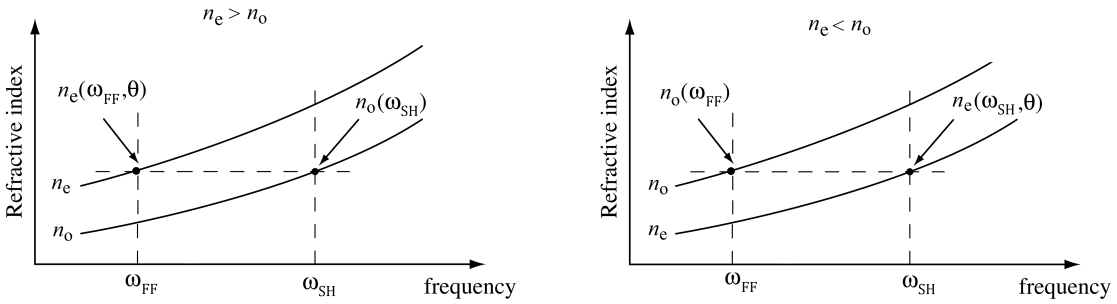

Figure 1.6: Phase-matching diagram for SHG *a.* in a positive uniaxial crystal; *b.* in a negative uniaxial crystal. Adapted from [6].

as shown in Figure 1.6. This kind of phase-matching condition is is called *Type I*, i.e. fundamental field has always an opposite polarization with respect to the second harmonic one. Another achievable condition is the *Type II* phase-matching, where the fundamental has both ordinary and extraordinary polarization, with a phase-matching condition

$$\begin{cases} 2n_o(\omega_{SH}) = n_o(\omega_{FF}) + n_e(\omega_{FF},\theta) = 0 & \text{if } n_e > n_o \\ 2n_e(\omega_{SH},\theta) = n_o(\omega_{FF}) + n_e(\omega_{FF},\theta) = 0 & \text{if } n_e < n_o \end{cases} \tag{1.52}$$

Table 1.1 summarize the conditions presented above.

Table 1.1: Phase-matching polarization direction scheme for positive and negative uniaxial crystals, where the two fundamental waves are symbolized at left, while the second harmonic on the right, as $\omega_{FF} + \omega_{FF} \rightarrow \omega_{SH}$.

Crystals	Type I	Type II
Positive uniaxial	$e + e \rightarrow o$	$o + e \rightarrow o$
Negative uniaxial	$o + o \rightarrow e$	$o + e \rightarrow e$

As phase-matching is essential for non-linear optical phenomena, the alignment of the θ-angle between crystal optical axis and the beam must be done with strict precision. It is usually done rotating the crystal itself. A possible alternative to is to use temperature control, by placing the crystal in an oven, to change the extraordinary refractive index to the required value.

Another method for achieving phase-matching is to perform periodic modulation of the sign of non-linear susceptibility coefficient $\chi^{(2)}$, leading to the so-called *quasi-phase-matching* (QPM) regime. Since the fundamental field and the second harmonic have same polarization, it is commonly referred to also as *Type 0* phase-matching. Looking to Fig. 1.3.a, if one can shift the phase of π after a length $z = l_c = \frac{\pi}{\Delta k}$ the SHG intensity

would rise, till $z = 2l_c$, where another π-shift should occur to maintain the crystal in QPM and so on. Adding a phase shift of π every l_c is equivalent to modulate the sign of $\chi^{(2)}$: this can be possible in some ferro-electrical crystals, as stoichiometric lithium tantalate (SLT) or lithium niobate ($LiNbO_3$, LN) cut at $\theta = 90°$, reversing the alignment of ferroelectric domains upon application of a suitable voltage, which is usually in the order of some kV. The phase-matching condition includes the grating wavevector, i.e.

$$\Delta k = k_{SH} - 2\,k_{FF} - k_G \qquad \text{with} \qquad k_G = \frac{2\pi}{l_c} \tag{1.53}$$

In practice, every l_c the phase-match is reset to zero: as a result, the second-harmonic intensity grows quadratically, although still less rapidly than the case of perfect phase-matching, as represented in Figure 1.7.

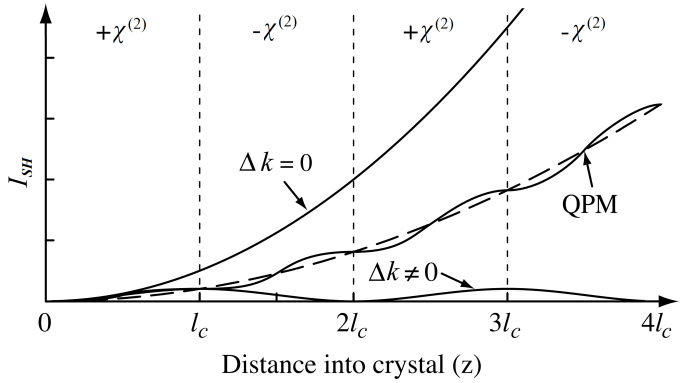

Figure 1.7: SHG intensity as a function of distance into a non-linear crystal, for $\Delta k = 0$, $\Delta k \neq 0$ and first-order QPM. The dashed line shows the average growth for QPM. Adapted from [6].

1.2.4 Difference Frequency Generation and Optical Parametric Amplifiers

Recalling the theory described in 1.2.1, the Difference Frequency Generation (DFG) and Optical Parametric Amplifiers (OPA) will be now described in detail [9] [8]. Since they are second order non-linear phenomena, they are governed by the equation (1.34), namely

$$\begin{cases} \dfrac{\partial A_1}{\partial z} + \delta_{13}\dfrac{\partial A_1}{\partial t} = -i\gamma_1 A_2^* A_3 e^{-i\Delta k z} \\ \dfrac{\partial A_2}{\partial z} + \delta_{23}\dfrac{\partial A_2}{\partial t} = -i\gamma_2 A_1^* A_3 e^{-i\Delta k z} \\ \dfrac{\partial A_3}{\partial z} = -i\gamma_3 A_1 A_2 e^{i\Delta k z} \end{cases} \tag{1.54}$$

where $\omega_3 = \omega_2 + \omega_1$ (or equivalently $\omega_2 = \omega_3 - \omega_1$) and γ is the constant defined as $\gamma_i = \frac{\omega_i \chi^{(2)}}{4 c n_i}$. The frequencies scheme, or theirs energy level, is represented in Figure 1.8.

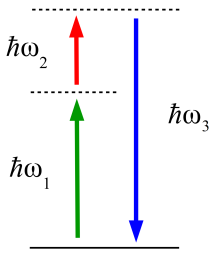

Figure 1.8: Energy levels for a three-wave mixing second order process [8].

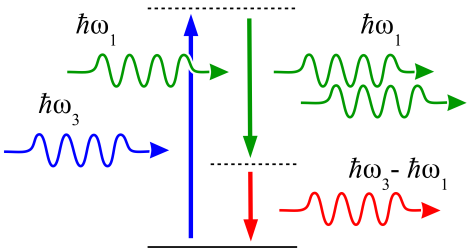

Figure 1.9: OPA process scheme: an input in the NL material of a weak seed signal at ω_1 and an intense pump at ω_3 amplify the seeder and generates the idler at ω_2 [8].

In case of DFG, the process purpose is to obtained a new frequency, i.e. ω_2, making two two beams at frequency ω_3 and ω_1 interfere in a NL medium. Therefore, it involves high fields $A_1(0,t)$ and $A_3(0,t)$ at the input, such that the latter loses energy in favour of $A_1(z,t)$ and the newly generated $A_2(z,t)$. This process can also be seen as a *photon cutter*, since a photon with energy $\hbar\omega_3$ is cut into two photons of energy $\hbar\omega_1$ and $\hbar\omega_2$.

In case of OPA, the process involves the same levels but with different fields amplitude: the purpose is to amplify a very weak signal at ω_1, called *seed*, with an intense beam at ω_3, referred as *pump*, which transfers to it energy and therefore it generates also the ω_2 signal, called *idler*. The process setup is represented in 1.9: the pump is induced to amplify the signal at ω_1 since it is seeded, producing also ω_2 idler photons. Even if the idler appears to be a waste product, its signal can be interchanged with the seed and additionally it has some useful properties for the laser carrier-envelop phase (CEP) stabilization, which is not dealt with here. Obviously, not all frequencies can freely take part in the amplification process. Two conditions have to be fulfilled: *energy conservation* and *momentum conservation*, or equivalently phase-matching. In fact the process required

$$\hbar\omega_3 = \hbar\omega_1 + \hbar\omega_2 \qquad \text{and} \qquad \hbar\vec{k}_3 = \hbar\vec{k}_1 + \hbar\vec{k}_2 \tag{1.55}$$

The first condition binds the idler frequency to the pump and seed ones; the second statement, i.e. the phase-matching condition $\Delta k = \vec{k}_3 - \vec{k}_2 - \vec{k}_1 = 0$, requires the use of a birefringent crystal or a ferromagnetic periodic-poled crystal as seen in Section 1.2.3. Since uniaxial crystals can be tuned with the angle θ to phase-match a corresponding frequency, handling the crystal orientation it is possible to tune with precision the amplified frequencies during the process: this explains why it is called *parametric* amplification. Further, if the seed signal has a large bandwidth, it is possible to select which part of the spectrum amplify tilting the NL crystal. Since for certain crystals the phase-matching bandwidth can be made to be extremely large, also large bandwidth seeder, or ultrashort pulses, can be amplified thus resulting in one of the most used techniques for femtosecond pulse amplification.

Other two schemes similar to OPA can be used. *Optical Parametric Generation* (OPG) is a process where no input seed is provided. Signal and idler gain results from amplification of spontaneous emitted photons, produced by the zero-point fluctuations of the

electro-magnetic quantum field. Spatial and spectral properties of the output beams are not induced by a seed, but only determined through the phase-matching angle θ and spectral bandwidth. This turns out to higher intensities but with poor quality control on output spectra. Conversely, in an *Optical Parametric Oscillator* (OPO), a resonant cavity reflects the signal wave back and forth in the non-linear crystal. The oscillation of signal wave becomes quite similar to a laser, with a portion of the intensity transmitted out of the cavity. Figure 1.10 schematizes the three parametric processes.

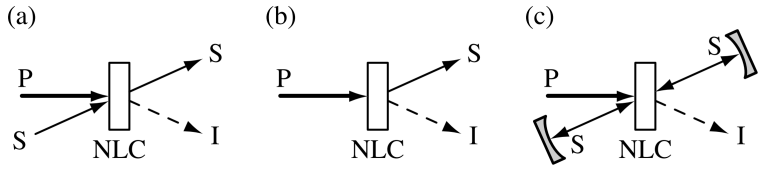

Figure 1.10: Optical parametric gain processes in a second-order non-linear crystal (NLC), (a) OPA; (b) OPG; (c) OPO. The three interacting waves are the strong pump field (P) at ω_3, the signal field (S) at ω_1, and the idler field (I) at ω_2 [6].

Now the equation (1.34) will be solved in case of OPA. Recalling the no-depletion approximation, the pump is assumed to be nearly constant during propagation: $A_3(z,t) \approx A_3(0,t) = A_{3,0}$. Also assuming the fields to be monochromatic waves, thus $\dfrac{\partial A_i}{\partial t} = 0$, the resulting equations are

$$\begin{cases} \dfrac{dA_1(z)}{dz} = -i\gamma_1 A_2(z)^* A_{3,0} e^{-i\Delta k z} \\ \dfrac{dA_2(z)}{dz} = -i\gamma_2 A_1(z)^* A_{3,0} e^{-i\Delta k z} \\ A_3(z) = A_{3,0} \end{cases} \tag{1.56}$$

Taking the second derivative and solving for $A_1(z)$ with some arithmetic, the master equation becomes

$$\frac{d^2 A_1(z)}{dz^2} + i\Delta k \frac{dA_1(z)}{dz} - \Gamma^2 A_1(z) = 0 \tag{1.57}$$

where it has been defined $\Gamma = \dfrac{\chi^{(2)}}{2\,c}\sqrt{\frac{\omega_1\omega_2}{n_1 n_2}}\left|A_{3,0}\right|$ with $n_i = n(\omega_i)$. Γ is constant under no-deplation approximation, but in general depends on the pump amplitude.

Now, the idler is assumed to be initially zero: $A_2(z=0) = 0$, while the seed works as a weak input fiels $A_1(z=0) = A_{1,0} \ll A_{3,0}$. The solution to the previous equation can be demonstrated to be

$$\begin{aligned} A_1(z) &= A_{1,0} e^{-i\frac{\Delta k}{2}z}\left[\left(1 + i\frac{\Delta k}{2g}\right)e^{gz} + \left(1 - i\frac{\Delta k}{2g}\right)e^{-gz}\right] = \\ &= A_{1,0} e^{-i\frac{\Delta k}{2}z}\left[\cosh(gz) + i\frac{\Delta k}{2g}\sinh(gz)\right] \end{aligned} \tag{1.58}$$

where the g is defined as $g = \sqrt{\Gamma^2 - \frac{\Delta k}{2}}$, called *small-signal gain*. Its intensity can be computed as

$$I_1(z) = \frac{1}{2}\varepsilon_0 cn\left|A_1(z)\right|^2 = I_{1,0}\underbrace{\left[1 + \frac{\Gamma^2}{g^2}\sinh^2(gz)\right]}_{G(\Delta k, z)} \tag{1.59}$$

where it is highlighted the *parametric gain* G, which is the gain factor for the initial seed $I_{1,0}$. In the large gain limit, i.e. $gz \gg 1$ and $e^{-gz} \simeq 0$, the parametric gain is

$$G(\Delta k, z) = \frac{I_1(z)}{I_{1,0}} = 1 + \frac{\Gamma^2}{g^2}\sinh(gz) \approx \frac{1}{4}\frac{\Gamma^2}{g^2}e^{2gz} \tag{1.60}$$

It is evident the gain has an exponential trend with respect to the material length z. This behaviour is guaranteed from the non-depletion approximation: for exponential gain, pump intensity I_3 must always be much greater then amplified signal intensity I_1. If the approximation is not more valid, thus the seed has gained power, the parametric gain G saturates at a constant value. Note that the term Γ^2 depends on I_3 too, providing further gain. In the pulsed regime, the highest intensity is at the pulse peak, and depends on the pulse duration, its energy and the beam size. Ultrashort pulses, thanks to their high peak intensity, can easily achieve high pumping and provide huge gains. In Figure 1.11

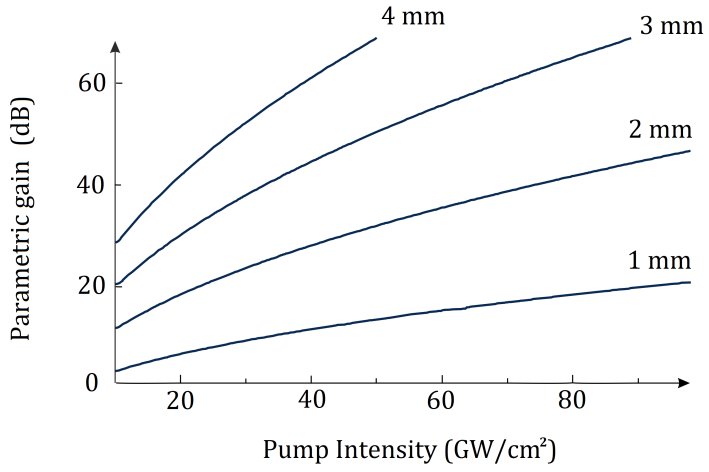

Figure 1.11: Parametric gain BBO crystal for various crystal lengths and pump intensities. The pump has $\lambda_3 = 800\,\text{nm}$ while the seed $\lambda_1 = 1200\,\text{nm}$. Adapted from [9].

typical values of G are shown as a function of pump intensity $I_{3,0}$ in NL crystal of β-barium borate (β-BaB_2O_4 or BBO) with different thickness: in NIR region, with a pump intensity $I_{3,0} = 50\,\text{GW/cm}^2$ that can be reached strongly focusing the pump beam, the OPA retrieve a gain of 50 dB with a 3 mm-long crystal. It is fundamental to underline that parametric gain strongly depends on g: it is maximum when the phase-matching

condition $\Delta k = 0$ is reached. In the case, $g = \Gamma$ and the parametric gain expression simplifies in

$$G(\Delta k = 0, z) \approx \frac{e^{2\Gamma z}}{4} \tag{1.61}$$

For the idler intensity expression, once $A_1(z)$ is known, calculation from coupled equations (1.56) is possible. In alternative, by suitably manipulating them, it is possible to get the *Manley-Rowe relations*, thus

$$\frac{1}{\omega_1}\frac{\partial I_1}{\partial z} = \frac{1}{\omega_2}\frac{\partial I_2}{\partial z} = -\frac{1}{\omega_3}\frac{\partial I_3}{\partial z} \tag{1.62}$$

Therefore,

$$I_2(z) = \frac{\omega_2}{\omega_1} I_{1,0} \frac{\Gamma^2}{g^2} \sinh^2(gz) \tag{1.63}$$

so the idler gain has nearly the same behaviour (the "1+" which represent the seed contribution in eq. (1.59) is negligible) of the signal gain, simply scaled proportional to the pulses energy $\frac{\hbar\omega_2}{\hbar\omega_1}$.

It is interesting notice that G scales as the exponential of the crystal length $z = L$, which is different from the one seen for SHG, whose gain scales quadratically with L. This happens because during the non-linear interaction inside the crystal, the idler beam is generated at the difference frequency between pump and signal. Thanks to the symmetry between $A_1(z)$ and $A_2(z)$ of equation (1.56), also the idler can undergo parametric amplification: it may be imaged as a new OPA seed, while the signal at ω_1 becomes its idler, swapping roles. Therefore, further photons at ω_1 are generated, adding power to the signal. This mechanism acts as *positive feedback* giving rise to an exponential gain of the signal during propagation and it makes OPA a perfect method for real amplification. With respect to a classical optical amplification based on stimulated emission of a population inversion at a frequency linked to an atomic transition, it does not have any energy storage capability, i.e. the gain is present only during the temporal and spatial overlap of the interacting pulses which creates the virtual levels without excitation. Even if this forces to use complex experimental setups to guarantee the overlaps, since no atomic excitation is involved also no thermal relaxation processes and consequentially no material heating takes place. Additionally, the gain frequency is not fixed, but can be continuously adjusted by varying the phase-matching condition (see Section 1.2.5) and the gain bandwidth is not limited by the line-width of an electronic or vibration transition, but rather by the possibility of satisfying the phase-matching condition over a broad range of frequencies, which it will be now briefly described.

Till now, the discussion has considered monochromatic fields, thus time-infinite single frequency beams. Removing this assumption on the ω_1 signal, it is now considered, as the seed, a time-finite pulse with a certain bandwidth centred on ω_1 (see Fig. 1.4). Keeping the pump monochromaticity assumption, if a frequency shifted by $+\Delta\omega$ from the central seeder frequency is considered, then the respective idler frequency shifts is $-\Delta\omega$, as shown in Figure 1.12.

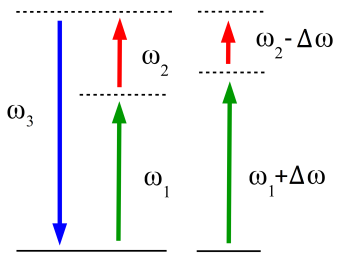

Figure 1.12: Energy levels in case of a seed or idler frequency shift (broadband OPA).

It is assumed that the central frequencies are phase-matching, i.e. $\Delta k = k(\omega_3) - k(\omega_1) - k(\omega_2) = 0$. Making use of the group velocity and group velocity mismatch definitions, the phase mismatch can be computed developing in series the wave vector, obtaining

$$\begin{aligned}\Delta k &= k(\omega_3) - k(\omega_1 + \Delta\omega) - k(\omega_2 - \Delta\omega) = \\ &= \cancel{k(\omega_3)} - \cancel{k(\omega_1)} - \left.\frac{\partial k}{\partial \omega}\right|_{\omega_1} \Delta\omega - \cancel{k(\omega_2)} - \left.\frac{\partial k}{\partial \omega}\right|_{\omega_2} (-\Delta\omega) = \\ &= \Delta\omega \left(-\frac{1}{v_{g_1}} + \frac{1}{v_{g_2}} \right) = -\delta_{12}\Delta\omega\end{aligned} \tag{1.64}$$

The amplification bandwidth, namely the band for which the phase-mismatch reduces gain of a factor 2, is calculated imposing $G(\Delta k) = \frac{1}{2}G(0)$ under the hypothesis of small mismatch, resulting in

$$\Delta k_{FWHM} = 2\sqrt{\ln 2}\sqrt{\frac{\Gamma}{L}} \tag{1.65}$$

and expressing it with respect to frequency shift $\Delta\omega$

$$\Delta\omega_{FWHM} = -\frac{2}{\delta_{12}}\sqrt{\ln 2}\sqrt{\frac{\Gamma}{L}} \tag{1.66}$$

It is clear the inverse dependence from the square root crystal length L, so crystal thickness variation affects less the pulse amplification bandwidth than SHG process.

In case of group velocity matched OPA (see Section 1.2.5), i.e. when $v_{g_1} = v_{g_2}$ and $\delta_{12} = 0$, the bandwidth does not become infinite: in the (1.64) development, only the first term was considered. Adding also the role of group velocity dispersion, the second order mismatch can be calculated as

$$\begin{aligned}\Delta k^{(2)} &= \cancel{k(\omega_3)} - \cancel{k(\omega_1)} - \cancel{\left.\frac{\partial k}{\partial \omega}\right|_{\omega_1} \Delta\omega} - \frac{1}{2}\left.\frac{\partial^2 k}{\partial \omega^2}\right|_{\omega_1} \Delta\omega^2 - \cancel{k(\omega_2)} + \cancel{\left.\frac{\partial k}{\partial \omega}\right|_{\omega_2} \Delta\omega} - \frac{1}{2}\left.\frac{\partial^2 k}{\partial \omega^2}\right|_{\omega_2} \Delta\omega^2 = \\ &= -\frac{1}{2}(GVD_1 + GVD_2)\Delta\omega^2\end{aligned} \tag{1.67}$$

giving, with the above described procedure, a second order frequency bandwidth of

$$\Delta\omega^{(2)}_{FWHM} = \frac{2\sqrt{2}\sqrt[4]{\ln 2}}{\sqrt{|GVD_1 + GVD_2|}}\sqrt[4]{\frac{\Gamma}{L}} \tag{1.68}$$

which is even less sensitive to the crystal length L variation, since it goes with $\propto \frac{1}{\sqrt[4]{L}}$.

With ultrashort pulses the optimum crystal length has to be chosen considering also temporal duration and group velocity of the interacting pulses. Since pulses have different spectra, therefore different group velocities, they accumulate relative delay during the propagation, which is called *temporal walk-off*. When their relative group delay (δ_{13} and δ_{23}) becomes larger than the pulse-lengths, the pulses do not temporally overlap anymore and their interaction vanishes. Given that the pump pulse has the FWHM duration τ, the distance after which the idler or the signal pulses separate from the pump one, i.e. *pulse-splitting length*, is

$$l_{i3} = \left| \frac{\tau}{\delta_{i3}} \right| \tag{1.69}$$

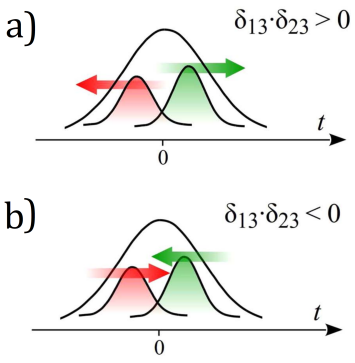

Figure 1.13: Scheme of signal-idler pulse-splitting length type: *a)* if $\delta_{13} \cdot \delta_{23} > 0$; *b)* if $\delta_{13} \cdot \delta_{23} < 0$ [8].

where the index $i = 1, 2$ for signal and idler respectively. The pulse-splitting length becomes shorter for decreasing pulse duration and for larger group velocity mismatch, which depends on the crystal type, pulse wavelengths and type of phase-matching.

It is interesting to note that a different behaviour is observable if the pump group velocity is larger or smaller than both idler and signal, thus $v_{g_3} > v_{g_2} > v_{g_1}$ (or $v_{g_3} < v_{g_2} < v_{g_1}$), and when it has a value that stays in between, thus $v_{g_2} > v_{g_3} > v_{g_1}$. In the first case $\delta_{13} \cdot \delta_{23} > 0$ and both signal the idler pulses walk away from the pump in the same direction, so that the amplification process stops for propagation distances longer than the pulse-splitting length. In the second case $\delta_{13} \cdot \delta_{23} < 0$ and signal and idler pulses walk in opposite direction with respect to the pump and temporally localises signal and idler under the pump pulse: high parametric gain with positive feedback can only occur where the leading edge of one pulse and the trailing edge of the other are temporally superposed under the pump pulse. However, the idler generated photons at ω_1 move in the opposite direction, towards the pump pulse, and the same do the ω_2 generated photons by the signal pulse: this process can make the gain growing exponentially even for crystal lengths in excess of the pulse splitting length. This effect, sketched in Fig. 1.13, allows to use crystals significantly longer than the pulse-splitting length and to reach more easily the saturation value occurring at pump depletion.

1.2.5 OPA phase-matching and group velocity matching

So far it has been assumed to be in the phase-matching condition for the spectrum central frequency, i.e.

$$\Delta k = k(\omega_3) - k(\omega_2) - k(\omega_1) = \frac{\omega_3 n(\omega_3)}{c} - \frac{\omega_2 n(\omega_2)}{c} - \frac{\omega_1 n(\omega_1)}{c} = 0 \tag{1.70}$$

This kind of condition can be achieved in uniaxial birefringent crystals, as discussed in detail in Section 1.2.3. For a positive uniaxial crystal ($n_e > n_o$), since $\omega_3 = \omega_1 + \omega_2$ is the greater frequency, the pump beam has to be polarized on ordinary axis whose refractive

index have a lower value. Conversely, for a negative uniaxial crystal, being $n_o > n_e$, the polarization must be parallel to extraordinary axis. In case the idler and signal beams have the same polarization it is called *Type I* phase-matching, while if their polarization is different is the *Type II* case. Also quasi-phase-matching (*Type 0*) may be suitable. Table 1.2 summarizes different phase-matching conditions.

Table 1.2: Phase-matching polarization direction scheme for positive and negative uniaxial crystals, with the scheme $\omega_1 n_X(\omega_1) + \omega_2 n_Y(\omega_2) \to \omega_3 n_Z(\omega_3)$ synthesized in $X + Y \to Z$.

Crystals	Type 0	Type I	Type II
Positive uniaxial	$o + o \to o$	$e + e \to o$	$o + e \to o$ $e + o \to o$
Negative uniaxial	$e + e \to e$	$o + o \to e$	$o + e \to e$ $e + o \to e$

Phase-matching for a monochromatic wave is easily obtained through a correct crystal orientation, tilting the angle θ in such a way that $n_e(\theta)$ meets the right condition. For example, in case of a negative uniaxial crystal (as BBO) in Type I configuration, the seed polarization is set on the ordinary axis, while the pump must have a polarization aligned to extraordinary one. The idler wave will rise during amplification with an ordinary polarization. Then the crystal should be tilted by an angle determined by

$$\theta_{BBO,\,I} = \arctan\left(\sqrt{\frac{1-U}{W-1}}\right) \qquad \text{where} \qquad \begin{cases} U = \left[\frac{n_o(\omega_1)\omega_1 + n_o(\omega_2)\omega_2}{n_o(\omega_3)\omega_3}\right]^2 \\ W = \left[\frac{n_o(\omega_1)\omega_1 + n_o(\omega_2)\omega_2}{n_e(\omega_3)\omega_3}\right]^2 \end{cases} \tag{1.71}$$

The complete set of formulas for each phase-matching type can be found in literature [10].

When an ultrashort seeder is taken into account, in order to get the right amplification it is fundamental that all of its bandwidth is phase-matched. The ideal setup would be a broadband amplifier, i.e. an OPA which, for a fixed pump frequency, provides a constant gain over an as broad as possible band of seed frequencies. As seen in (1.66), the amplification bandwidth is inversely proportional to the seed-idler group velocity mismatch δ_{12}, so this quantity should be as smaller as possible: the seed and idler group velocities should be equal, i.e. $v_{g_1} = v_{g_2}$. Therefore, recalling the definition as $v_g = \frac{\partial\omega}{\partial k}$ with $k = \frac{\omega\, n(\omega)}{c}$, the condition is fulfilled if and only if

$$\delta_{12} = 0 \qquad \Longleftrightarrow \qquad \omega_1 = \omega_2 = \frac{\omega_3}{2} \tag{1.72}$$

which is the so called *degenerate OPA* condition. Summarizing, if the seed frequency is half of the pump one (or $\lambda_1 = 2\lambda_3$), then it is possible to amplify large-bandwidth signal. Unfortunately, this is a significant constraint.

Nevertheless, till now the wave vectors $\vec{k}$ have been considered all parallel to the propagation z-axis ($\vec{k}$ was considered a scalar quantity): all three light beams – seed,

idler, pump – were *collinear* (neglecting the little spatial walk-off, described below in Section 1.2.6) and the phase-matching condition was a scalar equation, namely $k_3 = k_2 + k_1$, with $k_i = k(\omega_i)$. It is possible to remove this assumption: when pump, signal and idler beams propagate in different directions, the phase-matching condition becomes the vector expression

$$\Delta\vec{k} = \vec{k}_3 - \vec{k}_2 - \vec{k}_1 = 0 \tag{1.73}$$

which adds a degree of freedom for phase-matching and zero group-velocity-mismatch requirements. Since the three beams are not parallel to each other, this kind of configuration is called *non-collinear OPA* (NOPA).

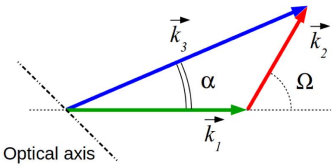

Figure 1.14: Phase matching condition in NOPA configuration [8].

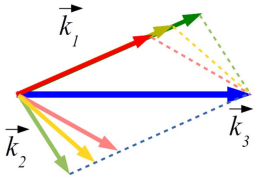

Figure 1.15: NOPA phase-matching in ultrashort pulse regime [8].

Figure 1.14 shows the wave-vectors relation for phase-matching, in a plane containing crystal optical axis and the three vectors: this ensures that only one ordinary and one extraordinary polarization direction is defined in common to all three beams, as in Figure 1.5. The angle between them is α, which represent the pump-seed angle at crystal input, while Ω is the seed-idler angle which is forcibly defined by phase-matching condition. Pay attention that these two angles are defined inside the crystal: for propagation directions outside the crystal, Snell's law must be applied and therefore the angles become larger.

In practice, for a given frequency to be amplified (ω_1) and a given pump (ω_3), only one pair of solution (α; θ) can retrieve both the phase-matching requirement ($\Delta\vec{k} = 0$, guaranteeing high parametric gain) and the group-velocity matching requirement ($\delta_{12} = 0$, which ensure high constant gain for a seeder with broad spectrum). The solution is retrieved applying the vectorial phase-matching condition, namely in two planar direction. Choosing $\vec{k}_1$ as a reference, $\Delta\vec{k}$ can be decomposed in

$$\begin{cases} \Delta k_{\parallel} = k_3 \cos\alpha - k_1 - k_2 \cos\Omega = 0 \\ \Delta k_{\perp} = k_3 \sin\alpha - k_2 \sin\Omega \end{cases} \tag{1.74}$$

In order to consider the seed bandwidth, the frequency is detuned from ω_1 to $\omega_1 + \Delta\omega$ and the idler from ω_2 to $\omega_2 - \Delta\omega$, thus obtaining with the usual expansion

$$\begin{cases} \Delta k_{\parallel} = \cancel{k_3 \cos\alpha} - \cancel{k_1} - \dfrac{\partial k}{\partial\omega}\Big|_{\omega_1}\Delta\omega - \cancel{k_2 \cos\Omega} - \dfrac{\partial k}{\partial\omega}\Big|_{\omega_2}(-\Delta\omega)\cos\Omega + \\ \qquad\qquad - k_3(-\sin\Omega)\dfrac{\partial\Omega}{\partial\omega}(-\Delta\omega) = 0 \\ \Delta k_{\perp} = \cancel{k_3 \sin\alpha} - \cancel{k_2 \sin\Omega} - \sin\Omega\,\dfrac{\partial k}{\partial\omega}\Big|_{\omega_2}(-\Delta\omega) - k_2\cos\Omega\,\dfrac{\partial\Omega}{\partial\omega}(-\Delta\omega) = 0 \end{cases} \tag{1.75}$$

With a bit of arithmetic and recalling that $\left.\frac{\partial k}{\partial \omega}\right|_{\omega_i} = \frac{1}{v_{g_i}}$, the two equation are true if and only if the following relation is satisfied:

$$v_{g_1} = v_{g_2} \cos \Omega \tag{1.76}$$

namely the projection of $\vec{k}_2$ on $\vec{k}_1$ must be of the same length of k_1: in this way seeder, idler and pump are phase-matched (so the phase front are in constructive interference, since their phase velocity is equal) and group-velocity matched, therefore broadband spectra amplification is guaranteed. Group-velocity-matching condition can also be stated in the concise form, as

$$\frac{\partial \vec{k}_1}{\partial \omega_1} = \frac{\partial \vec{k}_2}{\partial \omega_2} = -\frac{\partial \vec{k}_1}{\partial \omega_2} \tag{1.77}$$

As an example, in Figure 1.16 is represented a typical NOPA configuration: the optical axis is on the horizontal plane, hence defining the extraordinary polarization direction and the propagation plane of all beams. Angles α' and Ω' are the corresponding seed-pump and seed-idler angles outside the crystal, namely

$$\sin \alpha' = n_o(\omega_1) \sin \alpha \qquad \text{and} \qquad \sin(\Omega' - \alpha') = n_o(\omega_2) \sin(\Omega - \alpha) \tag{1.78}$$

for a negative Type I crystal (both seed and idler polarized on the ordinary axis, while the pump is polarized along the extraordinary one).

In this configuration, with the correct angles, the pump (green beam) efficiently amplifies the seeder pulse (red one), thus generating the idler beam (yellow) which is angularly dispersed. This effect happens because, once fixed pump and seed frequencies and theirs relative phase-matched angles θ and α, the only free degree-of-freedom is Ω, which will vary with frequency because group matching condition $v_{g_1} = v_{g_2} \cos \Omega$. In other words, each frequency composing the seed spectrum is set to have an angle α with pump beam (and with the z-axis in this example), so $\vec{k}_1$ direction is fixed but not its magnitude which will vary with ω, thus making $\vec{k}_2$ changing direction to preserve phase-matching condition, implying $\Omega = \Omega(\omega)$, as shown in Figure 1.15.

It is worth noting in Fig. 1.16 that a mild red circle appears around the pump beam. This is the effect of the *amplified parametric fluorescence* (APF), i.e. the amplification of quantum noise due to two-photon emission from a virtual level excited by the intense pump field and stimulated by the signal or idler frequency zero-point fluctuations. The APF is the phenomenon at the basis of signal generation in OPG. APF is generated when crystal is phase-matched to the pump beam, namely once set the right angle θ. Since this kind of amplified signal is not stimulated from seed, thus $\vec{k}_1$ has not a single predefined direction, photons will be amplified to a corresponding phase-matched angle α but with a rotational symmetry because the incidence plane has not been defined by a seeder beam, therefore creating a circular signal propagating around the pump signal as a cone. The APF signal can be used to easily identify, without calculation, the so called *magic angle*, i.e. the angle α at which to place the seed signal to be correctly amplified.

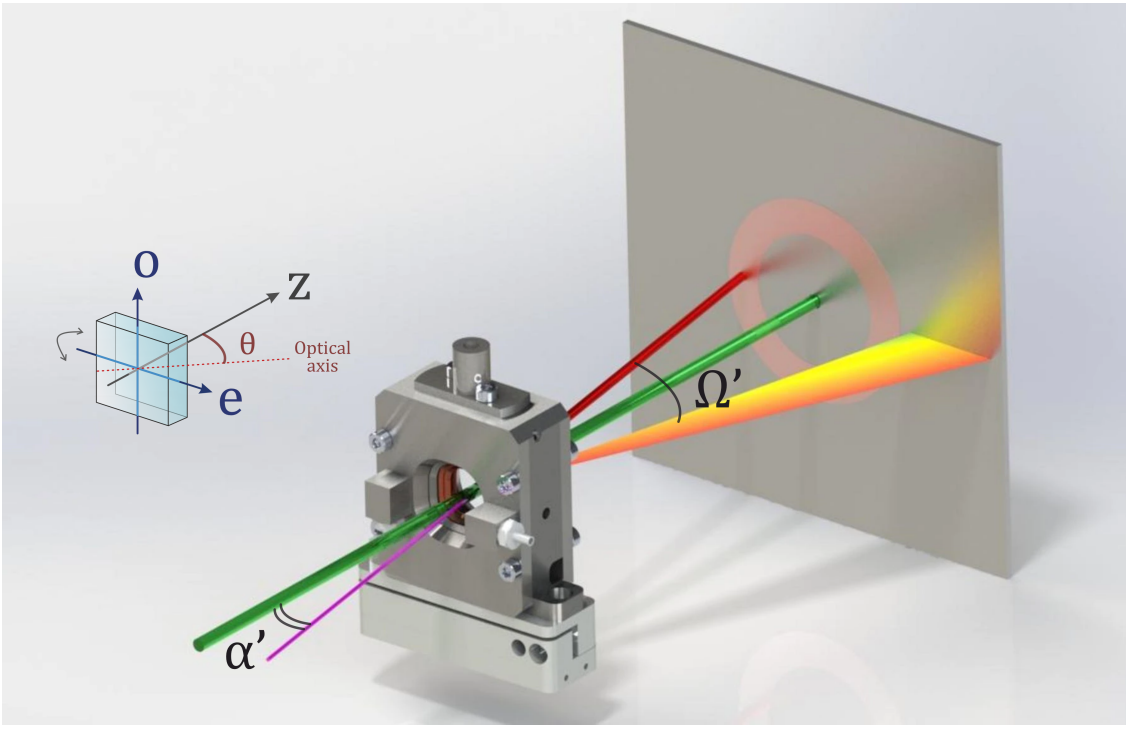

Figure 1.16: Non-collimated OPA typical setup for a negative uniaxial crystal in type I polarization. The seed beam is red, the pump green while the idler yellow. The angles α' and Ω' are the free space propagation one, seen outside the crystal. A scheme of crystal polarization axis is illustrated on the left, where the angle θ is between pump propagation direction (z) and the crystal optical axis, indicated with a dotted line. Adapted from Trumpf laser catalogue.

1.2.6 Spatial walk-off and NOPA configurations

Before moving towards the OPA discussion conclusion, a quick mention to spatial walk-off is now presented. Having described the operation of a NOPA in detail, it is known that non-collinear beams diverge on their way into the crystal. In order to get high amplification, seed and pump pulses have to be temporally and spatially overlapped. Focusing on the previously seen case of Type I negative crystal (where pump is extraordinary polarized and seed is aligned to ordinary crystal axis), the pump experiences spatial walk-off due to the propagation along the extraordinary axis: in fact, the Poynting vector $\vec{S}_3$, which indicates where the energy flows (the beam direction), is no more parallel to its wave-vector $\vec{k}_3$, thus tilting from the z axis and deflecting it from the seed beam. The spatial walk-off can be derived taking into account also (x, y) direction of propagation. At the crystal input a monochromatic field

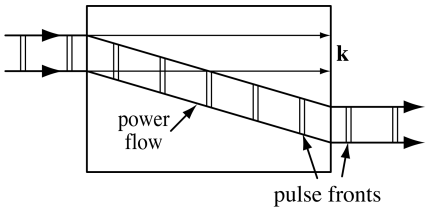

Figure 1.17: Spatial walk-off of a wave propagating in an anisotropic medium on the extraordinary axis [6].

travelling along z-axis can be written as

$$E(x,y,z,t) = \frac{1}{2}[A_0(x,y,t)e^{i(\omega_0 t - k_z z)} + c.c.] \tag{1.79}$$

where A_0 is made explicit as the sum of its spatial and spectral component in Fourier domain, as

$$A_0(x,y,t) = \Big(\frac{1}{2\pi}\Big)^3 \int \tilde{A}_0(\tilde{\omega},k_x,k_y)\, e^{-i(k_x x + k_y y)}\, e^{i\tilde{\omega}t}\, d\tilde{\omega}\, dk_x\, dk_y \tag{1.80}$$

where k_x and k_y are the lateral component of the wave vector $k^2 = k_x^2 + k_y^2 + k_z^2$ and $\tilde{\omega}$ is the Fourier integration variable.

In an anisotropic medium, the refractive index n depends on frequency but also on the direction of lateral wave-vectors, namely $n(\omega_0, k_x, k_y)$. Its expression can be derived with an expansion

$$k_z(\omega,k_x,k_y) = k_{z_0} + \tilde{\omega}\frac{\partial k}{\partial \omega} + \frac{\omega_0}{c}\Big(\frac{\partial n}{\partial k_x}k_x + \frac{\partial n}{\partial k_y}k_y\Big) \tag{1.81}$$

with $k_{z_0} = \dfrac{\omega_0}{c} n(\omega_0,0,0)$. Substituting the latter equation in (1.79), the obtained expression is

$$E(x,y,z,t) = \frac{1}{2}\Big[e^{i(\omega_0 t - k_{z_0} z)} A_0\Big(x + \frac{\omega_0}{c}\frac{\partial n}{\partial k_x}z, y + \frac{\omega_0}{c}\frac{\partial n}{\partial k_y}z, t - \frac{\partial k}{\partial \omega}\Big) + c.c.\Big] \tag{1.82}$$

The electric field is equal to a carrier term oscillating at ω_0 multiplied by an envelope that propagates without distortion (because only first order expansion has been made: taking into account also the GDD also reshaping effects would be evident), but with a different frame of reference changing along z, since $x \to x + \frac{\omega_0}{c}\frac{\partial n}{\partial k_x}z$ and $y \to y + \frac{\omega_0}{c}\frac{\partial n}{\partial k_y}z$. As sketched in Fig. 1.17, the spatial envelope propagates at an angle ρ with respect to the z axis. This is the direction in which the energy flows, which can be calculated with a simple calculus with the dielectric tensor, resulting in [6]

$$\rho = \arctan(-\frac{1}{n(\theta)}\frac{\partial n}{\partial \theta}) \tag{1.83}$$

Instead, the pulse fronts, given by constant $t - \frac{\partial k}{\partial \omega}$, propagate with the usual phase velocity and remain perpendicular to the carrier propagation direction (z). Since the magnitude of k, hence the value of the refractive index, depends also on k_x and k_y, the pulse fronts are no longer perpendicular to the energy flow as initially stated, resulting in a lateral shift while travelling in the crystal.

Returning to the topic of NOPA, it is useful to underline two possible configurations [11], which are linked with the spatial walk-off just seen. Once fixed the phase-matching angle θ, efficient broadband parametric amplification in NL crystal can be achieved by directing the signal beam at the magic angle α from the pump beam. However, due to crystal birefringence the direction of the pump Poynting vector $\vec{S}_3$ has not the same direction of its wave-vector $\vec{k}_3$ and the degree of spatial overlap between pump, signal

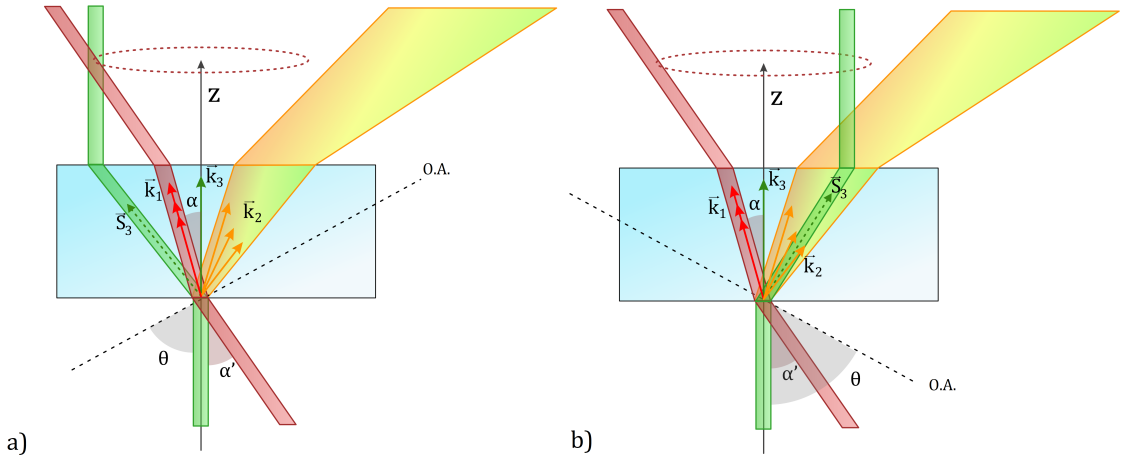

Figure 1.18: NOPA possible configurations. The seed pump pulse is coloured in greed, the seeder in red, the angular dispersed idler in yellow, with the respective $\vec{k}_i$. O.A. is the crystal optical axis (dotted line). $\vec{S}_3$ is pump Poynting vector. The dotted ellipsoid represent the APF. *a)* Poynting Vector Walk-off Compensation geometry (PVWC); *b)* Tangential Phase-Matching geometry (TPM). Angles are intentionally exaggerated.

and idler beams depends on the crystal orientation. In one configuration (Fig. 1.18.a), the Poynting vector walk-off leads to better spatial overlap between pump and signal beams; this geometry is called *Poynting Vector Walk-off Compensation geometry* (PVWC). In this case the input angle α lies in the half plane opposite to the spatial walk-off direction: so, inside the crystal the signal beam propagates in the same half plane of the pump. In the opposite case, shown in 1.18.b the signal beam moves away from the pump and the latter propagates very close to that of the angular dispersed idler beam: this configuration is called *Tangential Phase-Matching geometry*.

Both geometries are commonly can be used in NOPA and allow for similar gain efficiencies. However, the spatial and spectral properties of the amplified signal differ appreciably due to specific pulse shaping dynamics and different parasitic frequency mixing processes. The PVWC configuration offers a much better near-field profile, even if a parasitic SHG may affect the shape of amplified spectrum. On the other hand, TPM geometry may suffer from spectral phase modulation. This effect can also be seen in the APF ring, which amplitude is not uniform: in one of the two horizontal half-plane divided by the z-axis (the one corresponding to PVWC configuration) the amplification of spontaneous florescence is more evident as in Figure 1.19.

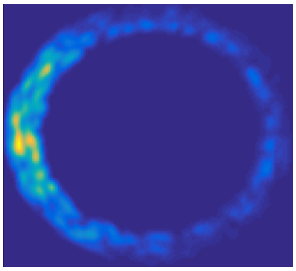

Figure 1.19: Typical APF shape. Numerical simulation from [11].

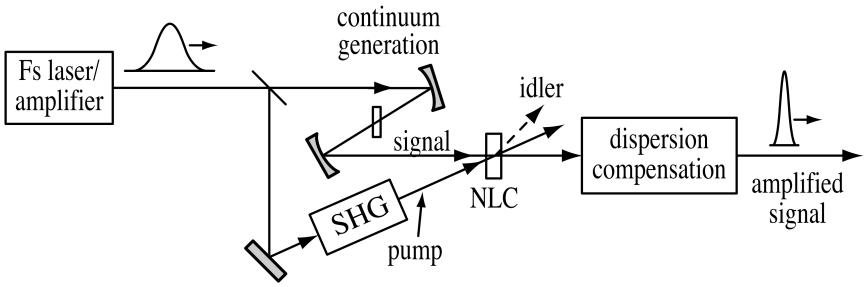

Figure 1.20: Typical ultrabroadband NOPA. The seed is obtained via WLC generation and then amplified in a nonlinear crystal (NLC) in the presence of a strong pump pulse generated by SHG [6].

1.2.7 Final remarks on OPAs

OPAs are widely used to generate high power ultrashort pulses in the VIS spectral region, because is difficult to access directly with mode-locked solid-state lasers in this area. A typical widely tunable OPA arrangement in this band is composed by four stages:

1. A femtosecond ML laser and its amplifier, usually a diode-pumped solid state laser (tipically Nd^{3+}, Yb^{3+} or Ti^{3+}-doped crystals, as sapphire, YAG, YLG YVO_4, KGW or KYW), which provides 100-500 fs pulses with 10 nm bandwidth at frequency in the range of 800 nm-1 µm and several hundred µJ of pulse energies at 1-100 KHz.

2. A SHG stage which generates the pump beam at a frequency $\omega_3 = 2\omega_{FF}$, which is needed since the pump frequency is the sum of idler and seed one $\omega_3 = \omega_2 + \omega_1$. It is usually done with a BBO (β-BaB_2O_4) in case of free propagation setup or with a periodically poled LN (lithium niobate) in guided optics regime;

3. A seed generation stage with the third linear process (which will be described in the Section 1.3) of White Light Generation (WLC), pumped with a small amount of the input energy, typically about few µJ. It produces an ultrabroad-bandwidth pulse which is used as seed in the next stage;

4. A non-linear crystal (typically BBO), which is the element that constitutes the actual OPA: pump and seed pulses directed onto the crystal with the right phase-matching angles to allow parametric amplification, temporal and spatially overlapped (with a delay line, not shown in figure).

As a result, the signal pulse is amplified into the microjoule range while maintaining a bandwidth that far exceeds that available from the input laser. Furthermore, by compensating the chirp which come either from WLC process and from subsequent propagation through dispersive elements as lens or the BBO crystal itself, such pulses can be compressed to durations below few fs.

It is worth underlining that the gain in an OPA occurs only for a narrow temporal window during which the pump and seed pulses overlap. The extent of this window

is commonly determined by the pump duration and the pump–signal temporal walk-off: under typical conditions this is limited to at most a few hundred femtoseconds. Therefore, if the pump duration is much lower than the seed ones, since the latter is chirped, only a part of the spectrum will be amplified, which can be tuned with the delay line that shifts in time the seeder in respect to the pump. This permits the tuning of amplified band across the VIS range, with pulse durations that may still be below 20 fs duration. Instead, if the seed and pump pulse has the same temporal duration, the full band can be amplified, thus reaching with the suitable compression the diffraction limited pulse. This combination of short pulse duration and wide tunability is useful for applications in ultrafast spectroscopy, which will be described in Section 1.4.

1.3 Third order optics

As done with second order non-linear effects in Section 1.2, an introductory discussion to third order optics is discussed in this chapter, retrieving the master equation in Section 1.3.1, focusing in particular on the degenerate phenomenon of self-effects (Sect. 1.3.2).

1.3.1 Master equation

Recalling the general non-linear propagation equation, now third order effects are consider, namely the polarization field is expressed as

$$P_{NL}(z,t)^{(3)} = \varepsilon_0 \chi^{(3)} E^3(z,t) \tag{1.84}$$

where the electric field is a combination of three pulses

$$E(z,t) = \frac{1}{2}\left[A_1(t)e^{i(\omega_1 t - k_1 z)} + A_2(t)e^{i(\omega_2 t - k_2 z)} + A_3(t)e^{i(\omega_3 t - k_3 z)} + c.c\right] \tag{1.85}$$

Calculating the cube, many phenomena of *four-wave mixing* are involved, which can be modelled considering four wave such that $\omega_4 = \omega_1 - \omega_2 + \omega_3$ or $\omega_1 + \omega_3 = \omega_2 + \omega_4$. The third order polarization waves at the respective frequency are

$$\begin{cases} P_{NL}^{\omega_1}(z,t) = \frac{3}{4}\varepsilon_0 \chi^{(3)} A_2 A_3^* A_4 e^{i[\omega_1 t - (k_2 - k_3 + k_4)z]} + c.c. \\ P_{NL}^{\omega_2}(z,t) = \frac{3}{4}\varepsilon_0 \chi^{(3)} A_1 A_3 A_4^* e^{i[\omega_2 t - (k_1 + k_3 - k_4)z]} + c.c. \\ P_{NL}^{\omega_3}(z,t) = \frac{3}{4}\varepsilon_0 \chi^{(3)} A_1^* A_2 A_4 e^{i[\omega_3 t - (-k_1 + k_2 + k_4)z]} + c.c. \\ P_{NL}^{\omega_4}(z,t) = \frac{3}{4}\varepsilon_0 \chi^{(3)} A_1 A_2^* A_3 e^{i[\omega_4 t - (k_1 - k_2 + k_3)z]} + c.c. \end{cases} \tag{1.86}$$

and inserted in the NL equation (1.28), four equations governing the four waves propagation are generated, being

$$\begin{cases} \dfrac{\partial A_1}{\partial z} + \dfrac{1}{v_{g_1}}\dfrac{\partial A_1}{\partial t} - \dfrac{i}{2}GVD_1\dfrac{\partial^2 A_1}{\partial t^2} = -i\dfrac{\mu_0\omega_1 c}{2n_1}\dfrac{3}{4}\varepsilon_0\,\chi^{(3)}\,A_2\,A_3^*\,A_4\,e^{-i\Delta kz} \\ \dfrac{\partial A_2}{\partial z} + \dfrac{1}{v_{g_2}}\dfrac{\partial A_2}{\partial t} - \dfrac{i}{2}GVD_2\dfrac{\partial^2 A_2}{\partial t^2} = -i\dfrac{\mu_0\omega_2 c}{2n_2}\dfrac{3}{4}\varepsilon_0\,\chi^{(3)}\,A_1\,A_3\,A_4^*\,e^{i\Delta kz} \\ \dfrac{\partial A_3}{\partial z} + \dfrac{1}{v_{g_3}}\dfrac{\partial A_3}{\partial t} - \dfrac{i}{2}GVD_3\dfrac{\partial^2 A_3}{\partial t^2} = -i\dfrac{\mu_0\omega_3 c}{2n_3}\dfrac{3}{4}\varepsilon_0\,\chi^{(3)}\,A_1^*\,A_2\,A_4\,e^{-i\Delta kz} \\ \dfrac{\partial A_4}{\partial z} + \dfrac{1}{v_{g_4}}\dfrac{\partial A_4}{\partial t} - \dfrac{i}{2}GVD_4\dfrac{\partial^2 A_4}{\partial t^2} = -i\dfrac{\mu_0\omega_4 c}{2n_4}\dfrac{3}{4}\varepsilon_0\,\chi^{(3)}\,A_1\,A_2^*\,A_3\,e^{i\Delta kz} \end{cases} \tag{1.87}$$

where it has been introduced the usual wave-vector mismatch $\Delta k = k_4 + k_2 - k_1 - k_3$. The equations are pretty similar to the ones seen in second order optics: on the left hand-side part there is the linear pulse propagation equation, while on the right hand-side part there is the third order non-linear source, which is now composed from three interacting fields.

Now particular attention is put to the self-effects, thus when a NL material is crossed by only a beam, with such intensity that it interferes with itself (or, in a quantum view, with a such number of photons to make a three-quanta interaction likely to happen): the so called *degenerate four-wave mixing* (DFWM). In this case, only a frequency is considered, i.e. $\omega_1 = \omega_2 = \omega_3 = \omega_4 = \omega_0$, and the phase-matching condition is automatically verified, since $k_1 = k_2 = k_3 = k_4 = k_0$. The equation is simplified in

$$\frac{\partial A}{\partial z} + \frac{1}{v_g}\frac{\partial A}{\partial t} - \frac{i}{2}GVD\frac{\partial^2 A}{\partial t^2} = -i\frac{\mu_0\omega c}{2n}\frac{3}{4}\varepsilon_0\,\chi^{(3)}\,|A|^2\,A \tag{1.88}$$

and applying the usual Lorentz transformation $t \to t - \frac{z}{v_g}$, the final formulation is found

$$\frac{\partial A}{\partial z} - \frac{i}{2}GVD\frac{\partial^2 A}{\partial t^2} + i\sigma|A|^2\,A = 0 \tag{1.89}$$

where all constants are grouped in $\sigma = \dfrac{3\,\omega_0}{8\,n(\omega_0)\,c}\,\chi^{(3)}$. The equation is also known as the *Non-Linear Schrödinger Equation* (NLSE) for the great similarity with the respective quantum equation describing the motion of a 1D particle in a potential directly influenced by the presence of the particle itself.

1.3.2 Self-effects

As seen in the equation (1.89), the polarization term is influenced from the amplitude term $|A|^2$. The analysis of self-effects can be done looking for the expression of the wave-vector $k(\omega) = \frac{\omega}{c}n(\omega)$, since $n(\omega)$ is influenced by non-linear effects. The refractive index expression is derived bearing in mind the relation between polarization $\vec{P}$ and the electric field $\vec{E}$. Considering a pulse travelling in a centro-symmetric material (which have no

birefringence behaviour, as $\chi^{(2)} = 0$) the total polarization is composed by a linear term and the third-order non-linear one, namely

$$\begin{aligned} P(z,t) = P_L(z,t) + P_{NL}^{(3)}(z,t) &= \varepsilon_0 \chi^{(1)} A(z,t) e^{i(\omega_0 t - k_0 z)} + \varepsilon_0 \frac{3}{4} \left|A(z,t)\right|^2 A\, e^{i(\omega_0 t - k_0 z)} = \\ &= \varepsilon_0 \left[\chi^{(1)} + \frac{3}{4}\chi^{(3)} |A(z,t)|^2\right] A(z,t)\, e^{i(\omega_0 t - k_0 z)} = \\ &= \varepsilon_0 \Big[\underbrace{\chi^{(1)} + \frac{3}{4}\chi^{(3)} |A(z,t)|^2}_{\chi}\Big] E(z,t) \end{aligned} \tag{1.90}$$

where it has been highlighted the relation between $P(z,t)$ and $E(z,t)$, which is the electrical susceptibility χ tensor.

Thanks to linear refractive index definition, i.e. $n_0^2 = \varepsilon_r = 1 + \chi^{(1)}$, the actual refractive index is

$$n^2 = 1 + \chi = \underbrace{1 + \chi^{(1)}}_{n_0} + \frac{3}{4}\chi^{(3)} |A(z,t)|^2 = n_0 \left[1 + \frac{3}{4}\frac{\chi^{(3)}}{n_0^2} |A|^2\right] \tag{1.91}$$

whose square root can be developed with the geometrical series $(1+x)^\alpha \approx 1 + \alpha x$ for small value of x, resulting in

$$n = n_0 \sqrt{1 + \frac{3}{4}\frac{\chi^{(3)}}{n_0^2} |A|^2} \approx n_0 \Big(1 + \frac{3}{8}\frac{\chi^{(3)}}{n_0^2} |A|^2\Big) = n_0 + n_2 |A|^2 \tag{1.92}$$

where it has been introduced $n_2 = \dfrac{3}{8}\dfrac{\chi^{(3)}}{n_0}$. Therefore, the refractive index has a linear term and a non-linear one that depend on the field intensity. The pulse carrier propagation will change its behaviour in function of the pulse envelope. In fact a pulse is modelled as

$$E(z,t) = A(z,t)\, e^{i(\omega_0 t - k_0 z)} = A(z,t)\, e^{i\varphi(z,t)} \quad \text{with} \quad \varphi(z,t) = \omega_0 t - \frac{\omega_0}{c}(n_0 + n_2 |A(z,t)|^2)\, z \tag{1.93}$$

It is evident that the phase itself depends on pulse intensity. The same result can be achieved calculating the result of equation (1.89) under the hypothesis of *Pure SPM* behaviour, thus neglecting the temporal broadening due to GVD. In fact it is simple to demonstrate that $\sigma = n_2 \frac{\omega_0}{c}$.

If the pulse instantaneous frequency is computed

$$\omega_{inst}(t) = \frac{\partial \phi}{\partial t} = \omega_0 - \frac{\omega_0}{c}\, n_2\, \frac{\partial |A(z,t)|^2}{\partial t}\, z \tag{1.94}$$

a frequency shift over time is shown. This kind of phenomenon is called *Self-Phase Modulation* (SPM), since the pulse itself induces its phase changing over time. In particular, it depends on the time derivative of the intensity.

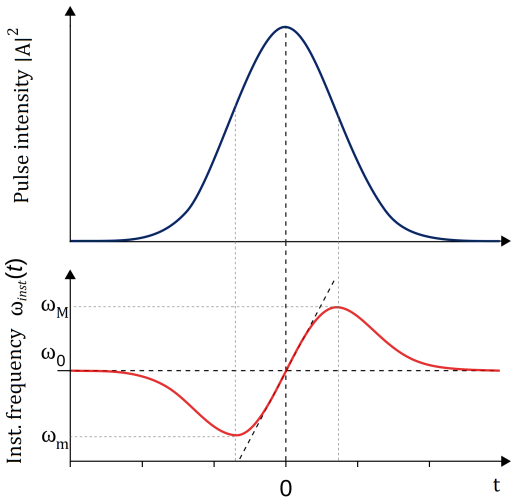

Figure 1.21: Typical pulse shape intensity, in blue. The instantaneous frequency generated by SPM is represented in red. The curve follows the time derivative of pulse intensity.

Considering a typical Gaussian pulse profile as shown in Figure 1.21, the instantaneous frequency generated by SPM is lower than ω_0 on the rising pulse edge, while higher than ω_0 on the trailing edge. At the pulse inflection points the generated frequency is at its maximum and minimum level (ω_M and ω_m), while when the derivate is null, i.e. on the pulse peak, the generated frequency is ω_0. Therefore, lower frequencies are generated before than higher frequency. It can be noted, referring to the expression (1.93) that neglects the GVD contribution, that the pulse shape does not change over propagation for third-order nonlinearities: only the spectrum is affected, since new frequencies are generated. They depend also on z: the more the pulse propagates inside the material, the wider the spectrum becomes, since the the maximum instantaneous frequency is pushed up while the minimum is pulled down with the travelled distance.

As represented in Figure 1.21, the function of frequency genesis over time is not monotonic, so the same frequency is produced two times during non-linear propagation: since the pair of frequencies are generated with different phase relationships, some will constructively interfere while others will be deleted due to destructive interference. Hence, the spectrum is modulated, as represented in Figure 1.22.a, where the interference pattern is clearly visible. The two peaks at the outer edges are the one corresponding to ω_M and ω_m, since the two frequencies do not interfere.

Till now the GVD has been neglected. Recalling the equation (1.89), the *pure SPM* solution (GVD=0) has been found in eq (1.93), while the pure linear solution (no SPM)

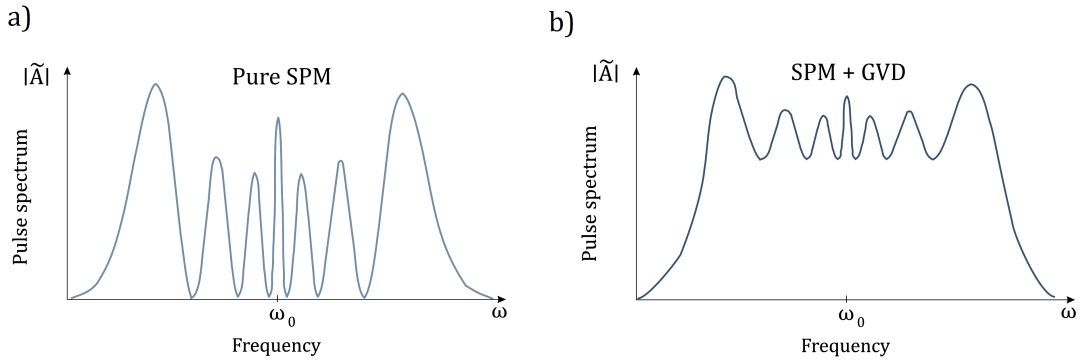

Figure 1.22: Self-phase modulation effects on spectra: *a)*: pure-SPM condition (GVD= 0); *b)*: both SPM and GVD are present (full NLSE equation).

was computed in the first section, resulting in the eq (1.23). Both contributions should be taken into account to solve the complete equation. This is usually done with the so called *split step method*, i.e. considering separately linear and non-linear effects on an infinitesimal propagation dz. Linear propagation broadens the pulse in time, without change its spectrum shape but only adding a phase term $\frac{GVD}{2}\omega^2 dz$, resulting in

$$A_L(z+dz,t) = \frac{1}{2\pi}\int_{-\infty}^{+\infty} \tilde{A}_L(z,\omega)\, e^{-i\frac{GVD}{2}\omega^2 dz}\, e^{i\omega t}\, d\omega \tag{1.95}$$

The non-linear propagation, instead, modifies the spectrum shape but not the pulse time evolution, which maintains constant its modulus while adds a phase term depending on SPM, namely

$$A_{NL}(z+dz,t) = A_L(z+dz,t)\, e^{-i\sigma|A_L(z+dz,t)|^2 dz} \tag{1.96}$$

Without entering into many details, two kind of behaviours are possible. As represented in the Fig. 1.21 lower frequency are always generated earlier than the higher ones. Recalling that when $GVD > 0$ lower frequencies travels at higher phase velocity, it causes them to advance further and further in respect to ω_0 during propagation, while higher frequencies are generated later and travels at lower velocity, moving them further and further back: the pulse gets time broadened, even more than linear propagation behaviour because also the spectrum is wider. So, the peak intensity decreases, reducing the SPM effect (Figure 1.23.a). On the other hand, if $GVD < 0$ lower frequencies, first generated, are slower than the high frequency, which are generated late, so the pulse remains temporally compressed, compensating the GVD effect as in Figure 1.23.b.

In conclusion, SPM is used to broaden a pulse spectrum by exploiting self third-order effects. Every transmitting material can theoretically generates the phenomenon, if passed through an high intensity beam. In order to achieve suitable values of intensity, strong focusing is needed. The simple way to provide an efficient SPM effect is to use *Photonic Crystal Fibres* (PCF), in which very low values of GVD maintain high pulse intensity thus producing very wide spectra that can reach *one octave* ($\omega - 2\omega$ bandwidth), or an *Hollow Core Fibre* (HCF), in whose core a noble gas with high $\chi^{(3)}$ is inserted, broadening the spectrum and supporting very high energies. Another technique is to focus the beam into bulk materials and exploits the *Kerr Lens effect*, thus producing further focusing required for SPM. In this way *White Light Continuum* generation (described in detail in 2.5.1) can occur.

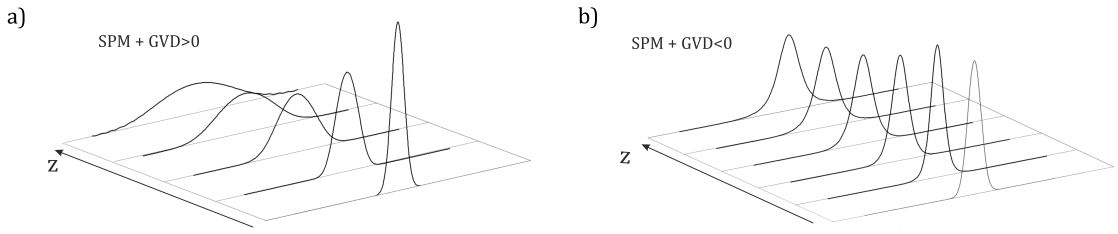

Figure 1.23: *a)* Pulse evolution in positive dispersion regime in the presence of SPM; *b)* Pulse evolution in negative dispersion regime in the presence of SPM. Adapted from [12].

1.4 CARS Spectroscopy

In this section, spectroscopy based on Raman scattering is discussed. As seen in the introduction, Raman scattering is used for substance identification because its spectrum, characterized by a peak pattern portraying specific atomic bond configurations, is a molecular fingerprint. Like all substances, pathogens have a characteristic spectrum. By detecting Raman radiation it is therefore possible in right circumstances to describe the chemical composition of samples under examination, without coming into contact with them.

This is the reason why Raman scattering could be also exploited for stand-off revelation of chemical and biological warfare. In Section 1.4.1 and 1.4.2 Raman scattering is presented. Coherence techniques that make use of third-order linear phenomena to enhance Raman signal are introduced in Sect. 1.4.3, while in Sect. 1.4.4 and 1.4.5 CARS is presented and modelled. At the end, time-resolved CARS and hybrid CARS techniques are described in Section 1.4.6.

1.4.1 Raman scattering introduction

Raman scattering takes its name from C. V. Raman who discovered it in 1928. From that year, a huge amount of techniques based on the phenomenon have grown. It was based on a simple observation: when a monochromatic light beam at frequency ω_0 passes through a transparent material the majority of the incident light gets transmitted without any change, while a smaller portion is scattered within the whole solid angle. The spectral analysis of the scattered light shows that, in addition to Rayleigh scattering i.e. radiation which have changed the wave-vector direction but not its modulus, keeping the incident frequency ω_0, there are also discrete components at different frequencies constituting the Raman scattering. In general, lines are grouped in pairs symmetrically positioned with respect to the Rayleigh frequency, namely $\omega_R = \omega_0 \pm \Omega$. These new, shifted components are referred to as *Raman shift* (Ω) and the set of lines forms the *Raman shift spectra*.

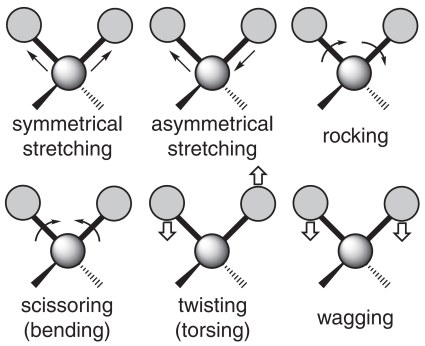

Figure 1.24: Typical molecular modes. To each is associated a *normal coordinate* Q_k which is a linear combination of the Cartesian ones [13].

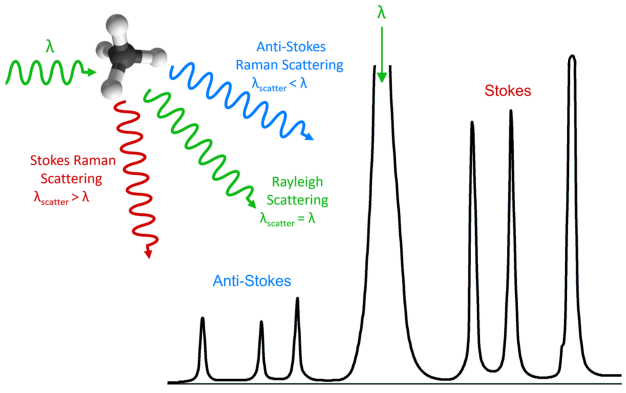

Figure 1.25: Molecular scattering diagram: Rayleigh (green), anti-Stokes Raman (blue) and Stokes Raman (red).

Scattered frequencies (ω_R) are usually referred to as Raman shift wave-numbers, being $\tilde{\Omega} = \frac{\Omega}{2\pi c} = \frac{\omega_R - \omega_0}{2\pi c}$ and expressed in cm^{-1}. Negative shift, thus with $\lambda > \lambda_0$, are called *Stokes lines*, while positive shifts with $\lambda < \lambda_0$, are called *anti-Stokes lines*, as pictured in Fig. 1.25.

A Raman shift corresponds to the excitation of low frequency motion of molecular system. In general, as presented in Sect. 1.1 when electro-magnetic fields travel through material, molecules are excited by light such that they oscillates at the same frequency (polarization effect), emitting light in every direction as they are oscillating dipoles differently oriented in space, which explains the Rayleigh scattering. However, a molecule has further modes that can be activated, as it is composed by atoms that can move harmonically one with respect to one another activating vibrations which are schematized in Fig. 1.24. Strong bonded atoms will have higher oscillation frequency, as they are linked by a harder spring (the usual harmonic oscillator model). This kind of collective molecular oscillations correspond to low energy levels (frequencies Ω in mid-wavelength or far infrared spectrum) and they can be activated from VIS-NIR radiation. The resulting Raman radiation (ω_R) is the interference of this two phenomena, thus two new frequencies scatter at $\omega_S = \omega_0 - \Omega$ (the excitation happens when molecule is initially relaxed) and $\omega_{AS} = \omega_0 + \Omega$ (excitation from molecules with already active vibrational states). Since most of the molecules are initially in the ground state, the Stokes signal is usually stronger. The interfering pattern can be completely superimposed on the phenomenon of optical beat notes, described in detail in Section 4.2.2.

The quantum view of the phenomenon is even clearer. As represented in Fig. 1.26, the molecule in ground state is excited from a pump beam to a virtual energy level. Then it relaxes on the vibrational level Ω, emitting a photon at Stokes frequency $\omega_S = \omega_0 - \Omega$. If the pump photon hits a molecule already in the vibrational excited state, it is further excited to an higher virtual level and it can relax to ground state emitting an anti-Stokes frequency photon at $\omega_{AS} = \omega_P + \Omega$.

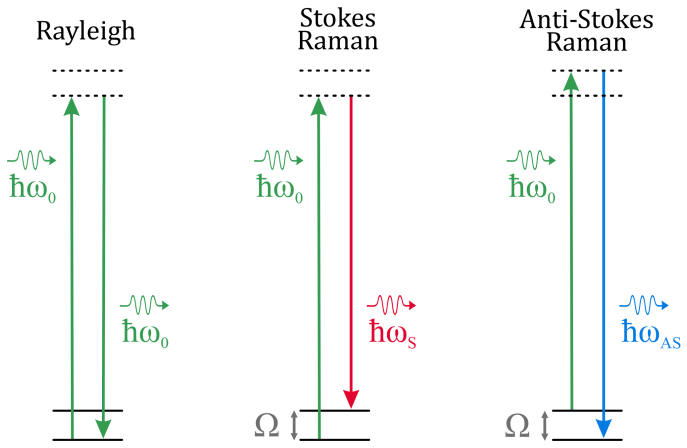

Figure 1.26: Scattering energy levels: grounds-state levels are represented by a straight line, while virtual excited ones in dotted line. Only one vibrational low frequency level is represented (Ω), even if they are a multitude, different for each molecule Ω_k. The exciting wave (green) has a frequency of ω_0, while ω_S and ω_{AS} are the Stokes and Anti-Stokes frequency respectively.

A molecule has several vibrational and rotational levels Ω_k and the resulting spectrum is composed from many Raman shifts. Because different molecules with different atoms and bonds have different vibrational modes, each substance has a different Raman spectrum, which is used as a fingerprint to identify unknown molecules.

It is fundamental to be clear that the Raman scattered signal does not contain the IR radiation (at frequency Ω) but the shift from a probing frequency ω_0 (i.e. $\omega_R = \omega_0 \pm \Omega$). The shift is usually in between 0 and 3500 cm^{-1}, which correspond to bandwidth of 93 nm for a probing frequency of 515 nm. This has an intrinsic advantage: the shifts are independent from the probing frequency, so in principle any source could be used, producing identical results. If dealing with organic molecules or solutions, the 400-600 nm range is usually a good choice because of water low absorption coefficient.

Raman scattering is a very weak effect, about 3–4 order of magnitude lower then the Rayleigh scattering, which in turn is about 0,01–0.1 % of the total incident light for transparent media. The reason for incredibly low intensity of Raman scattering is twofold. First, the Raman cross-section (approximately 10^{-30} cm^2, eleven order of magnitude smaller than the IR absorption cross-section) is very small compared to the Rayleigh cross-section, so the photons interact with a lower probability. Moreover, different molecules can oscillate at same frequency modes but with different phases, so the emitted waves are not phase-matched. The problem has been overcome with the *Coherent Raman Scattering*, described in Section 1.4.3.

1.4.2 Classic model

Before continuing, a simple description for Raman scattering modelling is now introduced [14]. In a classic physics frame, dipoles are the most efficient elements responsible for light-matter interaction, hence all magnetic poles and higher order electric multi-poles can be neglected in the discussion. The dipole is represented by two point charges $\pm q$ separated by a distance $\vec{d}$, defined as $\vec{\mu} = q\vec{d}$. In a polyatomic molecule, the electric dipole is formed when the center of positive charge is displaced from the negative one. When a vibrational mode is activated, the dipole harmonically changes over time as

$$\vec{\mu} = \vec{\mu}_0 \cos(2\pi c\tilde{\nu} t) \tag{1.97}$$

with $\tilde{\nu}$ the wave-number associated with the harmonic oscillator model, once stated the relation $\tilde{\mu} = \dfrac{1}{2\pi c}\sqrt{\dfrac{K}{m}}$, where K is the bond strength and $m = \frac{m_1 m_2}{m_1 + m_2}$ the reduced mass of the nuclei.

Oscillators can generate electromagnetic radiation at frequency ν or absorb it, exciting the respective molecular vibration. As mentioned before, electric dipole-induced oscillation is the phenomenon behind the scattering of light. The external electric field polarizes the molecule, shifting charges. The relation between induced dipole moment vector ($\vec{\mu}'$) and the electric field can be expanded as done in equation (1.12) with the polarization (note it is the same phenomenon: once described locally, the other macroscopically since $\vec{P} = \dfrac{\sum_i \vec{\mu}'_i}{V} = \dfrac{\langle \vec{\mu}' \rangle}{V}$). Considering only the first order interaction, i.e. a linear relationship

where the proportionality constant α is called *polarizability*, namely

$$\vec{\mu}' = \boldsymbol{\alpha}\vec{E} \tag{1.98}$$

Generally speaking, different polarization directions of the electric field induce different dipoles, so first order polarizability is a tensor (expressed in bold) and the extended relationship is

$$\begin{bmatrix} \mu'_x \\ \mu'_y \\ \mu'_z \end{bmatrix} = \begin{bmatrix} \alpha_{xx} & \alpha_{xy} & \alpha_{xz} \\ \alpha_{yx} & \alpha_{yy} & \alpha_{yz} \\ \alpha_{zx} & \alpha_{zy} & \alpha_{zz} \end{bmatrix} \cdot \begin{bmatrix} E_x \\ E_y \\ E_z \end{bmatrix} \tag{1.99}$$

The polarizability can be interpreted as the measure of the flexibility of the electron cloud: how much it is deformed or displaced when influenced by an external electric field. When vibrational modes of the molecule are excited, nuclei move towards each other and the polarizability also oscillates. The polarizability motion can be modelled expanding it in series. The expansion variables are the normal coordinates Q_k (the system of reference commonly used in molecular mechanics, associated with the wave-number $\tilde{\nu}_k$) which may represent a distance or an angle or whatever quantity is involved in molecular motion. Hence, each element of the polarizability tensor is expanded as

$$\alpha_{ij} = \alpha_{ij_0} + \sum_k \left.\frac{\partial \alpha_{ij}}{\partial Q_k}\right|_{\vec{Q}_{eq}} Q_k + \sum_{k,\,l} \left.\frac{\partial^2 \alpha_{ij}}{\partial Q_k \partial Q_l}\right|_{\vec{Q}_{eq}} Q_k Q_l + \dots \tag{1.100}$$

where $\vec{Q}_{eq}$ identify the situation of equilibrium. For small amplitude vibrations near the equilibrium, the expansion can be truncated at the first order and the coordinates motion is assumed to be purely harmonic: $Q_k = Q_{k_0}\cos(2\pi c\tilde{\nu}_k t)$. If a monochromatic field, $\vec{E} = \vec{E}_0\cos(2\pi c\tilde{\nu}_0 t)$, hits the molecules, then the induced dipole moment is

$$\begin{aligned} \vec{\mu}' = \boldsymbol{\alpha}\vec{E} &= \boldsymbol{\alpha}_0\vec{E}_0\cos(2\pi c\tilde{\nu}_0 t) + \sum_k \left.\frac{\partial \boldsymbol{\alpha}}{\partial Q_k}\right|_{\vec{Q}_{eq}} Q_{k_0}\vec{E}_0\cos(2\pi c\tilde{\nu}_k t)\cos(2\pi c\tilde{\nu}_0 t) = \\ &= \boldsymbol{\alpha}_0\vec{E}_0\cos(2\pi c\tilde{\nu}_0 t) + \\ &\quad + \frac{1}{2}\sum_k \left.\frac{\partial \boldsymbol{\alpha}}{\partial Q_k}\right|_{\vec{Q}_{eq}} Q_{k_0}\vec{E}_0\big[\cos(2\pi c(\tilde{\nu}_0 - \tilde{\nu}_k)t) + \cos(2\pi c(\tilde{\nu}_0 + \tilde{\nu}_k)t)\big] \end{aligned} \tag{1.101}$$

where the prosthaphaeresis relation $\cos\beta\cos\gamma = \frac{1}{2}\cos(\beta+\gamma) + \frac{1}{2}\cos(\beta-\gamma)$ has been used. Now it is very clear the presence of three harmonic oscillations, whose wave-number is $\tilde{\nu}_0$, $\tilde{\nu}_0 - \tilde{\nu}_k$ and $\tilde{\nu}_0 + \tilde{\nu}_k$ which correspond to Rayleigh scattering, Stokes Raman and anti-Stokes Raman respectively. These beat note frequencies are produced when the dipole oscillating at ω_0 is modulated by the molecular vibration ω_k.

Additionally, both oscillation amplitudes (Rayleigh and Raman) are proportional to the electric field intensity $\vec{E}_0$, but while the Rayleigh scattering depends on equilibrium tensor $\boldsymbol{\alpha}_0$ Raman scatterings is governed by its weak derivative, that reflects the sensitivity of molecular polarizability to small changes of nuclei position along normal coordinates.

Then, the radiation is emitted by oscillating dipoles, as the known relation

$$\vec{E} = \frac{3(\vec{\mu}' \cdot \vec{r} - r^2\vec{\mu}')}{4\pi\varepsilon_0 r^5} \tag{1.102}$$

producing the scattering events described above.

It is worth underline the difference between standard absorption or emission IR spectroscopy, where the molecules are directly excited by a photon with energy equal to $\hbar\Omega$: in this case one component μ_i of the electric dipole moment $\vec{\mu}$ changes during this vibration, i.e. when the value of a dipole moment derivative differs from zero, i.e.

$$\left.\frac{\partial \mu_i}{\partial Q_k}\right|_{\vec{Q}_{eq}} \neq 0 \tag{1.103}$$

Instead, in case of Raman scattering, a given normal vibration appears in Raman spectrum if at least one component of the polarizability tensor changes during this vibration, which is linked to nuclei position, namely

$$\left.\frac{\partial \alpha_{ij}}{\partial Q_k}\right|_{\vec{Q}_{eq}} \neq 0 \tag{1.104}$$

In conclusion, with a simple classic model some of the main properties of Raman scattering have been derived. The complete phenomenon description involves a long digression on quantum theories, as the time-dependent perturbation theory and the quantum field theory, which is beyond the scope of this work. It can be found in [15].

1.4.3 Coherent Raman Scattering

As mentioned in Section 1.4.1, the spontaneous Raman signal is an incoherent signal, since the molecular phase of emitted wave molecule is not correlated with the others. Nevertheless, if a further wave oscillating at Stokes frequency ω_S affects all the molecule, then they are bound to oscillates at the same phase, since the emission is no more spontaneous but stimulated. This rises the Stokes and anti-Stokes signal amplitude of several order of magnitude.

Two synchronized pulses at ω_P and ω_S (with $\omega_P > \omega_S$), called *pump* and *Stokes* respectively, are sent on a material. The molecule Raman response depends on its vibrational level Ω: if it has a vibrational level separation which is exactly $\Omega = \omega_P - \omega_S$ then it is coherently excited. Since each molecule is oscillating with the same phase, having been hit by the same pulses, then Stokes and anti-Stokes signals are emitted in phase with grater intensity. In practice, pump and Stokes are used together to create vibrational coherence within the collective motions of molecules.

Generally speaking, *Coherent Raman Scattering* (CRS) is a parametric four-wave mixing process, since it involves four energy levels tangled by light-matter interaction. Thus the description is carried out starting from the equation (1.87). There are different kind of spectroscopy techniques, which differs from the type of signal detected from Raman scattering spectra and from the pulse shape and spectrum used to excite the sample:

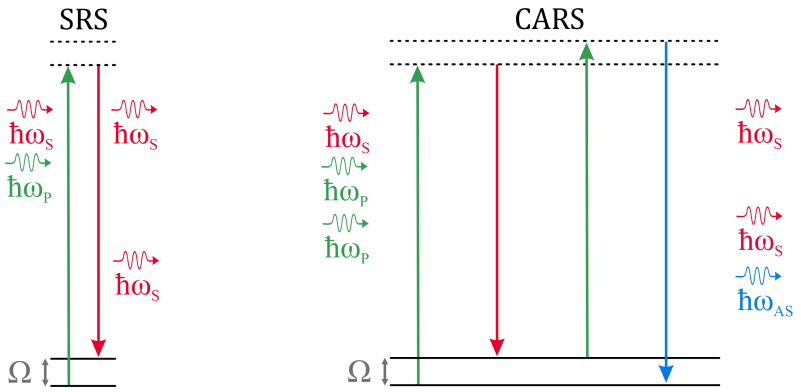

Figure 1.27: Energy levels diagram in techniques based on Coherent Raman Scattering: Stimulated Raman Spectroscopy (SRS), which analyses Stokes spectrum; Coherebt Anti-Stokes Raman Spectroscopy (CARS), that is focused on anti-Stokes lines.

- *Stimulated Raman Spectroscopy* (SRS) at frequency $\omega_P - (\omega_P - \omega_S)$, detecting the scattered coherent Stokes radiation;
- *Coherent Anti-Stokes Raman Spectroscopy* (CARS) at $\omega_P + (\omega_P - \omega_S)$, which is the dual of SRS, detecting the scattered coherent anti-Stokes spectrum;
- *Stimulated Raman Gain* (SRG) at ω_S, which detects the increase of Stokes signal;
- *Stimulated Raman Loss* (SRL) at ω_P that is based on intensity loss of the pump signal.

For the latter two, signal relative variations are in the order of 10^{-3}–10^{-4}: lock-in amplifiers and other signal recovery techniques must be employed. In the next section CARS technique will be described in detail.

1.4.4 Coherent anti-Stokes Raman Scattering

In coherent processes, two pulses (pump and Stokes) are sent to make vibrational levels ($\Omega = \omega_P - \omega_S$) resonate. The further interaction of Raman resonances with the intense pump beam at ω_P generates two optical beat notes, one at Stokes frequency ($\omega_P - \Omega$, which increase Stokes signal intensity) and the other at anti-Stokes one ($\omega_P + \Omega = 2\omega_P + \omega_S$). The latter is the signal detected in CARS. Note that anti-Stokes beat note is always present even in SRS, otherwise energy conservation would not apply (see Fig. 1.27): it is simply neglected. In CARS, instead, the information of low frequency vibrational modes is carried right by anti-Stokes signal.

The key thing about CARS is that the anti-Stokes frequency is spectrally separated from the pump and Stokes ones, as pictured in Fig. 1.30: this allows to suppress all the reflected power coming from the source with a high pass filter, acquiring only the weak anti-Stokes signal containing sample information without damage ultra-sensitive instruments.

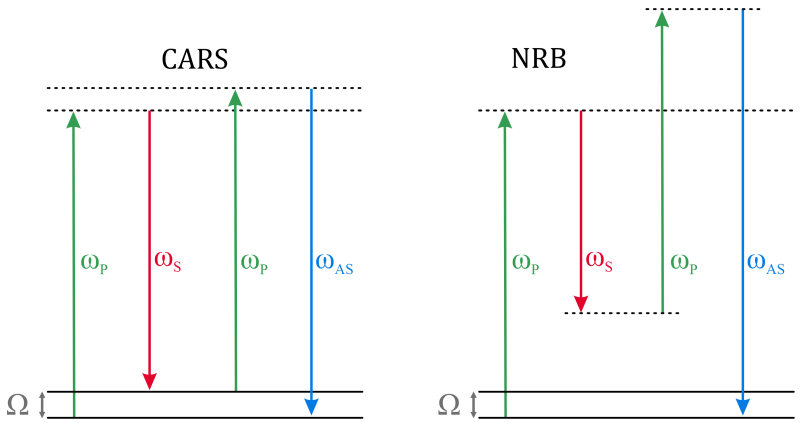

Figure 1.28: On the left: CARS level diagram, when $\omega_P - \omega_S = \Omega$. On the right: non-resonant third-order non linear effect occurring even if $\omega_P - \omega_S \neq \Omega$.

CARS mathematical description takes advantage of what has already been discussed in third-order optics Section 1.3.1. Recalling the four-wave mixing equation (1.87), since $\omega_4 = \omega_1 + \omega_3 - \omega_2$, the anti-Stokes frequency is writeable as

$$\omega_{AS} = 2\omega_P - \omega_s = \omega_p + \Omega \tag{1.105}$$

where it is set $\omega_4 = \omega_{AS}$, $\omega_3 = \omega_1 = \omega_P$ and $\omega_2 = \omega_S$. Note that the third order interaction does not require to have a vibrational level Ω, but takes place regardless of molecular resonances. This unwanted effect creates the so called *non resonant background* (NRB), which goes on thanks to virtual levels, as represented in Figure 1.28: if the pump and Stokes pulse frequency difference matches a vibrational level Ω, then a strong coherent signal is generated; if not, a non-resonant signal rises anyway.

Now, the anti-Stokes pulse generation is derived from the ω_4 equation (see page 43), namely

$$\frac{\partial A_{AS}}{\partial z} + \frac{1}{v_{g_{AS}}}\frac{\partial A_{AS}}{\partial t} - \frac{i}{2} GVD_{AS}\frac{\partial^2 A_{AS}}{\partial t^2} = -i\kappa_{AS}\,\chi^{(3)}\,A_P\,A_S^*\,A_P\,e^{i\Delta k z} \tag{1.106}$$

where the constants have been grouped under $\kappa_{AS} = \dfrac{3\,\omega_{AS}}{8\,c\,n(\omega_{AS})}$ and the wave-vector mismatch is $\Delta k = k_{AS} - 2k_P + k_S$. Considering monochromatic pulses and neglecting the GVD term, the equation becomes

$$\frac{dA_{AS}}{dz} = -i\kappa_{AS}\,\chi^{(3)}\,A_P^2\,A_S^*\,e^{i\Delta k z} \tag{1.107}$$

Under both pump and Stokes no depletion approximation, i.e. $A_P(z) = A_P$ and $A_S(z) = A_S$, the equation is uncoupled from the other ones (pump and Stokes equations are not reported for compactness) and the solution is straightforward

$$A_{AS}(z) = -i\kappa_{AS}\,\chi^{(3)}\,A_P^2\,A_S^*\,z\,e^{i\frac{\Delta k}{2}z}\,\mathrm{sinc}\left(\frac{\Delta k z}{2}\right) \tag{1.108}$$

where z is distance travelled in the medium by pump and Stokes pulses. The CARS signal intensity can be calculated from $I = \frac{1}{2}\varepsilon_0 cn|A(z)|^2$, obtaining

$$I_{AS} = \frac{4}{\varepsilon_0^2 c^2 n^2}\,\kappa_{AS}^2\,|\chi^{(3)}|^2\,I_P^2\,I_S\,L^2\,\mathrm{sinc}^2\left(\frac{\Delta kL}{2}\right) \tag{1.109}$$

Moreover, in case of a tight focused beams the section in which CARS signal is generated is very narrow, i.e. $\frac{L}{2} \to 0$, and the sinc is approximate to one, even if the condition of phase-matching is not precisely fulfilled, reaching the final formula

$$I_{AS} \propto \kappa_{AS}^2 \left|\chi^{(3)}\right|^2 I_P^2 I_S L^2 \tag{1.110}$$

CARS signal depends on the square of pump beam intensity, on the Stokes intensity and on modulus squared of the third order optical susceptibility. In the latter term are contained all the molecular properties and vibrational levels. Generally, it will be composed from a non-resonant term, which can be assumed nearly constant over a certain bandwidth, and a resonant one

$$\chi^{(3)} = \chi_R^{(3)}(\omega) + \chi_{NR}^{(3)} \tag{1.111}$$

The resonant part may be composed of a series of peaks, coinciding with the vibrational modes of the molecule, which can be modelled as any classical resonant behaviour with a Lorentzian-shape function. Considering a set of Raman resonances at frequency Ω_k (whose wave-number is $\tilde{\nu_k} = \frac{\Omega_k}{2\pi c}$) with a line-width of Γ_k, the resonant electric susceptibility can be written as a sum of this set

$$\chi_R^{(3)}(\omega) = \sum_k N_k \frac{A_k}{(\omega - \Omega_k) - i\Gamma_k} \tag{1.112}$$

where N_k indicates the number of Raman scatterers for k^{th} mode and A_k a term which takes into account polarization of pump and Stokes and the effect of anisotropies. In fact, in general $\chi^{(3)}$ is a tensor depending on light polarizations direction. Note that the frequency ω in the formula is nothing but the virtual level excited from pump and Stokes beam, i.e. $\omega = \omega_P - \omega_S$: if $\omega = \omega_P - \omega_S = \Omega$, $\chi^{(3)}$ assumes its local maximum value, on the resonance peak; if $\omega \neq \Omega$, it follows the Lorentzian line-shape. For each Raman resonance, the real and imaginary part of $\chi^{(3)}$ can be separated: it is clear that the peak information is mainly contained in the imaginary part, as represented in Figure 1.29

$$\mathbb{R}e\{\chi_R^{(3)}\} = \frac{\omega - \Omega}{(\omega - \Omega)^2 + \Gamma^2} \qquad \mathbb{I}m\{\chi_R^{(3)}\} = \frac{\Gamma}{(\omega - \Omega)^2 + \Gamma^2} \tag{1.113}$$

Since the CARS measured intensity is proportional to its modulus squared

$$|\chi^{(3)}|^2 = |\chi_R^{(3)} + \chi_{NR}^{(3)}|^2 = |\chi_R^{(3)}|^2 + |\chi_{NR}^{(3)}|^2 + 2\,\chi_{NR}^{(3)}\,\mathbb{R}e\{\chi_R^{(3)}\} \tag{1.114}$$

the signal has three components, whose the latter two do not contain Raman information. The non-resonant constant term creates a *non-resonant background* (NRB) signal which buries the resonant signal, as shown in Figure 1.29. If the NRB increases reaching high amplitude, the Raman peaks are completely hidden in anti-Stokes spectrum.

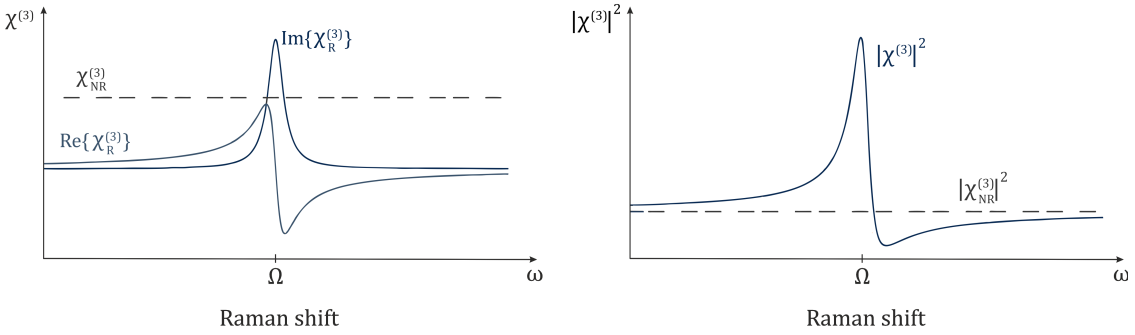

Figure 1.29: On the left: third order electrical susceptibility components for resonance behaviour. On the right: modulus squared of $\chi^{(3)}$: if the non-resonant behaviour (dotted lines) has high amplitude, then the resonance peak is buried into NRB.

Since the non-resonant contribution is in general unknown, this distortion makes the interpretation of CARS spectra and the extraction of molecular fingerprints difficult, resulting in the major drawback of this technique. Several approaches for NRB reduction have been developed during the last twenty years, including epi-detection CARS, polarization CARS, time-resolved CARS, interferometric/heterodyne CARS, pulse-shaping CARS, phase-retrieval CARS and frequency modulation CARS [1]. Those used during the laboratory work will be described in the Section 1.4.6.

1.4.5 Broadband CARS

Up to now, the theory has been developed assuming monochromatic beams: both pump and Stokes have a single fixed frequency of ω_P and ω_S, respectively. The consequence is that only a single vibrational mode $\Omega = \omega_P - \omega_S$ can be excited. It may be useful only for concentration density detection of a single molecule with known resonances, which is not particularly practical. The problem can be overcome by using a broadband Stokes signal and a narrowband pump signal, in such a way to reveal a broad spectrum of Raman resonances: ω_S is now a continuous set of frequencies, all the Raman vibration modes $\Omega_k = \omega_P - \omega_S$ are excited. Figure 1.30 shows the spectral properties of pump and Stokes beams.

This allows to probe the whole molecular vibrational spectrum with a single pump-Stokes shot. A single acquisition can be realized in a time scale of milliseconds: then hyperspectral imaging is possible together with dispersive elements which separates spectral component for detection process. Alternatively, *Fourier Transform CARS* provides the Raman spectrum Fourier transforming a modulated signal with interferometric techniques. In any case, *Broadband CARS*, also referred to as *Multiplex CARS* or *Multicolours CARS*, is widely used in many fields where molecular recognition is needed.

The narrow bandwidth of pump pulse determines the inherent peaks resolution. The Stokes bandwidth affects instead the spectral width of the generated CARS and so the extent of the Raman measurable region. In order to cover broad bandwidth, the source

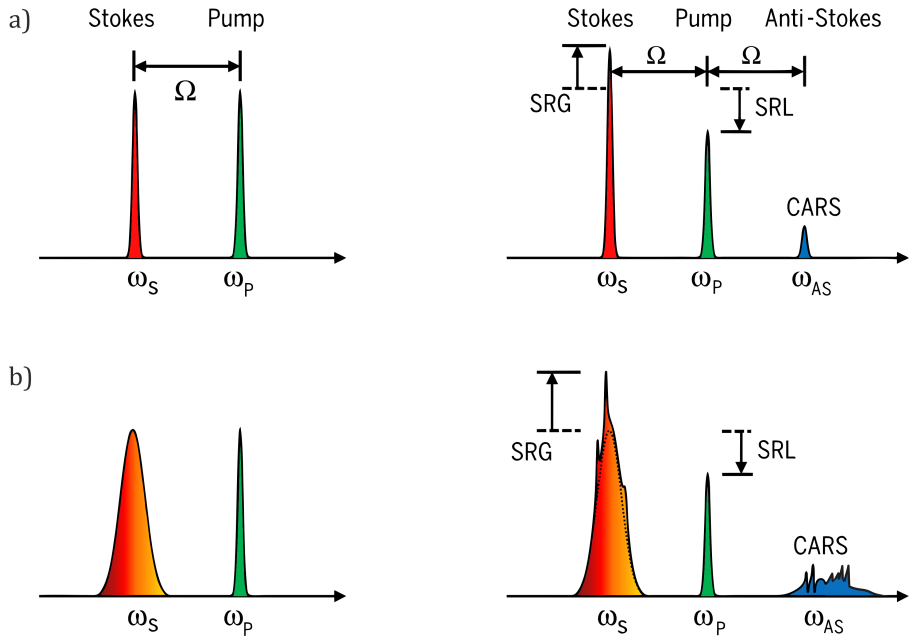

Figure 1.30: *a)* On the left, pump and Stokes spectra for a single frequency CARS. On the right, the three possible techniques to investigate Raman vibrational spectra, i.e. Stimulated Raman Gain, Stimulated Raman Loss and CARS. *b)* Broadband CARS: the Stokes pulse has a wide spectrum that can excite all possible Raman modes. Even if with SRL is still detectable, it does not contain spectral information. Only SRS or CARS are suitable for molecular fingerprint recognition. Adapted from [16].

must drive particularly wide-spectrum, thus ultrashort, pulses: this is why femtosecond pulses are used in broadband CARS configurations. In addition, femtosecond pulses are able to broaden their spectrum due to non-linear phenomena, as seen in Section 1.3.2, and their short duration allows them to reach high intensities and then an higher CARS signal.

1.4.6 NRB reduction techniques: TR-CARS and hybrid-CARS

Two techniques used during the laboratory work to reduce the non-resonant background (NRB) are now presented.

The first one, called *Time-Resolved CARS* (TR-CARS) is based on the idea to involve a third pulse (the *probe*) in order to add a temporal degree of freedom during the CARS non-linear process. In fact, referring to Fig. 1.28 in a quantum frame description, two photons at frequency ω_P are required in the process: one comes together with the Stokes pulse (ω_S) to excite the Ω_k vibrational mode, while the other is absorbed by the virtual level which emits the anti-Stokes photon. Since the vibrational mode has a long dephasing time (typically picoseconds) with respect to short pulse duration, the molecule stays excited on vibrational level Ω for a while. So, the second photon can be delayed with respect to the first pump-Stokes pulses, without any constraint. The level diagram is represented in Figure 1.31.

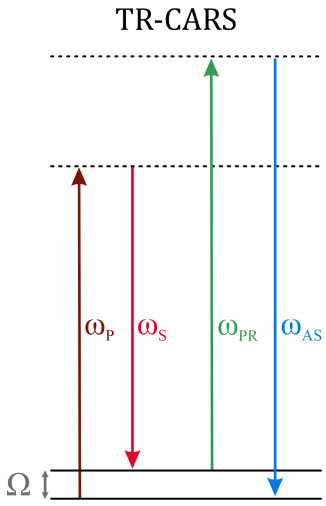

Figure 1.31: TR-CARS energy level diagram. TR-CARS is also referred to as *three colours CARS*, since it involves three pulses at different frequency.

The scenario can be pictured also with a classical description: pump and Stokes pulses strike the molecule, its atoms nuclei are perturbed from their equilibrium position and begin to oscillate, causing polarizability motion. The phenomenon lasts for a longer time than the pump-Stokes duration, so when they are gone the molecules is still oscillating. At this point, the third impulse comes into play and interacts with the vibrational mode, probing its resonance state, which interferes and originates the two optical beats of Stokes and anti-Stokes frequency.

The probe pulse must have a narrow-band spectrum, since it is the reference frequency (namely ω_{PR}) for Raman shifts and it determines the spectral resolution, which is often less than tens of cm^{-1}. In Figure 1.32 the pulse spectra and their time evolution is represented. The Stokes pulse has a broadband spectrum which activates together with pump pulse all Raman resonances, so it will have shorter temporal duration. Note that, as a third probing pulse has been introduced, now the role of pump and Stokes beam can be interchanged: pump can have a broad spectrum and Stokes a narrow one, without any change: It is just a matter of nomenclature: what counts is their difference. The probe interaction moment can be set with a variable delay line: different delays probes the sample at different time instants.

Therefore, the third-order polarization will be a superposition of a pump pulse $E_P = A_P(t)e^{i\omega_P t}$ coming together with a Stokes pulse $E_S = A_S(t)e^{i\omega_S t}$ and a τ-delayed probe $E_{PR} = A_{PR}(t-\tau)e^{i\omega_{PR}}$ [17]

$$P^{(3)}(\tau,t) = -\int_0^{+\infty} A_P(t+\tau-t')A_S^*(t+\tau-t')A_{PR}(t)\, e^{i(\omega_P-\omega_S)t'}\boldsymbol{\alpha}(t')dt' \qquad (1.115)$$

where $\boldsymbol{\alpha}(t)$ is the linear polarizability response tensor. In case of equal polarization direction, the tensor element is

$$\alpha(t) = A_{NR}\delta(t) + \sum_k A_k e^{-i2\pi c\tilde{\nu}_k t}\left[\left(\frac{1}{\rho_k}-\frac{4}{3}\right)e^{-\frac{t}{T_{2_k}}} + \frac{4}{3}e^{-t(\frac{1}{T_{rot_k}}+\frac{1}{T_{2_k}})}\right] \qquad (1.116)$$

where the response of the system k-th Raman-active vibrational mode is modelled as damped exponentials of amplitude A_k with a centre wave-number $\tilde{\nu}_k$, vibrational de-phasing time T_{2_k}, rotational correlation time T_{rot_k}, and depolarization ratio ρ_k. Without entering into details, it is worth noting that the first term represent the NRB: the delta function scaled by its factor A_{NR} (depending on $|\chi^{(3)}_{NR}|$) is present only when $\tau = 0$, i.e. the three beams are temporally superposed. The excited population, which the probe can interact with, has a double exponential decay, one vibrational and one rotational, depending on activated Raman modes. So, the probe must be delayed enough not to interact with the pump and Stokes pulse but not too late because the sample would be already in the ground state, with an exponential decay behaviour with de-phasing time T_2.

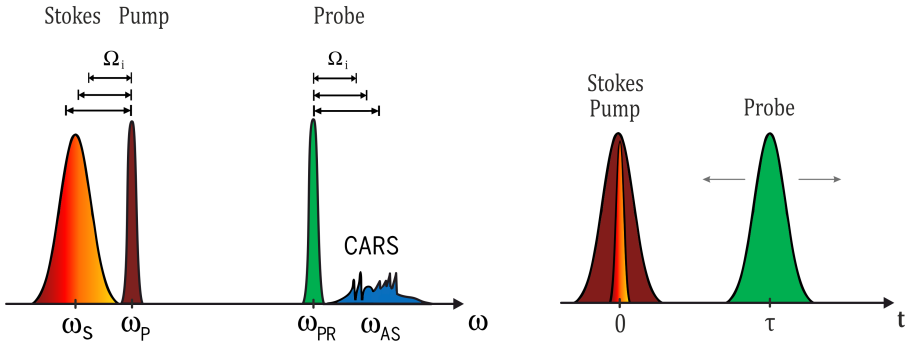

Figure 1.32: Time-resolved CARS spectra and time evolution of pulses.

The possibility of using three different pulses has four great advantages:

1. It is possible to chose a probe frequency completely different from the pulse and Stokes one. As seen in 1.4.1, Raman spectrum does not depend on exciting frequency, but only on the resonances relative shift from the probing pulse. This allow a one-to-one map of resonance frequencies ω_i into higher optical frequencies as represented in Fig. 1.32.

2. Since the excitation process is detached from the probing one, the probe can be time delayed as desired. Performing multiple acquisitions at different probe delays, it is possible to reconstruct the entire molecular free-induction-decay dynamics, analysing its behaviour with a temporal resolution of femtoseconds. From two-dimensional maps of Raman spectrum evolution with increasing delay, lot of information can be retrieved.

3. Moving away the probe pulse from the other two, the NRB is drastically reduced: the pure virtual levels involved in the non-resonant process (Right Fig. 1.28) require the simultaneous coexistence of all the three pulses. If even one of is delayed, NRB efficiency is culled. Nevertheless, the downside is that excited molecular populations decrease exponentially with time: if the probe gets to the sample too late, no Raman mode is activated and CARS signal is not generated. The probe delay must be set optimizing the CARS signal-to-noise ratio.

4. Lastly, also the spectral amplitude, phase, and time shape of the probe can be manipulated for further refinement, with no repercussion on excitation process. Hybrid-CARS discussed below is one example of probe manipulation.

The second approach here described for NRB reduction is the so-called *hybrid-CARS*, because of its mixture of time- and frequency-resolved techniques. In the frame of TR-CARS just described, the probe should be as much as possible temporally close to pump-Stokes pulses (taking advantage of the maximum number of excited molecules) but not superimposed with them, although the simultaneity would give rise to non-resonant noise. The ideal behaviour would be to have a $sinc^2$-shaped pulses, in order to superimpose the pump pulse in its first node, as pitcured in Figure 1.33. In this way, NRB is attenuated

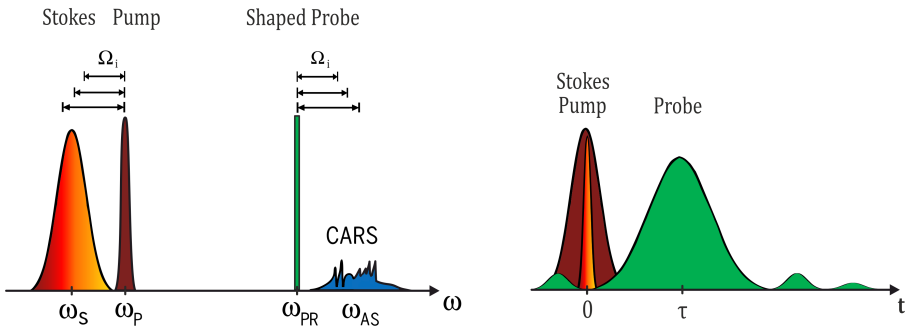

Figure 1.33: Hybrid-CARS spectrum and time evolution of pulses.

(even if not completely removed because of tails superposition) and the peak is very close to pump-Stokes pulses.

This kind of time-shaping can be done working on its Fourier transform domain, properly modulating the spectrum [18]. Since the Fourier transform of a sinc-shaped function is

$$\mathscr{F}^{-1}\Big\{\operatorname{sinc}(at)\Big\}(\omega) = \frac{1}{\sqrt{2\pi a^2}}\operatorname{rect}\left(\frac{\omega}{2\pi a}\right) \tag{1.117}$$

then the spectrum must be modulated with a rectangular window.

Note that acting on spectral width it is possible to widen or shrink in time the probe pulse, adding a further parameter to the CARS setup control: a super-narrowband probe spectrum guarantees high resolution in Raman spectra but enlarge the time duration (some tens of picoseconds), resulting in a deterioration of temporal resolution. In addition, also the probe signal intensity is reduced, having narrowed its power spectral density. The right balance point must be found, based on detection type and sample constraints. Further description of this technique can be found in 2.4.2. Other kind of spectral shaping techniques and various combination including sinc-square, square-sinc, exponential-Lorentzian and Gaussian-Lorentzian have been adopted in literature [19].

In conclusion, a combination of broadband arranging and frequency-resolved multicolours acquisition with time-delayed narrowband probing yields a sensitive and robust method, which has a great potential for detection applications in substance fingerprint recognition and molecular free-induction decay analysis.

Chapter 2

Hybrid-CARS source design

Coherent Anti-Stokes Raman Spectroscopy (CARS) is a technique used to obtain molecular information. Generically speaking, molecules have different compositions, conformations and atomic bonds that determine different vibrational levels. So, each molecule can associated to a specific characteristic Raman spectrum, whose peak pattern acts as a molecular fingerprint. Vibrational information can be used for both identification of unknown substances or for researching a specific molecule on a sample. Since it is a third order process an high intensity source is needed, which is usually reached thanks to a very tight focus in microscopy configuration [20]. Instead, for a stand-off detection geometry where sources are much less focused, ultrashort pulses are a key feature for signal enhancing. The source must deliver pulses of sufficient energy and time duration to generate a very intense Raman signal. Moreover, in case of scattering samples only a small portion of the radiation will be collected from the detector, increasing the source power requirements. Imaging purposes further boosts the need of strong CARS signals so as to be able to lower sensor exposure times.

As presented in Section 1.4.4, three pulses are needed for time-resolved, low NRB broadband CARS: pump, Stokes and probe. Pump and Stokes arrives on the sample simultaneously, activating the molecular vibrational mode (Ω) that matches the difference between pump and Stokes frequencies. To excite a wide set of Raman modes, two pulses are needed: a broadband and a narrowband one. From now to on, the broadband pulse will be called *CARS pump* (or simply *pump*), while the narrowband will be referred to as *Stokes*. Once vibrational levels have been activated and the molecular modes are oscillating coherently, a third pulse comes, probing the molecular state: the narrowbanded *probe*. Thanks to the interference between the probe and the Raman vibrations, two optical beatnote signals are emitted (Stokes and anti-Stokes), as described in 1.4.1.

Summarizing, the source must be capable of generating three different ultrashort high energy pulses, two of them narrowband and one broadband that could be tuned. All three pulses must be temporally and spatially handled in such a way they impact on the sample overlapped. In addition, with a delay stage on probe pulse line, it is possible to retrieve the temporal evolution of the vibrational excited state. Probe shaping is also operated for NRB reduction, thus applying the hybrid-CARS principles.

In the next sections, generation of the three CARS pulses will be discussed in detail,

focusing on spectral, temporal and spatial manipulation implemented to obtain the requirement mentioned before. First, a brief remark on laboratory measure instrumentation is done in Sect. 2.1, introducing the FROG setup for femtosecond pulse time characterization. Then, the general CARS setup overview is presented in Section 2.2, where the master laser characteristics are also discussed. Sections 2.3, 2.4, 2.5 present the Stokes, probe and pump pulse design, respectively. Finally, Section 2.6 describes the overall source output which will be used for experiments discussed in Chapter 3.

2.1 Instrumentation

Before going through the experimental setup, a brief mention on the laboratory instrumentation is presented.

The power measure are carried out by means of various thermopiles, which convert optical to thermal energy through an absorber and generate an electrical signal via Seebeck effect.

The spectra are retrieved from a fibre optic spectrometer (AvaSpec, linear CMOS) with a maximum resolution of 0.55 nm from 1 µm-slit and a 300 lines/mm grating spanning over a bandwidth between 200-1000 nm.

For spatial characterization, a camera (Ophir SP620U, 1200x1600, 7.1×5.4 mm, 62 dB dynamic range) and its software BeamGage® are used to get the beam width. Since there are several definition of beam waist, as $1/e^2$ width, FWHM or D86, also depending on the measure technique, the ones used in this thesis the 4σ-diameter (ISO standard), i.e. the width of a beam in the horizontal or vertical direction is 4 times the standard deviation of the horizontal or vertical marginal distribution, respectively. Mathematically, it is expressed by

$$D_{4\sigma_x} = 4\sqrt{\frac{\int_{-\infty}^{+\infty} I(x,y)(x-\bar{x})^2}{\int_{-\infty}^{+\infty} I(x,y)}} \tag{2.1}$$

where $I(x,y)$ is the beam intensity and $\bar{x}$ is the beam *centroid* (the intensity-weighted mean) calculated as

$$\bar{x} = \frac{\int_{-\infty}^{+\infty} I(x,y)x}{\int_{-\infty}^{+\infty} I(x,y)} \tag{2.2}$$

Same calculus is performed for $D_{4\sigma_y}$ and $\bar{y}$.

Temporal characterization is performed with the FROG (*Frequency-resolved optical gating*) technique. It is based on the principle of pulse autocorrelation. Since there is no electronic instrumentation capable of measuring femtosecond pulses, the beam is duplicated and the copy is used to interfere with itself at varying delays. In practice the duplicated pulse is spatially separated, delayed and made to interact with the original pulse on a second harmonic crystal. The generated sum frequency pulse (SFG) is the autocorrelation figure of the pulse itself, which contains time duration information. By varying the delay between the two copies, the autocorrelation changes according to the

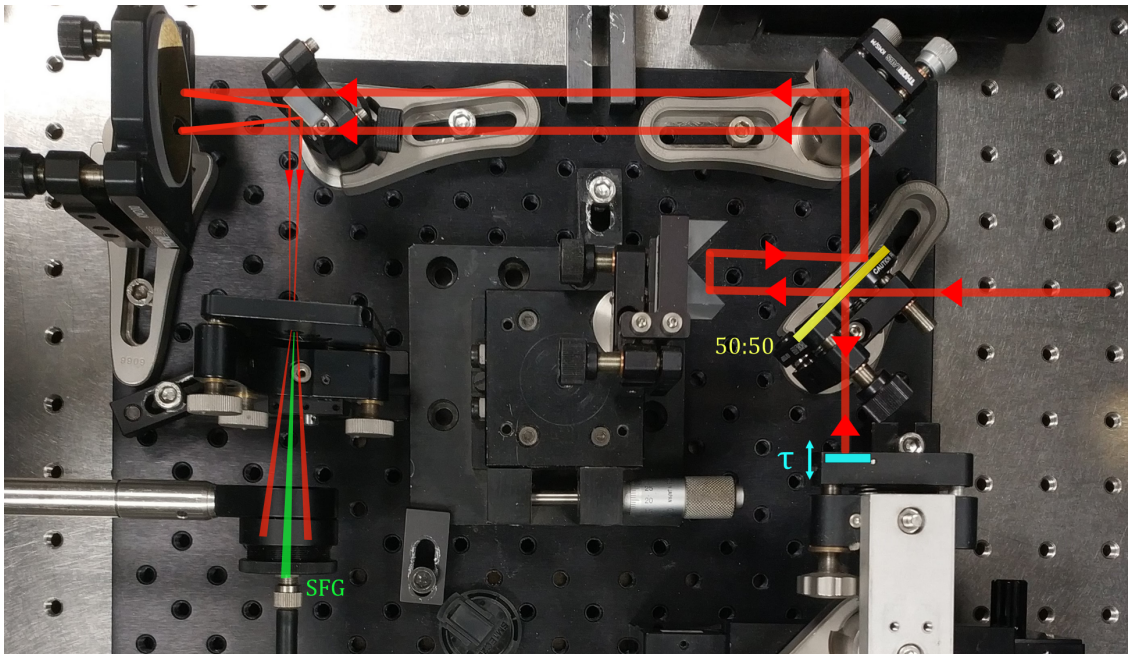

Figure 2.1: FROG setup: a pellicle beam splitter (yellow) divides the pulse into two copies. One is delayed by a computer-controlled slide (light blue). The beams are then focused by a spherical mirror ($f = 50\,\text{mm}$) on a 10 µm-thick BBO crystal mounted on a angle-tunable holder. The non-collinear SFG, whose wave-vector $\vec{k}$ is the sum of the source beam ones, is spatially separated from each pulse SHG and it is collected by the spectrometer fibre.

delay-dependant sliding window. The *gated* autocorrelation (i.e. SFG signal) can be written as the product of the beam and its delayed copy

$$A(t,\tau) \propto E(t)\,E(t-\tau) \tag{2.3}$$

Measuring the spectra at each delay, it is possible to acquire with a spectrometer a *spectrogram*, namely a map of SFG intensity, as a function of delay and frequency

$$S(\omega,\tau) = \left| \int_{-\infty}^{+\infty} A(t,\tau) e^{-i\omega t} dt \right|^2 = |\tilde{A}(\omega,\tau)|^2 \tag{2.4}$$

Since the spectra do not contain the pulse phase information but only its modulus, the first can be retrieved from a feedback-loop software. Without entering in details, it is possible to construct a recursive procedure that derive the spectral phase information from the equation

$$\sqrt{S(\omega,\tau)}e^{\varphi(\omega,\tau)} = \int_{-\infty}^{+\infty} A(t,\tau) e^{-i\omega t} dt \tag{2.5}$$

by doing an initial impulse hypothesis $E(t)$, calculating its autocorrelation and iteratively comparing it with the actual data contained in the spectrogram. It can be demonstrated that the solution gets to numerical convergence after finite steps. This allows to obtain a complete reconstruction of the pulse shape, in both modulus and phase, thus determine

its real temporal evolution. The FROG setup is represented and briefly explained in Figure 2.1.

2.2 Setup overview

All three CARS signals are generated starting from a unique master laser.

The master source is a Yb:KWG regenerative amplifier system (Pharos, LightConversion) capable of generating 250 µJ pulses at 10 kHz with a central wavelength at 1022 nm, for an overall power of 2.5 W. The output linear polarization is horizontal. The mode-locked oscillator seed, generated by Kerr lens effect in diode-pumped medium, has a central frequency of 1040 nm with a FWHM of 20 nm (Fig. 2.4), resulting in an output power of about 470 mW if pumped with 25.0 A, which can be tuned via software and power-feedback stabilized. The ML threshold diode-current is ∼23 A. The active medium temperature is maintained at 23.5 °C through an active water-based chiller. The regenerative amplifier stage is based on diode-pumped Yb:KGW, which provides an output power of 2.5 W if pumped with a current of 43 A with a cavity damping time set to 218.5 ns. Figure 2.2 shows the laser output power curve as a function of pumping current. Built-in second and third order dispersion compensators can be tuned in order to minimize the pulse duration.

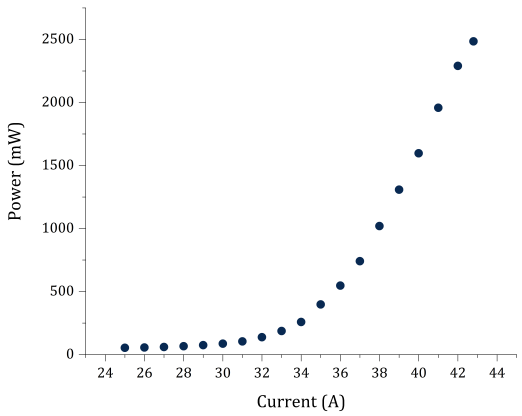

Figure 2.2: Regenerative amplifier output power in function of diode current pumping.

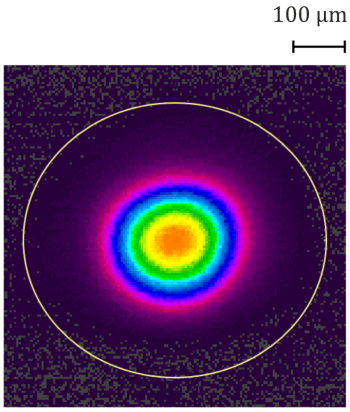

Figure 2.3: Master laser spatial profile, collimated by a $f = 500$ mm.

The spatial mode collimated with a 500 mm-focal lens is represented in Fig. 2.3. It results in a diameter of $D_{4\sigma_x} = 291$ µm and $D_{4\sigma_y} = 262$ µm.

The pulse characterization, measured at working parameters described above, is presented in Figure 2.4 and 2.5. Both spectrum and time evolution has been reconstructed with the FROG technique, which achieves also the temporal and spectral phase. The spectrum has a peak frequency of 1022 nm with a FWHM of ∼5 nm. The estimated temporal FWHM is 254 fs.

Figure 2.6 at page 66 shows a scheme of the overall CARS source setup. It is composed of several stages: the CARS pump beam, coloured in yellow, is generated by a WLC

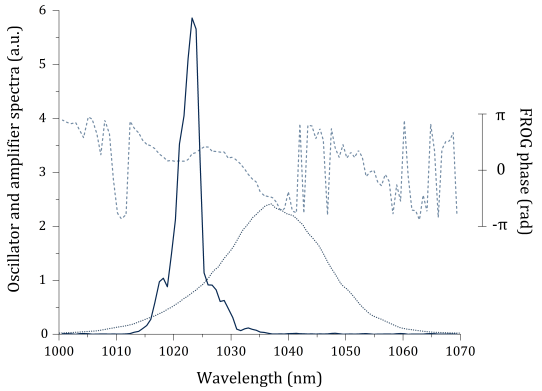

Figure 2.4: Master laser spectrum, calculated by FROG algorithm: it is peaked at 1022.7 nm with a FWHM of 4.4 nm (dark straight line). Its relative spectral phase is represented in dashed line. Oscillator seeder spectrum, without amplification stage, is pictured as a light dotted line.

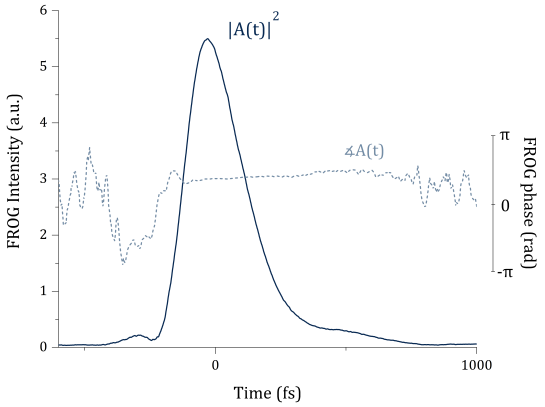

Figure 2.5: Master laser pulse time evolution reconstructed by FROG algorithm: amplitude envelope (straight line) and phase (dashed one).

stage (see Section 2.5.1), amplified by three OPA stages, described in Section 2.5.2, and compressed by a prism compressor (cfr. 2.5.4). The probe signal represented in green is generated by a SHG stage and spectrally manipulated for hybrid-CARS technique in the probe shaper. The Stokes beam, red coloured, is the remaining power exiting from the NL crystal which has not been converted into second harmonic.

Beam polarizations are specified with arrows (horizontal) or circled dots (vertical). Above the beams are indicated pulse energies. Each optic element is labelled with an acronym which is explained in the figure caption or during the next section discussion. Crystals are highlighted with a 3D shape.

In order to produce a Raman anti-Stokes signal, each pulse must arrive on samples at the same time and with perfect spatial overlap. So each CARS beam, namely pump, Stokes and probe, must be delayed with appropriate delay stages and spatially manipulated so as to get an equal focused profile: telescopic lens systems (TS) and irises are used for the scope. In the final stage all beams are coupled by dichroic mirrors for a tight focused collinear geometry CARS and sent to the sample illumination and detection stages, described in Section 3.1.

Each beam generation and manipulation stage will be described in detail in the next sections, together with spectral, temporal and spatial mode pulse characterisation.

The actual setup is pictured in Figure 2.7 at page 67.

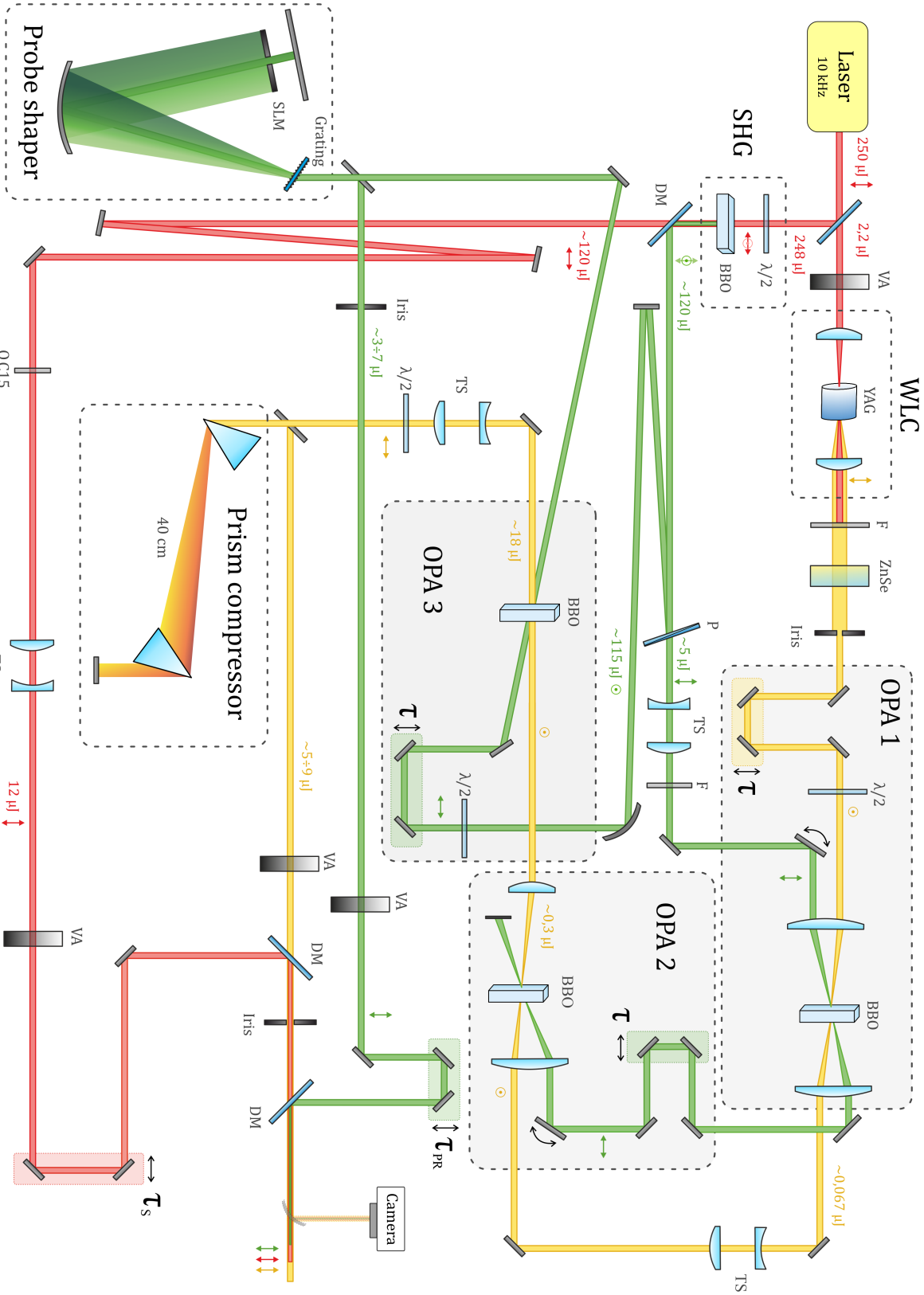

Figure 2.6: CARS laser source scheme: pump (yellow), Stokes (red) and probe (green) lines. TS: telescopic system; F: low pass filter at 1 µm; $\frac{\lambda}{2}$: half-wave plate; VA: variable attenuator; DM: dichroic mirror; SLM: spatial light modulator; P: polarizer.

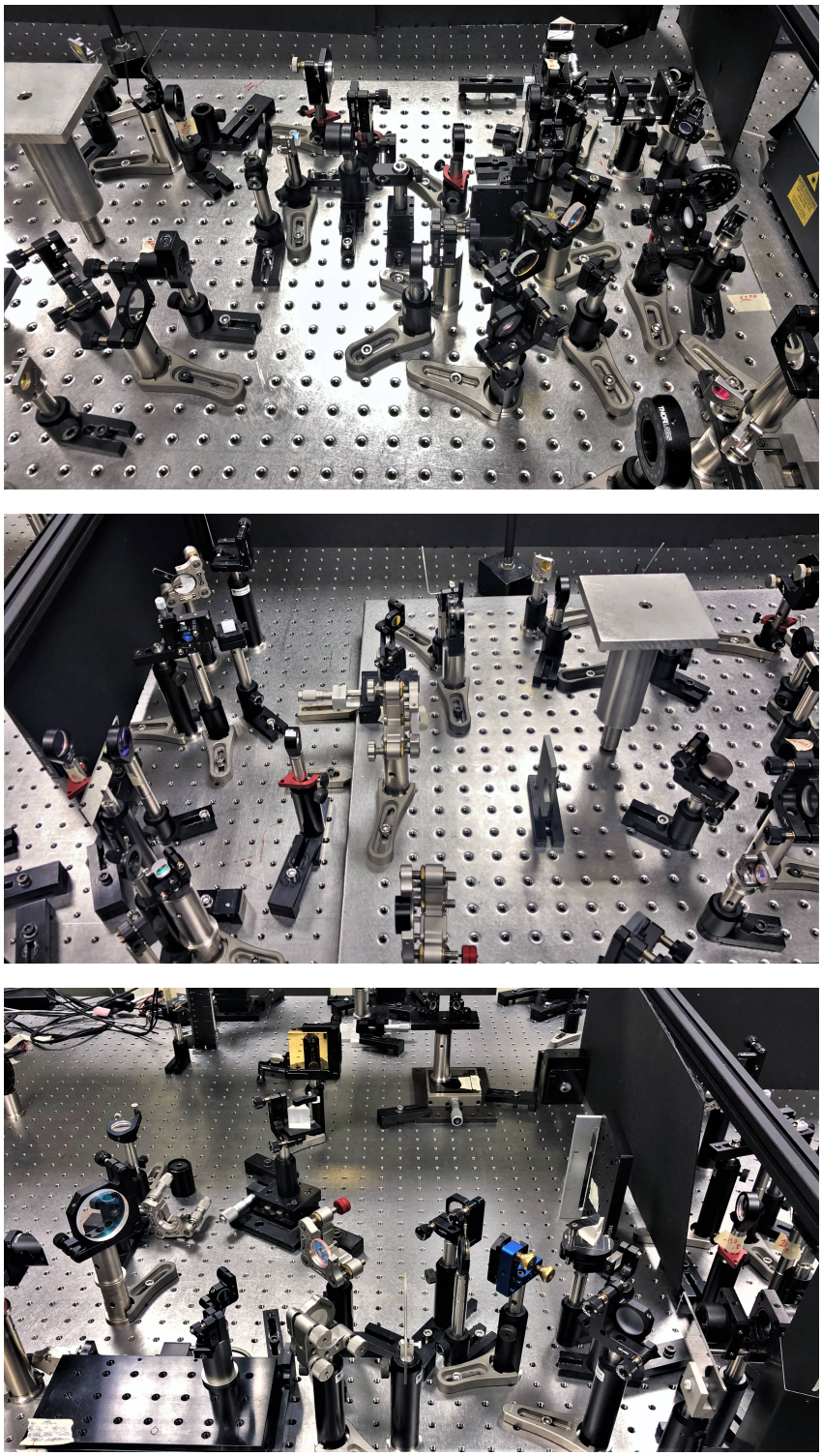

Figure 2.7: From the top: WLC, SHG and first two OPA stages; third OPA and probe shaper; prism pair compressor, dichroic mirrors, Stokes delay and motorized probe delay stage.

2.3 Stokes pulse

Stokes pulse is essentially the one coming from the master 1022 nm laser: its temporal characterization is shown in Figure 2.5 while the spectrum is represented in Figure 2.9. As pictured in Figure 2.6, the master beam is first split into two branches by a dielectric mirror used as a 99:1 beam splitter. A little power is sent to the seed generation stage (WLC) for the CARS pump beam, described in Section 2.5.1. The remaining energy is sent through a $\frac{\lambda}{2}$ wave-plate in order to set the correct polarization for the SHG stage, described in detail in Section 2.4. The remaining NIR power of about 1.2 W is decoupled from its second harmonic via a dichroic mirror. The beam travels along some dielectric mirrors in order to be delayed as pump and probe. A 15 % optic coupler (OC15 in the setup scheme) with neutral dispersion spectrum is used to attenuate the optical power. A telescopic system, composed by a coated lens pair of focal 300 mm and −150 mm, make the Stokes beam dimensions to match with the pump and probe ones when they are all collimated on the sample. Its near field mode after the telescopic system is shown in Figure 2.8, consisting a profile with $D_{4\sigma_x}$ of 2.457 mm and $D_{4\sigma_y}$ of 2.244 mm with an optical power of about 120 mW.

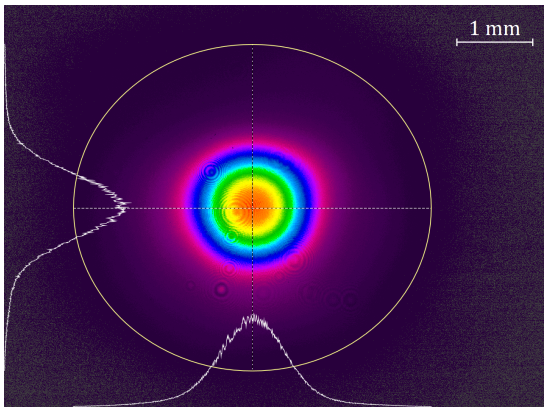

Figure 2.8: Near field profile of Stokes beam, at 60 cm from laser output.

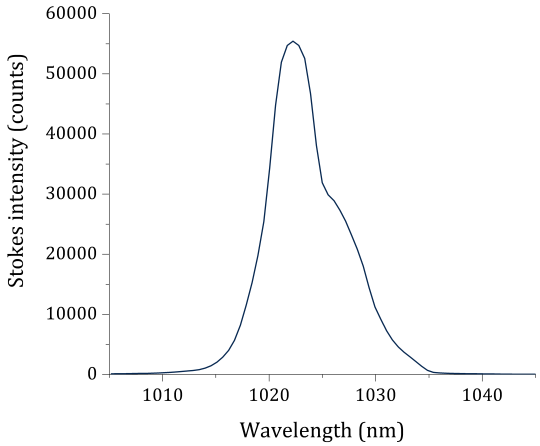

Figure 2.9: Stokes pulse spectrum.

2.4 Probe pulse

The strongest requirement for the probe pulse is to be narrow-banded, since its bandwidth is intrinsically linked to the detection resolution. If two Raman peaks are separated less then its bandwidth, then they can't be singularly resolved. Then, there is no requirement on probe central frequency value, since Raman signal is an interference one. A good choice is often a pulse between 400-600 nm, where it is visible by human eye and the water absorption has its minimum, as well for the availability of optics elements in VIS range. Since the fundamental pulse is peaked at 1022 nm, its second harmonic can be used both as the pump beam for seed amplification in OPAs and as the CARS probe.

2.4.1 Second Harmonic Generation stage

The probe pulse is firstly generated in the Second Harmonic Generation stage (SHG in Fig. 2.6. The 1022 nm-beam polarization is set by a half wave-plate, in such a way to minimize the number of wave-plates in following stages slightly rotating the horizontal polarization of few degrees. The crystal, a 6×6 mm 2.5 mm-long β-BaB_2O_4 (BBO, Eksma Optics), is coated and cut at 23.4° with respect to the optical axis, which is the Type I phase-matched angle. In this configuration, BBO has a walk-off angle of 55.9 mrad and an effective non-linear optical coefficient of 2 pm/V. The crystal is slightly rotated on propagation axis so that the 1022 nm beam polarization is aligned with ordinary axis. Figure 2.10 shows the phase-matching relation in function of pump wavelength.

With an output of 2.5 W at 10 kHz, each pulse brings 250 µJ in 250 fs, thus a peak power of 1 GW. The pump intensity can be estimated considering an active area of $A = \frac{\pi D_{4\sigma_x} D_{4\sigma_x}}{8}$, with a near field profile measured at 60 cm from the laser output hole of $D_{4\sigma_x}$= 3.03 mm and $D_{4\sigma_y}$= 2.86 mm thus about 29 GW/cm^2. An output power of 1.2 W at 511 nm is generated, with a conversion efficiency of about 48 %. The near field SH profile is shown in Fig. 2.11 ($D_{4\sigma_x}$= 1.943 mm and $D_{4\sigma_y}$= 1.872 mm). The pulse temporal duration follows the one of the fundamental (Fig. 2.4) without a noticeable dispersion since it has a narrow-banded spectrum.

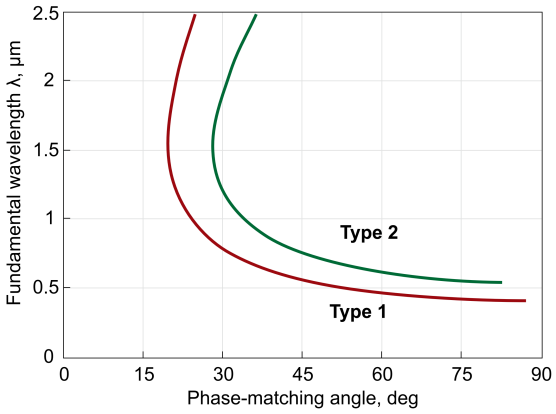

Figure 2.10: BBO phase-matching tuning curve [21].

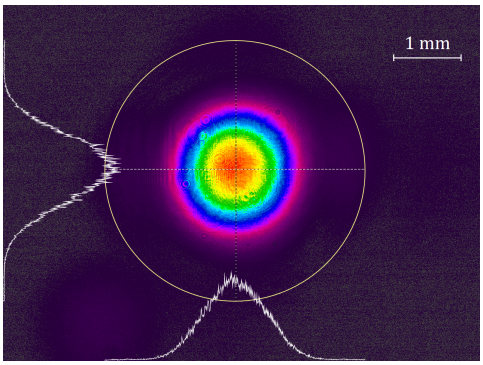

Figure 2.11: Near-field second harmonic spatial profile.

The SHG polarization is aligned to the BBO extraordinary axis. Due to crystal rotation, it is slightly tilted from a vertical direction, such that it can be decomposed into two contribution: a low power horizontally polarized one (sketched in light green in Fig. at page 66) and an high power one with vertical polarization.

The second harmonic is then separated from the fundamental via a dichroic mirror (DM) and sent to amplification stages. A polarizer divides the radiation into two branches: the low power (50 mW) horizontally polarized one is used to amplify the first two OPAs, while the other of about 1.15 W, vertically polarized, is sent to the high gain third OPA stage. Amplification stages are described in detail in Section 2.5.2.

2.4.2 Probe shaper

After having pumped the OPA, the remaining power is sent to the *probe shaper* stage. Recalling hybrid-CARS technique described in Section 1.4.6, the idea is to manipulate the probe spectrum in such a way to transform its temporal evolution to get some nodes in amplitude. Pump and Stokes beams will then be delayed in order to temporally match the probe node, eliminating the non-resonant background (NRB). In this case, a sinc-like temporal evolution is pursued, as shown in Fig. 1.33 at page 59. The Fourier transform of a sinc function is the rectangular function (eq. (1.117)), so the spectrum must be rectangularly shaped.

Firstly, the beam is dispersed via a transmitting grating (Ibsen Photonics, FSTG-XVIS-1274-904) providing high diffraction efficiency (80 %) combined with high dispersion (0.079°/nm). The diffraction efficiency curve is shown in Figure 2.12. The grating is a 4×4 mm 0.625 mm-thick dielectric-coated fused silica with 1274 l/mm and an angle of incidence of 17.3°. Then a cylindrical silver mirror (ThorLabs CCM254-100, $f = 100\,\text{mm}$) focuses the dispersed beam on a adjustable vertical slit (Spatial Light Modulator, SLM) which spatially filter out the outermost frequencies of probe spectrum, rectangularly modulating it as the slit shape. A dielectric mirror reflects back the radiation, which is re-collimated spatially by the cylindrical mirror and spectrally by the transmission grating. The shaped probe is finally extracted with a small gold mirror and sent through an iris for both easy alignment with other beams and spatial profile manipulation (reducing the iris diameter, diffraction make the pulse profiles larger, in order to match the Stokes and pump ones).

Lot of power is lost in this stage: two passes in the transmission grating the optic power is reduced of 40 %, the spectral power density of the frequencies outside the rectangular shape is lost and also the presence of the iris contributes. The final probe power is ∼70 mW. Spectrum and probe mode are shown in Section 2.6.

Probe bandwidth and temporal duration can be derived from maps pictured in the next chapter: they show a NRB figure with a FWHM between 0.73 ps and 2.67 ps (see page 101), so probe duration can be estimated to be between ∼470 fs and ∼1.3 ps, depending on the SLM aperture. Finally, probe band can be estimated from the Raman peak resolution. Referring to the image 3.13 the peaks spectral FWHM it varies between 15 and 25 cm^{-1}, corresponding to a probe bandwidth of 0.65 nm and 0.39 nm.

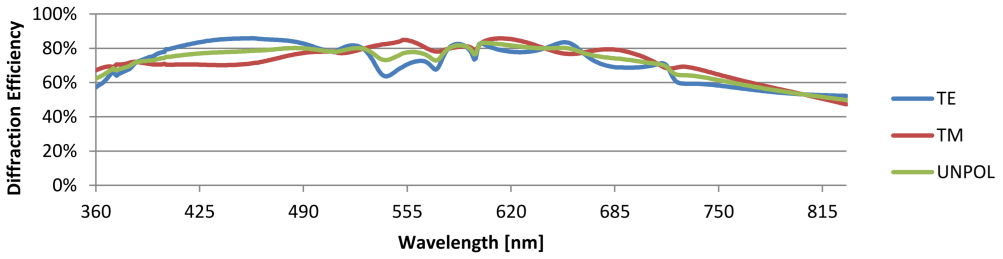

Figure 2.12: Grating transmission efficiency, from [22].

2.5 Pump pulse

As mentioned in the Section 1.4.5, a pump and Stokes pulses are needed to excite coherently Raman resonances at frequency corresponding to their difference: $\Omega_k = \omega_P - \omega_S$. To cover the entire Raman frequency spectrum (0–3500 cm^{-1}), it is necessary that the pump pulse contains a continuum of different frequencies, i.e. a broadband spectrum, so as to excite all modes at Ω_k. The third-order non-linear self-effect of *Self Phase Modulation* (SPM) discussed in Section 1.3.2 is exploited to achieve the pump wide spectrum seed, which is then amplified.

As shown in Figure 2.6 at page 66, the narrowband master beam at 1022 nm is split into two branches by a dielectric mirror used as a 99:1 beam splitter. About 2.2 µJ are driven to a WLC stage where a broadband seed is generated and sent in the three non-collinear parametric amplification stages (NOPA, or simply OPA from now to on) that amplify it. The OPAs are pumped by a fraction of SHG pulse at 511 nm, described in Section 2.4.1.

2.5.1 White Light Continuum generation

The OPA seed is generated in a third-order non-linear material with a process called *Whilte Light (Continuum) generation* (WLC or WLG), where both SPM and Kerr-lens effects take place. A brief description is now presented.

Recalling the equation (1.92), it is known that an intense beam has influence on a non-linear material refractive index. The latter can be decomposed in two contribution: one, n_0 is constant (depending on first order electrical susceptibility $n_0 = 1 + \chi^{(1)}$), while the other depends both on third order optical properties ($n_2 = \frac{3}{8}\frac{\chi^{(3)}}{n_0}$) and on the beam intensity $|A|^2$, thus

$$n = n_0 + n_2|A|^2 \tag{2.6}$$

This kind of material response determines the SPM effect, namely the generation of new frequencies in function of the time derivative of pulse envelope (see Eq. (1.94)). However, in order for spectrum broadening to take place, it is necessary to achieve high intensity in the medium. This is accomplished by the pulse itself thanks to the Kerr-lens effect. In fact, a generic laser pulse has an intensity spatial distribution on the plane (x, y) that changes along propagation on z-axis. In most of the cases it can be assumed to be a Gaussian TEM_{00}, namely

$$|A(x, y, z)|^2 = |A_0|^2 \Big(\frac{w_0}{w(z)}\Big)^2 e^{-2\frac{x^2+y^2}{w^2(z)}} \tag{2.7}$$

where $w(z)$ is the beam $1/e^2$ diameter and w_0 the beam waist. Hence, also the refractive index depends on plane coordinates ($n = n(x, y)$) with higher values in the center (on propagation axis) as compared with the wings of the spatial distribution. So the wavefronts are deformed and the NL material results in a lens, whose focal power is determined by the beam intensity itself: the so called *self focusing* or *Kerr lens* effect. In case of positive third-order optical susceptibility ($\chi^{(3)} > 0$) the beam diameter is reduced

during propagation and the effect is stronger when the pulse amplitude is higher. In the opposite case, when $\chi^{(3)} < 0$ the beam is self-defocused.

Self-focusing occurs when the phase shift due to Kerr effect compensates for the phase shift of Gaussian beam diffraction, namely $\phi_{diff} = \frac{2\pi}{\lambda} n_0 \frac{L}{2 z_R^2 n_0^2}(x^2+y^2)$ while the Kerr-lens phase change is

$$\phi_{Kerr} = \frac{2\pi}{\lambda} L\Delta n = \frac{2\pi}{\lambda} L n_2 I_0 e^{-2\frac{x^2+y^2}{w_0^2}} \approx \frac{2\pi}{\lambda} L n_2 I_0 \Big(1 - 2\frac{x^2+y^2}{w_0^2}\Big) \tag{2.8}$$

where $z_R = \frac{\pi w_0^2}{\lambda}$ is the Rayleigh length and I_0 the beam intensity. Equalizing the two phase contributions, the minimum intensity I_0 to get a Kerr-lens effect can be found. The corresponding power threshold, i.e. $P_{th} = \frac{I_0}{\pi w_0^2/2}$, is [23]

$$P_{th} = \frac{3.77\lambda^2}{8\pi n_0 n_2} \tag{2.9}$$

When the threshold is reached, the process of *filamentation* appears: the pulse is propagating through the medium without diffraction, collapsing in a very thin beam. Note that P_{th} does not depend, to a first approximation, on focusing conditions or intensity. If the beam is not focused, above-threshold filamentation will take place after a longer travel in a NL material, namely [24]

$$z_{fil} = \frac{0.367 \frac{2\pi}{\lambda} a_0^2}{[(\sqrt{P/P_{th}} - 0.852)^2 - 0.0219]^{\frac{1}{2}}} \tag{2.10}$$

where a_0 is the entrance beam 1/e diameter. The beam is thereby pre-focused in order to get filamentation in a given crystal thickness of some millimetre, in order to reduce a_0.

In addition to self-focusing, the NL material can exhibit laser-induced breakdown, in which an electron plasma is generated due to the high intensity of focused pulses. The electron density grows explosively and serves to absorb and scatter the remaining pulse energy, thus shielding the area beyond the focus from further radiation. Two kind of process are responsible for the plasma generation: in the avalanche ionization process a seed electron is heated by the field until it has sufficient energy to excite another electron into the conduction band by collision and thus creating an avalanche reaction; in the multi-photon excitation, the high photon density make possible the molecular ionization due to multiple photon absorption (MPE), which on their own would not have sufficient energy to displace the electrons. The presence of free electron plasma can enhance the continuum generation mechanism.

Therefore, the pulse gets increasingly focused during propagation: the more focused it becomes, the higher the intensity rises till it gets to the filamentation threshold. During the propagation, the SPM effect makes the spectrum wider generating new frequencies (cfr. Section 1.3.2). The produced radiation has a modulated spectrum and the same polarization direction of the input pulse. When it is projected onto a screen the femtosecond continuum beam appears to the eye as a white disk, surrounded by a concentric rainbowlike pattern, which usually removed by an iris in order to exclude the conical emission.

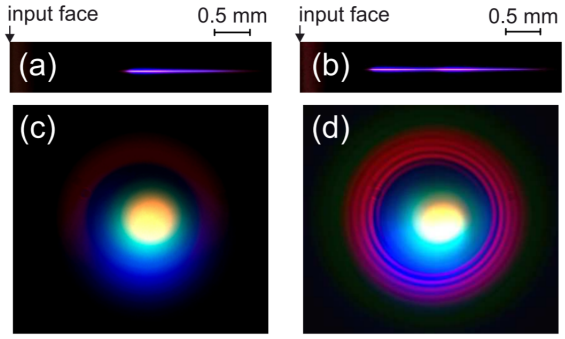

Figure 2.13: Plasma fluorescence traces in a YAG crystal from 100 fs pulses (λ=800 nm) in case of above-threshold condition (a) and multi-filamentation (b) with their respective WLC patterns (c, d) [24].

If the input power is highly above the self-focusing threshold, *multiple filamentation* may occur, i.e. beam breaks up into several long and narrow filaments, which has to be avoided to eliminate possible spectral interference patterns and bad spatial modes. In the left Figure 2.13 is shown a typical optimum WLC seed far-field image, with its filament image. The right one shows what multi-filamentation causes to the pulse. Also the spectrum (not shown) presents more and more artefact, with a less smooth continuum. It is worth noting that the WLC mode does not depend on the pump pulse one. Also asymmetric profiles can produce a good supercontinuum spatial distribution.

Theoretically, every material including gases and liquids, can perform self-focusing and self-phase modulation behaviour. As seen in Section 1.3.2, PCF are used for extremely wide spectra generation even from low energy pulses. However, this kind of seed creation shows imperfect coherence, energy fluctuation and highly modulated spectra energy densities [25]. Instead, bulk materials of a few millimeters of thickness have been shown to generate white continua with a very broad and smooth spectrum, high temporal and spatial coherence, as well as very high stability and lower input energy requirements than gases (even they yield less output power).

So, having fixed a crystal material and thickness, there is a range of pulse energies and input beam diameter which produces a good WLC seed, both in spectrum and spatial domain.

In the setup presented in Fig. 2.6 (page 66), a laser pulse energy of about 2.2 µJ is obtained by splitting, trough a dielectric mirror, the master laser. The 1022 nm, 254 fs is sent on a 6 mm-thick YAG plate (Yttrium Aluminium Garnet, $Y_3Al_5O_{12}$). The YAG was chosen for its typical WLC plateau and its spectral stability over time [25], even if no such big differences were noticed with respect to sapphire plates.

The WLC threshold for sapphire is 1.3 MW, calculated from eq. (2.9) with n_0=1.815 and $n_2 = 6.9 \times 10^{-20}\,\mathrm{m^2/W}$ [25]. Since the optical power correspond to $P = \frac{E}{\tau_P} \simeq 9\,\mathrm{MW}$ is much above the threshold of YAG, a variable filter is added to avoid multi-filamentation and introduce a fine tuning on WLC pumping power. Recalling the equation (2.10), in order to obtain a single plasma filament within the crystal thickness of 3 mm it is necessary to focus the beam. This is done by a $f = 60\,\mathrm{mm}$ lens, which reduces the entrance beam width to $D_{4\sigma_r} \simeq 35\,\mu\mathrm{m}$, associated with a z_{fil} of about 1 mm.

The WLC radiation is then collected through a one inch lens ($f = 30\,\mathrm{mm}$) and the collimated beam results in a far-field profile of dimension $D_{4\sigma_x}$= 890 µm and $D_{4\sigma_y}$= 1010 µm.

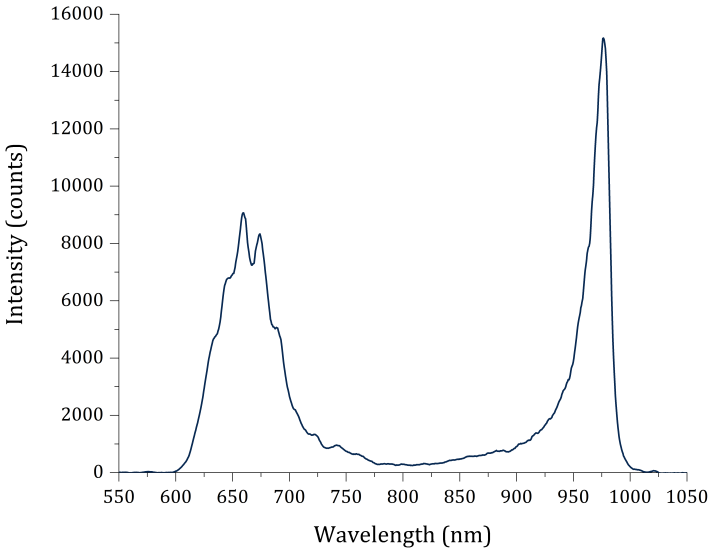

Figure 2.14: WLC spectrum from YAG.

The obtained WLC spectrum is shown in Figure 2.14. It spans over a range of frequencies between 600 nm 1000 nm with a central plateau and two peaks at the spectrum edge, as expected from theory (cfr. Section 1.3.2).

Since the WLC beam has an intrinsic chromatic angular dispersion, an iris is put after the collimation to select the spectrally uniform central 20 % (about 1.5 mm diameter): this results in a markedly improved mode and compressibility of the final amplified output, while only marginally reducing the output power.

1022 nm radiation is blocked by a low-pass filter (F) at 980 nm. Since the spectrum was often still affected by remaining fundamental power and the spectral distortion around 980 nm introduced by the filter, a zinc selenide (ZnSe) 2 mm-long plate ($n = 2.492$) was introduced to enhance dispersion, in order to temporally separate it from the WLC radiation to be amplified.

The seed is now ready to move on to next stages. It has a positive chromatic dispersion due to its travel inside the YAG, in the collimation lens (thickness of 8.6 mm). Hence, since the WLC frequencies are time dispersed, a delay line will be exploited to allow spectral tuning over a selected spectrum bandwidth in the OPAs.

2.5.2 Amplification stages

A multistage OPA system combines the advantage of short pulse implementation together with high energies at longer durations. It allows also a distribution of overall gain that enables spatial filtering between stages, use of shorter crystals and better compensation of pump-signal group velocity mismatch (GVM) in each stage. More importantly, it provides the possibility for signal spectrum shaping as slightly different part of the pulse can be amplified in each stage.

Referring to the scheme represented in Fig. 2.6 (page 66), the CARS-pump amplification setup is made of three OPA stages, two pre-amplifiers and one high gain stage: each consists of a delay line, a polarizer, a focusing lens, a NL crystal and a collimation lens.

As presented in Sect. 1.2.4 and 1.2.5, OPA are used to amplify a seeder beam in a non-linear crystal, in presence of a strong non-depleted pump beam. The phase-matching condition ($\Delta k = 0$) is obtained by tuning the crystal angle and correctly polarizing the beams. Group-velocity matching ($\delta_{12} = 0$), required for a broadband amplification, is fulfilled through non-collinear geometry (NOPA), with the right choice of the "magic angle" α between pump and seed beams. A detailed discussion for finding the correct angle value exploiting amplified parametric fluorescence (APF) is presented in Section 2.5.3.

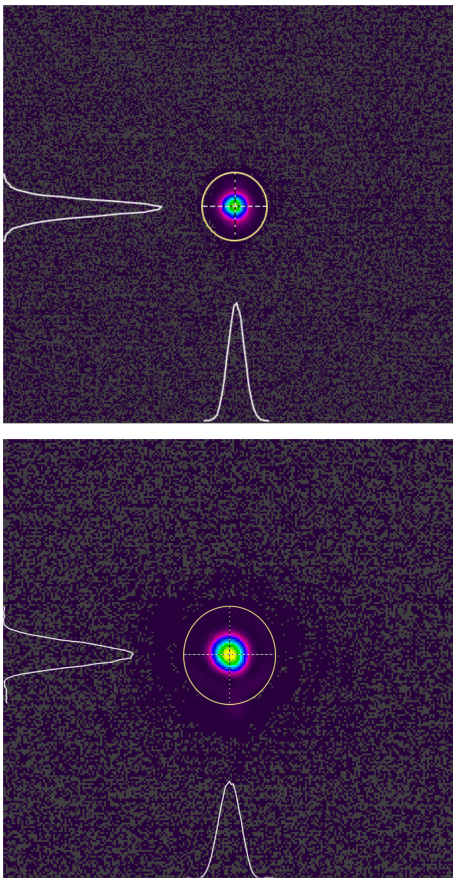

Figure 2.15: Pump (above) and seed (below) profile in first OPA BBO crystal.

The WLC seed passes through a tunable delay line, which is needed for temporal overlap with the OPA pump beam and provides also spectral tuning. A half wave-plate aligns the WLC polarization vertically, to match the ordinary crystal axis. The OPA pump is provided by the SHG stage (see Section 2.4) at 511 nm. A polariser divided second harmonic (green beam) into two branches, depending on polarizations: 50 mW are sent to the first two OPAs, while the remaining 1.1 W pumps the third high gain OPA. A low-pass filter (F) reflects the little remaining power of the fundamental frequency. The 50 mW beam passes through a telescopic system in order to set the correct diameter for OPAs. In fact, in the first OPA, both pump and seed beams are collimated by the same $f = 200$ mm lens. After focusing, the pump presents a profile with dimensions $D_{4\sigma_x} = 103.6$ µm and $D_{4\sigma_y} = 113.8$ µm while the seed has dimension of 105.2 µm and 129.2 µm respectively, as shown in Figure 2.15. Diameter matching is not mandatory, although it results in higher conversion efficiency: the only requirement is that the pump profile is smaller than the seed one, so as not to affect the spatial mode quality. In fact, signal spatial properties depend on the pump: a bigger seed guarantees a full overlap and thus spectral uniformity over the entire profile.

Seed and pump beams are focused on a 1-mm thick BBO crystal, cut at 23.4° with respect to the optical axis (OPA1). β-BaB_2O_4 is a negative uniaxial crystal; referring to the Table 1.2, a type I phase-matching is performed: the seed beam polarization (vertical) is aligned to the ordinary axis, while the 511 nm-pump beam horizontal polarization is aligned to the extraordinary crystal axis.

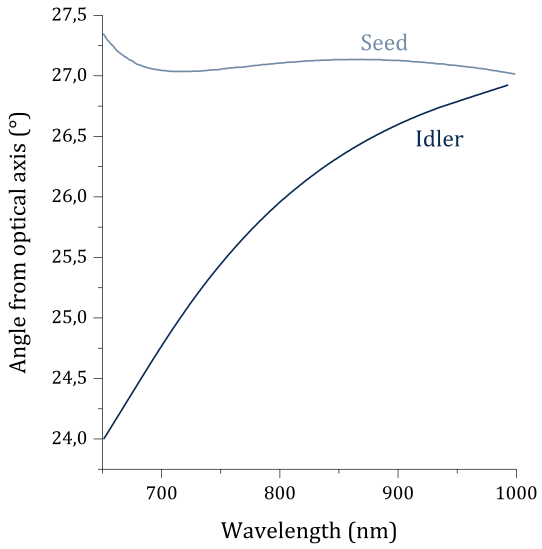

Figure 2.16: Phase matching condition with $\alpha = 2.5°$. For each frequency, the dark line represents idler phase-matching condition, while the light blue one indicates the seed phase-matching. Adapted from SNLO graphs.

The non-collinear setup requires an accurate alignment of both pump and seed with the crystal. For calculation, the software SNLO was used [26]. The *magic angle* α, i.e. the angle between pump and seed beams, was found to be 2.5°, as presented in Section 2.5.3. Considering a pump wavelength of 511 nm and a seed bandwidth of 650–1000 nm, the seed has to be tilted 27° in order to provide amplification over all frequencies. In Figure 2.16 the SNLO graph is represented: the light blue line represents the seed angle with respect to the optical axis. Note that the nearly constant behaviour over a 400 nm band has been achieved thanks to the group-velocity and phase-matching, which is guaranteed from the correct choice of α. Setting values other than 2.5° would result in a dramatically less constant curve, which would not allow proper amplification of the whole seed spectrum. Since the idler phase-matching values (blue curve) monotonically increase from 24° and 27°, the beam will be dispersed in space.

Poynting Vector Walk-off Compensation (PVWC) is the geometry chosen in order to have higher gain, thanks to a better spatial overlap during pump walk-off shift (see Section 1.2.6 for theoretical explanation). Figure 2.17 shows how the NOPA was engineered, with accurate indication of angle values. External angles were computed with Snell's law, considering the ordinary refractive index of $n_o(\lambda_1 = 800\,\text{nm}) = 1.6603$ and the extraordinary one oscillating between $n_e(\lambda_3 = 511\,\text{nm}) = 1.5559$ and $n_o(\lambda_3 = 511\,\text{nm}) = 1.6760$ in function of θ. The external angles values are 6° (signal) and 1.8° (pump) from the surface normal. Reflected beams were used to appropriate align the overall system, knowing the right reflection angle. Each OPA stage is designed with the characteristics described above. Tiltable mirrors on pump beam line (indicated by a curved arrow in the setup scheme at page 66) provide fine tuning for the correct pump-signal spatial superposition inside the BBO crystals.

After the first OPA, the signal pulse has been amplified to an energy of about 67 nJ, giving an average optical power of 0.67 mW. The signal profile is then slightly manipulated with a telescopic system and focused with a 200 mm focal lens to a second 23.4° BBO crystal, with thickness of 1 mm (OPA2). The remaining pump radiation coming from OPA1 is collected by a mirror, sent to a delay line, and focused with the same 200 mm lens into the OPA2 BBO. Gain provided from the second OPA stage is 7 dB and the signal energy is brought just over 3 µJ.

The third OPA stage, instead, is pumped from the high power beam (1.1 W) coming

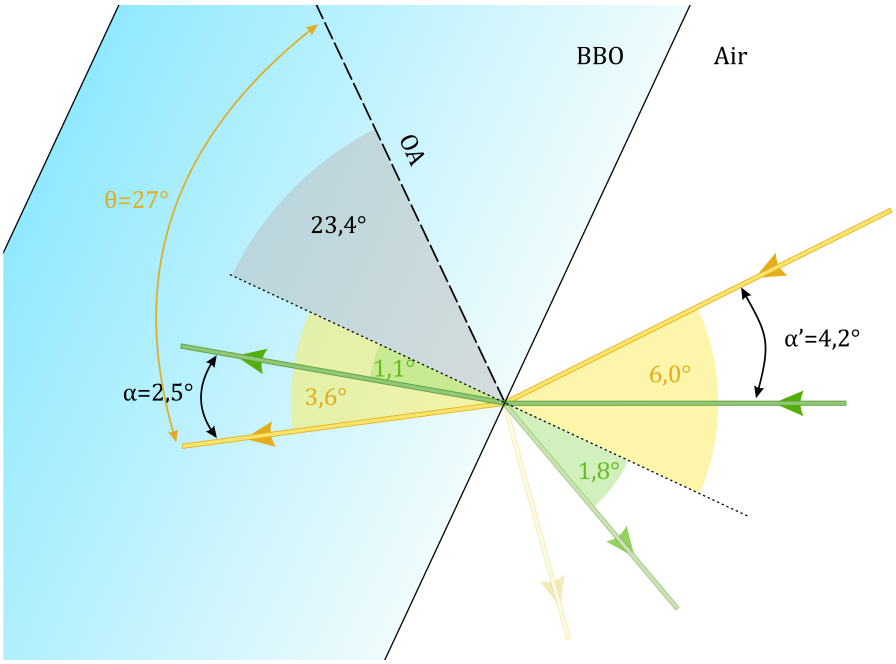

Figure 2.17: NOPA phase-matching angles for broadband amplification. The internal signal angle α is 27° from the optical axis (OA) and 2.5° from the pump beam, corresponding to external incidence angle of 6° and 1.8° respectively, in case of PVWC geometry. The TWR configuration, instead, would require an internal angle of 22° between signal and optical axis. α' means the external magic angle.

from the SHG stage. The pump is slightly collimated with a spherical mirror with a radius of curvature of 10 m in order to match the signal spatial profile, which is not focused. Its polarisation is rotated by a $\frac{\lambda}{2}$-waveplate to be horizontal as required. The crystal, a 2 mm-long BBO cut at 23.4°, brings the signal energy to 18 µJ, with an amplification factor of 60.

Signal far field profile and the spectrum of each OPA stage are represented in Figure 2.18. On the left, the succession of spectra centred in 920 nm shows that the first stage amplifies a bandwidth of about 120 nm, which is then further amplified by second and third OPAs without affecting its shape. Acting on the delay stage of first OPA, different spectral windows can be amplified, allowing frequency tuning of pump pulse without touching anything else. The hole at 970 nm becomes more evident since the amplification depends on the signal intensity. The spatial modes show some asymmetries in the first two OPA, which are however eliminated in the third stage thanks high gain uncollimated amplification, forming an excellent TEM_{00} Gaussian mode.

After being amplified, the pump beam passes through a telescopic system for a slight profile adjustment, in order to perfectly match probe and Stokes profile when collimated. A $\frac{\lambda}{2}$-plate rotate the polarization horizontally, as the other beams. Then is finally sent to the prism compressor to compensate all the group velocity dispersion acquired through the numerous optical components, described in Section 2.5.4.

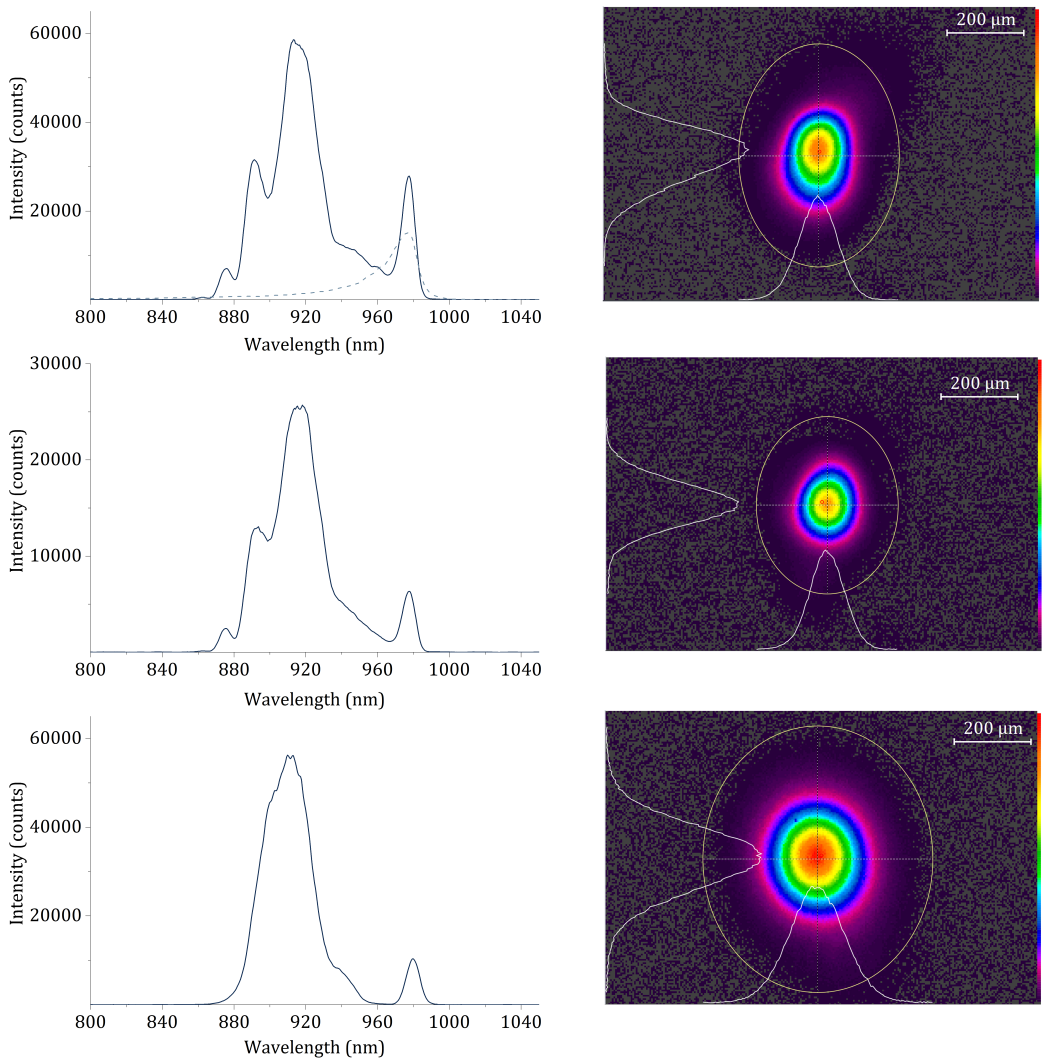

Figure 2.18: Spectrum (left) and far field ($f = 500\,\text{mm}$) beam profile (right) of first, second and third OPA stage respectively. In the first graph the WLC spectrum is also pictured (dashed line).

2.5.3 Amplified Parametric Fluorescence and Magic Angle

In this section, phase-matching condition in non-collinear OPAs is discussed more in detail.

A precise angle α between pump and idler beam is needed for broadband phase-matching, as seen in Section 1.2.5 (or equivalently, a precise angle Ω between idler and pump, such that $v_{g_1} = v_{g_2} \cos\Omega$). If the process is not seeded, spontaneous fluorescence photons, i.e. quantum vacuum fluctuations, may be amplified if they are in the phase-matched spectral range. Referring to the Fig. 1.16 at page 38, they produce a light cone around the pump beam, thanks to cylindrical symmetry since no preferential direction is set. This light cone can be used in order to experimentally estimate the right NOPA angles.

The image continues in the next page.

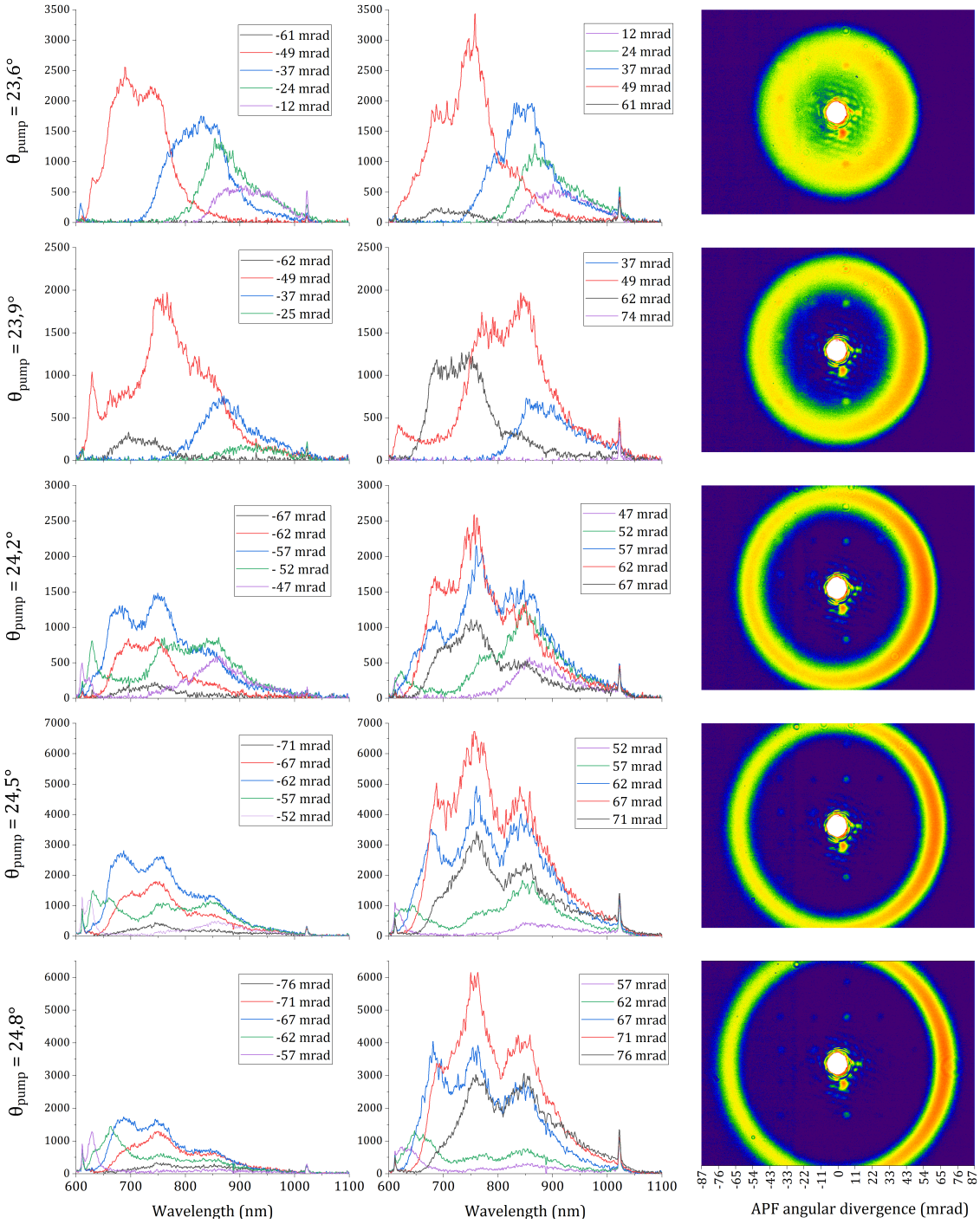

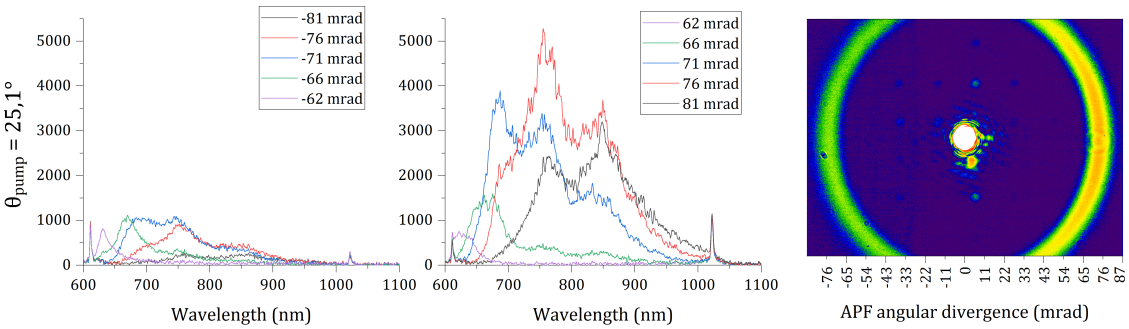

Figure 2.19: APF ring profiles (right column) and their respective spectra taken for discrete radial position, both on the left side of ring (TWR geometry, left column) and on the right one (PWVC geometry, central column) following the horizontal diameter direction, containing the pump beam image (central bright dot), at a distance of 36 mm from BBO crystal. Pump beam ($\lambda_3 = 511$ nm) is polarized along the extraordinary axis and tilted from the optical axis six different θ_{pump}, whose value is reported on the left.

The procedure is the following: the pump beam is focused into the NL crystal and amplified parametric fluorescence (APF) rises. Since each frequency has its own phase-matching condition, it will be emitted with a different angle α from the pump beam. So, the APF projected on a plane perpendicular to pump propagation axis results in a ring with a certain thickness. Putting a fiber spectrometer in each point of the ring, spanning in the radial direction, the actual phase-matched spectrum can be detected. Figure 2.19 shows the spectra taken at different radial positions on the APF ring profile, with the corresponding angular divergence. Six different configurations were tested, corresponding to an internal pump angle from the crystal optical axis of θ_{pump} = 23.6°, 23.9°, 24.2°, 24.5°, 24.8°, 25.1° (see Fig. 2.17). Each APF profile, taken at a distance of 3.6 cm from the crystal, is represented on the right and five spectra are detected in different positions (labelled with their angular divergence), both on left and right with respect to the pump beam (the bright point in the middle of the images).

Changing the pump angle (or, equivalently, tilting continuously the crystal) the APF ring thickness varies: since the pump is polarized on the extraordinary axis, different θ_{pump} configurations correspond to different APF phase-matching conditions and thereby changing the angle α' at which the amplified fluorescence is emitted. As shown in the figure, with an angle of θ_{pump} of 23.6°, the APF is strongly angular dispersed, even it has low angle α, being gathered around the pump beam. Increasing the angle θ_{pump}, α gets bigger and bigger while the dispersion smaller, meeting in a well-defined ring. From left and central column graph, spectral information can be retrieved. At low θ_{pump}, different radial positions on the ring correspond to different APF bandwidths which are amplified. A similar behaviour can be observed at large angles: at θ_{pump}=25.1° the purple spectrum is low-frequency shifted while the black one represents higher bandwidth.

The ideal APF profile would be a ring with an infinitesimal thickness, such that each frequency is phase-matched at the same angle θ_{pump}: in this situation, the magic angle α could be computed from this ultra-thin ring divergence. In a real situation, the optimized

configuration is the one with the minimum ring thickness. Figure 2.20.a shows the APF horizontal profile at different pump angles, Gaussian fitted. Their relative FWHM are reported on Figure 2.20.b. The minimum ring thickness is reached when θ_{pump} is between 24.2° and 24.8°. The result is consistent with their relative spectra: observing the central graph column in Fig. 2.19 it is noticeable that the one corresponding to θ_{pump}=24.5° has a lower divergence. In fact each spectrum has approximately the same pattern as the others, meaning that all bandwidth is phase-matched. Further, being the angular dispersion at minimum, the spectral amplitude reaches the maximum values. The peak shortly after 1000 nm represent a little power coming from the unfiltered fundamental frequency after SHG stage.

It is worth noting that the APF ring is not cylindrical uniform: the rightmost area has higher amplitude than the left one: this is the experimental evidence of the two geometrical configuration discussed in Section 1.2.6. The PWVC geometry leads to a better spatial walk-off compensation, then to higher APF gains with respect to TWR one: so, an asymmetrical gain behaviour on the extraordinary crystal axis plane has to be expected. By comparing the PWVC and TWR spectra of the different rings, it can be seen that the difference between the two geometries becomes more pronounced as the pump angle increases, up to a factor of 5 at θ_{pump}=25.1°. The further the pump moves away from the optical axis direction, the more walk-off experiments: the difference between the two geometries becomes more pronounced.

Hence, a wide bandwidth amplification correspond to the minimum APF ring thickness: the pump must be tilted 24.5° with respect to the optical axis. In a crystal cut at 23.4° this correspond to an internal incident angle of 1.1° and an external one of 1.8°. The respective APF ring has its amplitude peak at a radius of 2550 µm at a distance of about 36 mm from the crystal, corresponding to an external angle α' of 4.05° and an internal angle α of 2.4°. This result is quite similar to the one computed with SNLO software as sketched in Figure 2.17. So, if the OPA seed signal beam has the correct

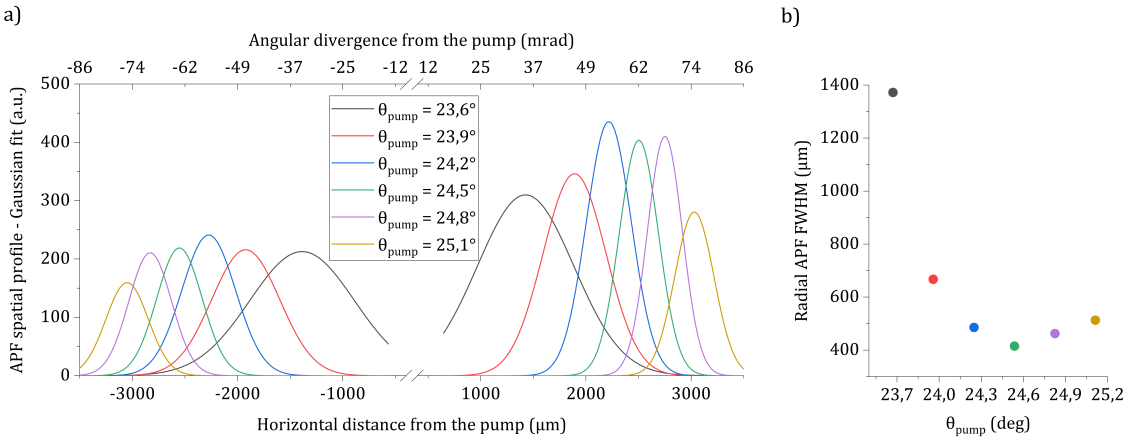

Figure 2.20: *a)* Gaussian fit of the horizontal APF ring profiles (shown in the figure above) at different θ_{pump}. The central pump intensity has been removed for better visualization. *b)* APF ring profile width. Colours are referred to the graph *a)*.

incidence angle in such a way it is internally tilted 2.4° from the pump, then the OPA is phase-matched over a wide bandwidth, thanks to group-velocity-matching properties of non-collinear geometry.

In conclusion, the APF arising when a non-linear crystal is traversed by the pump beam alone has been presented and its main spatial and spectral characteristics as a function of the angle of incidence θ_{pump} have been illustrated. The seed beam impinges on the crystal at an external angle of about 4.2° from the pump beam, which in turn is inclined at an external angle of 1.8° to the normal to the crystal. In this way, the magic angle α of 2.5° allows to amplify a broadband seeder at the best condition.

2.5.4 Prism pair compressor

The OPAs amplification process is pumped by the narrowband 511 nm pulse, whose temporal duration of ∼250 fs allows to amplify only a portion of the positive chirped seed. In fact, when a broadband femtosecond signal travels along an optical medium, it gets temporal broadened and frequency chirped (see Sect. 1.1.2). The optical elements composing the setup are made of crown glass (BK7), fused silica (FS) or CaF_2, which all have positive GVD in the visible range (as shown in Fig. 2.21). From the graph it is evident that BBO is the material with the highest dispersion values.

Each OPA stage includes a BBO crystals, polarisers and lenses, thus resulting in tens of millimetres during which the CARS pump signal becomes more and more positively chirped.

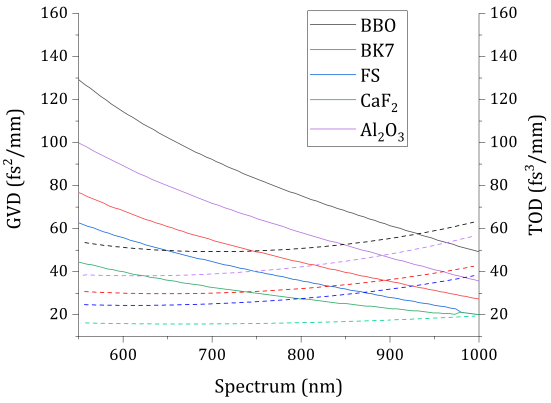

Figure 2.21: Group velocity dispersion (GVD, solid line) and third order dispersion (TOD, dotted line) curves for several materials.

To allow the CARS pump pulse to efficiently excite all Raman vibrational levels, it is necessary to compensate the chirp. Several techniques can be employed for such a goal: chirped mirrors, Fourier plane compressors, grating pairs (described in Section 4.3) and prism pairs compressor. The latter is the technique used in the actual setup, since it can compensate both GVD and TOD, being also simple and tunable. Without entering into much detail, the idea is to separate spectrum components (adding spatial chirp) and compensate the chirp between them, making faster frequencies travel more. As pictured in Fig. 2.22, white light is first spectral dispersed from a first triangular prism, because the refraction angle in the Snell's law depends on the refractive index, i.e.

$$\delta(\lambda) = \vartheta_{in} + \arcsin\left[n(\lambda)\sin\left(\alpha - \arcsin\left(\frac{\sin\vartheta_{in}}{n(\lambda)}\right)\right)\right] - \alpha \simeq (n(\lambda)-1)\alpha \qquad (2.11)$$

where ϑ_{in} is the incidence angle and α the prism apex angle. The formula has been asymptotically simplified for small angle values. Then, a second prism is positioned with

the entrance face parallel to the first prism exit side, in such a way that all diffracted frequencies will propagate parallel to each other upon exiting. Later, another prism pair symmetrically disposed can make the frequencies regrouped collinearly into a unique beam. This is usually done inside the same prism, with a mirror back reflecting the dispersed beams. The first prism is positioned in order to have incidence at the Brewster's angle, i.e. $\vartheta_{in} = \vartheta_B = \arctan(n)$, in order to minimise p–polarized reflected radiation and thus minimising energy loss.

It is possible to demonstrate that this kind of configuration achieves a Group Delay Dispersion (GDD) of [27]

$$GDD = GVD \cdot L \simeq \frac{\lambda^3}{2\pi c^2}\Big[-8L_{sep}\left(\frac{dn}{d\lambda}\right)^2 + 2L_P\left(\frac{d^2n}{d\lambda^2}\right)\Big] \tag{2.12}$$

where L_{sep} is the distance between the prisms and L_g the path travelled in the material. These two distances can be adjusted at desire simply translating the second prism (following the blue arrows in Fig. 2.22): any value of dispersion can be compensated with continuous fine tuning, since L_{sep} acts on negative second order dispersion, while L_P on positive one.

In the setup a dense flint glass (SF10, $n = 1.711$ at 800 nm) high dispersive prism pair (ThorLabs AFS-SF10) with an apex angle of $\alpha = 60.6°$ is used, together with a 50.8×50.8 mm square protected gold mirror to retroreflect the dispersed beam. The prisms are positioned for the beam to impact them at the Brewster angle of 59.7°. Flint glass prisms ensure enough dispersion to compensate a GVD of $-97.5\,\mathrm{fs}^2/\mathrm{cm}$ and a third order dispersion of $-388\,\mathrm{fs}^3/\mathrm{cm}$. For the pump pulse compression, L_{sep} was set to be 40 mm, compensating for positive dispersion in amplification stages (BBO crystals, focusing lenses and telescopes) as well as in prism glass, calculated taking into account the different materials composing the optical elements. Pulse compression was then fine tuned with live-view optimization, using a FRAC (*Fringe Resolved Autocorrelator*). Finally, a FROG scan was taken, whose result is shown in Fig. 2.23. The FROG reveals a pulse FWHM duration of 30 fs. The spectrum obtained from the algorithm shows that all amplified frequencies are in phase (Fig. 2.23.b). The comparison with the experimental spectrum shows a a pretty good similarity, meaning the FROG reconstruction is reliable.

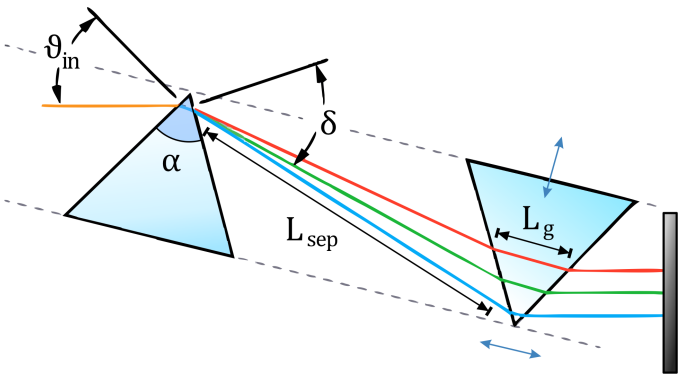

Figure 2.22: Schematic representation of a prism pair compressor. ϑ_{in} is the incidence angle, which is set to Brewster's angle. δ is the minimum deviation angle. The rightmost prism can be shifted (see arrows) for fine tuning, adjusting separation length L_{sep} or the glass optical paths L_g.

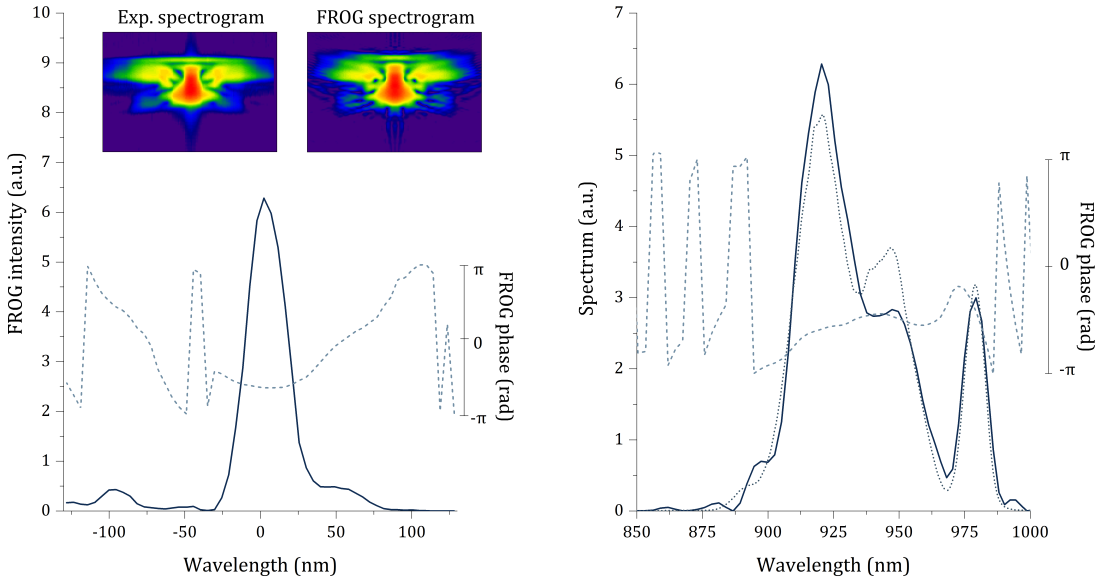

Figure 2.23: *a*. Temporal profile of amplified pump pulse, reconstructed by FROG algorithm, both modulus (straight line) and phase (dashed line). FWHM linewidth of 30 fs. Experimental and reconstructed spectrograms are shown on top. *b*. Pump spectrum, reconstructed by FROG (straight line) and its relative phase (dashed line). For comparison, the experimental spectrum is shown (dotted line).

2.6 Laser source output

At the end, the three beams must be aligned so that they propagate collinearly. This is done by two dichroic mirrors (labelled DM in the setup scheme at page 66): the first shortpass one combines pump and Stokes, transmitting the former and reflecting the latter. An iris is put immediately after to facilitate near field alignment. With a second longpass dichroic mirror the probe beam joins the other two. When the beams are all near-field aligned, dichroics are fine tilted to guarantee perfect alignment over long distances. The operation is usually performed daily with the help of a camera, to which the beams are temporarily deflected and collimated by a spherical 500 mm-focal mirror, put over a flip mount. On each beam line a variable attenuator is put, allowing to adjust the optical power of each beam and consequently the pulse energies.

Moreover, pulses must be temporally overlapped and their modes must match when they are focused on the sample. Delay stages are installed on Stokes and probe lines (τ_S and τ_{PR} in the scheme). The latter is also mounted on a digital-controlled slide, allowing probe scanning which will be described in Section 3.1.

Furthermore, it is essential that once focused the pulses have same line profile, so that the whole beam can take part in the Raman process on the sample. For this purpose, telescope systems are placed on pump and Stokes lines. Probe beam profile, which is narrower due to collimation before the third OPA stage, is adjusted by exploiting the diffraction of the iris located immediately after the probe shaping stage. In practice, by

closing the iris slightly, its diffraction pattern (jinc^2, the FT of a circle aperture) widens: in this way probe profile matches the ones of other two pulses. Profile matching is also daily checked with the camera, making adjustments where necessary.

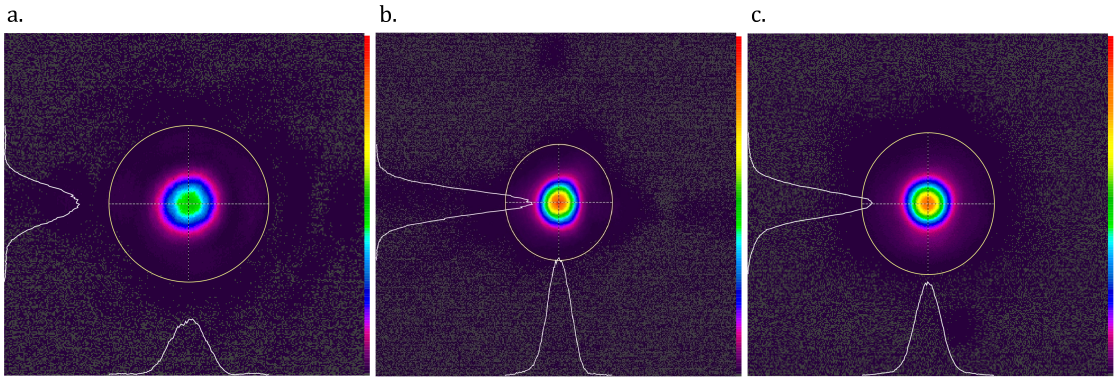

Figure 2.24: Probe (*a.*), pump (*b.*) and Stokes (*c.*) far field intensity profiles (not in scale).

Figure 2.24 shows the final intensity profile of probe, pump and Stokes respectively. The typical jinc^2 shape can be observed in the probe profile, because of iris diffraction. The far field profiles are pictured in Figure 2.25, showing good overlap between them. Beam diameters of $D_{4\sigma_x} \approx 270\,\mu m$ and $D_{4\sigma_y} \approx 290\,\mu m$ are measured when focalized by a mirror with radius of curvature of 1 m.

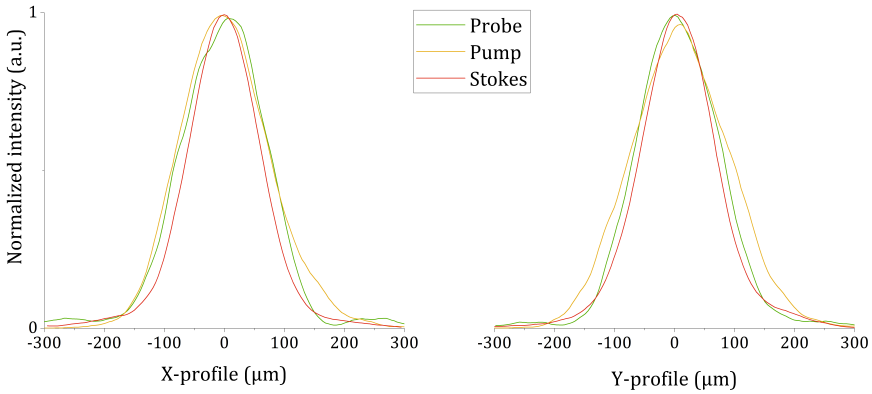

Figure 2.25: Intensity profile on two dimension, in far field geometry with a 500 mm-focal mirror.

Source spectral properties are summarized in Figure 2.26, evidencing spectra of all pulses, i.e. the narrow-banded shaped probe (green, centred in 511 nm with an estimated FWHM of ∼0.5 nm), the narrow-banded Stokes (red, centered in 1022 nm with a FWHM of 5 nm) and the broadband pump at different amplification delays (from yellow to orange, peaks centred in 880, 890, 910 and 920 nm with a bandwidth varying in range 30–80 nm). The pump spectrum is tunable with the delay stage in the first OPA, since the WLC seed is strongly chirped.

Pump stability analysis is shown in Fig. 2.27: in a time frame of ∼250 ms (acquisition

rate 909 Hz), the spectrum centred in 920 nm appears uniform and stable. The pump energy, i.e. the integral of spectra (Fig. 2.27.b) expressed as the percentage deviation from the mean value, shows ±3 % oscillations (relative standard deviation of 1.19 %).

Regarding energies, the source is capable of delivering a Stokes power of ∼120 mW, a probe power between 30 mW and 75 mW (depending on the slit width of probe shaper) and a pump power between 50 mW and 90 mW (depending on amplified bandwidth), in a 10 kHz regime.

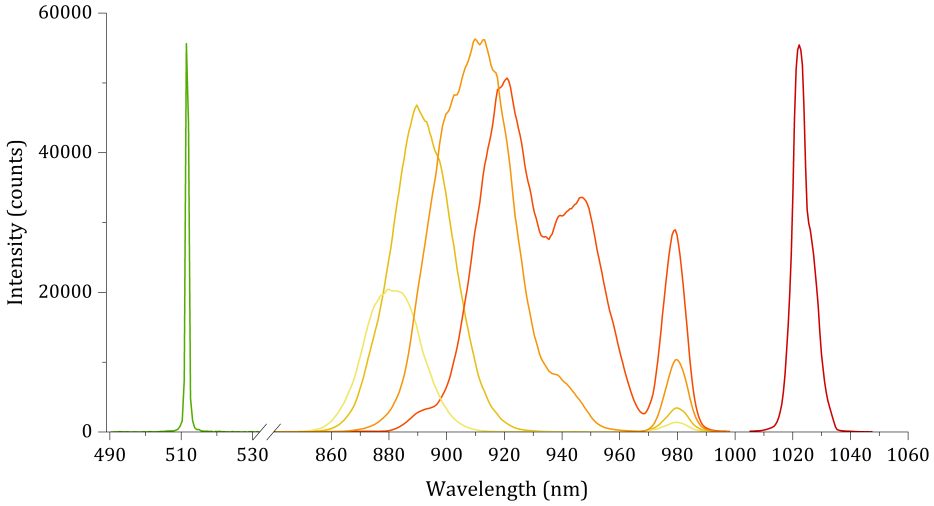

Figure 2.26: Overall spectrum for the three pulses: probe (green), Stokes (red) and pump at different amplification delay (from yellow to orange).

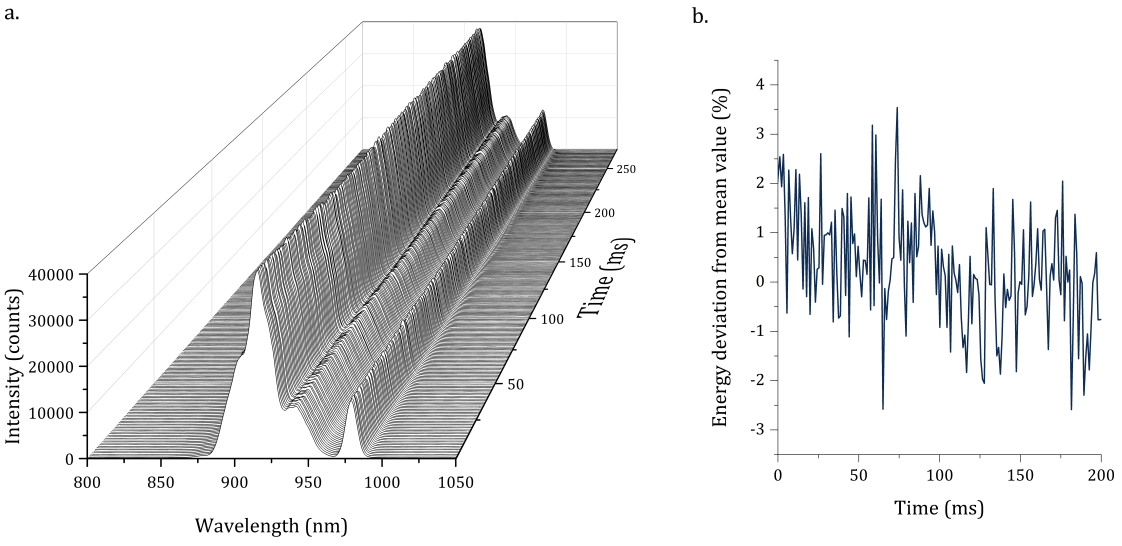

Figure 2.27: *a.* Time evolution of pump spectrum profile. Each spectrum is acquired every 1.1 ms. *b.* Pump spectral stability over time: for each spectrum, its integral is calculated (i.e. the pulse energy); in the graph is visualized the normalized deviation from its mean value.

Chapter 3

CARS detection

The laser source for broadband CARS allows to excite a certain bandwidth of Raman vibrations, bringing out the resonances and their peaks. The Raman spectrum can then be used to recognise the presence of a certain molecules.

The final goal is to detect the presence of chemical and biological agents in a stand-off configuration, preventing further contamination. In particular, as explained in the introduction, *B. anthracis* spores are still a danger today. They resist a wide range of stresses in nature and rapidly return to vegetative growth as soon as they sense the presence of nutrients [28]. The anatomy is unique among bacteria, being comprised of a series of specialized concentric shells, each of which provides specific critical functions and help the spore to persist for long time periods in the environment, survive host defences after entering the body and cause disease when the correct location is reached. The possibility of having a fast system for scanning samples and large surfaces that is able to detect the presence of contaminants form their Raman fingerprint is therefore of primary importance, both for environmental and health safety and for prevention from terrorist attacks [3].

In this chapter, the development of the sample illumination and detection setup is presented in Section 3.1. CARS measures are first experimented on different substances which are known to be strong Raman emitters, as toluene, to calibrate all the system (Sect. 3.1.1) and to become aware of how best to use the source, both with liquid and solid samples. In Section 3.2 the detected anti-Stokes signal intensity has been related with source energies and system numerical aperture, in order to simulate more distant stand-off configurations. Then, the probe shaping effects on CARS are presented in 3.3, deepening the topic of optimisation for spectral and temporal resolutions.

After detected signal characterization, examples of molecular fingerprints are introduced in Sect. 3.4. The discussion continues in more detail on sodium dipicolinate (NaDPA) signal: the substance contained within the spores in higher concentrations is in fact the calcium salt of dipicolinic acid (CaDPA), which has a similar Raman spectrum and it is therefore a good simulant for spores. Section 3.5 addresses NaDPA sample preparation, the measurements made, as well as an analysis on damage thresholds. In fact, like any biological molecule, exposure to tight focused high-energy laser beams is

likely to damage the molecules in short times, charring them and quickly decaying Raman resonances.

A measurement on a bacterial spore sample is presented in Section 3.6. *B. subtilis* spores are used since they are very similar to the *anthracis* ones but without safety issue.

Finally, a setup for stand-off source scan for imaging purposes is presented in Section 3.7. With this system, Raman spectra from different sample points are quickly and sequentially captured: they are analysed from machine learning algorithms which, thanks to Raman fingerprint recognition, can identify where contaminants are in larger areas. Conclusion and possible future development are discussed in Section 4.3.2.

3.1 Illumination and detection setup

The sample illumination and detection stages is represented in Fig. 3.1. The illumination stage is quite simple. As seen in previous chapter, pump, Stokes and probe beams are collimated and travel collinearly. Stokes pulse is delayed (τ_S in Fig. 2.6) such as it is temporally overlapped with the pump one. The probe pulse is instead delayed by a step motor slide, controlled via a settable Matlab script.

The pulses pass through a computer controlled galvo-mirror pair system (ThorLabs GVS001; scan angle of $\pm 12.5°$; step responce time of 300 µs), which will be used for imaging purposes described in Section 3.7. They are mounted over a 2D-galvo adapter (ThorLabs GCM102) and linked to their servo boards.

The source is finally focused on the sample thanks to a spherical mirror. Two kind of illumination configurations were tested: one with a focal of 150 mm and the other of 500 mm. The first one was used for analysis in low energy condition, since the focused area is smaller. The other mirror were used in high energy condition with a bigger sample active area. As seen in Section 2.6, the 500 mm-focal mirror focus beams in an effective area of $A_{500} = \dfrac{\pi w_0^2}{2} = \dfrac{\pi D_{4\sigma_x} D_{4\sigma_y}}{8} \approx 300 \times 10^{-6}\,\mathrm{cm}^2$ while with the 150 mm one effective area is $A_{150} \approx A_{500}\frac{150}{500} \approx 90 \times 10^{-6}\,\mathrm{cm}^2$. In the less focused arrangement, pulse energies can be increased without exceed damage threshold intensities (see Section 3.5.2), as the illuminated area is larger. Having a larger area means also that more molecules are activated by the source and therefore the Raman signal increases. In addition, longer focal lengths correspond to longer Rayleigh distances, thus the sample is less sensible to focus position.

In order to collect and analyse Raman scattering, the radiation must be collected and each frequency must be dispersed to get the Raman shift spectral image. Measure on both solid and liquid sample were made, in the reflection geometry setup pictured in Fig. 3.1.a and Fig. 3.1.b. In case of solid scatterers, beams are focused directly on the surface and the radiation is back-scattered over the entire hemisphere. A 1:1 imaging system (a pair of coated lens with a diameter of 50.8 mm and a focal of 150 mm) is used to bring the scattered radiation to the input of a monochromator. As the Raman signal is much weaker than the scattered pump, Stokes and probe radiation, the latter are blocked by a 500 nm high-pass bandwidth filter (F) to prevent camera sensor damage.

Instead, liquids or solutions are inserted in a cuvette (1 mm or 2 mm thick) and the

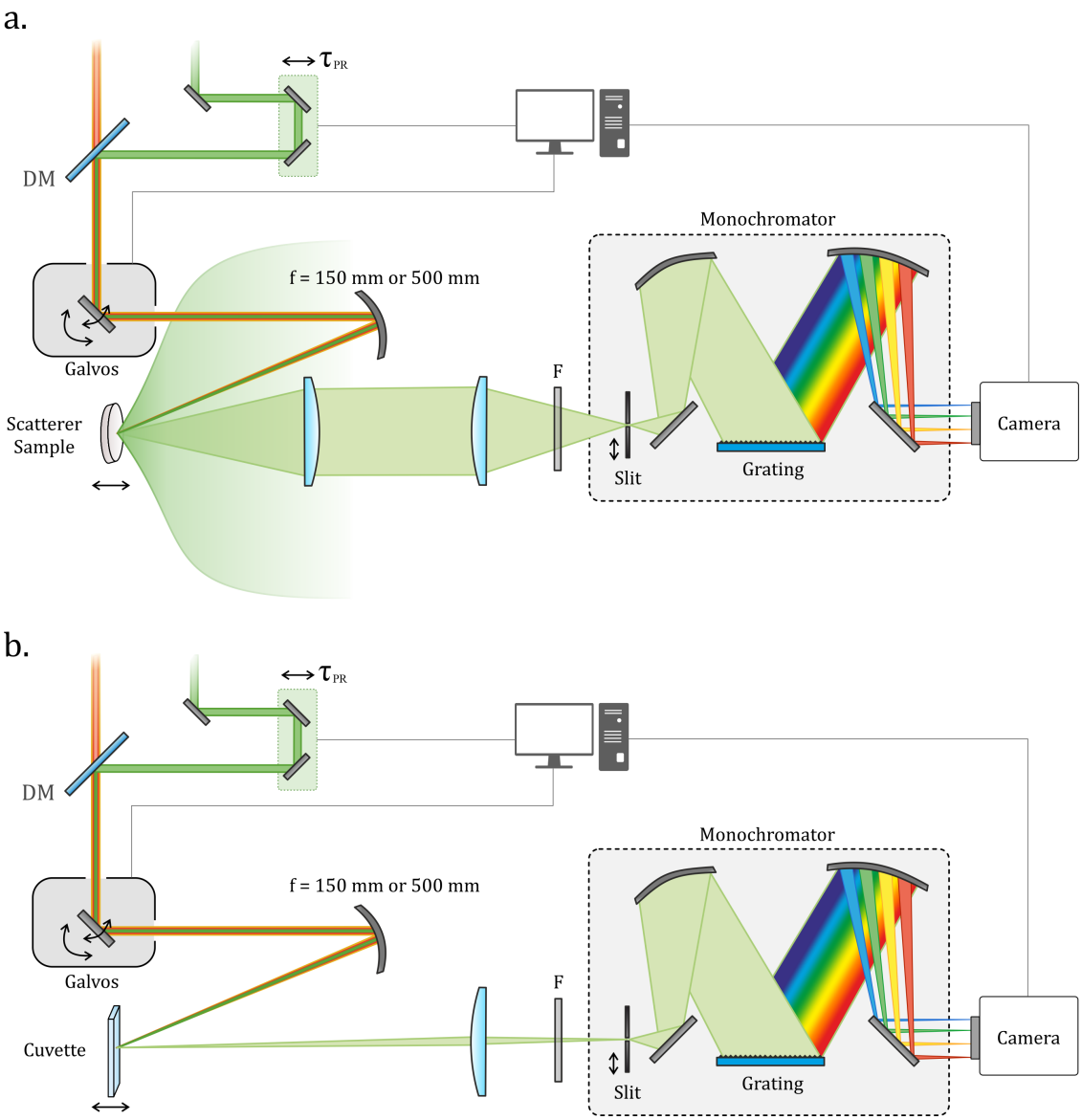

Figure 3.1: *a.* Detection setup scheme for scattering materials; *b.* Detection setup scheme for liquids and solutions. F: filter blocking wavelength above 500 nm. The laser source passes through a galvo mirrors system, is focused on the sample and CARS signal is collected and sent to the CCD camera through a monochromator. Probe delays, radial position on samples via galvos and camera acquisition process are all digitally controlled. Angles and colours are exaggerated on purpose for clarity.

CARS source is focused into the gap. Since the laser beam crosses the two glass sides of the cuvette two reflections appear: the first one comes from first surface, without crossing the liquid so it does not carry any useful information, while the second one is from the rear glass so its radiation has interacted with sample molecules. Tilting appropriately the cuvette it is possible properly align just the latter with the 150 mm lens focusing it on

monochromator entrance, after being filtered. No collimation is needed since the laser radiation is not scattered.

Samples and lens are put on a 3-axis linear transition stages to be finely aligned and focused. In addition, solid samples are mounted on a pivot connected to a rotary motor, which gives the possibility to rotate the specimen while testing, preventing surface damage (see 3.5.2). The cuvette is blocked on a tiltable mount giving it two more degree of freedom for correct reflection alignment.

Cuvettes are used when the substance under investigation is liquid but also with salt solutions, for signal improvement: in fact in this configuration the Raman scattering radiation is laser and can be entirely sent to the monochromator, increasing signal-to-noise ratio. However, the laser beam passes twice over the cuvette glass and third order interaction with the material is a further source of unwanted non-resonant background (NRB), which can bury Raman signal if they are weak. In addition, also water Raman peaks could appear.

Conversely, for scatterers only the interaction with sample molecules occurs, without any interference from water or glass. Nonetheless, when the radiation is scattered anywhere only a portion of the hemispherical solid angle is subtended to the collimation lens and only a small amount of radiation is sent to the detector. The radiant flux Φ collected by a lens parallel to the sample surface which subtends an angle 2θ (see scheme at page 98) is in fact

$$\Phi = \int_0^\theta I_0 \cos\vartheta d\Omega = \int_0^\theta I_0 \cos\vartheta \sin\vartheta d\vartheta d\phi = 2\pi I_0 \int_0^\theta \frac{\sin 2\vartheta}{2} d\vartheta = \frac{\pi I_0}{2}(1-\cos 2\theta) \quad (3.1)$$

where the maximum Lambertian intensity is $I_0 = \frac{\Phi_{tot}}{\pi}$ and the integral on radial angle ϕ is 2π. Thus the percentage of collected radiant flux is

$$\frac{\Phi}{\Phi_{tot}} = \frac{1-\cos 2\theta}{2} \quad (3.2)$$

A 50 mm-diameter lens placed at 150 mm from the scattering point subtends an angle of $\theta = \arctan(\frac{D}{2f}) = 9.46°$. Assuming the source is Lambertian (see 3.2.1) only the 2.70 % of the total radiant flux is collected by the lens.

In order to increase Raman signal two are the viable ways: choosing a lens with highest numerical aperture possible or intensify CARS signal. While the first one is determined by external constraint, the second one can be achieved working both on source energy and focusing area. In fact, recalling equations (1.110) and (1.114), the anti-Stokes intensity is proportional to the intensities of source pulses (pump I_P, Stokes I_S and probe I_{PR}) and on the third order electrical susceptibility $\chi^{(3)}$

$$I_{AS} \propto I_P I_S I_{PR} |\chi_R^{(3)} + \chi_{NR}^{(3)}|^2 \quad (3.3)$$

Hence, it depends both on illuminated area and pulse power, and therefore on their energy and time duration: decreasing the active area with highly focused beams, increasing energies and temporally compressing the pulses are possible ways to raise the signal. The two latter are limited by the source, but the focus dimension can easily be enhanced with higher focal. However, if the illuminated sample area is smaller, fewer molecules will be

scattered and therefore the signal is reduced. In addition, tighter focus means shorter Rayleigh distances: the active volume inside the solid which can scatter is reduced too. Lastly, too high powers lead to local sample damaging and carbonisation, bringing down the CARS signal. An example of damage thresholds analysis is presented in Section 3.5.2.

Returning to Fig. 3.1, in both scattering or laser configurations the radiation is filtered and focused on a vertical slit, placed one the monochromator entrance. The monochromator role is to create a 1:1 spatially chirped replica of the entrance: in practice it separates each the spectral component (i.e. Raman shifts) dispersing them on horizontally direction. In this way an intensified camera placed on the slit conjugate plane directly image the Raman spectrum. The monochromator is composed by two big spherical mirrors (a collimator and a focusing one) and a highly dispersing reflection grating (1200 lines for millimetre, 70×70 mm) which is able to span over a Raman shift band of about $1500\,\mathrm{cm}^{-1}$. Since each frequency is imaged on the camera sensor as the image of the entrance vertical slit, the latter determines the detection spectral resolution. In fact, to distinguish two adjacent peaks, the image of each one has to be spatially separated from the other. Obviously, a very narrow slit reduces the anti-Stokes intensity collected by the monochromator: the right trade-off between resolution and intensity must be found depending on acquisition type.

The CCD camera used for detection is an iKon-M 934 low noise 1024×1024 pixels ($13\,\mu\mathrm{m}$ large), providing both high range dynamics and high readout rate (up to 5 MHz) with a quantum efficiency of about 90 %. It is cooled to a working temperature of $-80\,^{\circ}\mathrm{C}$. The CCD readout process can be set via Andor Solis® software, modifying exposure time, shuttering and registers reset. The hardware binning option is capable of merging adjacent pixels to improve sensibility at the expense of resolution: in practice, electrons trapped in various pixel wells are counted together. As the image detected by CCD camera is a series copy of the vertical entrance slit horizontally separated in spectral components by the monochromator, CCD hardware vertical binning is performed in order to count all vertical pixels in one row. This contributes to improve a lot to improve S/N, reducing HF noise. Moreover, since the slit image width appears to be of few pixels, also horizontal binning of 2 adjacent pixels is set. In addition, CCD regions which are not illuminated are excluded from the readout process, so that noise is further reduced and acquisition speed improved.

In the next section a typical CARS acquisition procedure with the described setup is presented.

3.1.1 CARS acquisition and instrumentation calibration

Recalling the theoretical principles described in Section 1.4.6 and in particular the Figure 1.33, Stokes and pump pulses must hit the sample at the same moment: Stokes delay (see page 66) is tuned to match the pump one. Probe delay is instead controlled via software: from moving the probe slide by predefined steps at regular time intervals and acquiring a CCD image for each step, it is possible to get a Raman spectrum for each probe delay and reconstruct the time evolution of vibrational levels.

Stokes, pump e probe pulse energies are regulated using variable attenuators. Dichroic

mirrors can be angle tuned in order to ensure a perfect spatial overlap of beam modes. The pump spectrum is tuned using the first OPA delay line, as described in Section 2.6, optimizing the active Raman bandwidth. Beam collimation and profile overlap are checked both with in near field with irises and in far field with the Ophir camera, using a 500 mm-focal equivalent mirror.

After source optimizations, sample is placed in the beam focus and lens are aligned to maximize scattered signal on CCD camera. Further source improvements can be done live, optimizing Raman signal.

Raman shift scale is calibrated using Raman spectra of known substance, typically toluene since it provides strong signal. After calibration, each pixel is associated to a Raman shift wavenumber k, expressed in cm^{-1}, which measure its distance from the probe wavelength of 511 nm.

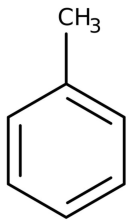

Figure 3.2: Toluene molecule.

After instrumentation calibration, the CCD exposure time (T_{exp}) has to be set: for strong CARS signals (for example, toluene), it was found an exposure of 1–5 ms was enough to retrieve a S/N of 15 dB. For weaker signals as solid scattering powders, typical values between 50 ms and 200 ms were set. Exposure time is a critical value for CARS, especially talking about imaging: the faster is the acquisition of a single point in the image, the more points that can be acquired in a fixed time, or the shorter the entire acquisition will last. Section 3.7 illustrates in details the imaging process.

The probe slide is controlled to be shifted by a fixed step when the camera has concluded the exposure and completed the readout process. So, every time the slide is moved by a length Δl, i.e. the probe is delayed of $\tau_{PR} = \frac{2\Delta l}{c}$, one spectrum is acquired. Typical values of slide steps are 5–10 µm, corresponding to delays of 33–67 fs. After a complete scan, a 2D-map containing both temporal and spectral information is built with Matlab.

In Figure 3.3 at page 93 is shown as a CARS maps example (on left). On x-axis is placed the probe delay while on y-axis the Raman spectrum: signal intensity is visualized with colours. Sectioning the map along horizontally or vertically, the temporal decay of a single frequency or the Raman spectra in a time instant can be plotted, respectively. All three pump, Stokes and probe pulses have an energy of 0.5 µJ and are focalized with a 150 mm equivalent focal mirror. Camera integration time was set to 50 ms. The probe scans with a resolution of 67 fs (10 µm slide steps). In Fig. 3.3.a and 3.3.b Raman peaks of toluene (contained in 2 mm- and 1 mm-thick cuvettes) are shown, consisting in a clearly recognizable spectral pattern of five peaks. The first two spectra (on the right) are taken with probe delays (τ_{PR} of 12.28 ps and 13.45 ps) which exclude the non-resonant background (NRB), avoiding the unwanted third order effects occurring when the pulses come temporally overlapped as discussed in Section 1.4.6. The NRB is shown instead in 3.3.c: Raman peaks are completely buried into the background and no information is retrievable. Note the toluene map shows a spotty figure due to etalon effect created by the cuvette glass wall with a thickness l. A Faby-Pérot interferometer modulates a signal intensity by

$$\Delta\nu_{FSR} = \frac{c}{2L}\frac{\cos\theta}{n} \qquad \text{or} \qquad \Delta k_{FSR} \simeq \frac{\cos\theta}{2Ln} \tag{3.4}$$

where θ is the incidence angle. The free spectral range is calculated from graph data: a

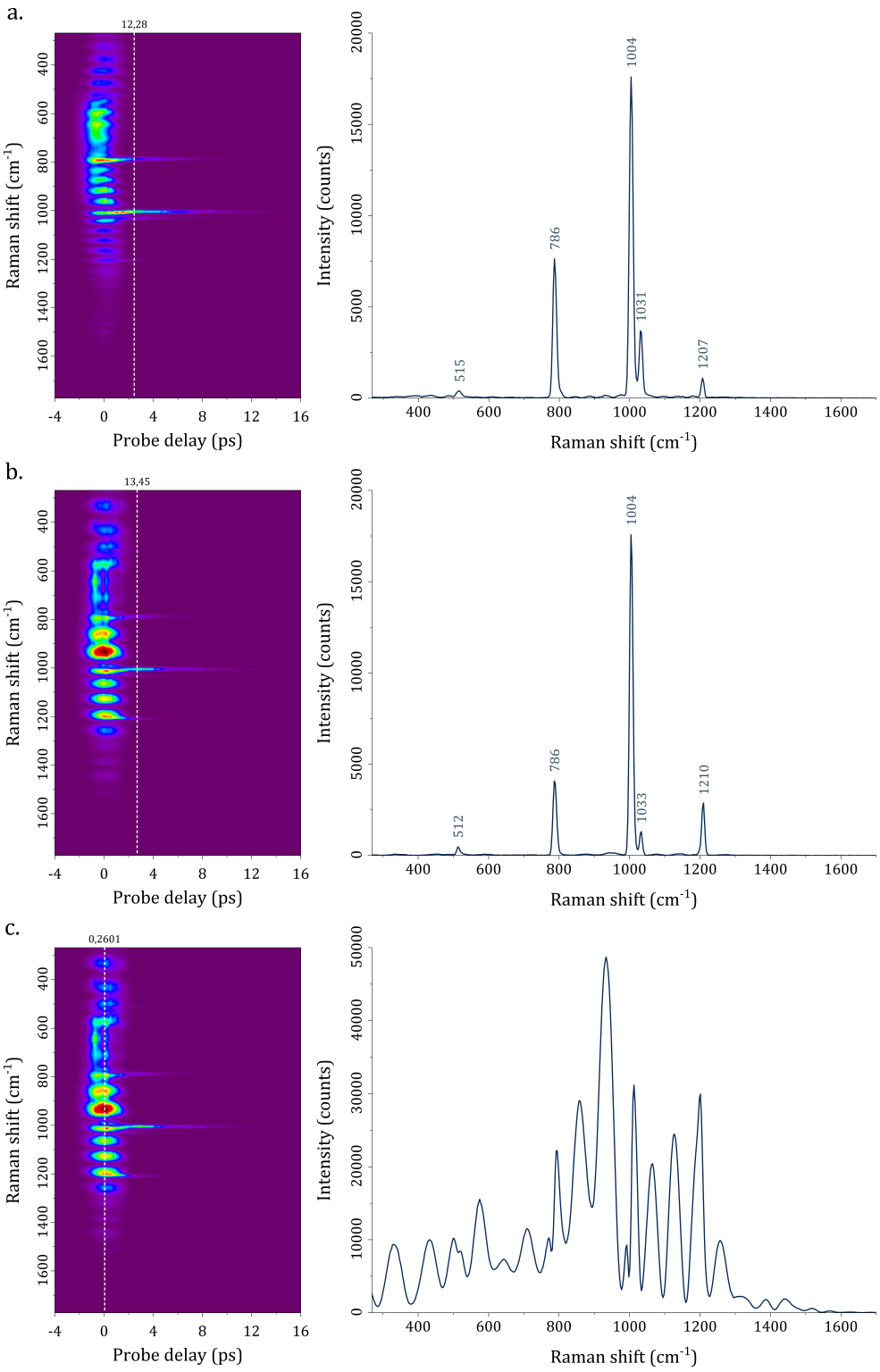

Figure 3.3: CARS maps of pure toluene (left) and Raman spectrum with a probe delay τ_{PR} at white dashed line. All pulses energy is 0.5 µJ; $f_{mirror} = 150$ mm. CCD exposure time: 50 ms. *a.* Toluene in 2 mm-thick cuvette; *b.* and *c.* Toluene in 1 mm-thick cuvette.

Δk_{FSR} of 50 and 80 cm^{-1} corresponds to a thickness l of 73 µm and 45 µm, considering glass refractive index at 500 nm is about 1.46 and an incidence angle of 20°. The 1 mm cuvette has a lower glass thickness, thus a larger free spectral range, while the 2 mm one has a larger thickness, hence a narrower modulation step, as it is evident comparing maps *a.* and *b.* in Fig. 3.3.

Thanks to time-resolved CARS technique is possible to delay the probe pulse in order to get rid completely of NRB. This occurs because the probe pulse does not interact with Stokes and pump pulses, but only with excited vibrational levels which have much longer relaxation times then the pulse durations. Obviously, the more probe pulse is delayed from pump-Stokes, the weaker anti-Stokes signal is, since the de-excitation process has a decreasing exponential-shape. Hybrid-CARS technique with a sinc-shaped probe helps to make the pulse as close as possible to pump-Stokes with lower NRB because of the sinc node (see Fig. 1.33, page 59).

In conclusion, thanks to its well defined peaks and high intensity anti-Stokes signal, toluene is one of the most used reference molecule. CCD camera pixels are calibrated associating each pixel to a Raman shift, exploiting toluene spectrum as the reference one.

3.2 Signal intensity

As discussed in Section 1.4.4, anti-Stokes signal has an intensity which goes linearly with the pump, Stokes and probe ones, i.e.

$$I_{AS} \propto \kappa_{AS}^2 \, |\chi^{(3)}|^2 \, I_P \, I_S \, I_{PR} \, L^2 \, \mathrm{sinc}^2 \left(\frac{\Delta k L}{2} \right) \tag{3.5}$$

So, increasing one pulse energy and leaving all the other parameters untouched, the CARS signal should linearly increase. This was experimentally verified.

Two of the three pulses were set to have a fixed energy value of 0.5 µJ (5 mW optical power): being the beams focused on the same area, their intensities remained constant. The third pulse energy was instead varied from 0.1 µJ to 1.5 µJ. For each possible combination a Raman spectrum was acquired, at the same probe delay. 1 mm cuvette filled with toluene was used as sample. The acquired spectra are shown in groups in Figure 3.4. For each spectrum, the value of the 1210 cm^{-1} peak (after baseline removal) is shown on right, represented with the respective colour. In practice, the graphs show that CARS signal intensity goes linearly with probe, Stokes and pump intensities, respectively, as predicted from the above equation. Linear fitting reveals a R^2 value of 0.99, 0.99 and 0.96 for probe, Stokes and pump intensity relation respectively.

The 1210 cm^{-1} was chosen to as a reference peak for intensity calculation because it was the most stable one. In fact, peaks at 789 cm^{-1}, 1004 cm^{-1} and 1031 cm^{-1} showed some temporal instability: although the source was relatively stable, their intensities varied by more than a factor 2, in a time frame of some seconds. Instead, 1210 cm^{-1} peak was much less affected by the phenomenon. Figure 3.5 shows the peak evolution as a function of time. 789 cm^{-1} and 1004 cm^{-1} peaks exhibit much more instability than the 1210 cm^{-1} one.

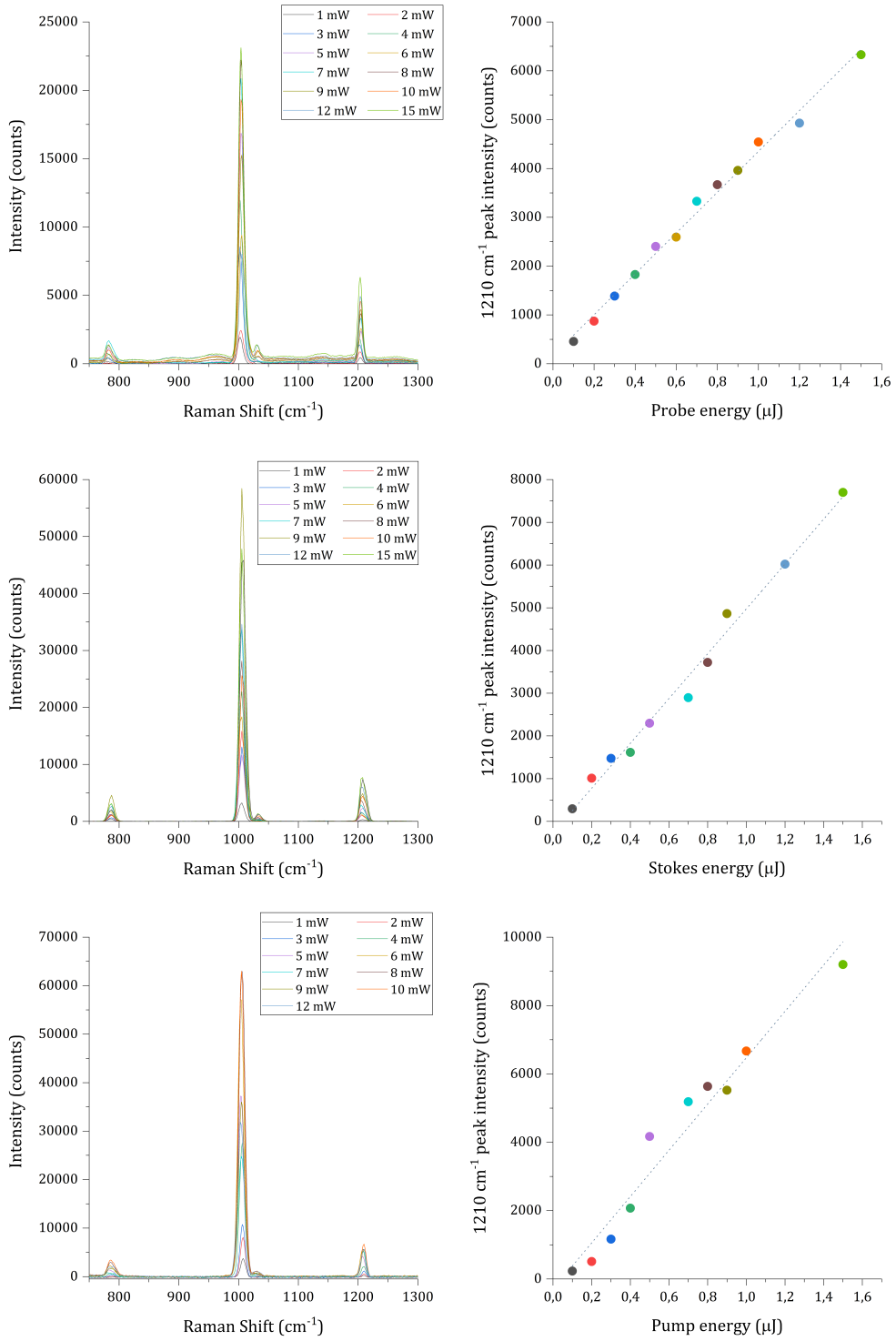

Figure 3.4: Toluene Raman spectra (left) and intensity of 1210 cm^{-1} peak in function of pulse energy. Two pulses are set to 0.5 µJ, while the third pulse energy is scanned from 0.1 µJ to 15 µJ. $f_{mirror} = 150$ mm. $T_{exp} = 50$ ms.

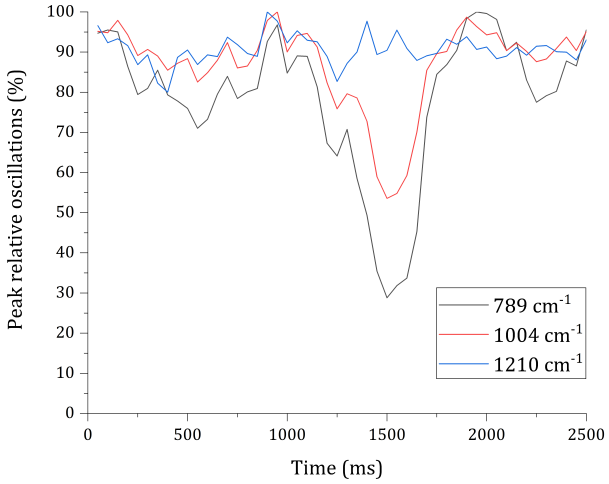

Figure 3.5: Time evolution of toluene Raman peaks. Pulses energy fixed at 0.5 µJ. T_{exp} = 50 ms. The values are expressed as percentage of their maximum value over time, for easy visualization. 789 cm^{-1} and 1004 cm^{-1} peaks are much more unstable.

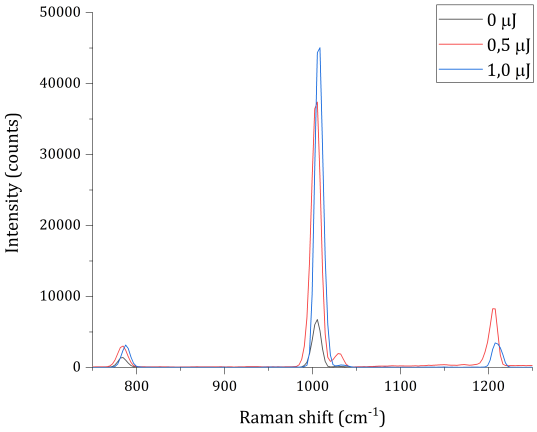

Figure 3.6: Toluene Raman spectrum for Stokes energy of 1.0 µJ (blue line), 0.5 µJ (red line) and without Stokes pulse (black one). Pump and probe beam energies are fixed to 0.5 µJ. Raman scattering is observed even without Stokes signal.

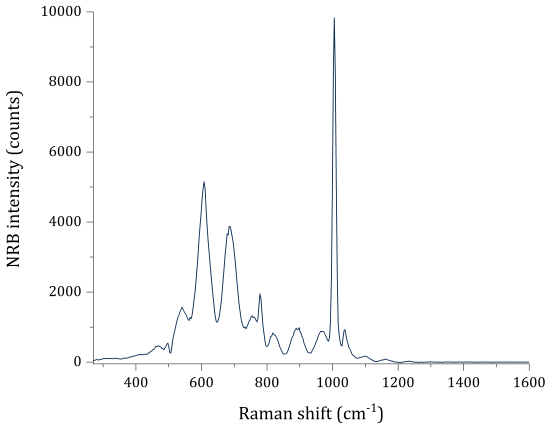

Figure 3.7: Toluene Raman spectrum of non-resonant background without Stokes pulse. $E_P = 0.5$ µJ, $E_{PR} = 0.5$ µJ, $E_S = 0$ µJ.

Several hypothesis were done, until it was found another third order non linear process was taking place, interfering with the standard CARS signal. In fact, Raman scattering was observed even in absence of Stokes pulse, although with lower intensity. In Fig. 3.6 Raman spectra of toluene in presence and absence of Stokes pulse are represented: the leftmost peaks are activated even without Stokes pulse. Figure 3.7 shows the NRB without Stokes frequency: a parasitic third order process is clearly activated. Nonetheless, only lower wave-numbers are affected: in the bandwidth 1200–1600 cm^{-1} no anti-Stokes signal is generated. This explains why the rightmost peak exhibits more stability over time.

The phenomena can be explained considering that pump spectrum is wide enough to excite itself vibrational levels. In fact, Raman frequencies Ω are excited if they match pump-Stokes difference $\omega_P - \omega_S$. But since ω_P is not unique, it is possible that Ω equals the difference of two pump frequencies ($\Omega = \omega_{P_1} - \omega_{P_2}$), giving birth to the observed parasitic phenomenon. In addition, the pump spectrum is wide but it has however certain bandwidth: the highest Ω that can be activated without Stokes is equal to the outermost pump frequencies, so only low Raman shifts are affected by this behaviour. Obviously, without the Stokes intensity, Raman signal has less strength. A scheme is shown in Fig. 3.8.

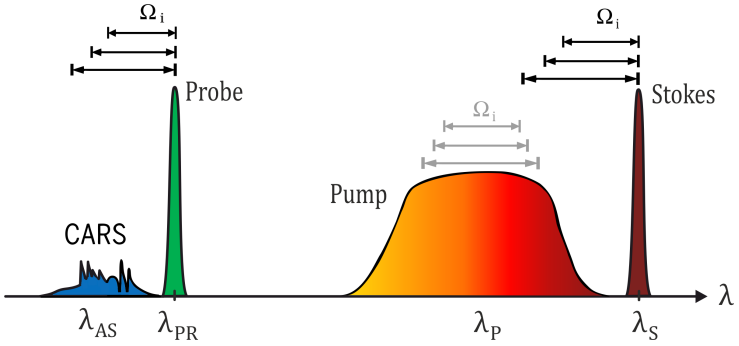

Figure 3.8: Scheme of pulses spectra and vibrational levels: low Raman wavenumbers can be excited from both Stokes-pump frequency difference (black arrows) and pump alone (grey arrows).

3.2.1 System scalability

The amount of photons emitted from a scattering sample and collected by a detection system depends on the numerical aperture (NA), i.e. the diameter of the collimating lens and its distance from the sample, as shown in the scheme in Fig. 3.9, namely

$$NA = \sin\theta \qquad \text{where} \qquad \theta = \arctan\left(\frac{D}{2L}\right) \tag{3.6}$$

As described in Section 3.1, the radiant flux collected by the lens from a Lambertian emitter is directly linked to NA, as

$$\Phi = \Phi_{tot}\frac{1-\cos 2\theta}{2} = \Phi_{tot}\sin^2\theta = \Phi_{tot}NA^2 \tag{3.7}$$

Moreover, for small angles $\sin\theta \approx \tan\theta = \frac{D}{2L}$, so its relation with respect to sample distance and lens diameter is approximate as

$$\Phi \approx \Phi_{tot}\frac{D^2}{4\,L^2} \tag{3.8}$$

From this relation it is possible to evaluate the right system scaling in order to acquire a Raman signal from a generic configuration. For example, the system described in Section 3.1 with a collecting lens of 50 mm diameter and focal 150 mm has a NA of 0.166.

If the sample is put far away from the detection setup, as in a stand-off configuration, the numerical aperture is further reduced. To simulate this configuration, instead of moving the sample far away and increasing L (which would require a proper lens/mirror change), the lens diameter D was virtually reduced, adding an iris just after. In this way the NA is reduced as well, without setup overturn.

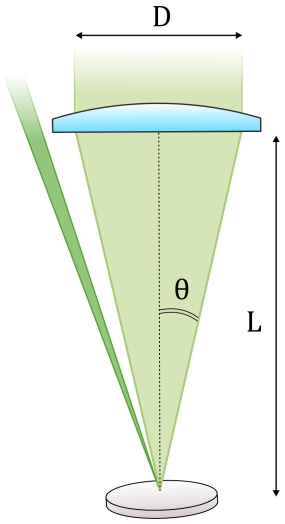

Figure 3.9: Detection numerical aperture.

Several Raman spectra were detected with different NA configuration. The iris aperture was settled to halve the area at each acquisition. Pump and Stokes energies were set to 8 µJ while probe to 2.7 µJ, focalized with the 500 mm-focal mirror. CCD exposure time was raised up to 2 s, to ensure readable spectra even in worst condition and reduce noise. The results are shown in Figure 3.10. Halving the iris area, the virtual lens diameter (and therefore the NA) is rescaled of $\frac{1}{\sqrt{2}}$, so the collected radiant flux halves, since $\Phi \propto NA^2$. With a NA of 0.021, the minimum achievable with iris, the Raman peaks are well distinguishable with a S/N ratio of 20. This is equivalent to place a 50 mm-diameter lens at a distance of 1.20 m, which is far enough for a stand-off detection configurations. Certainly by decreasing the CCD exposure time, the signal to noise ratio will also decrease. However, there is enough margin for measurements at lower times. Or, alternatively, larger lenses may be used to increase NA.

Data contained in the spectra described above were also used to verify the hypothesis of Lambertian source. The intensity counts of three higher peaks in the spectra are plotted,

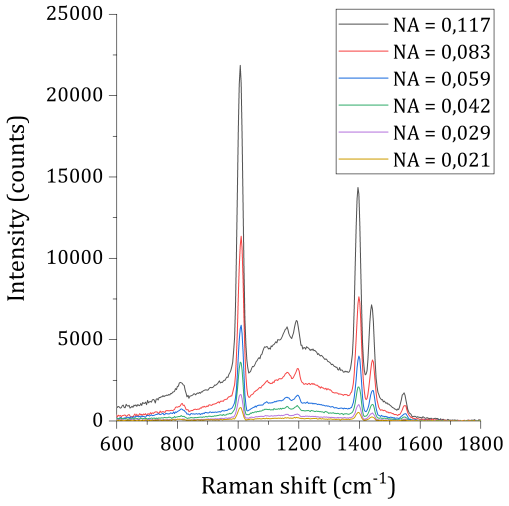

Figure 3.10: NaDPA Raman spectra for different numerical apertures. CCD exposure time of 2 s. $E_P = 8\,\mu J$, $E_S = 8\,\mu J$, $E_{PR} = 2.7\,\mu J$.

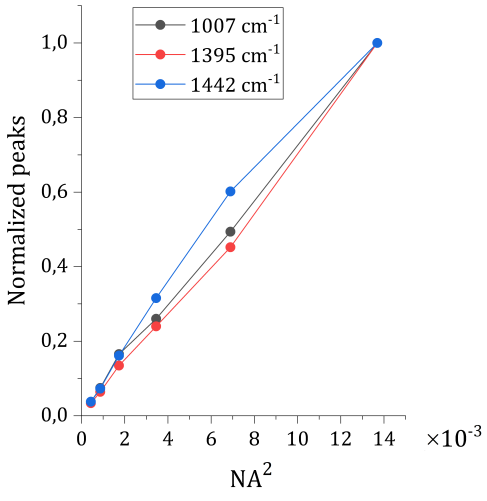

Figure 3.11: Intensity of three higher peaks of Fig. 3.10, normalized, as a function of NA^2 or $\frac{1-\cos 2\theta}{2}$.

normalized, in Figure 3.11. They are an indirect measure of radiant flux, since the CCD counts the number of photons with a specific frequency in a constant time interval. The graph relates photons count with iris numerical aperture, or the angle θ, expressed on x-axis as $\frac{1-\cos 2\theta}{2}$ values (or, equivalently, NA^2), and shows a linear relation which confirms the validity of Lambertian source hypothesis.

3.3 Sinc^2-shaped hybrid-CARS

Hybrid-CARS technique, discussed in Section 1.4.6, is used to manipulate the probe spectrum to have a control on pulse duration and shape. The probe shaper (see page 70) filters probe spectrum with a rectangular mask, hence the pulse envelope shape becomes sinc-like (its Fourier transform). Since the mask is a adjustable slit, different kind of probe pulse can be produced: the more the slit is closed, the more the spectral filter is narrow, the more frequencies are cut and the more the pulse widens over time, reaching the picosecond domain. The effect of probe shaping on CARS signal is clearly visible in Figure 3.12: here six maps are represented, with exactly the same acquisition parameters (pump and Stokes energy of 7 µJ, exposure time of 500 ms, time resolution of 33 fs), increasing slit aperture of 3 µm on each acquisition. The probe energy was set to be 0.4 µJ, which was the maximum value obtainable with the slit nearly closed. Following scans maintained the same value (reducing optical power with variable attenuators as the slit widened) for results comparison.

The first map (*a.*) shows the configuration with smallest opening, thus with the narrower probe spectrum. Narrow spectra correspond to larger pulse duration, thus the map appears smashed. As the slit widens, in 3 µm steps, the probe spectrum widens, its time width narrows and the non-resonant background becomes more intense, being the peak power (and intensity) much higher. In the last three maps (*d.*, *e.* and *f.*) looking on the horizontal direction (probe delay axis) a sinc^2-like shape can be observed, whose first local maximum is getting closer and closer the NRB area. Note that it is not the probe temporal evolution, but the Raman signal, which depends also on correlation with pump and Stokes pulses. Hence the picture is an indirect measure of probe temporal shape.

For a more accurate analysis, the two extreme configuration maps (*a.* and *f.*, corresponding to a nearly closed slit and ∼15 µm opening) are zoomed and sectioned in Figure 3.13. Comparing the maps temporal sections (blue line), the sinc^2 shape is visible only in the right map, since the signal intensity is much higher (more than triple) and time squeezed, hence the sinc^2 local maxima are very close to NRB. In addition, in this case the probe can be shifted temporally closer to the excitation event of vibrational modes, thereby CARS signal is stronger. With longer probes, NRB reduction results when probe is delayed from pump-Stokes a lot more, then vibrational coherence has decayed.

Looking instead their relative Raman spectra (red line), both taken at a delay with a comparable NRB, another effect of probe shaping is noticed: spectral resolution change. In fact, with a longer probe, peaks are well defined, in contrast with the smoothed spectrum on the right, which could be a problem for distinguish two close peaks. the cause is to be sought in probe spectral properties: in the left map it is almost monochromatic, therefore Raman oscillation interfere with a very narrow range of probe frequencies, resulting in a

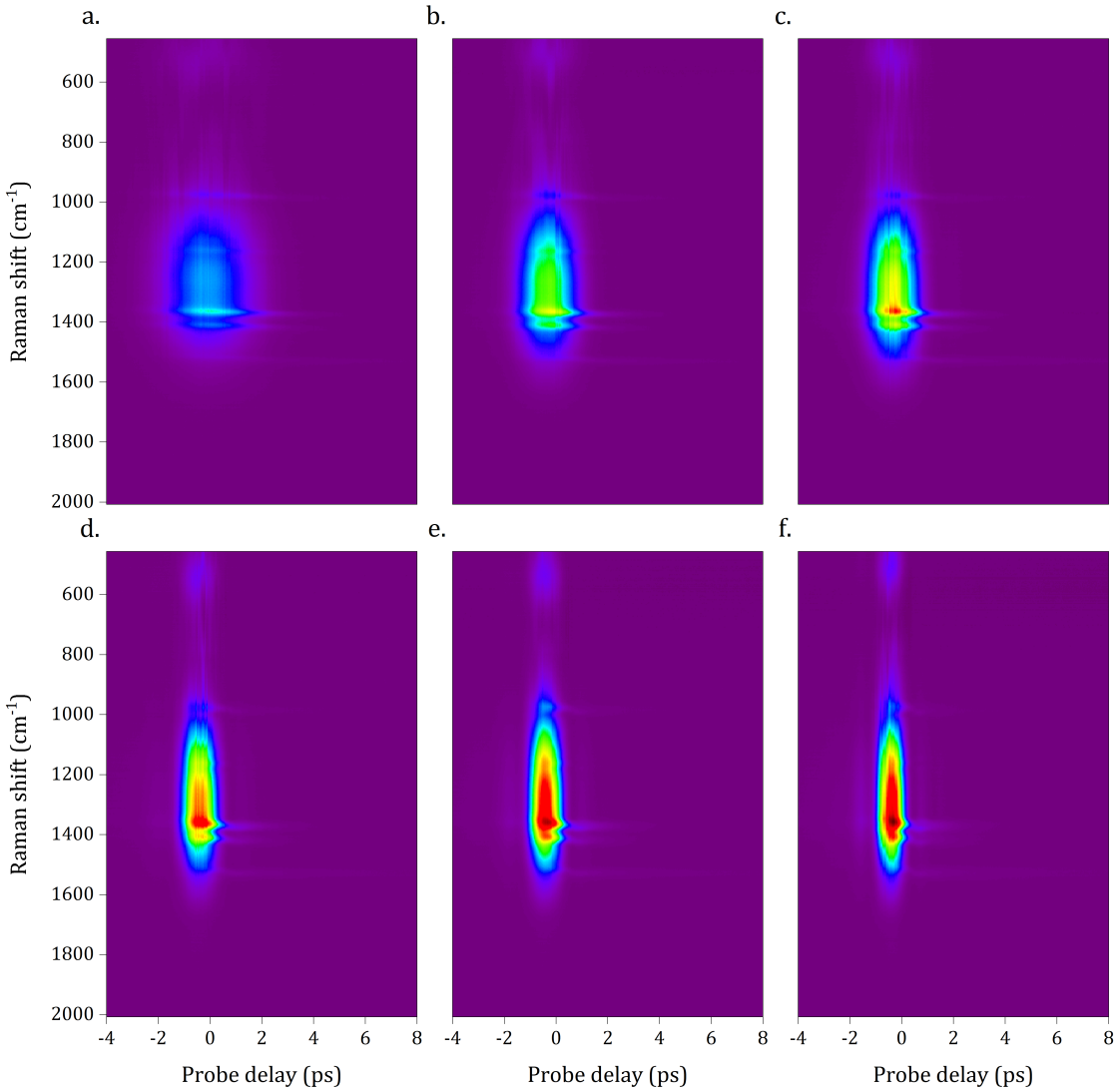

Figure 3.12: NaDPA CARS maps for different probe shaping (hybrid-CARS): the spectrum goes wider and wider, from *a.* to *f.*, thus reducing its temporal duration. Each scan is done with constant pulses energy: $E_P = 7\,\mu J$, $E_S = 7\,\mu J$, $E_{PR} = 0.4\,\mu J$. Resolution $\Delta\tau = 33\,fs$. $T_{exp} = 500\,ms$. The first map is acquired with the shaper slit nearly closed, then for each step it is widen of $3\,\mu m$.

CARS signal with tight peaks. An anti-Stokes peak is indeed a narrow spectral line at $\omega_{AS} = \omega_{PR} + \Omega$. Whilst with broader probe spectrum, ω_P could can fall into a certain wider range, resulting in less defined peaks. However, the signal intensity is far higher thanks to probe lower time duration.

So, summarizing: for high spectral resolution purposes (e.g. Raman peaks identification), longer probe pulses must be chosen performing a narrow spectrum shaping, at the cost of losing CARS intensity; for high temporal resolution ones (e.g. molecular dynamics), a little tight filtering must be done, gaining signal thanks to high peak probe intensity but loosing spectral resolution. Thereby, slit aperture can be tuned according to the type of data to be acquired. Since resolution was already limited by the dispersive capacity of the monochromator, an intermediate configuration was typically chosen usual acquisition processes.

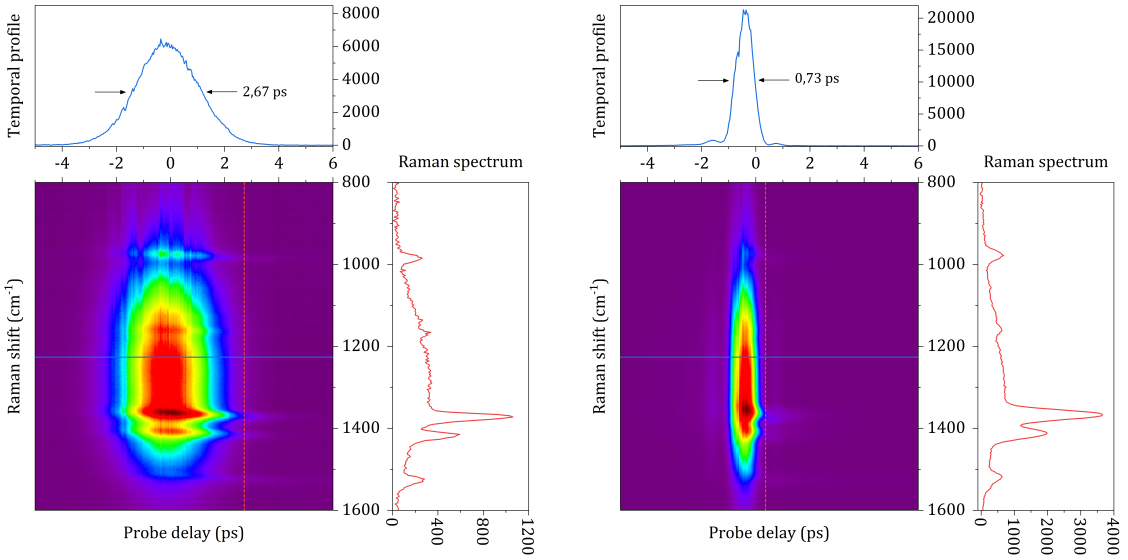

Figure 3.13: CARS maps *a.* and *f.* of Fig. 3.12 zoomed, with both temporal (blue line) and spectral profile (red line) for comparison. Both intensities were rescale.

3.4 Molecular fingerprint

Several molecules were tested – both liquids and scatterers – and their Raman vibrational spectra scanned for different probe delays. In addition to the above mentioned toluene (see Fig. 3.3 at page 93), acetone ($(CH_3)_2CO$) and ethanol (C_2H_5OH) were tested, placed in the cuvettes. However, due to linear shape of the two substances, unlike toluene with its benzene ring, Raman resonances have a very short de-excitation time. In addition, there was a high NRB caused by the presence of the glass walls of the cuvette. The peaks are therefore buried in the NRB, modulated by an etalon effect, and decay very fast preventing finding a clear Raman spectrum. As an example, in Figure 3.14 is shown the acetone map. The weak acetone resonances are buried in the background, except for peaks at $1712\,cm^{-1}$ and $1062\,cm^{-1}$ which in any case decay almost immediately. Also ethanol, whose Raman spectrum is not represented here, showed a similar behaviour.

Conversely, sugars were found to be have well distinguishable Raman spectra, in a region between $500–1400\,cm^{-1}$, in particular fructose and glucose. Their crystals were

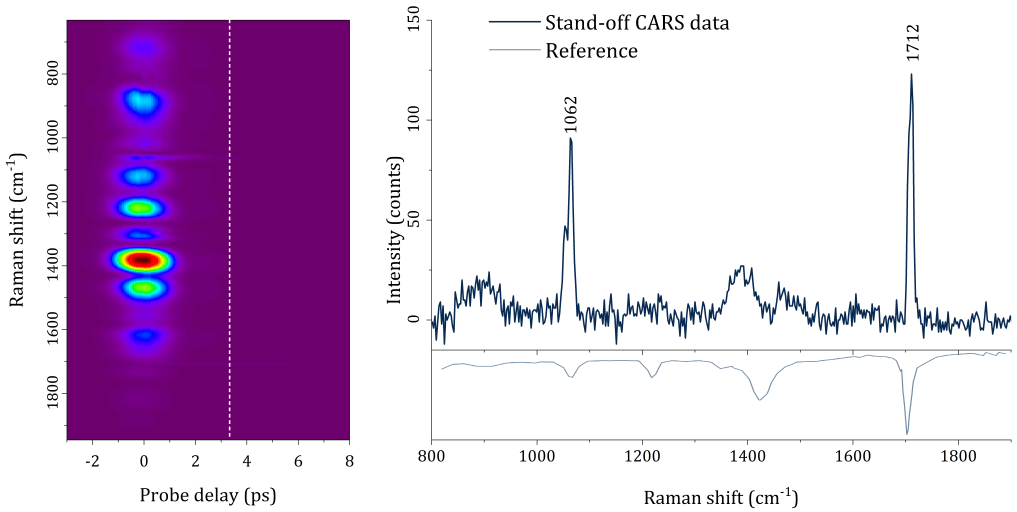

Figure 3.14: Acetone map. $E_P = 8.8\,\mu J$, $E_S = 8.8\,\mu J$, $E_{PR} = 1.9\,\mu J$. Resolution $\Delta\tau = 67\,fs$. $T_{exp} = 10\,ms$.

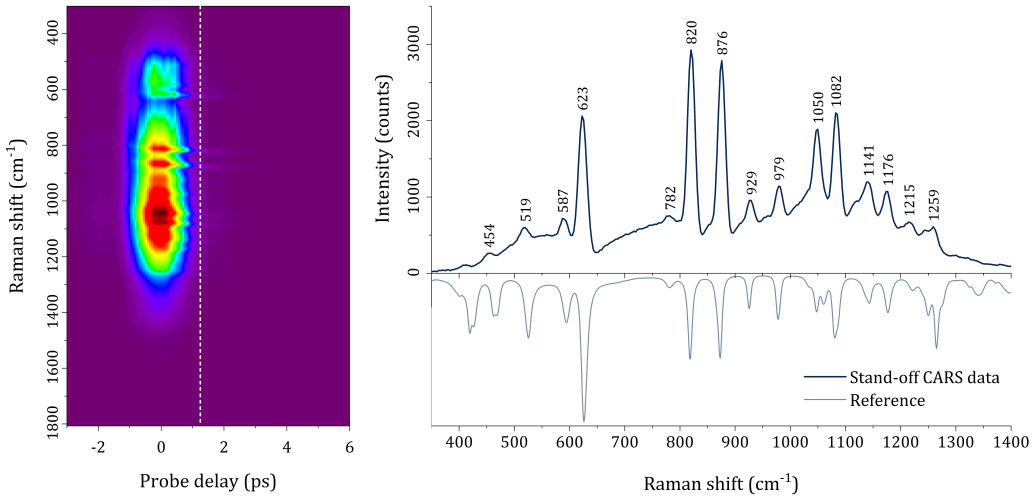

Figure 3.15: Fructose map. $E_P = 7.5\,\mu J$, $E_S = 8.0\,\mu J$, $E_{PR} = 7.5\,\mu J$. Resolution $\Delta\tau = 33\,fs$. $T_{exp} = 100\,ms$. Raman peaks are shown on right, together with a reference spectrum (from Food Technology KVL).

reduced in powder, smashed with a 10 t press until they become a solid 1.5 cm-diameter disk with a thickness of few millimetres. The scattering samples provided high intensity signals, shown in Figure 3.15 and 3.16.

Several peaks can easily be identified in both Raman spectra, with the probe delayed

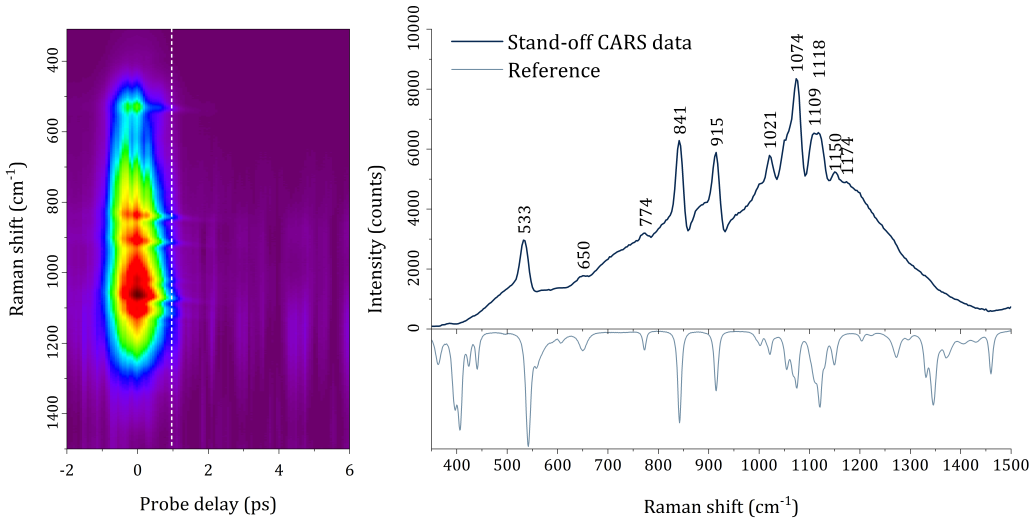

Figure 3.16: Glucose map. $E_P = 7.5\,\mu J$, $E_S = 8.0\,\mu J$, $E_{PR} = 7.5\,\mu J$. Resolution $\Delta\tau = 67\,fs$. $T_{exp} = 100\,ms$. Raman peaks are shown on right, together with a reference spectrum (from Food Technology KVL).

to reject NRB as the resonances last long enough. A broad group of peaks, some of which are well defined and can be used for molecular fingerprinting, appear. The glucose sample showed a very unstable background over time, even in absence of CARS signal, which makes peaks detection more uncertain.

It was also found that sugars has an high damage threshold: they could be exposed to the focussed source in a single point for about one minute before caramelisation.

3.5 NaDPA detection

The final goal of the experimental setup would be the stand off detection of *Bacillus anthracis* spores on surfaces. To ensure the safety of research laboratories, other types of bacterial spores with similar chemical composition, such as those of *Bacillus thuringensis* or *Bacillus subtilis*, are employed to perform analysis and optimize the CARS source. In addition, endospore core is composed for 5–15 % of its dry weight by dipicolinic acid (DPA, pyridine-2,6-dicarboxylic acid, $C_7H_5NO_4$), which is responsible for their low water content core and remarkable heat resistance [29]. The acid is present into spores as the Calcium salt, CaDPA and the spore Raman spectrum has its stronger peaks coinciding with CaDPA ones. Therefore, pure DPA salts can be used during experiments as simulants for anthrax spores, which provides both safety and higher signal. Thanks to a simpler chemical procedure to prepare it, Sodium dipicolinate (NaDPA) was used for experiments.

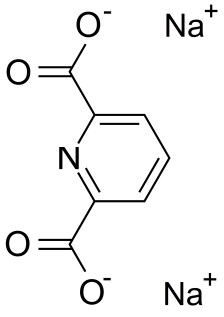

Figure 3.17: NaDPA molecule.

The salt was prepared as a stoichiometric solution with 1:2 molar proportion between DPA powder and Sodium hydroxide (NaOH), which, being a strong base, easily deprotonate the weak dipicolinic acid forming the respective salt. Their molecular masses are 167.120 g/mol and 39.997 g/mol respectively. First, 400 mg of NaOH was completely dissolved in 8 mL pure water contained in a beaker. Then 836 mg of DPA were added to the solution and vigorously mixed for some minutes, breaking any DPA remaining grains. When the salt is almost completely dissolved and the solution has taken on a whitish colour, it is left to evaporate for some ten hours or gently heated to 40–50 °C to speed up the process. After the evaporation, crystalline structures were present on the beaker walls, as shown in Figure 3.18. Crystals bond so well with the glass walls that it was nearly impossible to detach them completely from the surface, so they were finely smashed in powder.

Two kind of samples preparation techniques were tested. The first, rougher technique involved the rehydration of NaDPA powered by few millilitres of waters and mixing until it became a soft homogeneous paste. The paste was then spread on a clean glazed plastic surface, contained in a cylindrical housing. After some hours, the water evaporates and the thin NaDPA disk was removed with few blows to the housing. The surface in contact with the plane came to be smooth and reflective. The other, faster technique, is based on simple crushing of the powder, poured in a cylindrical mould, with a 10 tons press: an homogeneous disk with vitrified surface and constant few millimetres thickness was created.

Figure 3.18: From left to right: NaDPA crystals, once its solution is completely evaporated; drying stage for NaDPA paste disk in its housing; finished NaDPA disk.

The disk was glued on a nut so that it can be screwed to the sample support. The disk can be put into rotation thanks to a small motor to avoid sample damaging. In fact, it was found NaDPA has fairly low damage times, as described in more detail below. Because TR-CARS acquisition of the NaDPA, with a CCD exposure time of 200 ms and a resolution of 33 fs, can take a few minutes to complete, rotation prevents point-like sample carbonization and guarantees a certain degree of uniformity during probe delay scan. Further analysis on NaDPA sample damage threshold are discussed in Section 3.5.2.

3.5.1 NaDPA CARS map

To become proficient in the type of anti-Stokes signal that the NaDPA can give, many source configurations, samples and detection setups were experienced, acquiring and analysing each CARS signal. Two of them are shown below.

The pump seed spectrum was optimized acting on first OPA delay stage, such that the 1000–1600 cm^{-1} range of Raman wave-numbers was exited. The map shown in Figure 3.19

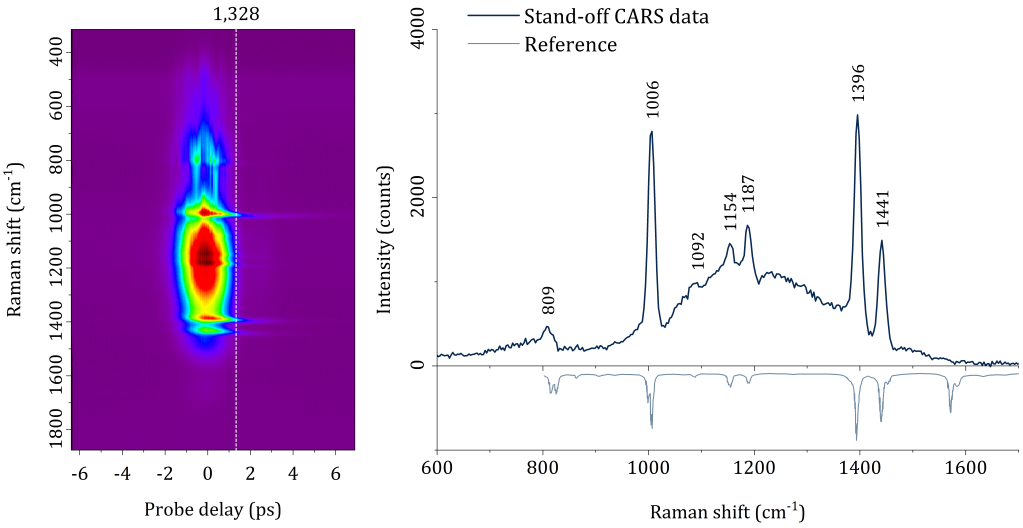

Figure 3.19: NaDPA CARS map with a resolution of 33 fs. $E_P = 1\,\mu J$, $E_S = 1\,\mu J$, $E_{PR} = 0.55\,\mu J$. $f_{mirror} = 150\,mm$ and $T_{exp} = 200\,ms$. Pump spectrum was red-shifted to highlight lower Raman wavenumbers. The Raman spectrum referred to a probe delay, marked with a dashed white line, is shown on the right. The Raman peaks wavenumber is reported on the top of each. Reference from [5].

was acquired with 1 µJ of both pump and Stokes pulses and a probe energy of 0.55 µJ, focused with the 150 mm focal spherical mirror. CCD exposure time of 200 ms guaranteed a good S/N ratio. Placing the probe at a delay of 1.3 ps from the pump-Stokes pulses, Raman spectrum with low NRB is shown on the right part of the figure: peaks at 1006 , 1396 and 1441 cm^{-1} stand out from the background. Also peaks at 1092 , 1154 and 1187 cm^{-1} are highlighted. From literature it is known that 1441 , 1154 and 809 cm^{-1} resonances are actually two very close peaks, which the resolution of the system is unable to distinguish.

Another maps is shown in Figure 3.20. In this case pulse energies are 8 µJ for pump and Stokes and 2.5 µJ for probe, all focused via $f = 500\,mm$ mirror. The anti-Stokes signal is acquired for 50 ms. Raman spectrum shown on the right, acquired in a low NRB condition, is taken at 1.4 ps probe delay. Compared to the spectrum shown in Fig. 3.19, a peak at 1552 cm^{-1} appears while the one at 809 cm^{-1} is no longer visible. This happens because the pump seed was slightly blue-shifted to highlight higher Raman wavenumbers.

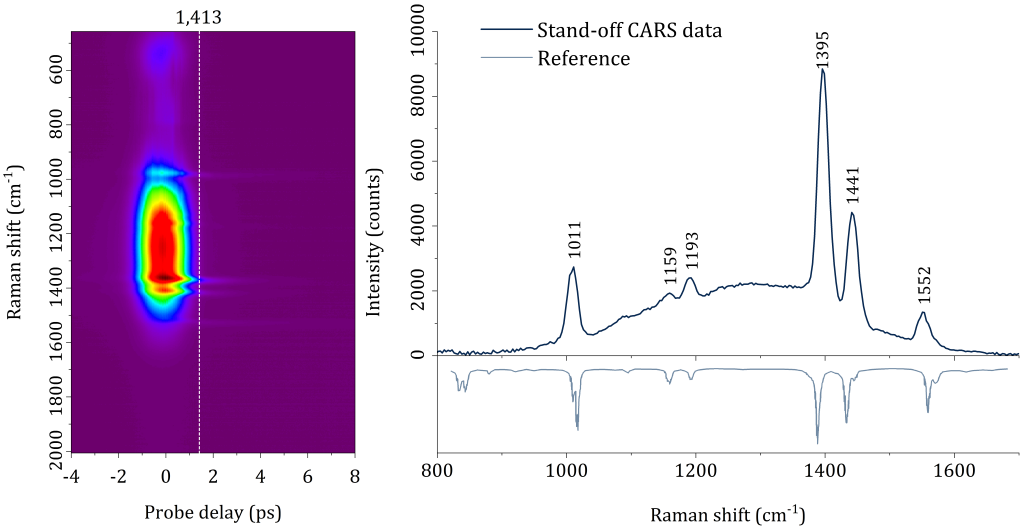

Figure 3.20: NaDPA CARS map with a resolution of 33 fs. $E_P = 8\,\mu J$, $E_S = 8\,\mu J$, $E_{PR} = 2.5\,\mu J$. $f_{mirror} = 500\,mm$ and $T_{exp} = 50\,ms$. Pump spectrum was blue-shifted to highlight lower Raman wavenumbers. The Raman spectrum referred to a probe delay, marked with a dashed white line, is shown on the right. The wavenumber of Raman peaks is reported on the top of each.

3.5.2 NaDPA damage thresholds

Right from the beginning, it was found that focusing the source on NaDPA samples in a fixed point degraded the Raman signal within seconds until it disappeared completely. The sample surface appeared blackened. A typical time course of the spectrum is shown

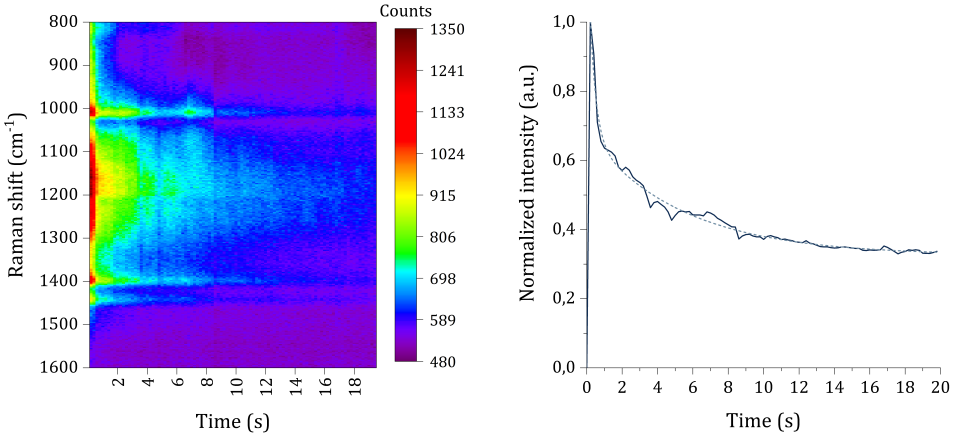

Figure 3.21: NaDPA Raman spectrum evolution over time on static solid sample (left). Time steps of 200 ms. $E_P = 1\,\mu J$, $E_S = 1\,\mu J$, $E_{PR} = 0.65\,\mu J$ focalized with $f_{mirror} = 150\,mm$. On right, $1007\,cm^{-1}$ Raman peak time evolution, normalized after baseline subtraction.

in Figure 3.21. On the left the temporal signal decay is shown, for each Raman wave number. The source was tightly focused with a 150 mm equivalent mirror, achieving an estimated effective area of $\frac{\pi w_0^2}{2} \approx 90 \times 10^{-6}\,\mathrm{cm}^2$. Pump and Stokes energies were set to 1 µJ, while probe one to 0.65 µJ, delivering on the samples surface an irradiance of $\sim$30 mJ/cm^2 for each pulse triplet. The temporal CARS signal decay is reconstructed by acquiring a spectrum every 200 ms, which provides good S/N ratio. On the right the averaged, baseline-subtracted and normalised trend of the three peaks at 1007, 1395 and 1442 cm^{-1} is shown: the signal falls to 60 % very rapidly, then drops to 30 % with a longer exponential decay. The light dotted line displays the fitted double exponential trend, with time constant of 33 ms and 5.5 s respectively. It is worth noting that not only Raman resonances decay but also the NRB, further confirming that the surface of the sample is entirely damaged. The two exponential behaviour could be explained by the fact that the smooth vitrified surface of the sample is immediately damaged, lowering the sample reflectivity very quickly. Then, subsequent pulses thermally damage the solid, with longer timescales.

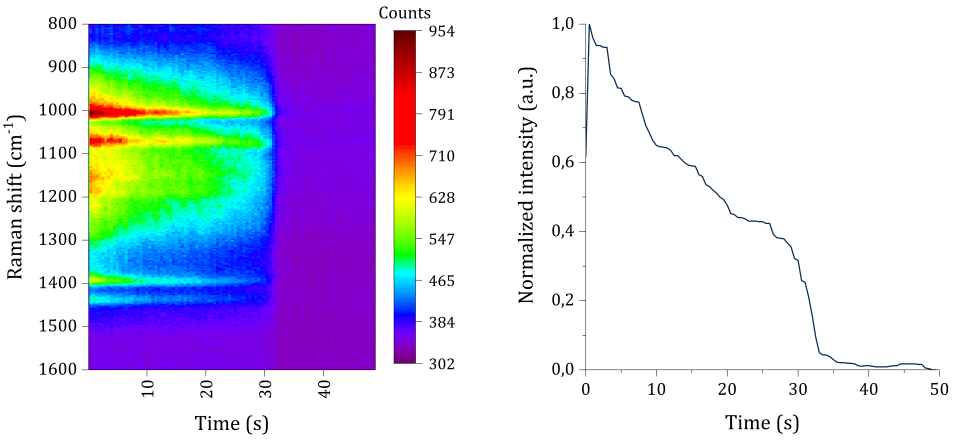

Figure 3.22: NaDPA Raman spectrum evolution over time on static solid sample (left). Time steps of 50 ms. $E_P = 1.3\,\mu\mathrm{J}$, $E_S = 1\,\mu\mathrm{J}$, $E_{PR} = 0.7\,\mu\mathrm{J}$ focalized with $f_{mirror} = 150\,\mathrm{mm}$. On right, 1007 cm^{-1} Raman peak time evolution, normalized after baseline subtraction.

Another acquisition in a similar conditions but in a longer time frame (Fig. 3.22), showed a complete signal deterioration after 30 s corresponding to a sample carbonization process in the focus point.

By lowering the pulse energies to 0.6 µJ (pump and Stokes) and 0.45 µJ (probe), the sample was not damaged for very longer times, corresponding at an irradiance of $\sim$18 mJ/cm^2. Figure 3.23 shows the signal stability for 90 s. After a 30 % loss in the first twenty seconds, the signal remains pretty constant. Due to very low source energy, the signal is weak even with a CCD exposure time increased to 500 ms, thus the acquisition appears noisy. Although, the trend is fairly clear. With even lower energies no Raman signal were noticeable.

The time resolution (200 ms) of previous acquisitions did not make it possible to determine whether there was a time range in which the signal remained almost constant before

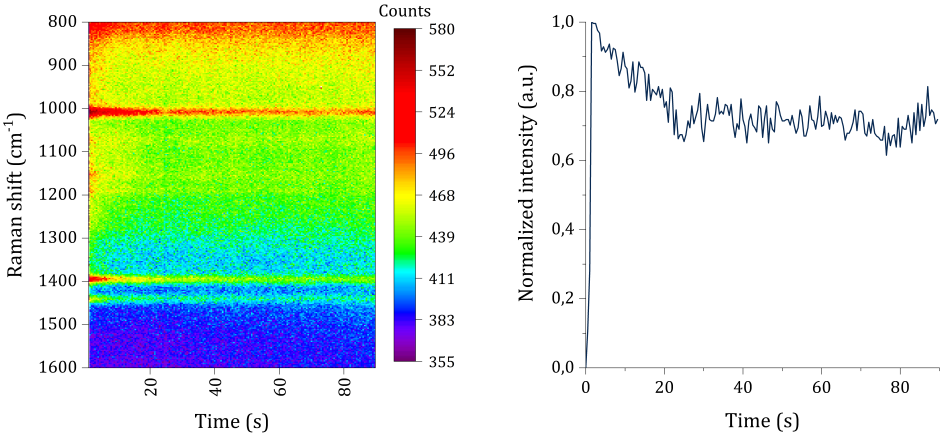

Figure 3.23: NaDPA Raman spectrum evolution over time on static solid sample (left). Time steps of 500 ms. $E_P = 0.6\,\mu J$, $E_S = 0.6\,\mu J$, $E_{PR} = 0.45\,\mu J$ focalized with $f_{mirror} = 150\,mm$. On right, $1007\,cm^{-1}$ Raman peak time evolution, normalized after baseline subtraction.

the sample was damaged and the signal decayed. So, other measurements were carried out at the lowest possible exposure time, set at 10 ms. Because of CCD readout time, one sample every 23 ms could be acquired, fixing the temporal resolution at this value. Pump and Stokes energies were set to 1 µJ, strong enough to make Raman vibrations resonating. Probe energy was instead varied from 0.4 µJ to 1.4 µJ. The time evolution of Raman signals with different probe energy are pictured in Figure 3.24. All samples show a trend that goes like a double exponential. As the energy increases, the times of the long exponential become shorter and shorter. When the probe energy reaches 1.0 µJ, corresponding to an irradiance of $\sim$11 mJ/cm^2 (to be summed with the 22 mJ/cm^2 of pump and Stokes pulses), sample is completely damaged after few seconds and the signal drops instantaneously. As the energy increases, sample carbonisation occurs faster and faster. However, after the sudden drop in signal the background increases a bit and a new weak peak at 1075 cm^{-1} appears in the spectrum, highlighting the presence of different type of substances. The right plot pictures the first instants frame, enlarged from the left graph. It reveals that NaDPA powder sample resists till $\sim$440 ms before been degraded by 0.4 µJ probe. This time frame corresponds approximately to 4400 pulses. Increasing energy to 0.6 µJ, the signal remains constant for $\sim$180 ms. Increasing further, the plateau breaks earlier and earlier, until it becomes shorter than the acquisition temporal resolution.

In conclusion, it has been shown that a NaDPA solid sample can be irradiated with 18 mJ/cm^2 without any damage for longer time. However, the CARS signal is so low that it is difficult to extract Raman spectra even with an exposure time of 500 ms. Maintaining Stokes and pump energies at 1.0 µJ and probe energies below 0.6 µJ, corresponding to a total irradiance of 28 mJ/cm^2, it is possible maintain high constant CARS signal for a few hundreds of milliseconds, which is a time frame more than adequate for imaging purpose, where spectra are taken in fixed sample points (see Section 3.7). For longer measures, as required in probe delay scanning, sample movement is needed to prevent damaging.

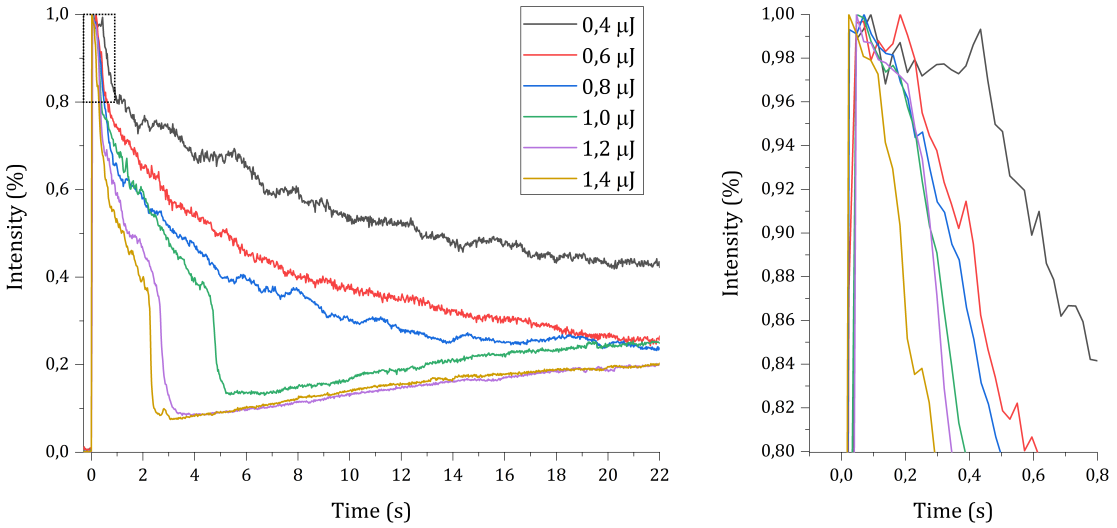

Figure 3.24: NaDPA Raman spectrum evolution over time on static solid sample for different probe energies (left). Time steps of 10 ms. $E_P = 1.0\,\mu J$, $E_S = 1.0\,\mu J$, E_{PR} varying (see legend), corresponding to irradiance from $16.8\,mJ/cm^2$ to $23.9\,mJ/cm^2$. First time instants area (dotted rectangle) is enlarged on right.

3.6 Spores detection

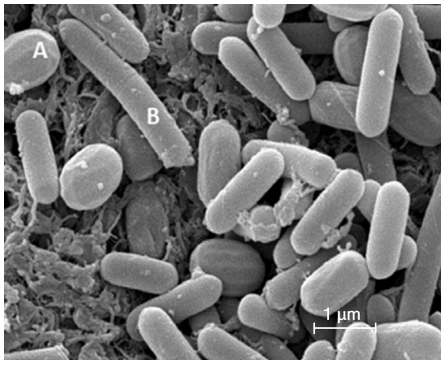

Figure 3.25: *B. subtilis* bacterium (B) and spore (A) [30].

The source was then employed for bacterial spores detection. To avoid contamination by the anthrax bacterium, other species of spore with a similar chemical composition were settled as samples. In particular, *Bacillus subtilis* spores were spread on a circular slide that could be connected to the motor shaft to be rotate, avoiding point damages during the measurements. Tight focusing configuration with low energy pulses was operated, with Stokes, pump and probe energies of 0.7 µJ, 0.7 µJ and 1.0 µJ respectively. Exposure time was increased to 2 s, since the spores are composed by only ∼5–15 % of CaDPA, which decreases the signal with respect to pure crystals. Moreover, the spore sample was a partially damaged by previous measures with other experimental setups. However, Raman resonances were detected.

Figure 3.26 pictures three CARS maps, taken with same measure parameters at different pump bandwidth. All maps are characterized by a strong NRB on which some weak short-decaying peaks appear, except for the one between 1500 and 1600 cm^{-1} that seems last far more over probe delay. Raman spectra at the same probe delay (at 1.5 ps, in a

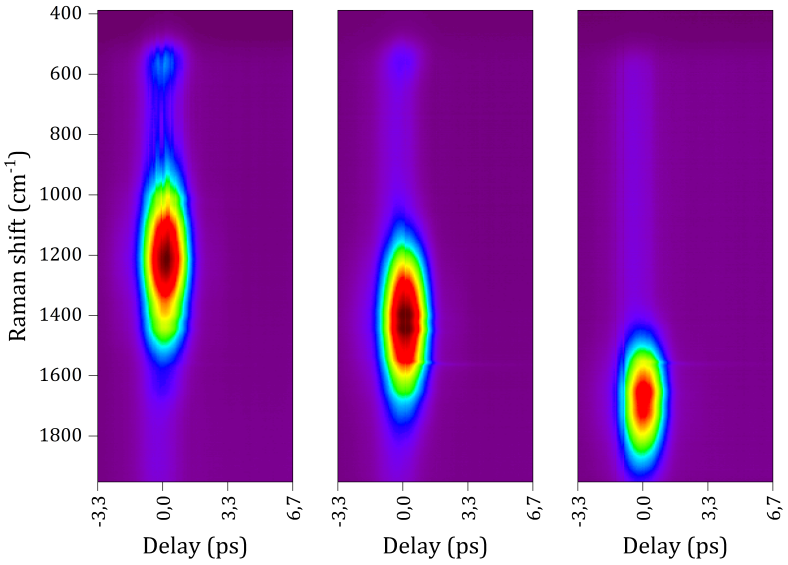

Figure 3.26: CARS maps of *B. subtilis*, with different pump bands. $E_P = 0.7\,\mu J$, $E_S = 0.7\,\mu J$, $E_{PR} = 1.0\,\mu J$. $T_{exp} = 2\,s$. Different Raman vibrations are excited when pump pulse is amplified in different spectral regions, selected by OPA delay.

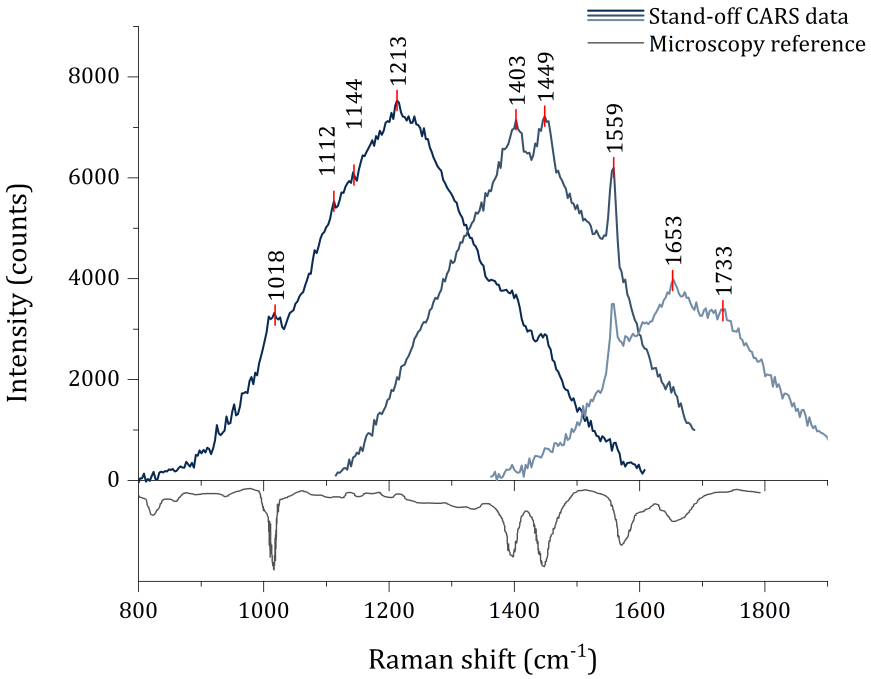

Figure 3.27: Raman spectra taken at the same 1.5 ps probe delay, for each map of Fig 3.26, with labelled peaks. Reference from [31].

region with lower NRB) were extracted and represented in Fig. 3.27: from this view several resonances appear, including some very distinct from the background. As a reference, CARS data coming from *subtilis* spores measured in microscopy layout are visualized underneath. The main NaDPA peaks at 1006, 1395, 1441 and 1552 cm^{-1} (see page 105) can be located on the graph, taking into account slight differences because the substance present in spores is CaDPA. The DPA salt pattern, as seen in Fig. 3.20, is recognizable in the most delineated peaks. In addition, some other weak peaks can be individuated with much more effort. They could corresponds to Raman excitations coming from other organic molecules present in spores. The comparison with reference microscopy data shows a good similarity: peaks at 1018, 1403, 1449, 1559 and 1653 cm^{-1} are easily recognized.

By increasing the probe delay to reduce the background, peaks decay quickly and weaker resonances disappear in CCD noise. An energy boost could increase CARS signal and keep peaks visible for a longer times, allowing the pulse to probe a low NRB region: Stokes was enhanced to 2.3 µJ and probe to 1.5 µJ. Although, power increasing damaged the spore samples. In a real-life context this is not a trouble, since the goal is sense the presence of spores and not to preserve them. However, in order to save the sample for future measurement, with a focused area of $\sim 90 \times 10^{-6}\,\mathrm{cm}^2$ ($f_{mirror} = 150\,\mathrm{mm}$) energies were usually kept below 0.7 µJ for Stokes and pump and 1 µJ for probe.

Another *B. subtilis* Raman spectrum is shown in Fig. 3.28. The peak pattern of a DPA salt emerges from the NRB with a single acquisition. All previously described peaks can be recognized in a single measure. For comparison, the NaDPA reference (microscopy layout from) is reported underneath.

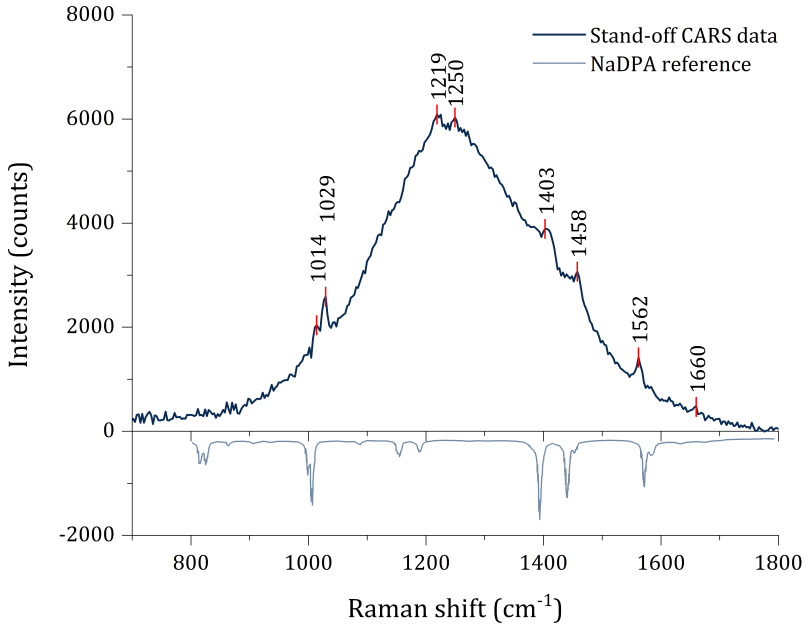

Figure 3.28: Raman spectrum of *B. subtilis* spore. $E_P = 0.5\,\mu\mathrm{J}$, $E_S = 0.6\,\mu\mathrm{J}$, $E_{PR} = 0.6\,\mu\mathrm{J}$. $T_{exp} = 2\,\mathrm{s}$. NaDPA reference from [5].

3.7 CARS imaging

In previous sections, the detection setup was described and optimizations for stationary source measures were discussed. Tests on different types of molecules, both in scattering samples and liquid state, have been made to verify the effectiveness of laser source and the robustness of the acquisition process.

The final step was to exploit the CARS signal detection for imaging purposes. In practice, the source is moved across the surface following a pattern and a spectrum is acquired for each point on the sample. By analysing the data, it is possible to reconstruct the presence of a specific molecule on the surface, or to recognise which molecules are present, by reconstructing a hyperspectral image of the sample. In addition, by using machine learning algorithms to recognise spectra and peaks relative positions, it is possible to extract information even from very noisy signals or with parasitic resonances.

The detection setup was the one described at page 91 and in Fig. 3.1. The sample was placed right centred in the focal point of the spherical mirror ($f_{mirror} = 500\,\text{mm}$). Then, the two galvo mirrors were used to sweep the laser source on the scatterer disk, following an s-shaped pattern from the top left corner downwards, as shown in Fig. 3.29. They are driven by two servo motors that move angles on two axis perpendicular to propagation direction and are controlled via a configurable LabVIEW script, which provides two stepped signals for x- and y-axis motion. Number of points (vertically or horizontally), pitch width and motion speed can be regulated in order to control scanned area, image resolution and acquisition times. Galvos and CCD camera were synchronized, both triggered by a common external wave generator (Siglent SDG 5162), such that as soon the laser has been shifted on a new point, CCD sensor integrates signal for the entire exposure time and sends data to the computer. The raw data are then organized and sorted in 3D matrix with a self-made Matlab script, which also deals the final display of the 2D image.

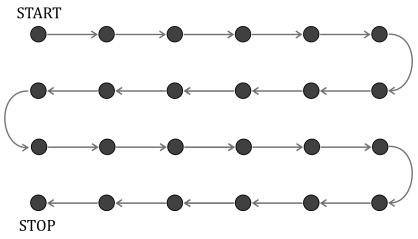

Figure 3.29: Galvo 6.4 scanning scheme for hyper-spectral image acquisition.

It should be noted that during the acquisition of an image, the source moves across sample surface, so three things must be considered. First, the outermost points from the sample centre will be slightly out of focus, because the source beam travels more before reaching those points. This will lead to a signal reduction and the effect is more evident the further away from the centre. The use of mirrors with long focal lengths which stretch the beam Rayleigh distance, together with the scan of sufficiently small areas (typical side of 1-2 cm) easily contains the issue.

Secondly, as the scattering point moves over the surface together with source, so does its image on the vertical monochromator slit, because the two detection lens forms a 1:1 image system. Hence, the slit must be fully open to allow the moving light dot to enter the monochromator during the scan. Conversely, the spectral resolution will worsen since the image on the camera sensor would have a wider spatial profile, not filtered from the slit. However, the aim of imaging is not to acquire high-resolution spectra but to recognise the presence of specific patterns of already known spectra. So this is a minor

issue. Indeed, the intrinsic reduction in spatial resolution allows binning on more CCD pixels, thus improving the S/N ratio and speeding up the readout process.

Thirdly, considering that the monochromator is also a 1:1 imaging system, for the same reason as before the image on CCD sensor, spectrally dispersed, shifts too. So, the Raman spectra drift from left to right and vice versa as the image scan goes on. As the drift depends only on source sweep and it is always the same, it was modelled using a reference sample (toluene) and used to properly align all the acquired spectra so that they share the same Raman shift scale, thanks to a Matlab script.

Two imaging tests were carried out. The first sample was a cuvette filled with toluene with which the instrumentation was calibrated and refined. Since the CARS signal is a laser beam, the first collimating lens was temporarily removed. Pump and Stokes pulse energy was set to 7 µJ, while probe to 4 µJ. Probe was delayed for a background-free acquisition. The scanned area was 1.6 × 1.6 cm, with 40 points on each axis (image resolution of 0.4 mm). The CCD exposure time was reduced to 5 ms. By adding also the CCD readout time of few ms, one spectrum of each 10 ms was acquired, for a total measure duration of $40 \times 40 \times 10\text{ms} = 16\,\text{s}$, which is quite fast. The spectra were analysed by a machine learning algorithm, which was trained to recognize toluene fingerprint, to determine if the toluene signal was present or not. Figure 3.30 shows on left a real image of the toluene cuvette on which the measurement was made, in the area highlighted by the red rectangle. The reconstructed Raman image is represented on right: the algorithm is able to recognize with excellent accuracy the presence of toluene, reconstructing an image faithful to the real model: for example, the meniscus shape can be noted, as well as some drops of liquid attached on the right wall. The toluene cuvette image was used in numerous tests to optimize the system, as well as to calibrate the Raman scale shift on the CCD sensor.

Finally, imaging was tested on a solid scattering sample. The phantom was built pressing together powders of two molecules whose Raman spectrum was previously known.

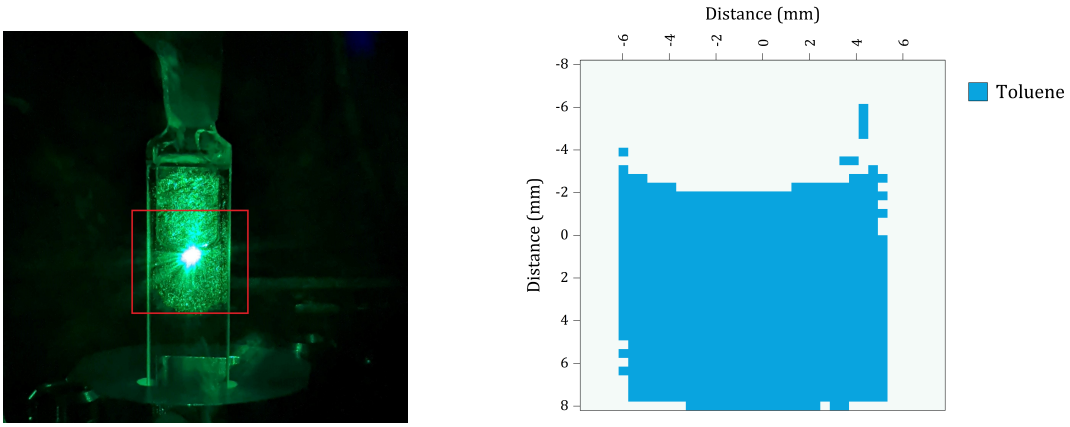

Figure 3.30: Toluene cuvette image. Left: real photo. Right: reconstructed image of red rectangle area with CARS imaging tecnique. $E_P = 7\,\mu\text{J}$, $E_S = 7\,\mu\text{J}$, $E_{PR} = 4\,\mu\text{J}$. $T_{exp} = 5\,\text{ms}$. 40×40 points. Scanned area $\sim 2.6\,\text{cm}^2$.

NaDPA and fructose (Raman spectra at page 105 and 102) were chosen. The powders were compressed in cylindrical mould such a way that about half was composed of NaDPA and the other half by fructose, without a net edge. The pressed disk appeared as a uniform white smooth surface, lacking the possibility to distinguish with the naked eye any difference between regions. The image scanning was performed with the same parameters for toluene measure, except for the CCD exposure which was increased to 90 ms since the collected signal is inherently weaker, being the radiation scattered. In this case the entire measure duration was $\sim 40 \times 40 \times 100\text{ms} = 2.7\,\text{min}$. The phantom disk photo is shown in Figure 3.31 on left, while on right it is pictured the reconstructed image of the red square. Thanks to the recognition algorithm trained with reference Raman spectra, the two disk areas, one composed by fructose and the other by NaDPA, can be distinguished.

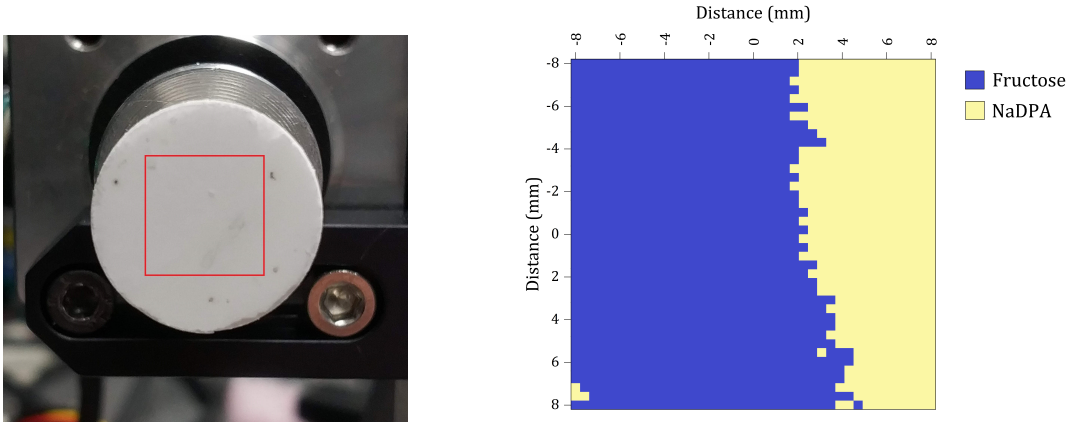

Figure 3.31: NaDPA-fructose disk image. Left: real photo. Right: reconstructed image of red rectangle area with CARS imaging tecnique. $E_P = 7\,\mu\text{J}$, $E_S = 7\,\mu\text{J}$, $E_{PR} = 4\,\mu\text{J}$. $T_{exp} = 90\,\text{ms}$. 40×40 points. Scanned area $\sim 2.6\,\text{cm}^2$.

Chapter 4

Absolute referencing of a 1015 nm laser for Boltzmann constant metrology

A side project has been followed during the laboratory work. A research group from Istituto Nazionale di Ottica (INO-CNR) LENS, Istituto Nazionale di Ricerca Metrologica (INRIM) and from the Department of Mathematics and Physics in Università degli Studi della Campania is carrying out a project for obtaining a new, more resolute measurement of the Boltzmann constant within the frame of a National project funded by the Italian Ministry for Education and Research, entitled "A new primary method of gas thermometry based upon Doppler broadened mercury spectroscopy in the UV region". They plan to use thermometry based on Doppler broadening for metrology purposes.

In particular, to perform ultra-precise spectroscopic measurements on gaseous mercury, they designed an optical setup starting from a monochromatic laser in the NIR (1015 nm) and generating light at higher frequencies through two second-harmonic generation processes, which excites a specific mercury energy level in the ultraviolet [32]. Boltzmann constant measure is derived indirectly from line broadening in a mercury transition due to atom thermal motion. To ensure that the broadening is entirely attributable to the Doppler effect and not to the frequency drift of the monochromatic laser which would limit the measure resolution, the NIR laser must be locked with a laser comb to be stabilized. However, the teeth of the comb laser available to the researchers do not reach wavelengths below 1050 nm, making it ineffective for stabilisation. A system to broaden the comb spectrum is therefore needed, so that a few teeth reach the desired wavelength. Thanks to the presence of a twin comb laser in the laboratories of the Department of Physics in Politecnico di Milano, a spectrum widener was built and successfully tested.

In the Section 4.1 a brief presentation of the metrology framework is introduced followed by a mention on the Doppler broadening thermometry. Then the researcher optical setup is presented in its current state. Some theoretical hints useful for understanding how a comb laser lock is done are described in Section 4.2. Then, design of the comb widener is discussed in Section 4.3, where the test results are also presented. A short conclusion and possible future developments of this project close the chapter.

4.1 Introduction

In 2019, on the 20^{th} of May – the anniversary of *Metre Convention* – some International System (SI) unit definitions were modified in order to be linked values of atomic characteristics or fundamental constants of nature. As the meter was redefined in 1983 in terms of distance travelled by light in vacuum thus referring to the exact value of the constant speed of light c, so now the kilogram, kelvin, ampere and mole are defined relying on the exact values of the Planck constant (h), Boltzmann constant (k), elementary electric charge (e) and the Avogadro constant (N_A), respectively [33]. This kind of formulation has the aim to disconnect the unit definition from the realization: this offers the possibility that completely different or new practical implementations can be developed as technologies evolve to measure constants with increasingly accuracy, without the need to change the units definition [34].

One of the four redefined units of measurement, the kelvin (K), will now come into focus. The previous definition was based on the quasi-artefact of a thermodynamic property of water, namely

> *The kelvin is the fraction* $1/273.16$ *of the thermodynamic temperature of the triple point of water* [35].

Instead, the current settlement states

> *The kelvin is defined by taking the fixed numerical value of the Boltzmann constant* k *to be* $1.380\,649 \times 10^{-23}$ *when expressed in the units* $J \cdot K^{-1}$*, which is equal to* $kg \cdot m^2 \cdot s^{-2} \cdot K^{-1}$*, where the kilogram, metre and second are defined in terms of* h*,* c *and* $\Delta\nu_{Cs}$ [35].

This definition implies the exact definition of the Boltzmann constant, $k = 1.380\,649 \times 10^{-23}\, kg \cdot m^2 \cdot s^{-2} \cdot K^{-1}$. Inverting the relation, it gives an exact expression for the kelvin, being

$$1\mathrm{K} = \frac{1.380\,649 \times 10^{-23}}{(6.626\,070\,15 \times 10^{-34})(9\,192\,631\,770)} \frac{\Delta\nu_{Cs} h}{k} \tag{4.1}$$

So from now to on, all temperature measure are an indirect comparison with the amount of energy per molecular degree of freedom as specified by the Boltzmann constant, which is an exact value. For a rapid comparison, in table 4.1 the seven defining constants are shown in relation to the units they finalize.

As a consequence of the new definition, now the triple point of water ceases to have an exact value and now has an uncertainty given by

$$T_{TPW} = 273.160\,00\,\mathrm{K} \pm 0.000\,10\,\mathrm{K} \tag{4.2}$$

as a result of inheriting the old uncertainty that Boltzmann constant k had.

To ensure a secure definition of the kelvin, new determinations of the Boltzmann constant needed to be made. In the last ten years the value has been the subject of intense scrutiny and new estimates have been reported with lower uncertainties, till the nowadays value. This was made in several institutions using a number of different technical approaches [36].

Table 4.1: International System defining constants.

Name	Symbol	Value	Unit
Hyperfine transition frequency of ^{133}Cs	$\Delta\nu_{Cs}$	9 192 631 770	Hz
Speed of light in vacuum	c	299 792 458	$\mathrm{m\,s^{-1}}$
Planck constant	h	$6.626\,070\,15 \times 10^{-34}$	J s
Elementary charge	e	$1.602\,176\,634 \times 10^{-19}$	C
Boltzmann constant	k	$1.380\,649 \times 10^{-23}$	$\mathrm{J\,K^{-1}}$
Avogadro constant	N_A	$6.022\,140\,76 \times 10^{23}$	$\mathrm{mol^{-1}}$
Luminous efficacy	K_{cd}	683	$\mathrm{lm\,W^{-1}}$

In principle any physical law that involves temperature can be exploited to determine the new kelvin from Boltzmann constant. However, the most common techniques used and actively pursued are the *Acoustic Gas Thermometry (AGT)*, which relies on a determination of the sound speed in a gas, the *Dielectric Constant Gas Thermometry* (DCGT), measuring the electrical permittivity of a gas, the *Johnson Noise Thermometry* (JNT), based on the value of mean-square noise voltage developed in a resistor, and the *Doppler Broadening Thermometry* (DBT). Although the latter does not reach the same accuracy of other techniques nowadays, Doppler Broadening Thermometry (DBT) is widely recognized as a very promising technique that would be overcome the actual value precision.

4.1.1 Doppler Broadening Thermometry

Doppler broadening thermometry is based on spectral line shape and width properties of a gas in thermal equilibrium, which are directly linked to transition dipole moment between two quantum state. Similar data for diatomic and triatomic molecules can be used to develop new methods for computing SI constants with extreme precision. In particular, if the shape of a given line is accurately recorded as a function of the gas pressure, then line broadening and shifting coefficients can be determined using laser absorption spectroscopy. This is where the DBT technique comes [37]. DBT relies on measuring the Doppler width of a Doppler-broadened spectral line in a molecular gas under the linear regime of absorption. The relationship between the Doppler half-width at half maximum of a spectral line, $\Delta\nu_D$, and thermodynamic temperature is given in equation

$$\Delta\nu_D = \frac{\nu_0}{c}\sqrt{\frac{2\ln 2(kT)}{m}} \tag{4.3}$$

where m is the absorber mass, ν_0 the line-center frequency and T is the thermodynamic temperature.

If the central frequency and the molecular mass are known, by inverting the equation, then it is possible to determine the thermal energy and, consequently, the gas temperature.

Therefore, interrogation with a sub-kHz-line width laser would allow approaching the ppm level in temperature measure, making DBT a viable method for new estimations of k.

The first experiment where DBT technique was used for metrology was conducted in 2005, using the isolated line at 10.35 µm of ammonia (NH_3). Boltzmann constant k was determined with an uncertainty of 800 parts over 10^6. After 10 years of technical development and optimizations, DBT is nowadays approaching a precision at the ppm level, with the perspective of bringing the global uncertainty of k below 10 ppm.

The research group is using mercury vapour, in particular the transition $6s^2\,{}^1S_0 \rightarrow 6s6p\,{}^3P_1$ at 253 nm, in mercury isotopes ^{200}Hg and ^{202}Hg [32]. The temperature of the gas is set to one of triple point of water, where the vapour pressure of mercury is sufficiently high enough for a good signal-to-noise ratio but small enough to neglect the collisional broadening and allowing accurate modelling without nearby resonances or quantum interference effects. In order to get the proper absorption frequency, they designed a double-staged SHG laser, briefly described in the next section.

4.1.2 The laser setup

For the practical implementation, a general DBT laser source must feature, in addition to a sub-kHz line-width, absolute frequency traceability, continuous tunability over 6 GHz to ensure a sufficiently broad scanning region around the line center, relative intensity stability at the level of 10^{-4} and a high-quality spatial intensity profile. In particular, a TEM_{00} mode would be desirable. On the other hand, few µW of optical power are sufficient.

The setup used is shown in figure 4.1. It consists of tunable laser, a frequency stabilization system, an intensity stabilization feed-back loop, an isothermal cell filled with the mercury and a detection chain.

For obtaining a 235 nm beam for mercury transition, the setup relies on several stages: an extended cavity CW diode laser (ECDL) at 1014.8 nm laser is exploited for second harmonic generation (SHG) using a a fibre-coupled periodically-poled lithium niobate. The produced radiation of 1.5 mW at 507 nm seeds a high-power diode laser, resulting in 80 mW of optical power. The second stage of SHG is performed using a 12 mm-long BBO crystal cut at $\theta = 51.2°$ in a cavity-enhanced setup. The 235 nm beam is then mode-cleaned using a $f = 50$ mm lens and a pinhole in order to eliminate the BBO spatial walk-off and obtain a TEM_{00}. At the final stage up to 250 µW of UV light are obtained, which is enough for DBT application. The source has 10^{-4} relative intensity stability and Gaussian shape. These features are necessary for retrieving the absorption profile with at least 10^{-6} accuracy.

The 20 mm-long spectroscopic cell, sealed at the two ends by a pair of wedged AR-coated quartz windows and filled with mercury vapours, is housed inside a cylindrical stainless-steel vacuum chamber and temperature-stabilized at the triple point of water measured by a pair of precision platinum resistance thermometers (Pt100). For frequency scanning, the 1015 nm master laser is continuously tuned by tilting a grating with some piezo-actuators, allowing over 10 GHz of scan without mode-hopping.

Nonetheless, this setup does not fully meet the stability requirement: thermal and mechanical noise can make the master laser frequency-drifting. To ensure a sub-kHz

stability, the UV spectrometer can be referenced to an SI-traceable frequency standard by direct stabilization of the master laser at 1015 nm. This can be done using a fibre optical frequency comb, allowing beat-note detection with sufficient signal-to-noise ratio thanks to optical heterodyne. Researchers already have a 250 MHz-spaced optical comb in the NIR region, covering a spectral region between 1050 nm and 2100 nm. The goal of the work described in the below section is to create a frequency widener system for the comb laser in order to get comb teeth in the 1015 nm region, with enough power for optical beating revelation at desired signal-to-noise ratio aimed to reference-lock the researcher's master laser.

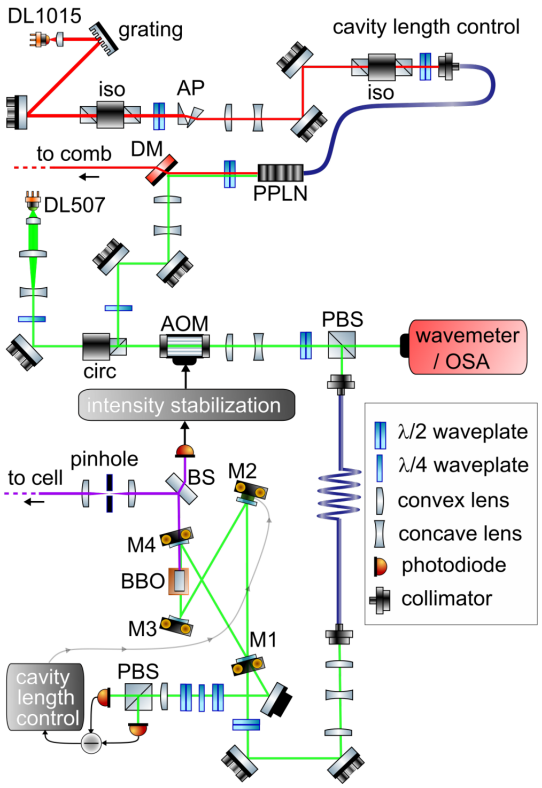

Figure 4.1: Laser source for DBT. PPLN: periodically-poled lithium niobate; AOM: acousto-optic modulator; BBO: crystal for second-stage duplication; (P)BS: (polarization) beam splitter; DM: dichroic mirror; DLx: diode laser at x nm; AP: anamorphic prisms [32].

4.2 Theoretical hints

Before going into detail, it is appropriate to give a brief overview of what a frequency comb is and how optical beats work.

4.2.1 Frequency comb lasers

A mode-locked laser is nothing but a laser in which a fixed phase relationship across a broad spectrum of frequency is established [38]. Thus, when all the frequencies are in

phase they constructively interference, the energy stored in the active medium is released and the pulses arises. This can be easily done by an active or passive saturable absorber. Pulses exit the laser cavity once per round-trip time, with a pulse repetition period of $T_{rep} = 1/f_{rep} = 2L/v_g$, where v_g is the pulse group velocity and L the laser cavity length. This is the typical time-based description of mode-locking.

Generally speaking, a laser pulse can be mathematically modelled as a continuous carrier wave with an angular frequency ω_C modulated by an envelope function $A(t)$, so that the electric field of the pulse is written as

$$E(t) = A(t)e^{i(\omega_c t + \phi_{ce}(t))} \tag{4.4}$$

where ϕ_{ce} is the carrier-envelope phase, i.e. the phase shift between the envelope peak and the closest maximum of the carrier wave, as illustrated in Figure 4.2. In any dispersive

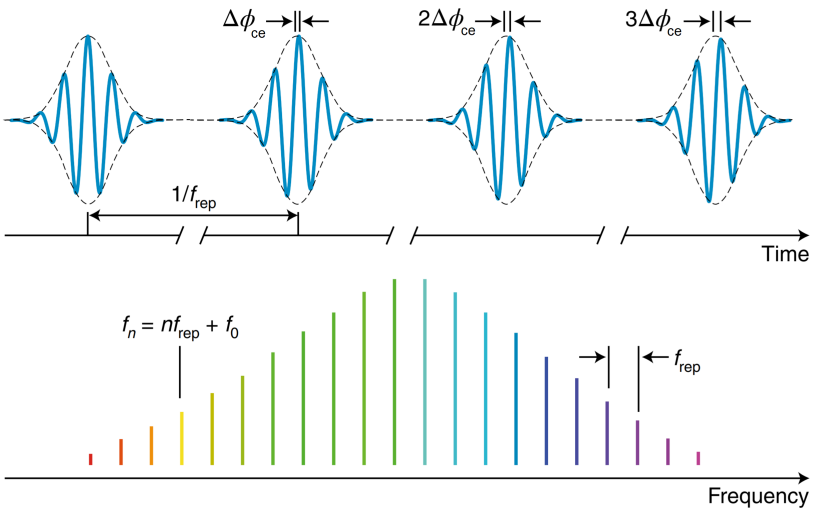

Figure 4.2: *a.* Comb pulses in time domain and the representation of $\Delta\phi_{ce}$. *b.* Comb spectrum [39].

material the phase and group velocities of a pulse are different, thus the carrier-envelope phase ϕ_{ce} evolves while pulse propagates. Considering two adjacent pulses, their phases will be shifted of $\Delta\phi_{ce} = (\frac{1}{v_g} - \frac{1}{v_p})L\omega_c$.

Shifting in a frequency domain description, the pulse train generated by the ML laser has a spectrum consisting of a discrete, regularly spaced series of sharp lines, the teeth of the so called *frequency comb* (Fig. 4.2). In fact, due to pulse time-periodicity, the field can also be described as a periodic Fourier series of optical modes, $\nu_n = \omega_n/(2\pi)$, with Fourier amplitude coefficients A_n such that

$$E(t) = A(t)e^{i(\omega_c t + \phi_{ce}(t))} = \sum_n A_n e^{i\omega_n t} \tag{4.5}$$

where n represent the mode number. So the spectrum corresponds to a discrete set of

evenly spaced narrow lines with optical frequency that can be written as

$$\nu_n = n f_{rep} + f_0 \tag{4.6}$$

where f_{rep} is the pulse repetition frequency and f_0 is the carrier–envelope offset frequency, related to the pulse-to-pulse phase shift $\Delta\phi_{ce}$ by the relationship $f_0 = f_{rep}\dfrac{\Delta\phi_{ce}}{2\pi}$ [40].

It is possible to retrieve an absolute frequency calibration knowing the repetition rate f_{rep}, easily measurable with a fast photo-diode, and the offset frequency f_0, which is derived from the value of $\Delta\phi_{ce}$, measured thanks to an interferometric homodyning of an octave spectrum (i.e. spanning at least in a range such that the highest frequency is a factor of 2 larger than the lowest one, $f - 2f$ spectrum).

In conclusion, a regularly spaced train of pulses produced by a mode-locked laser corresponds to a comb in the frequency domain that can be used as a reference for the master 1015 nm laser, in order to increase its frequency stability. This can be done looking at the beat notes shift.

4.2.2 Optical beat-notes

Generally speaking, in physics a beat-note is the result of interference of two waves at different frequencies. When two sound waves at frequency f_1 and f_2 are made interfering, a wave at frequency $f_H = f_1 + f_2$ and $f_L = f_1 - f_2$ arise, that consist in a sinusoidal carrier signal at f_H modulated by a sinusoidal signal at f_L, resulting in the so-called *beat*, as represented in Figure 4.3.

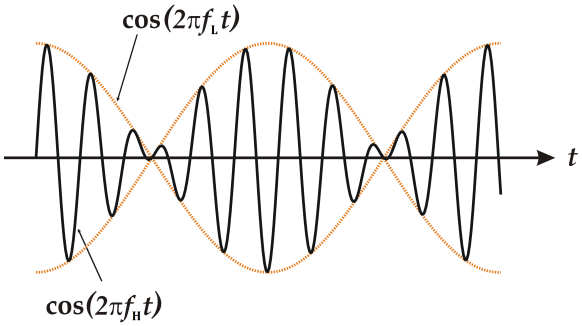

Figure 4.3: Beat-note signal.

This simple phenomenon can be observed in any kind of waves, including optical light radiation. Since optical frequencies span over a range between 400 THz and 800 THz, it is impossible to reveal such signals with electronic instrumentation, which has a bandwidth reaching at maximum some tens of gigahertz. Nonetheless, making two laser beams interfere on a detector, an intensity signal with a frequency f_L corresponding to their difference can be observed in the so called *heterodyne detection*, because it has a lower detectable frequency.

Considering two monochromatic linearly-polarized beams with a phase difference of $\Delta\phi_{12}$ collinearly impinging on a detector, under the hypothesis of same polarization direction – for sake of simplicity, thus preventing the use of vectors notation – the total

electric field is

$$E(t) = E_1 \cos(2\pi f_1 t) + E_2 \cos(2\pi f_2 t + \Delta\phi_{12}) \tag{4.7}$$

while the intensity is proportional to the electric, being $I(t) = \frac{1}{2}\varepsilon_0 nc|E(t)|^2$. Calculating the modulus squared of the total electric field $E(t)$

$$\begin{aligned} \left|E(t)\right|^2 &= \left|E_1 \cos(2\pi f_1 t) + E_2 \cos(2\pi f_2 t + \Delta\phi_{12})\right|^2 = \\ &= E_1^2 \cos^2(2\pi f_1 t) + E_2^2 \cos^2(2\pi f_2 t + \Delta\phi_{12}) + 2\, E_1^2\, E_2^2 \cos(2\pi f_1 t)\cos(2\pi f_2 t + \Delta\phi_{12}) \end{aligned} \tag{4.8}$$

Using the appropriate trigonometric identities, the equation can be written as

$$\begin{aligned} \left|E(t)\right|^2 =& \frac{1}{2} E_1^2 \left[1 + \cos(2\pi \cdot 2 f_1 t)\right] + \frac{1}{2} E_2^2 \left[1 + \cos(2\pi \cdot 2 f_2 t + 2\Delta\phi_{12})\right] + \\ &+ E_1^2 E_2^2 \left[\cos(2\pi(f_1 + f_2) + \Delta\phi_{12})\right] + E_1^2 E_2^2 \left[\cos(2\pi(f_1 - f_2)t - \Delta\phi_{12})\right] \end{aligned} \tag{4.9}$$

Since the detector is not fast enough to detect the signal at frequency $2f_1$, $2f_2$ and $f_1 + f_2$, the measured intensity is an integration over time of the electric field modulus, thus the fast oscillating terms have zero average

$$\begin{aligned} I(t) \propto \langle \left|E(t)\right|^2 \rangle &= \frac{1}{2} E_1^2 \left[1 + \cancel{\langle \cos(4\pi f_1 t) \rangle}\right] + \frac{1}{2} E_2 \left[1 + \cancel{\langle \cos(4\pi f_2 t + 2\Delta\phi_{12}) \rangle}\right] \\ &\quad + E_1^2 E_2^2 \left[\cancel{\langle \cos(2\pi(f_1 + f_2)t + \Delta\phi_{12}) \rangle} + \cos(2\pi(f_1 - f_2)t - \Delta\phi_{12})\right] \\ &= \frac{1}{2} E_1^2 + \frac{1}{2} E_2^2 + E_1^2 E_2^2 \cos(2\pi(f_1 - f_2)t - \Delta\phi_{12}) \end{aligned} \tag{4.10}$$

The equation can be rewritten in terms of impinging intensities, obtaining

$$I(t) = I_1 + I_2 + 2\sqrt{I_1 I_2} \cos[2\pi(f_1 - f_2)t - \Delta\phi_{12}] \tag{4.11}$$

Removing the polarization hypothesis, namely considering electric field vectors $\vec{E}_1$ and $\vec{E}_2$ with a planar angle of φ between the two, beating term intensity is reduced by a factor of $\cos(\varphi)$ due to the minor fields superposition, since $\vec{E}_1 \cdot \vec{E}_2 = E_1 E_2\, cos(\varphi)$

$$I(t) = I_1 + I_2 + 2\sqrt{I_1 I_2} \cos[2\pi(f_1 - f_2)t - \Delta\phi_{12}] \cdot \cos(\varphi) \tag{4.12}$$

Rotating the beam polarizations, i.e. with a simple $\frac{\lambda}{2}$ crystal, can optimize the beating signal working with $\varphi = 0$.

It worth noting that removing the collinear hypothesis, thus having two propagating vectors $\vec{k}_1$ and $\vec{k}_2$ of equal magnitude and an angle θ between them in a plane normal to the flat detector, introduces a spatial modulation with fringes of spatial period

$$\Lambda = \frac{\lambda/2}{\sin(\theta/2)} \tag{4.13}$$

which moves uniformly with a fringe-period of $T_{fringe} = \dfrac{1}{|f_1 - f_2|}$, due to interference of different frequencies. Nevertheless, the spatial fringes are not a constrain since the

detector signal is averaged over the area. The only requirement to be taken into account is that the detector side is broad enough to host two adjacent bright fringe, thus being larger than Λ. If the the detector does not satisfy the above condition, the beat signal will be detected in any case but it will suffer of time modulation. Moreover, the modes of the two beams must not be orthogonal (i.e. a TEM_{00} and TEM_{01} does not interfere).

In conclusion, having two beams interfere on a detector with a finite bandwidth, the output signal is the sum of two constant terms (the intensities of the single beams I_1 and I_2, which can be eliminated with an high pass filter) and an interference term oscillating at $f_1 - f_2$ frequency, whose intensity depends on the square-rooted product of both beam intensities, as shown in equation (4.11). The heterodyne effect inherently guarantees two great advantages:

1. beat-note *self amplification*: even if one of the two intensities is very weak, the other one can deliver enough power to amplify the beat-note signal and be detectable.

2. detection of optical frequency (THz) signals, which could not otherwise be detectable since a fast photo-detector can have a bandwidth of tens of GHz. Therefore a laser frequency can be measured by recording a beat note of the laser itself and a close-by optical signal with known frequency, for example a comb which can cover a wide range of well-defined optical frequencies: a sufficiently nearby reference tooth for a beat measurement is always found for any optical frequency in the range.

4.2.3 Optical heterodyne detection

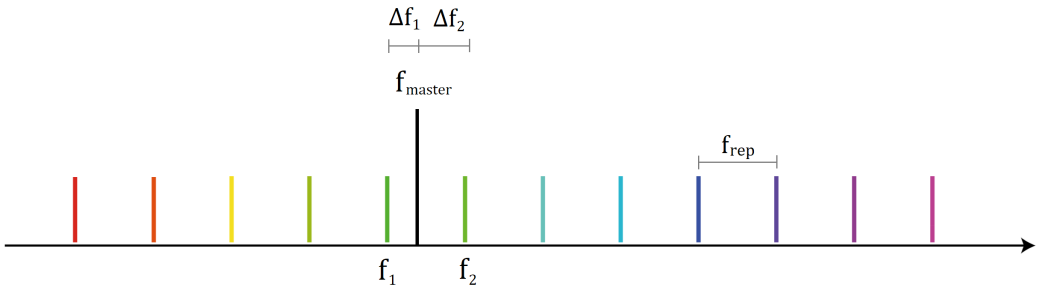

Figure 4.4: Frequency scheme of optical beat-note. The comb teeth are represented coloured, while the CW laser frequency is in black. The detector output will consist in two beating signal, at frequency Δf_1 and Δf_2.

This is the framework within which DBT master laser stabilization must take place. One of the two beams is the reference comb, which has a repetition rate, i.e. the distance between the comb frequency teeth, typically of some hundreds of megahertz (250 MHz in the setup described in 4.3.1); the other one is a continuous-wave (CW) laser. The heterodyne detection should reveal the beats, as their frequency difference is less than 250 MHz and it drops in a typical detector bandwidth. As shown in Figure 4.4, the CW laser has a frequency f_{master} which falls between two comb teeth, f_1 and f_2: two beating

of frequency $\Delta f_1 = f_{master} - f_1$ and $\Delta f_2 = f_2 - f_{master}$ will be detected, whose sum is fixed to the comb repetition rate, being

$$\Delta f_1 + \Delta f_2 = f_2 - f_1 = f_{rep} \tag{4.14}$$

When the CW laser mode is not stable, also the beat frequency behaviour experiences have the same instability: if the f_{master} drifts by δf, Δf_1 will drift in the same direction, while Δf_2 will drift in the opposite one, since their sum is fixed, namely

$$\begin{aligned} \Delta f_1' &= \Delta f_1 + \delta f \\ \Delta f_2' &= \Delta f_2 - \delta f \\ \Delta f_1' + \Delta f_2' &= \Delta f_1 + \Delta f_2 = f_{rep} \end{aligned}$$

Moreover, if the master laser has a multi-mode instability, each modes will produce a different beat-note thus a multitude of beats will be seen in the detected spectrum.

To conclude, the CW laser frequency drift δf can be therefore tracked looking at beat-notes and locked with an electronic feedback loop, providing the desired stability.

4.3 Comb spectrum widener

As mentioned before, the comb source owned by researchers has a spectrum with a lower limit frequency of 1050 nm. Hence, in order to have a comb tooth that interferes with the CW master laser at 1015 nm, it is necessary to:

1. Amplify the comb signal;
2. Broad the comb spectrum, till it reaches 1015 nm;
3. Filter out power coming from the unnecessary teeth.

The first goal was achieved using an Ytterbium Doped Fibre Amplifier (YDFA). Fibre amplifiers use fibres as gain media, i.e. glass doped by rare earth ion, to amplify a light beam input. The active element is pumped with a fibre-coupled diode laser and the pump light propagates through the fibre core together with the seeder signal to be amplified, once inserted with a coupler [41]. Thanks to the small mode area and the long length of the fibre, high gain can be achieved even with moderate pump power. Moreover, due to the small transition cross sections, significant pump energy can be stored in a fibre amplifier and be extracted by a short pulse, making them an excellent choice for amplifying ML pulses. The drawback of this technique is that the gain process is limited by the so called *amplified spontaneous emission* (ASE). Spontaneous emission is a quantum effect stimulated by vacuum noise, i.e. by the zero point fluctuations of the optical field. When a gain medium atom is excited, it may spontaneously return to its ground state or to some intermediate energy level emitting a photon. This kind of randomly emitted photons are then amplified by the YDFA itself, resulting in unwanted output power.

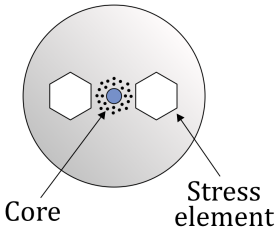

Figure 4.5: Typical polarization-maintaining photonic crystal fibre, in *panda* configuration.

The second target was reached by exploiting nonlinear effects in a polarization-maintaining fibre (PM fibre). In a standard optical fibre, random power coupling between two polarization modes can occur because few birefringence due to external perturbations or manufacturing imperfection. The PM fibre intentionally introduce uniform birefringence along the fibre (Figure 4.5) breaking rotational symmetry with stress elements, thereby guaranteeing constant field polarization [42]. The PM photonic crystal fibre widens the input spectrum with the effect of *self phase modulation* (SPM, see Sect. 1.3.2) to have some comb teeth also in the desired region. After travelling along YDFA fibres, the pulse presents a high positive dispersion that must be compensated; in fact, in order to get the right peak intensities for SPM, the pulse has to be time-compressed after the amplification and before entering in the PCF. This was done by a transmitting grating pair which introduces negative dispersion due to the difference in the optical path undergone by the different wavelengths. The working prin-

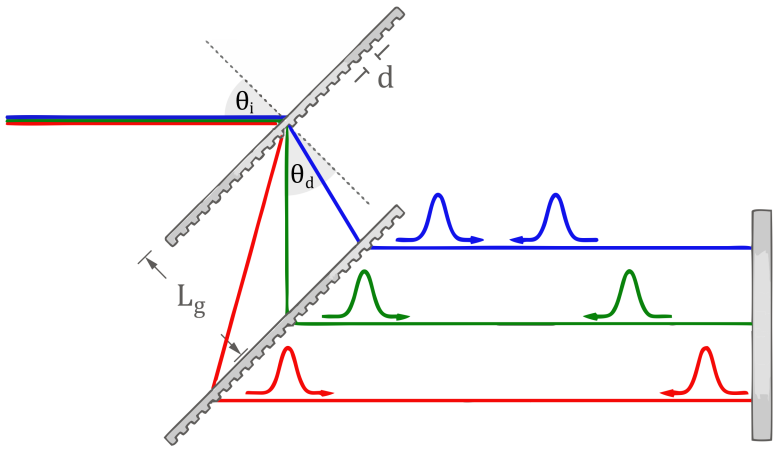

Figure 4.6: Illustration of a transmission grating pair.

ciple is illustrated in Figure 4.6. The frequencies of the incoming beam are separated by a diffraction grating, since the diffraction angle θ_d depends on the wavelength, with a relation

$$\sin(\theta_d) = \sin(\theta_i) + m\frac{\lambda}{d} \tag{4.15}$$

where θ_i is the input angle and d the grating period. It results in a tunable negative group

delay dispersion of

$$\frac{d^2\phi(\omega)}{d\omega^2} = -\frac{\lambda^3}{2\pi c^2}\frac{L_g}{d^2}m^2\left[1-\left(m\frac{\lambda}{d}+\sin(\theta_i)\right)^2\right]^{-\frac{3}{2}} \tag{4.16}$$

where L_g is the distance between the gratings and m the diffraction order [7]. Moreover, by retroreflecting the light back into the grating pair, the spatial coherence is preserved and a double amount of negative dispersion is reached.

Once the pulse spectrum was widened by the PM fibre, the third step was realized using an angle-tunable low-pass filter so that all radiation except few comb teeth near 1015 nm could be removed.

4.3.1 Setup design

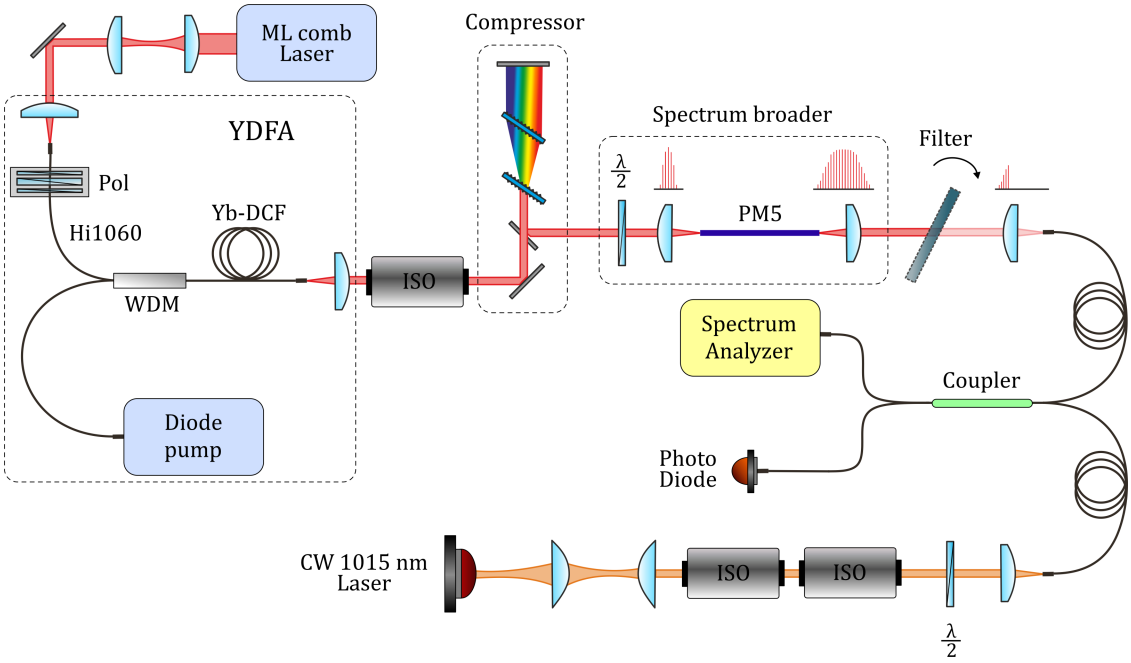

Figure 4.7: Overall setup scheme. Pol: polarization controller; Hi1060: input fibre; WDM: wavelength division multiplexer; ISO: optical isolator; Yb-DF: Yb-doped double-clad fibre; PM5: polarization-maintaining photonic crystal fibre.

The laser comb source is a Menlo System TC 1550, an Er^{3+}-doped fiber based mode-locked femtosecond laser with a repetition rate of 250 MHz. The ML output exhibits a comb-like spectrum centered around 1560 nm; it is coupled to an Erbium Doped Fiber Amplifier (P250-XPS EDFA) which amplify the pulses and than spectral broadened by an highly non-linear (NL) fibre in a range between 1050 nm and 2100 nm. The shape and width of the spectrum can be modified by acting on waveplates controller which change NL fibre input polarization. By phase locking the comb spacing and the offset frequency to a radio frequency reference source, the comb has an accuracy of 10^{-14} and a stability

of 5×10^{-13} [43]. For the actual setup, internal comb amplifier waveplates were set in order to maximize the output signal in a spectral region as close to 1050 nm as possible, reaching a power of 85 mW.

The Figure 4.7 shows the overall setup. The comb radiation is first amplified by Ytterbium Doped Fiber Amplifier (YDFA). Fibre (HI1060) injection of comb radiation is done by an aspheric collimation lens (ThorLabs F260APC, $f = 15.43$ mm, NA $= 0.16$, coated at 1064 nm). The correct lens acceptance waist diameter of 3.37 mm as obtained with a telescope lens system, while the input polarization was optimized by an in-line fiber polarization controller (ThorLabs CPC250) which exploits the effect of compression and rotation stress-induced birefringence to create changes in the light polarization. The YDFA pump radiation (976 nm) is coupled with the pulse through the use of a Wavelength Division Multiplexer (WDM, DKPhotonics PSC-21-25-105/125-6/125DC-20/125DC-T3-08). It multiplexes comb pulse coming from HI1060 fibre (core diameter 6 µm, cladding 125 µm) and the pump diode fibre (multimode with core of 105 µm, cladding 125 µm) into an output double-clad fibre of length 80 cm with core, first cladding and second cladding diameters respectively of 20, 105 and 125 µm. The double clad fiber propagates the comb signal within the core and the pump at 976 nm within the first cladding. Then, the double-clad fibre is spliced to an Yb-doped double-clad fibre of length 2 m (Coractive model DCF-YB-20/128E). The amplification mechanism occurs within the doped fibre.

The YDFA diode is set to a working temperature of 37 °C by a Peltier cell. A current of 1.655 A is supplied to the diode from a driver (Wavelength Electronics LDTC 2/2E), corresponding to an amplified optical power of about 155 mW measured by a Newport thermopile. The diode laser is be also cooled by a big radiator, that has been used in a passive way considering the not excessively high currents in play. The Figure 4.8 shows the relation between injected current in the amplifier diode and the output optical power.

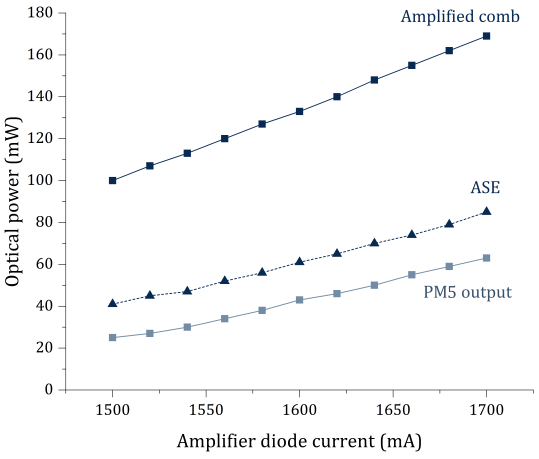

Figure 4.8: Optical power trends with diode pump current. Dark blue: total amplified signal (square) and relative ASE (triangle). Light blue: photonic crystal fibre power output.

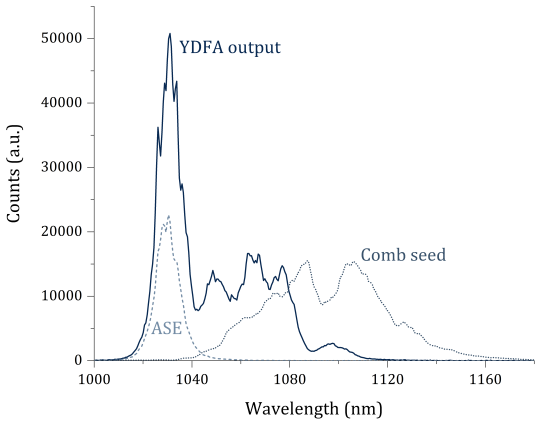

Figure 4.9: Spectrum of the YDFA input (comb seeder, dotted line), YDFA output (solid line) and relative ASE (dashed line).

As it can be seen from Figure 4.9 representing the amplifier input/output spectra, the comb seed has very little power at 1030 nm (peak value of Yb-doped amplifiers bandwidth, corresponding to $^2F_{\frac{5}{2}} \rightarrow {}^2F_{\frac{7}{2}}$ transition) but still enough to be amplified. ASE spectrum is also pictured in the graph: the inevitable unwanted spontaneous emission amplification effect determines noise worsening in the beats signal, so it should be kept as low as possible, thus working in a low pump current regime.

After the amplification stage, the beam is collimated (aspheric 15 mm-long focal lens) and passes through an optical isolator which avoids reflection re-entering in the fibre. The pulse is temporally compressed by a pair of transmitting pairs (LightSmyth T-1000-1040, 1000 lines/mm, diffraction efficiency of $\sim 94\,\%$ in a bandwidth of 1040 ± 20 nm with an angle of incidence $\theta_i = 31°$), compensating the fibre positive dispersion and increasing the peak power intensity of the amplified pulses. The distance L_g between the pair on which the negative dispersion depends on, according to equation (4.16), has been live-view optimized with a Fringe-Resolved Autocorrelator (FRAC). Then, the beam is launched in a polarization-maintaining photonic crystal fibre (NKT Photonics, LMA-PM-5 Large-Mode-Area PCF, called concisely PM5) with a core diameter of 5 µm and a length of about 5 cm via a $f = 4.5$ mm lens, mounted over a high-precision translation stage (Thorlabs, MAX313D/M). The coupling efficiency reached is 40 %, which can be derived from the Figure 4.8. After passing through the photonic crystal PM5 fibre the comb spectrum has

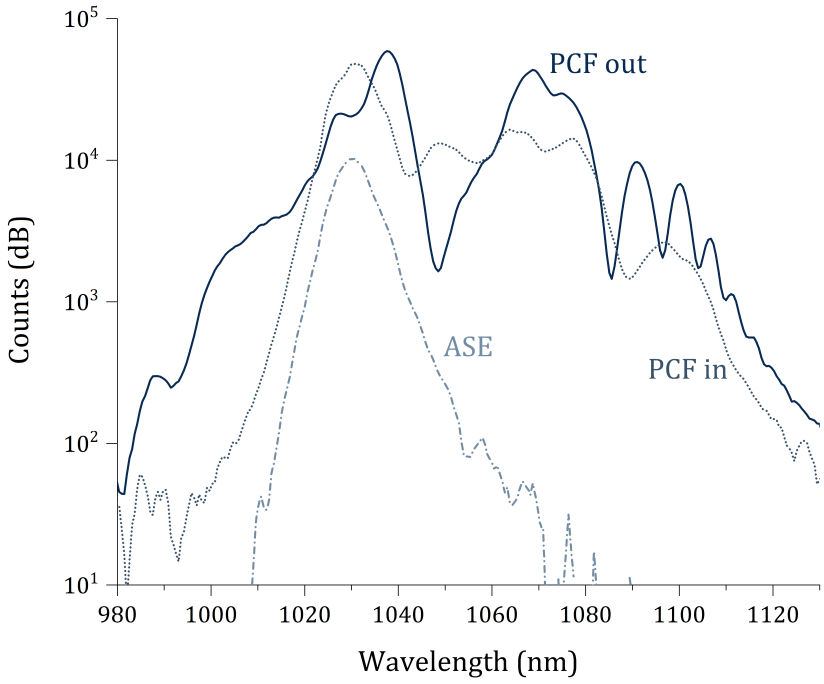

Figure 4.10: Logarithmic spectra of the fibre input pulse (dotted line), output (solid one) and ASE (dashed).

been broadened, as seen clearly in the Figure 4.10: in particular, in the 1015 nm region power has gained a factor 10. Typical spectral modulation of the SPM (cfr. 1.3.2) are also evident. The spectrum shape is further live-optimized fine tuning the gratings pair distance L_g: the goal is to maximize its power near 1015 nm, even if in this configuration a hole at 1050 nm appears.

The beam is ultimately collimated by an aspheric lens ($f = 11$ mm) and a tunable angle-variable low pass filter (Semrock VersaChrome Edge™, 979 nm–1128 nm) removes all the spectral power above 1015 nm which is not useful for the beat interference. The final spectrum is shown in Figure 4.13, where it is noticeable the filter role in culling the signal above 1016 nm and the presence of comb-broadened spectrum overlapping the CW one, delta-like shaped. Its collimated Gaussian mode is displayed in Figure 4.11. Figure 4.12 show a photo of the final setup.

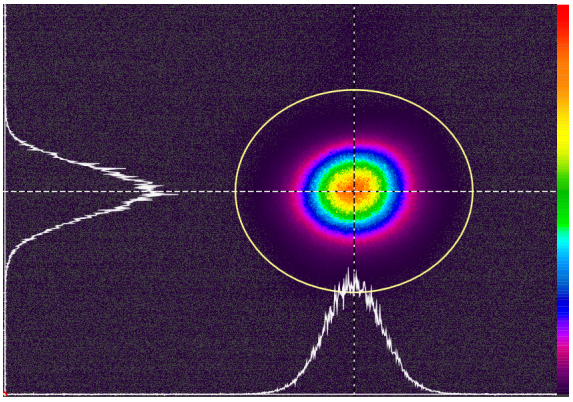

Figure 4.11: PM5 fibre output profile, after low pass filter: $D_{4\sigma_x} = 1.22$ mm and $D_{4\sigma_y} = 1.03$ mm.

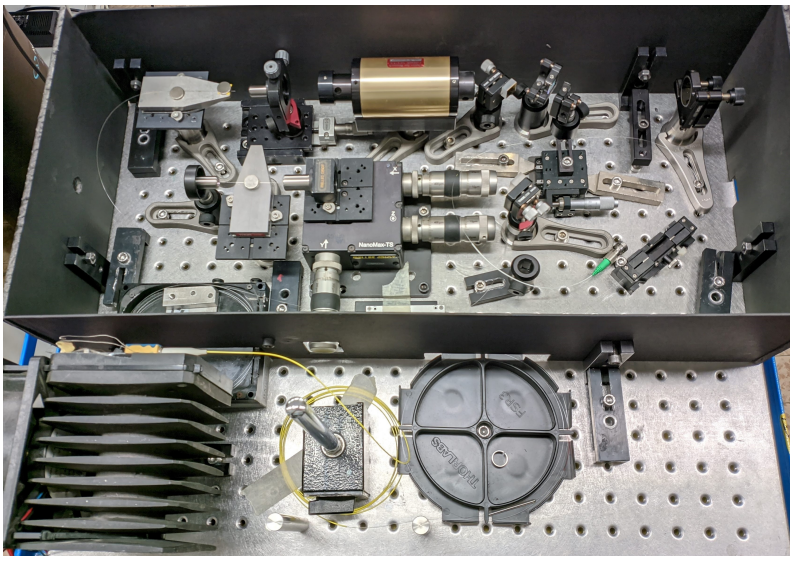

Figure 4.12: Setup photography.

4.3.2 Beat-notes measure

Finally, to verify the effective spectrum broadening of the laser comb, a check was experimented for the presence of beat notes. Therefore, both comb and CW laser were made to interfere in a fibre. Both comb and CW beams are coupled by aspheric collimation lens to one of the two coupler arms (setup at page 126).

The temperature of CW master laser is set to 22.755 °C by a Peltier cell. It is supplied by a tunable current of 378 mA providing an optical output power of 170 mW. The output radiation is spatially manipulated by a couple of cylindrical lens to get a Gaussian mode, then passes through two optical isolators preventing reflections and are polarization-tilted by a waveplate and injected in the coupler via another aspheric collimation lens.

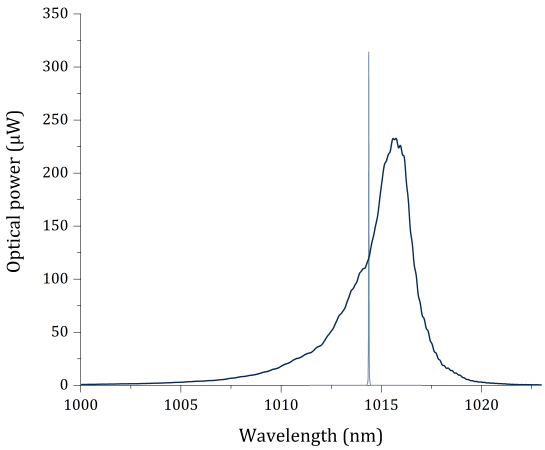

Figure 4.13: Spectra of the comb (dark blue) and CW laser (light blue), measured by the spectrum analyser.

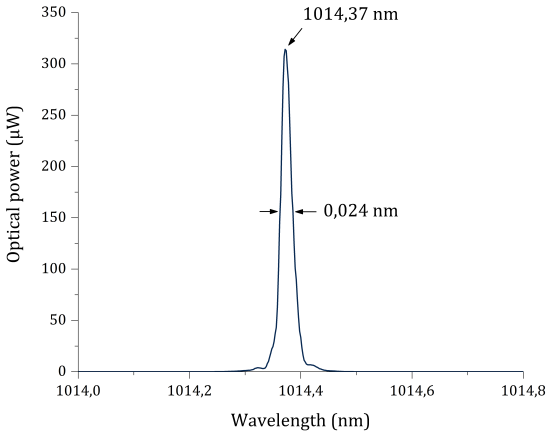

Figure 4.14: Detail of the CW spectrum.

The Figure 4.14 depicts the actual spectrum. The lab environment conditions shifted the peak from the planned value of 1014.8 nm to 1014.4 nm. This was not a trouble, since the experiment aim was to demonstrate beat notes were possible: the CW laser will simply interfere with a different comb tooth. The original working point could be restored acting on laser temperature control and cavity piezoelectric actuators moving the internal grating. Its spectral width is 0.024 nm.

The only coupler available at the moment was designed for a 50:50 coupling at 1550 nm, so it did not provide an equal power splitting in the right spectral region. At 1015 nm, the coupling ratio is about 90:10. However, the experiment goal was to prove optical heterodyning interference: since beat notes depend on the product of two laser intensities (cfr. equation (4.11)), an imperfect balance does not affect so much the output signal: in one branch the CW laser power is higher but the comb signal is weaker and vice versa in the other branch.

The two coupler output branches are connected to a photodiode (PD) with a bandwidth of 100 MHz (ThorLabs InGaAs PIN, model PDB415C) and a spectrum analyser

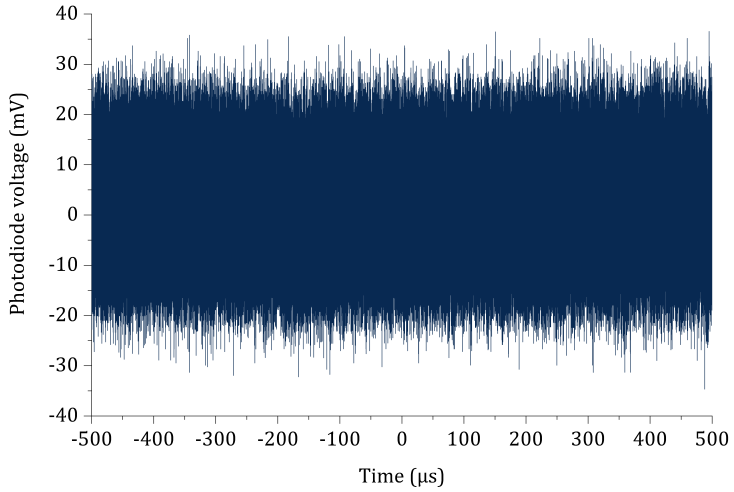

Figure 4.15: Photodiode output signal, coupled AC 50 MΩ.

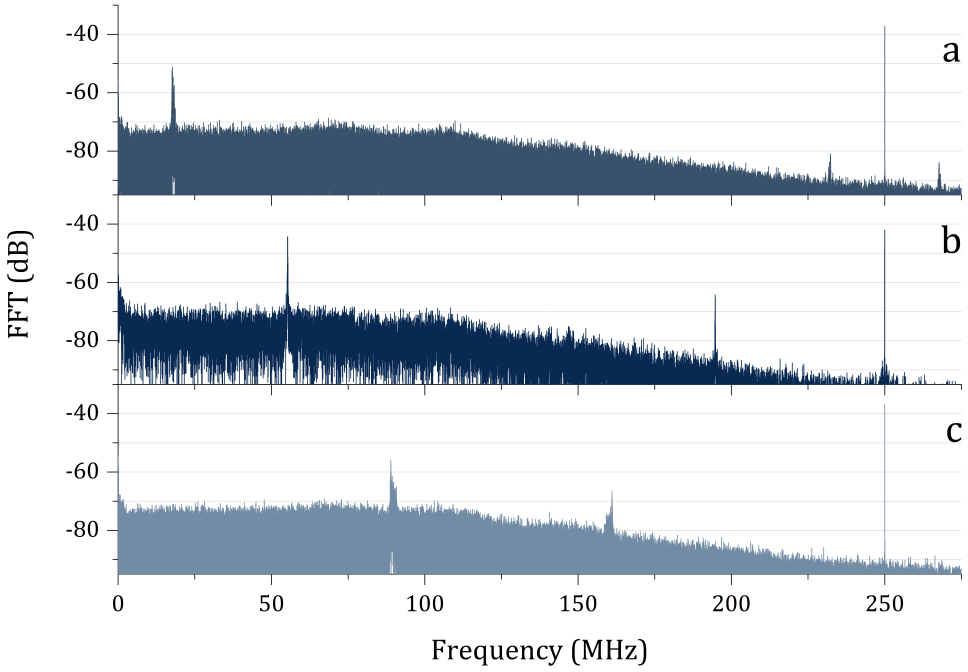

Figure 4.16: Three Fast Fourier Transform of the beats signal, taken at different times.

(Andor) which provides spectral information for further live-view optimizations of the setup. An oscilloscope handles the PD output signal which shown in Figure 4.15, with an amplitude of ±30 mV. In order to avoid PD saturation, the CW laser power is attenuated till the overall signal remains below saturation threshold (∼3 V). Then, the oscilloscope

is AC coupled with the correct impedance adapter and the Fast Fourier Transform (FFT) for an observation time of about 1 µs is computed, resulting in the PD signal spectrum shown in Figure 4.16.

The beat notes are clearly visible, with a signal-to-noise ratio between 20 dB and 25 dB. The peak at 250 MHz is the comb frequency rate, which is fixed, while the two beat peaks moves over time, as pictured in the graphs *a)*, *b)* and *c)* taken at different time instants. Since the CW laser frequency lies between two comb teeth, called f_1 and f_2, the detected interference signal is composed by two beats, one at frequency $\Delta f_1 = f_1 - f_C W$ and the other at $\Delta f_2 = f_2 - f_{CW}$, as described in Section 4.2.3 and Figure 4.4. In fact, the beats are counter-shifting over time: if one drifts in lower frequency, the other moves in higher ones and vice versa. This happens because the comb teeth are stabilized while the CW laser is not, hence its frequency oscillates between two teeth making the low frequency beats drifting. Since the distance between the two teeth is fixed at 250 MHz, if Δf_1 increases, then Δf_2 decreases, giving rise to the counter-shift behaviour. The rightmost beat a smaller amplitude due to the photodiode limited bandwidth. It is worth pointing out that multi-mode instabilities can also be detected with this setup, since beat has no more a delta-like shape, as shown for example in the plot *c)* of Figure 4.16.

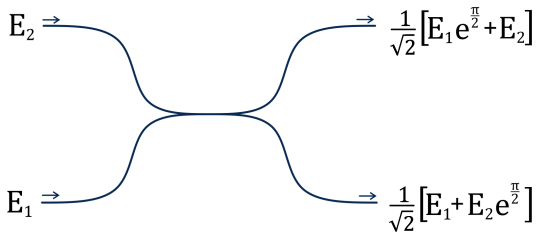

Figure 4.17: Schematic illustration of a synchronous 3 dB coupler.

In conclusion, the detection of beats between a suitably treated and amplified frequency comb source and a continuous laser in the spectral region of 1010 nm-1020 nm has been demonstrated. Further setup improvements could enhance signal-to-noise ratio. First of all, the use of a coupler designed for the correct spectral region can result higher mode-coupling efficiency, also removing Faby-Pérot modulation effects that can occur in the comb-broadened spectrum. In addition, using a 3-dB synchronous coupler the two output signals have the same optical power but a different phase: the fields are shifted of π. This effect can be exploited in a balanced detector, where two different photodiode signals are subtracted, thus reducing a lot the noise and amplifying the π-shifted signal (the ThorLabs PDB415C has a CMRR of 25 dB). In fact, as shown in Fig 4.17, each input signal is $\frac{\pi}{2}$-shifted between two output replicas.

So, recalling the results of Section 4.2.2, the PD first output, labelled as "+", will be a signal proportional to an intensity

$$I_+ = \frac{1}{2}\varepsilon_0 nc\langle\left|E_1 + E_2 e^{\frac{\pi}{2}}\right|^2\rangle = I_1 + I_2 + 2\sqrt{I_1 I_2}\cos(2\pi\Delta f t + \frac{\pi}{2}) \tag{4.17}$$

while at the PD second output, labelled as "-" there will be

$$\begin{aligned} I_- &= \frac{1}{2}\varepsilon_0 nc\langle\left|E_1 e^{\frac{\pi}{2}} + E_2\right|^2\rangle = \frac{1}{2}\varepsilon_0 nc\langle\left|e^{\frac{\pi}{2}}(E_1 + E_2 e^{-\frac{\pi}{2}})\right|^2\rangle = \\ &= I_1 + I_2 + 2\sqrt{I_1 I_2}\cos(2\pi\Delta f t - \frac{\pi}{2}) \end{aligned} \tag{4.18}$$

where Δf represents the frequency difference between CW and one comb tooth.

Hence, the balanced detector performs a subtraction, thus the constant terms are eliminated and the PD output is proportional to

$$I_+ - I_- = 2\sqrt{I_1 I_2}\left[\cos(2\pi\Delta f t + \frac{\pi}{2}) - \cos(2\pi\Delta f t - \frac{\pi}{2})\right] \tag{4.19}$$

which can be simplified making use of the known prosthaphaeresis formula, namely $\cos(\alpha) - \cos(\beta) = -2\sin(\frac{\alpha+\beta}{2})\sin(\frac{\alpha-\beta}{2})$, obtaining

$$I_+ - I_- = 2\sqrt{I_1 I_2}[-2\sin(2\pi\Delta f t)\sin(-\pi)] = 4\sqrt{I_1 I_2}\sin(2\pi\Delta f t) \tag{4.20}$$

So, a balanced photodiode can delate the equal constant intensities and sum the oscillating term as it is π-shifted. This kind of detection should also reduce the noise, since it is not self correlated thus cancelled in a balanced mode acquisition. Moreover, signal intensity has a straight 3 dB enhancement. This two effect should improve of several decibels the signal-to-noise ratio.

Another possible improvement is the use of a photodiode with wider voltage range, such that the oscilloscope can operate the FFT on higher signal amplitude than the actual 60 mV.

Lastly, to improve S/N any comb teeth except from the two interfering with CW laser should be eliminated, because they do not contribute thus being only a source of noise. This is quite impossible, but further tightening the comb spectral band is easily done with a suitable band-pass filter or adding an high-pass one to the actual setup (in series to the low-pass), reducing the power spectral density below 1014 nm.

Conclusion and future development

An ultrafast laser source for coherent Anti-Stokes Raman spectroscopy was designed for generating the three pulses (pump, Stokes and probe) needed for third order interaction with the sample, exploiting non-linear optics techniques for second harmonic generation, spectrum broadening and shaping, pulse amplification and time compression. After the realization of the acquisition system for CARS maps and related Raman spectra, the source has been tested in different configurations, excitation bands, powers, focal lengths and on different substances, both liquid and solid scatterer. Among all, a special focus was placed on NaDPA due to its high concentration in Bacillus anthracis spores. Well-defined spectra were acquired in a stand-off configuration at 15 cm, collecting less than 3 % of the scattered signal. Simulations of measurements at lower numerical apertures have shown the scalability of the system, capable of acquire good spectra even with low apertures and low exposure configurations. Raman fingerprinting of *B. subtilis* endospores has been successfully shown. Then, an imaging system was built, exploiting motor mirrors to move the laser source to different points of the sample and acquire their Raman spectra. Finally, the real possibility of exploiting such an experimental system to do imaging on unknown samples thanks to machine learning algorithms for molecular fingerprint recognition of known substances was shown.

Future developments could focus on further optimisation for stand-off measurements of bacterial spores, for examples using samples with different concentration to determine the detection threshold; spores sample was spread on a glass substrate: other kind substrates (as metal or wrinkled surfaces) could be experimented, pointing out differences and detection limits; more sophisticated algorithms for NRB removal or peaks recognition could be implemented; moreover, a larger number of reference spectra available for machine learning training would enhance its capability of molecule recognition, even with very weak signals: this would lower the exposure time, allowing faster measurements.

Regarding imaging, experimentation can continue on other more elaborate samples, different molecules with complex spectra or on substances that give a less intense CARS signal. In order to scan larger sample areas, it could be necessary to implement a telescope system that reduce the imaged area with compatible monochromator dimensions. Alternatively, it could be possible to motorize detection lenses so that they follow the source shift: the radiation would be always centred in monochromator slit and distortions at the edges of the image would be avoided, at the cost of a significant increase in the complexity of the detection system. An alternative, valid only for small samples at short distances, could be to motorize the sample, eliminating the galvo-mirrors (which have a transmission of 80 %) and keeping fixed and stable the illumination and detection stages.

Moving to the side work conducted on the laser stabilization for metrology purposes, a system has been developed to amplify and broaden the spectrum of radiation from a laser comb to reach lower frequencies, so that it can be coupled to a monochromatic laser performing Doppler broadening thermometry measurements. Using the technique of heterodyne detection, it is possible to visualise the frequency drift of the continuous laser by indirectly analysing its interference patterns with a comb tooth, the so called of optical beat notes, which can be detected with electronic instrumentation. A beat with a signal-to-noise ratio of 20-25 dB was achieved, even without the best possible measure conditions (unsuitable coupler and no PD balanced detection).

Further developments of the project have already been set up [44]. An ultrastable commercial oscillator around 1540 nm (master laser, OEwaves whispering gallery mode single mode CW laser, with a linewidth of 30 Hz) should transfer its frequency stability to the 1015 nm (slave) laser by direct-optical digital synthesis (DDS) that uses the comb as a bridge oscillator to cover the 100 THz difference between the two frequencies.

The master laser will be long term stabilized against the nearest tooth of the comb. A low bandwidth Phase-Loop-Lock (PLL) electronics controls the frequency drift of the master-comb lasers beatnote (δ_{mc}) against a stable local RF oscillator. In this way absolute frequency traceability of the master, and consequently the slave one (1015 nm) is guaranteed.

Indeed, comb teeth spacing (250 MHz) and carrier-envelope-offset frequency, f_{ceo}, will be phase-locked to a RF reference oscillator. In alternative, the locking can be supplied by beatnotes from a primary standard disciplined 1540 nm laser provided via optical fibre link from INRIM laboratories, providing a 1-s stability of 10^{-14} and an accuracy of 10^{-15}. The DDS systems will be used to compare frequency fluctuations of the 1015 nm laser against the ultra-stable 1540 nm oscillator avoiding the contribution of comb frequency noise.

Beatnotes of both CW lasers (master and slave) against the nearest teeth of the comb, once the f_{ceo} contribution is removed from them, will be compared and the 1540 nm one is multiplied by a factor that takes into account their frequency difference, allowing to directly relate the 1015 nm and 1540 nm frequencies (ν_s and ν_m), as

$$(\delta_{sc} - f_{ceo}) - \frac{N_s}{N_m}(\delta_{mc} - f_{ceo}) = \nu_s - \frac{N_s}{N_m}\nu_m \tag{4.21}$$

where N_m and N_s are the comb orders of closest teeth.

When this beatnote difference is phase-locked to a RF stable local oscillator by using a broad bandwidth PLL, the frequency linewidth of the slave laser is expected to be the master oscillator linewidth increased by the factor N_s/N_m, which leads to a final expected linewidth of 600 Hz with an absolute frequency traceability against the primary frequency standard, which is the one expected for DBT mercury measure. Coherence will be transferred from the ultra-stable oscillator to the 1015 nm laser, without being affected by comb noise which is used only as a long-band transfer. Consequently, all frequency conversion chain will be stabilized, including the 235 nm UV source for metrological spectroscopy on mercury transition.

Acronyms

A list of the most used acronyms in the thesis, followed by their full names and the page reference where to find more information.

SHG Second Harmonic Generation (page 22)

DFG Difference Frequency Generation (page 28)

OPA Optical Parametric Amplifier (page 28)

NOPA Non-collinear Optical Parametric Amplifier (page 34)

CARS Coherent Anti-Stokes Raman Spectroscopy (page 52)

NRB Non-Resonant Background (page 54)

WLC White Light Continuum (page 71)

APF Amplified Parametric Fluorescence (page 37)

SPM Self Phase Modulation (page 43)

DBT Doppler Broadening Thermometry (page 117)

SVEA Slowly Varying Envelope Approximation (page 15)

GVD Group Velocity Dispersion (page 16)

GDD Group Delay Dispersion (page 18)

TOD Third Order Dispersion (page 18)

FWHM Full Width at Half Maximum

IR Infrared: 0.75–1000 µm spectral region

NIR Near-Infrared: 0.75–1.4 µm spectral region

VIS Visible spectrum: 380–750 nm region

UV Ultarviolet spectrum: 10–380 nm region

BBO β-BaB_2O_4

PCF Photonic Crystal Fibre (page 125)

FROG Frequency Resolved Optical Gating (page 125)

CCD Charge-Coupled Device, sensor technology for cameras

NA Numerical Aperture (page 97)

CW Continuous Wave, referred to laser output

ML Mode-Locking (page 119)

YDFA Ytterbium Doped Fibre Amplifier (page 125)

FFT Fast Fourier Transorm

Bibliography

[1] Shaowei Li, Yanping Li, Rongxing Yi, Liwei Liu, and Junle Qu. Coherent anti-Stokes Raman scattering microscopy and its applications. *Frontiers in Physics*, 8:515, 2020.

[2] Edoardo Vicentini, Alessio Gambetta, Gianluca Galzerano, Paolo Laporta, Kelly Curtis, Kenneth McEwan, Christopher R Howle, and Nicola Coluccelli. Fiber laser system for standoff coherent Raman spectroscopy. *Optics Letters*, 45(21):5925–5928, 2020.

[3] Dmitry Pestov, Xi Wang, Gombojav O. Ariunbold, Robert K. Murawski, Vladimir A. Sautenkov, Arthur Dogariu, Alexei V. Sokolov, and Marlan O. Scully. Single-shot detection of bacterial endospores via coherent Raman spectroscopy. *Proceedings of the National Academy of Sciences*, 105(2):422–427, 2008.

[4] Marshall T. Bremer, Paul J. Wrzesinski, Nathan Butcher, Vadim V. Lozovoy, and Marcos Dantus. Highly selective standoff detection and imaging of trace chemicals in a complex background using single-beam coherent anti-Stokes Raman scattering. *Applied Physics Letters*, 99(10):101109, 2011.

[5] Dmitry Sergeyevich Pestov. Detection of bacterial endospores by means of ultrafast coherent Raman spectroscopy.

[6] Andrew M. Weiner. *Ultrafast optics.*

[7] G. Cerullo. Notes of the course *Physics of ultrafast processes.*

[8] Cristian Manzoni and Giulio Cerullo. Design criteria for ultrafast optical parametric amplifiers. *Journal of Optics*, 18(10):103501, 2016.

[9] Giulio Cerullo and Sandro De Silvestri. Ultrafast optical parametric amplifiers. *Review of scientific instruments*, 74(1):1–18, 2003.

[10] Nikogosyan D. N. Dmitriev V. G., Gurzadyan G. G. and Lotsch H. K. V. *Optics of nonlinear crystals Handbook.*

[11] Tomas Stanislauskas, Ignas Balčiūnas, Viktorija Tamuliene, Rimantas Budriūnas, and A. Varanavičius. Analysis of parametric fluorescence amplified in a noncollinear optical parametric amplifier pumped by the second harmonic of a femtosecond Yb:KGW laser. *Lithuanian Journal of Physics*, 56, 04 2016.

[12] Azhar H. Malik, M. Azeem, M. Yousaf Hamza, and S. Tariq. Comparison of interaction of GVD and SPM between normal and anomalous dispersion regimes of single mode fiber. In *2008 Second International Conference on Electrical Engineering*, pages 1–6, 2008.

[13] Marc-Michael Blum and Harald John. Historical perspective and modern applications of attenuated total reflectance – Fourier transform infrared spectroscopy (ATR-FTIR). *Drug Testing and Analysis*, 4(3-4):298–302, 2012.

[14] Gábor Keresztury. *Raman Spectroscopy: Theory*. American Cancer Society, 2006.

[15] Daniel F. Walls. Quantum theory of the Raman effect. *Zeitschrift für Physik A Hadrons and nuclei*, 237(3):224–233, 1970.

[16] Ji-Xin Cheng and X. Xie. Vibrational spectroscopic imaging of living systems: An emerging platform for biology and medicine. *Science*, 350:aaa8870–aaa8870, 11 2015.

[17] Andreas Volkmer, Lewis D. Book, and X. Sunney Xie. Time-resolved coherent anti-Stokes Raman scattering microscopy: Imaging based on Raman free induction decay. *Applied Physics Letters*, 80(9):1505–1507, 2002.

[18] Dmitry Pestov, Robert K. Murawski, Gombojav O. Ariunbold, Xi Wang, Miaochan Zhi, Alexei V. Sokolov, Vladimir A. Sautenkov, Yuri V. Rostovtsev, Arthur Dogariu, Yu Huang, and Marlan O. Scully. Optimizing the laser-pulse configuration for coherent Raman spectroscopy. *Science*, 316(5822):265–268, 2007.

[19] Hans U. Stauffer, Joseph D. Miller, Mikhail N. Slipchenko, Terrence R. Meyer, Benjamin D. Prince, Sukesh Roy, and James R. Gord. Time- and frequency-dependent model of time-resolved coherent anti-Stokes Raman scattering (CARS) with a picosecond-duration probe pulse. *The Journal of Chemical Physics*, 140(2):024316, 2014.

[20] Vikas Kumar, R. Osellame, R. Ramponi, G. Cerullo, and M. Marangoni. Background-free broadband CARS spectroscopy from a 1-MHz ytterbium laser. *Opt. Express*, 19(16):15143–15148, Aug 2011.

[21] Eksma Optics. *BBO - crystal manual*.

[22] Ibsen Photonics. *Spectrometer grating manual*.

[23] A. Brodeur and S. L. Chin. Ultrafast white-light continuum generation and self-focusing in transparent condensed media. *J. Opt. Soc. Am. B*, 16(4):637–650, Apr 1999.

[24] Audrius Dubietis, Gintaras Tamosauskas, Rosvaldas Šuminas, Vytautas Jukna, and Arnaud Couairon. Ultrafast supercontinuum generation in bulk condensed media (invited review). 06 2017.

[25] Maximilian Bradler, P. Baum, and Eberhard Riedle. Femtosecond continuum generation in bulk laser host materials with sub-µJ pump pulses. *Applied Physics B*, 97:561–574, 11 2009.

[26] Arlee V. Smith. *SNLO Guide*.

[27] Hongying Liu, Tian Lan, Xiaomei Chen, and Guoqiang Ni. Dispersion compensation based on prism compressor. In *Optical Manipulation Conference*, volume 10252, page 102521D. International Society for Optics and Photonics, 2017.

[28] Adam Driks. The Bacillus anthracis spore. *Molecular Aspects of Medicine*, 30(6):368–373, 2009. Anthrax.

[29] S. Stockel, S. Meisel, M. Elschner, P. Rosch, and J. Popp. Identification of Bacillus anthracis via Raman spectroscopy and chemometric approaches. *Analytical chemistry*, 84(22):9873–9880, 2012.

[30] Sandra R.B.R. Sella, Luciana P.S. Vandenberghe, and Carlos Ricardo Soccol. Life cycle and spore resistance of spore-forming Bacillus atrophaeus. *Microbiological Research*, 169(12):931–939, 2014.

[31] Ewelina Piktel, Katarzyna Pogoda, Maciej Roman, Katarzyna Niemirowicz, Grażyna

Tokajuk, Marta Wróblewska, Beata Szynaka, Wojciech M Kwiatek, Paul B Savage, and Robert Bucki. Sporicidal activity of ceragenin CSA-13 against Bacillus subtilis. *Scientific reports*, 7(1):1–12, 2017.

[32] Cecilia Clivati, Stefania Gravina, Antonio Castrillo, Giovanni A. Costanzo, Filippo Levi, and Livio Gianfrani. Tunable UV spectrometer for Doppler broadening thermometry of mercury. *Opt. Lett.*, 45(13):3693–3696, Jul 2020.

[33] Ian M. Mills, Peter J. Mohr, Terry J. Quinn, Barry N. Taylor, and Edwin R. Williams. Redefinition of the kilogram, ampere, kelvin and mole: a proposed approach to implementing CIPM recommendation 1 (CI-2005). *Metrologia*, 43(3):227–246, apr 2006.

[34] Miguel A. Martin-Delgado. The new SI and the fundamental constants of nature. *European Journal of Physics*, 41(6):063003, oct 2020.

[35] Bureau International des Poids et Mesures. *The International System of Units (SI) - 9th edition.*

[36] Graham Machin. The kelvin redefined. *Measurement Science and Technology*, 29(2):022001, jan 2018.

[37] Livio Gianfrani. Linking the thermodynamic temperature to an optical frequency: recent advances in Doppler broadening thermometry. *Philosophical Transactions of the Royal Society A: Mathematical, Physical and Engineering Sciences*, 374(2064):20150047, 2016.

[38] Steven T. Cundiff and Jun Ye. Colloquium: Femtosecond optical frequency combs. *Rev. Mod. Phys.*, 75:325–342, Mar 2003.

[39] Nathalie Picqué and Theodor W. Hänsch. Frequency comb spectroscopy. *Nature Photonics*, 13(1):146–157, 2019.

[40] Tara Fortier and Esther Baumann. 20 years of developments in optical frequency comb technology and applications. *Communications Physics*, 2(1):1–16, 2019.

[41] Charles J. Koester and Elias Snitzer. Amplification in a fiber laser. *Appl. Opt.*, 3(10):1182–1186, Oct 1964.

[42] Juichi Noda, Katsunari Okamoto, and Yutaka Sasaki. Polarization-maintaining fibers and their applications. *Journal of Lightwave Technology*, 4(8):1071–1089, 1986.

[43] Menlo Systems GmbH. *FC 1500 Optical Frequency Synthesizer User Manual.*

[44] Pablo Cancio Pastor, Roberto Eramo, Alessia Sorgi, and Cecilia Clivati. Ultra-stable optical oscillator transfer for precise UV spectroscopy. In *2018 IEEE International Frequency Control Symposium (IFCS)*, pages 1–2. IEEE, 2018.

[45] K. Razdan and D. A. Van Baak. Demonstrating optical beat notes through heterodyne experiments. *American Journal of Physics*, 70(10):1061–1067, 2002.

[46] A. Malik, M. Azeem, M. Y. Hamza, and S. Tariq. Comparison of interaction of GVD and SPM between normal and anomalous dispersion regimes of single mode fiber. *2008 Second International Conference on Electrical Engineering*, pages 1–6, 2008.

[47] T. Lang, A. Harth, J. Matyschok, T. Binhammer, M. Schultze, and U. Morgner. Impact of temporal, spatial and cascaded effects on the pulse formation in ultrabroadband parametric amplifiers. *Optics Express*, 21(1):949–959, 2013.

[48] R. Antipenkov, A. Varanavičius, A. Zaukevičius, and A. P. Piskarskas. Femtosecond Yb:KGW MOPA driven broadband NOPA as a frontend for TW few-cycle pulse systems. *Opt. Express*, 19(4):3519–3524, Feb 2011.

[49] Matz Liebel, Christoph Schnedermann, and Philipp Kukura. Sub-10-fs pulses tunable from 480 to 980 nm from a NOPA pumped by an Yb:KGW source. *Optics letters*, 39(14):4112–4115, 2014.

[50] Mikas Vengris, Nail Garejev, Gintaras Tamošauskas, Augustas Čepėnas, Lukas Rimkus, Arūnas Varanavičius, Vytautas Jukna, and Audrius Dubietis. Supercontinuum generation by co-filamentation of two color femtosecond laser pulses. *Scientific reports*, 9(1):1–9, 2019.

[51] Rimantas Budriūnas, Tomas Stanislauskas, and Arūnas Varanavičius. Passively CEP-stabilized frontend for few cycle terawatt OPCPA system. *Journal of Optics*, 17(9):094008, 2015.

[52] Light Conversion. *Orpheus: Collinear optical parametric amplifier of white light continuum.*

[53] J Piel, Eberhard Riedle, L Gundlach, R Ernstorfer, and R Eichberger. Sub-20 fs visible pulses with 750 nJ energy from a 100 kHz noncollinear optical parametric amplifier. *Optics letters*, 31(9):1289–1291, 2006.

[54] Maximilian Bradler, Christian Homann, and Eberhard Riedle. Mid-IR femtosecond pulse generation on the microjoule level up to 5 µm at high repetition rates. *Optics letters*, 36(21):4212–4214, 2011.

[55] Christian Schriever, Stefan Lochbrunner, Patrizia Krok, and Eberhard Riedle. Tunable pulses from below 300 to 970 nm with durations down to 14 fs based on a 2 MHz ytterbium-doped fiber system. *Optics letters*, 33(2):192–194, 2008.

[56] Julien Nillon, Olivier Crégut, Christian Bressler, and Stefan Haacke. Two MHz tunable non collinear optical parametric amplifiers with pulse durations down to 6 fs. *Optics express*, 22(12):14964–14974, 2014.

[57] Marcel Schultze, Thomas Binhammer, Guido Palmer, Moritz Emons, Tino Lang, and Uwe Morgner. Multi-µJ, CEP-stabilized, two-cycle pulses from an OPCPA system with up to 500 kHz repetition rate. *Optics express*, 18(26):27291–27297, 2010.

[58] J. Janszky, G. Corradi, S. A. Arakelian, R. N. Gyuzalian, and S.B. Sogomonian. Sum frequency beam analysis for the determination of the temporal characteristics of ultrashort light pulses. *Optical and quantum electronics*, 16(2):109–115, 1984.

[59] Daniel Herrmann, Raphael Tautz, Franz Tavella, Ferenc Krausz, and Laszlo Veisz. Investigation of two-beam-pumped noncollinear optical parametric chirped-pulse amplification for the generation of few-cycle light pulses. *Optics express*, 18(5):4170–4183, 2010.